



Ph.D. in Physics
XXXIII Cycle

Ph.D. Thesis

Characterization of AGB stars in the LMC
in the JWST era

Ph.D. candidate: Ester Marini

Supervisors: Prof. Paolo Ventura
Dr. Flavia Dell'Agli

Il cucchiaio non esiste

Acknowledgements

Mentre sono qui a cercare le parole giuste da scrivere in questa pagina, mi risulta impossibile non sorridere ripensando alla splendida esperienza vissuta in questi tre anni di dottorato. Il tempo passato all'osservatorio di Monte Porzio è fonte di bellissimi ricordi ed esperienze, che porterò sempre nel cuore. La mia gratitudine va alle persone con cui ho avuto il piacere e l'onore di interagire durante il mio dottorato e che hanno contribuito a rendere questa esperienza una grande occasione di arricchimento non solo professionale, ma anche personale. Sebbene questa possa sembrare una frase banale e prevedibile, nel mio caso non potrei trovare parole più adeguate e, soprattutto, veritiere.

La prima persona che sento di ringraziare è Paolo, per quanto sia davvero difficile riassumere la mia gratitudine in poche righe. Lo ringrazio per la generosità, la pazienza e l'inesauribile entusiasmo con cui mi ha seguita in questi quattro anni e per tutto quello che mi ha insegnato. Lo ringrazio per le risate che hanno riscaldato le mie (freddissime!) giornate di lavoro all'Osservatorio e per le bellissime giornate passate in luoghi meravigliosi, quando immersi nella natura, quando con i volti sollevati verso magnifiche, estasianti opere d'arte.

Ringrazio Flavia, altra colonna portante di questo mio percorso, per avermi supportata e guidata con estrema pazienza e disponibilità. Grazie per essere stata un'inesauribile fonte di approfondimenti, stimoli, complicità e, soprattutto, di ispirazione.

Ringrazio Franca, per i preziosi consigli e per l'entusiasmo che è riuscita a trasmettermi nelle occasioni in cui ho avuto il grande onore di interagire con lei.

Grazie alla prof Corinne, per aver giocato un ruolo fondamentale nel percorso che mi ha portato a questo grande momento di realizzazione personale e professionale.

Un grazie speciale va alle mie compagne di innumerevoli avventure, Lara, Rebecca, Carolina ed Elena, per avermi insegnato che “per essere una donna devi vestire il cervello di carattere, personalità e coraggio”. A Tommaso, per avermi mostrato che, in fondo, gli ostacoli esistono per essere superati. A Lorenzo, Cristian e Matteo, per stimolarmi a grattare la superficie, così da guardare oltre.

Ringrazio di cuore la mia famiglia, senza la quale non sarei diventata la persona che sono oggi. Ai miei genitori, per avermi sempre incoraggiata e sostenuta, per avermi insegnato

l'importanza di inseguire i propri sogni, e che la vera ricchezza a cui ambire nella vita non è quella che si trova nel portafogli. Alle mie sorelle, a cui più di tutti dedico questo lavoro e a cui tengo più che a me stessa. Grazie a zia Stefania e zio Pino, i miei secondi genitori, e a Pierluigi, mio fratello.

Infine, un grazie speciale ad Alessandro, che non si stanca mai di credere in me, anche quando io non riesco a farlo. Grazie per esserci sempre, per essere il mio porto sicuro dove rifugiarmi quando il mare è in tempesta.

Abstract

We study dust production by asymptotic giant branch (AGB) stars, by comparing *Spitzer* data of Large Magellanic Cloud evolved sources, with results from stellar evolution and dust formation modelling. This research will support the scientific community, to benefit from the data which will be provided by the incoming *James Webb* Space Telescope (*JWST*), to study AGB stars in galaxies.

Dust production by oxygen-rich AGBs is provided by low-mass stars, during the phases prior to becoming carbon stars, and by massive AGBs, experiencing Hot Bottom Burning.

On the other hand, carbon stars define a sharp reddening sequence, with the dust production rate connected with the amount of carbon dredged up in the surface regions.

Based on the distribution of AGB stars in the different colour-magnitude planes, we conclude that the filters of the MIRI camera, mounted onboard of *JWST*, most recommended to study AGB stars are F770W, F1000W, F1800W and F2550W.

Contents

List of Figures	xi
List of Tables	xix
Introduction	1
1 The Asymptotic Giant Branch evolution	7
1.1 Early-AGB evolution	8
1.2 The thermally pulsating AGB phase	8
1.2.1 Thermal Pulses	10
1.2.2 The Third Dredge Up	12
1.2.3 Hot Bottom Burning	14
1.3 AGB and post-AGB stars in the LMC: results from evolution modelling . .	18
1.3.1 Post-AGB evolution modelling	24
1.4 Formation of dust in the winds of AGB stars	26
1.4.1 Oxygen-rich AGB stars	29
1.4.2 Carbon stars	31
1.4.3 The overall dust production by AGB stars	34
1.4.4 Change in the optical depth of AGB stars	36
2 The <i>JWST</i>: a new perspective of the study of AGB stars in the Local Group galaxies	41
2.1 Past, present and future of the AGB investigations in the Local Group galaxies	41
2.2 Selection of the sample	45
2.3 Synthetic spectral energy distribution	48
2.3.1 C stars	50
2.3.2 M stars	51

2.4	Characterizing the sample: a methodology to determine the AGB stars progenitors and their dust production in the <i>JWST</i> diagrams	53
3	Peculiar sources in the LMC: from their SEDs to their origins	55
3.1	Stars surrounded by iron dust in the LMC	56
3.1.1	Iron dusty AGB stars in the LMC	56
3.1.2	Evolution and dust production of metal-poor, massive AGB stars	59
3.1.3	Understanding iron-dusty stars	61
3.2	Dual-dust evolved stars in the LMC	62
3.3	A class of post-AGB stars	64
3.4	Faint, dusty AGB stars	66
4	M-type stars: a <i>JWST</i> perspective	69
4.1	Scarcely obscured, dust-free stars	71
4.2	Low-mass dusty M-type AGB stars	73
4.3	Stars undergoing hot bottom burning	76
4.3.1	Massive AGB stars in the colour-magnitude planes	78
4.3.2	Stars undergoing soft HBB	79
4.3.3	Highly obscured O-rich AGBs	79
4.3.4	A class of massive AGBs in the very late AGB phases?	80
4.4	Iron-dust stars	81
4.4.1	Massive AGB stars with iron dust	81
4.4.2	Post-AGB stars with iron dust	82
4.5	Dual dust chemistry AGB stars	84
4.5.1	Dual-dust stars in the colour-magnitude planes	84
4.6	M-type evolved stars in the colour-colour diagrams	85
4.7	Studying oxygen-rich AGB stars with <i>JWST</i>	87
5	Understanding carbon stars in the LMC with a look at the <i>JWST</i>	91
5.1	An overall view of carbon stars in the LMC	91
5.2	Stars in the thermal pulse phase	95
5.3	A signature of hot bottom burning?	95
5.4	Extreme carbon stars	99
5.5	The winds of carbon stars: what we learn from IRS spectra?	104
5.5.1	Silicon carbide	104
5.5.2	MgS	104
5.5.3	Graphite	107

5.6	Carbon stars in the <i>JWST</i> observational planes	108
	Conclusions	121
6	Appendix	125
6.1	ATON	125
6.2	The equations of the wind structure and dust formation	127
6.3	Fit results of the LMC AGB sample	129
	References	153

List of Figures

1.1	Left: internal chemical stratification of a star of initial mass $5M_{\odot}$ and metallicity $Z = 0.008$, during an interpulse phase. Right: zoom of the stratification shown in the left panel, in the intershell region.	9
1.2	Left: evolution of the total luminosity (black) and of the CNO (blue), 3α (red) and pp (green) contributions as a function of time, during the evolutionary stage after ~ 5000 yr since the beginning of the TP-AGB phase. Right: same as the left panel, focused on two TPs in a row. Both panels refer to a $5M_{\odot}$ star with metallicity $Z = 0.008$	10
1.3	Left: Evolution of the total luminosity of the $5M_{\odot}$ star with metallicity $Z = 0.008$ shown in Fig. 1.1 and 1.2. Time is counted starting from the beginning of the TP-AGB phase. Right: variation of the mass loss rate for the same model shown in left panel. In both panels, the evolution of the mass of the star is indicated with a black line.	11
1.4	Internal structure of a $3M_{\odot}$, $Z = 0.008$, model star during two inter pulse phases. M_{core} (green, dashed line) and M_{H} (magenta, dotted-dashed line) indicate, respectively, the mass of the CO core and of the H-free region. M_{bce} (blue, solid line) refers to the base of the convective envelope. Time is counted from the beginning of the TP-AGB phase.	13
1.5	Evolution of the luminosity (left panel) and of the temperature at the base of the convective envelope (right), as a function of the current mass of the star, for stars with initial mass $7M_{\odot}$ (magenta), $6M_{\odot}$ (blue), $5M_{\odot}$ (red), $4M_{\odot}$ (green), $3M_{\odot}$ (black) and $2M_{\odot}$ (yellow), and metallicity $Z = 0.008$	14
1.6	Variation of the surface mass fractions of ^{12}C , ^{16}O and ^{14}N during the AGB phase of a $5M_{\odot}$, $Z = 0.008$ model star. The results are shown as a function of the current mass of the star.	16

1.7	Variation during the AGB phase of the surface mass fraction of ^{16}O as a function of the current mass of the star, for the same $Z = 0.008$ model stars shown in Fig. 1.5 and for the lower metallicity, $Z = 0.001$, model star (dashed lines).	17
1.8	Variation during the TP-AGB phase of the luminosity as a function of the current stellar mass, of model stars with initial mass $7M_{\odot}$ (magenta), $6M_{\odot}$ (blue), $5M_{\odot}$ (red), $4M_{\odot}$ (green), $3M_{\odot}$ (black), $2M_{\odot}$ (yellow) and $1.25M_{\odot}$ (cyan), for the metallicities $Z = 0.008$ (left panel) and $Z = 0.001$ (right panel). 18	18
1.9	Variation during the TP-AGB phase of the temperature at the bottom of the convective envelope, as a function of the current stellar mass, of the same models shown in Fig. 1.8.	19
1.10	The evolution of the surface $^{12}\text{C}/^{16}\text{O}$ ratio, as a function of the current stellar mass, of model stars of $3M_{\odot}$ (blue), $2.5M_{\odot}$ (red), $2M_{\odot}$ (green), $1.5M_{\odot}$ (black) and $1.25M_{\odot}$ (yellow), with metallicity $Z = 0.008$ (left panel) and $Z = 0.001$ (right panel).	20
1.11	The evolution of the surface mass fraction of ^{12}C , as a function of the current stellar mass, of models with initial mass $7M_{\odot}$ (magenta), $6M_{\odot}$ (blue), $5M_{\odot}$ (yellow), $4M_{\odot}$ (green), $3M_{\odot}$ (black), $2.5M_{\odot}$ (cyan) and $2M_{\odot}$ (red), for the metallicities $Z = 0.008$ (left panel) and $Z = 0.001$ (right panel).	21
1.12	The path traced in the HR diagram by stars of initial mass $1M_{\odot}$ (magenta line), $1.1M_{\odot}$ (black), $1.25M_{\odot}$ (red), $1.4M_{\odot}$ (black), $1.6M_{\odot}$ (blue), $1.75M_{\odot}$ (green), during the latest AGB phases and the post-AGB phase.	25
1.13	Size of the Al_2O_3 and olivine dust grains (orange and black lines, scale on the left axis) and the gas temperature (green line, right axis) as a function of the distance from the centre of the star, for a model star of initial mass $6M_{\odot}$ and metallicities $Z = 0.008$ (solid lines) and $Z = 0.001$ (dashed lines), during an intermediate stage of the AGB evolution, when HBB is active.	30
1.14	Size of the carbon and SiC dust grains (magenta and blue lines, scale on the left axis) and the temperature of the gas (green line, right axis) as a function of the distance from the centre of the star, for a star with initial mass $2.5M_{\odot}$. The figure refers to a late phase of the AGB evolution, before the beginning of the WD cooling.	31
1.15	Dust mass produced during the AGB phase by the various species of dust considered in the present work, as a function of the current mass of the star. Left and right panels refer to stars of metallicity $Z = 0.008$ and $Z = 0.001$, respectively.	35

- 1.16 The evolution of carbon stars of diverse initial mass as a function of the optical depth τ_{10} . The left and right panels show the variation of the luminosity and of the effective temperature, respectively. 37
- 1.17 The variation of the optical depth at $10\mu\text{m}$ as a function of the current mass of the star, for model stars of different initial mass and metallicity $Z = 0.008$ (left panel) and $Z = 0.001$ (right). For $M \leq 3M_{\odot}$ stars the coloured part of the track corresponds to the C-star phase, while the M-type phase is indicated in light, grey. 38
- 2.1 Left: faintest flux for a point source that can be detected at SNR= 10 in a 10,000s integration with *JWST*. Fluxes are given in Jy (scale on the left axis) and AB mag (right axis). Right: detail of the left panel, in the wavelength range $\lambda \leq 30 \mu\text{m}$ (<https://jwst.stsci.edu>) 45
- 2.2 Transmission curves of the MIRI filters (Glasse et al., 2015) 46
- 2.3 Variation of the expected SED during 4 different stages of the AGB evolution of a star of $2M_{\odot}$, when considering only solid carbon and SiC (left) and when also graphite and MgS are considered (right). The 4 phases are characterized by different optical depths, indicated in the three panels. In these examples the number density of the seeds of amorphous carbon dust relative to hydrogen is assumed 10^{-13} , whereas the density of the seeds of the other dust species are scaled with respect to amorphous carbon according to the percentages given in the two panels. Panels b1 and b2 show the transmission curves of MIRI filters in el. sec-1. 50
- 2.4 The expected variation of the SED during 4 evolutionary phases of the AGB evolution of a star of initial mass $1.5M_{\odot}$ (a1 and a2) and $5M_{\odot}$ (a3). For clarity's sake, a1 shows only the M-star stage of the $1.5M_{\odot}$ model star, whereas the phases after the carbon star stage is reached are shown on a2. The 4 phases are characterized by different optical depths in the three panels. Panels b1 b2 and b3 show the transmission curves of MIRI filters in el. sec-1. 52
- 3.1 The distribution of the M-stars sample described in Section 2.2, indicated by grey squares, in the colour-magnitude (F770W-F2550W, F770W) plane. Blue squares refer to the group of stars discussed in the present chapter. Green points and orange triangles indicate the synthetic colours assumed by stars of metallicity $Z = 0.008$ and mass, respectively, $4M_{\odot}$ and $6M_{\odot}$, during the AGB evolution. Magenta diamonds refer to the evolution of a $5M_{\odot}$ star of metallicity $Z = 0.001$ before the achievement of the C-star stage. 57

- 3.2 The comparison between the observed IRS spectra (in black) and the synthetic SED (in red), obtained by assuming different luminosities and percentages of the various dust species, for three stars in the LMC, interpreted as low-metallicity massive AGBs (see text for discussion). Blue diamonds refer to IRAC [3.6], [4.5], [5.8], [8.0] photometry. The green, dashed line in the middle panel refers to a synthetic SED, calculated assuming iron-free dust around the star. 58
- 3.3 The variation of the main physical and chemical properties of stars of metallicity $Z = 0.001$ and initial mass $4M_{\odot}$ (black lines), $5M_{\odot}$ (red) and $6M_{\odot}$ (blue), during the AGB phase. Times on the abscissa are counted since the beginning of the thermally pulsating phase. The left and middle panels show, respectively, the variation of the luminosity and of the surface mass fractions of ^{16}O (solid) and ^{24}Mg (dashed). The right panel, which refers to the $5M_{\odot}$ model, shows the AGB variation of the main quantities relevant to dust production, namely the number densities of silicon (red), magnesium (black), iron (blue, dashed) and water molecules (green), the latter being given by the oxygen excess with respect to carbon and silicon; all the four quantities are normalized to the number density of hydrogen. We mark the three AGB phases during which dust in the circumstellar envelope has the following composition: a) mainly silicates; b) a dominant solid iron contribution with traces of silicates and alumina dust; c) no silicates formation is possible, due to lack of water molecules. Grey shading in the left and right panels indicate the AGB phases of the $5M_{\odot}$ star corresponding to phase (b). 59
- 3.4 Distribution of the sample of M-stars in the LMC described in Section 2.2, indicated by grey points, in the colour-colour (left panel) and in the colour-magnitude diagrams (middle panel). Blue open diamonds and red full triangles indicate the two groups of stars discussed in the present paper. The black lines indicate a theoretical reddening sequence of M-stars, assuming a dust composition made up of silicates, alumina dust and solid iron. Typical values of the optical depth at $1 \mu\text{m}$ and the position of the sources SSID 8 and SSID 4595 are indicated. In the right panel is shown a diagram with a colours combination able to clearly separate the stars among the two groups described in Sections 3.3 and 3.4. Magnitudes come from (Zaritsky et al., 2004). 63

- 3.5 The comparison between the observed IRS spectra (in black) and the synthetic SED (in red) of the stars in the LMC sample described in 2.2: SSID 8 (left panel, see Fig. 3.4) and SSID 4595 (right). Blue diamonds show *Spitzer* photometry from Meixner et al. (2006) and optical + near IR data, available in the literature. The grey line in the right panel refers to SSID 111, classified as a post-AGB stars from Woods et al. (2011). In both panels we report the luminosity and effective temperature of the star, and the following parameters for the internal and outer dust shells: optical depth (at $10 \mu\text{m}$), dust temperature, dust composition and distance from the central star. For SSID 8 we modelled the emission from the central star with a COMARCS atmosphere corresponding to the best-fit effective temperature, while for SSID 4595 we used a black body spectrum. 65
- 3.6 The evolution of the luminosity during the AGB evolution of stars of initial masses $1.2M_{\odot}$ (black line), $1.5M_{\odot}$ (blue) and $2M_{\odot}$ (orange). 67
- 4.1 The distribution of the LMC stars belonging to the sample described in Section 2.2 in various observational planes, built with different combinations of the filters of the MIRI camera and 2MASS K_S filter. The values of the magnitudes have been obtained by convolving *Spitzer* IRS data with the transmission curves of the various filters. For the stars indicated with open points, the IRS data were truncated to $\sim 14.2 \mu\text{m}$; in these cases we used the MIPS [24] magnitude, when available, as a rough estimate of F2550W, as the difference between them is only a few hundredth of magnitudes. The different symbols refer to the various classes of objects, according to the legend reported in the top, left panel. Among these, grey triangles indicate sources for which we could not provide a reliable interpretation on the basis of their SED. The solid and dashed lines indicate the reddening sequence of low-mass, oxygen-rich AGB stars and of massive AGBs experiencing HBB, respectively (see Section 4.2 and 4.3 for details). The black points along the two sequences refer to typical values of the optical depth τ_{10} , which are indicated in the top, left panel. 70
- 4.2 Period - Luminosity diagram of the LMC M-type stars in the sample presented in Section 2.2, for which OGLE periods are available. Luminosities are those reported in Table 4.1. Symbols are the same used in Fig. 4.1. . . . 72

4.3	The <i>Spitzer</i> IRS spectra (black line) of two stars, selected among those interpreted as low-mass AGBs, taken along the obscuration sequence of low-mass stars shown in Fig. 4.1. The photometry is indicated with blue diamonds. The best fit, indicated with the red line, is obtained by assuming the luminosity, dust composition and optical depth indicated in the two panels.	73
4.4	Best-fit model for the source SSID 22 (same symbols and colours as in Fig. 4.3 are used), interpreted as a low-mass star that has just reached the C-star stage (see text for details). The values of the overall luminosity and of the parameters of the internal and external dust layers are indicated.	75
4.5	The <i>Spitzer</i> IRS spectrum (black line) of 4 stars, selected among those interpreted as massive AGBs, currently experiencing HBB, taken along the obscuration sequence indicated with a dashed line in Fig. 4.1. The photometry and the best-fit (red line) are shown, with the parameters adopted.	77
4.6	IRS, photometry results and best-fit models for SSID 4267, interpreted as a post-AGB star surrounded by dust, whose composition is dominated by iron grains, evolving through the AGB and the post-AGB phase, respectively. We report the flux in the $\log(\lambda F_\lambda)$ scale, to better understand why this object was misclassified as an AGB star (see text for a discussion on this point). . .	83
4.7	The evolved, M-type stars in the sample considered in this study in the various colour-colour planes, obtained by using MIRI filters.	86
5.1	Comparison between the IRS (black lines) and the synthetic (red) spectra of a few sources in the LMC sample of carbon stars, with various luminosities and degrees of obscuration. The values of luminosities and τ_{10} reported in each panel are those allowing the best fit, corresponding to the red lines. . .	93
5.2	Luminosities and optical depths derived for the stars in the sample analysed in the present work. Green squares and red triangles indicate the progeny of $M < 2M_\odot$ stars and the higher mass counterpart, respectively; orange asterisks refer to stars with luminosities below $5000L_\odot$; magenta crosses indicate stars brighter than $20000L_\odot$; blue diamonds indicate extremely obscured objects, taken from Gruendl et al. (2008), plus the source SSID 9; the stars indicated with open diamonds are SSID 125 and SSID 190. The black lines and points in the figure refer to the evolution of models discussed in Chapter 1; the initial masses are indicated next to the corresponding track. Magenta stars indicate the results obtained by artificially increasing the mass loss rate of the stars of initial mass $1.1M_\odot$, $2.5M_\odot$, $3M_\odot$, after reaching the C-star stage.	94

5.3	Left: IRS SED of the source SSID 141, compared with our interpretation, based on synthetic modelling. Right: AGB evolution with time of the luminosity of 1.5, 2, 2.5 M_{\odot} stars; the O-rich phase was omitted for readability. The sequence of the 2.5 M_{\odot} was artificially shifted by 1 Myr for readability. The grey shaded region indicates the luminosity range of the low-luminosity stars SSID 3, SSID 66, SSID 103 and SSID 141.	96
5.4	IRS and best-fitting SED for the sources SSID 4451 (left panel) and SSID 4109 (middle). Right: evolution with time (counted since the beginning of the TP-AGB phase) of luminosity (black) and surface C/O (red track, scale on the right) of a 3.5 M_{\odot} star. The grey-shaded area indicates the phase during which the star is carbon-rich.	97
5.5	Left: IRS SED of the source SSID 4540, compared with our interpretation, based on synthetic modelling. Right: AGB evolution with time of the luminosity (black line, scale on the left) and of the surface C/O ratio (red line, scale on the right) of a 5 M_{\odot} model with metallicity $Z = 0.001$. The grey-shaded area indicates the evolutionary phase during which the star evolves as a carbon star.	98
5.6	SED fitting of 4 out of the extremely red objects studied by Gruendl et al. (2008)	100
5.7	The IRS (black) and synthetic (red) spectra of the source SSID 190.	101
5.8	Evolution of the radius (black lines, scale on the left) and surface C/O ratio (red, scale on the right) during the AGB phase of stars of initial mass 1.1 M_{\odot} (left panel), 2.5 M_{\odot} (middle) and 3 M_{\odot} (right). The thin, blue horizontal lines indicate the C=O condition, whereas the green arrows indicate the phase of rapid expansion of the star, as a consequence of the surface carbon enrichment.	103
5.9	IRS spectrum of SSID 18 (black line) compared with synthetic SEDs, corresponding to the same luminosity and τ_{10} , and different percentages of SiC+MgS and of the relative width of the MgS mantle (a_{man}) on top of SiC core. The various lines correspond to the following: red - our best-fit model, with SiC+MgS= 9% and $a_{man} = 0.05 \mu\text{m}$; green - SiC+MgS= 35% and $a_{man} = 0.02 \mu\text{m}$; blue - SiC+MgS= 9% and $a_{man} = 0.02 \mu\text{m}$; orange - SiC+MgS= 6% and $a_{man} = 0.05 \mu\text{m}$	105
5.10	IRS spectra of the sources SSID 4197 (top-left panel), SSID 4783 (top-right), SSID 4002 (bottom-left) and SSID 4692 (bottom-right), with the best fit models, obtained with the luminosities, optical depths and dust mineralogy indicated in the individual panels	106

- 5.11 IRS spectrum of SSID 4722 compared with synthetic SED, differing for the percentage of graphite. The different lines refer to percentages of 0% (orange), 15% (red), 30% (blue). 108
- 5.12 IRS spectra of the sources SSID 4794 (top-left panel), SSID 4238 (top-right), SSID 4589 (bottom-left) and SSID 4150 (bottom-right), with the best fit models, obtained with the luminosities, optical depths and dust mineralogy indicated in the individual panels. 109
- 5.13 Left: Stars in the sample described in Section 2.2 are shown in the colour-magnitude (F770W-F1800W, F1800W) plane. Same symbols of Fig. 5.2 were adopted. Black squares and triangles indicate the expected evolution of stars of metallicity $Z = 0.008$ and initial mass $1.5M_{\odot}$ and $3M_{\odot}$, respectively. Dashed lines refer to the expected evolution of $1.5M_{\odot}$ and $3M_{\odot}$ stars, when the presence of SiC+MgS and graphite grains are considered in the computation of the synthetic SED. Blue squares and red triangles, connected with dotted tracks, refer to the evolution of $Z = 0.002$ stars of initial mass $1.5M_{\odot}$ and $2.5M_{\odot}$, respectively. Magenta pentagons indicate the tracks of $1.1M_{\odot}$, $2.5M_{\odot}$ and $3M_{\odot}$ (from fainter to brighter) models, obtained by artificially increasing the mass loss rate after the jump in the stellar radius caused by the increase in the surface carbon, according to the discussion in Section 5.4. Right: distribution of stars in the colour-magnitude (F1000W-F1800W, F1800W) plane. 111
- 5.14 Left: position of the stars in the sample presented in Section 2.2 in the colour-colour (F770W-F1800W, F770W-F1130W) plane. The symbols for the stars and the evolutionary tracks are the same as in Fig. 5.13. Right: zoom of the same plane shown in the right panel, to outline the bifurcation between stars of different metallicity. 113
- 5.15 Position of the stars in the sample presented in Chapter 2 in the colour-magnitude (F1800W-F2550W, F1800W) plane. The symbols for the stars and the evolutionary tracks are the same as in Fig. 5.13. 114

List of Tables

1.1	Main properties of the $Z = 0.008$ and $Z = 0.001$ models of various initial mass. Only the mass range of the stars which become carbon stars is reported in this table. The various columns report the following quantities: 1 - initial mass; 2 - formation epoch; 3 - duration of the TP-AGB phase; 4 - luminosity range of the inter-pulse phases; 5 - final surface C/O; 6/7 - largest \dot{M} (6) and optical depth (7) reached.	23
1.2	Main physical and chemical properties of the post-AGB models discussed in the text. Cols. 1 – 3 indicate the initial mass of the star, the mass at the beginning of the AGB phase and the final mass. The time scales reported in col. 4 and 5 indicate, respectively, the age of the star and the crossing time, defined as the time interval from the point when the mass of the envelope drops below 1% of the stellar mass and the time when the effective temperature becomes $\log T_{\text{eff}} = 3.85$. The last four cols. report the surface chemical composition, in terms of the mass fractions of helium, carbon, nitrogen and oxygen.	26
1.3	Dust species considered in the present work, their formation reaction and the corresponding key element (see the text).	28
4.1	The interpretation of the sample of M-type stars analysed in the present work. The different columns report the SSID of the star (1), OGLE period (2), estimated luminosity (3), dust mineralogy (4), optical depth τ_{10} (5), evolutionary characterization (6). In the case of stars with dual-dust chemistry, we also report the optical depth and the percentages of solid carbon and SiC of the inner layer.	88
5.1	The interpretation of the sample carbon stars analysed in the present work. The different columns report the SSID of the star (1) estimated luminosity (2), dust mineralogy (3) and optical depth τ_{10} (4).	116

Introduction

Towards the final phases of the evolutionary history, the stars of mass $1 M_{\odot} < M < 8 M_{\odot}$, before the slow agony of the White Dwarf cooling, evolve through the asymptotic giant branch (hereinafter AGB) phase (see e.g. the reviews by Busso et al., 1999; Herwig, 2005; Iben & Renzini, 1983; Karakas & Lattanzio, 2014).

Despite being relatively short when compared to the hydrogen and helium core burning periods, the AGB phase is extremely important to understand the stellar feedback to the host environment, because it is characterized by large mass-loss rates (up to, or in some case higher than $10^{-4} M_{\odot}/\text{yr}$), which triggers the loss of the entire external mantle of the star. This process causes the pollution of the interstellar medium, because the surface chemical composition of the gas expelled during the AGB phase can be altered significantly with respect to the initial chemistry, by two physical mechanisms taking place in the stellar interiors: Third Dredge Up (TDU; Fujimoto et al., 1976; Iben, 1975) and Hot Bottom Burning (HBB; Renzini & Voli, 1981).

The loss of the external envelope takes place via cold and dense winds, that prove an extremely favourable environment for the condensation of gas molecules into dust. Indeed, the effects of radiation pressure on dust grains trigger the acceleration of the stellar wind, associated to the large mass-loss rates mentioned earlier. For this reasons AGB stars have been proposed among the main, if not the most important, dust manufacturers. On the other hand their role as cosmic dust producers has still to be fully understood: contrary to early investigations, which outlined the dominant role of supernovae (Maiolino et al., 2004), more recent studies stressed an important contribution from AGB stars, even at high redshift (Valiante et al., 2017, 2009, 2011).

It is for all these reasons that the interest towards AGB stars has increased considerably over the past few decades, and their important role in various astrophysical contexts has been stressed. For instance AGB stars have been recognized as important actors in the formation and evolution of their host galaxy, given the central role played by these objects in dust production and in influencing the star formation process (Draine, 2003; Gong et al., 2017;

Hollenbach & Salpeter, 1971; Mathis, 1990). Of extreme interest is also their effect on the determination of the masses and star formation rates of low- and high-redshift galaxies (Conroy et al., 2009; Maraston et al., 2006), such as their role in the chemical evolution of the Milky Way (Ginolfi et al., 2018; Kobayashi et al., 2011; Romano et al., 2010), Local Group galaxies (e.g. Schneider et al., 2014; Vincenzo et al., 2016), the interstellar medium of galaxies (e.g. Romano et al., 2017; Schneider et al., 2016), up to very high redshifts (e.g. Mancini et al., 2015). Furthermore, AGB stars have been suggested to be the main responsible of the formation of the second generation of stars in globular clusters (D’Ercole et al., 2008; Ventura & D’Antona, 2009, 2010, 2011; Ventura et al., 2001). Furthermore, the importance of studying the yields of the CNO elements from AGB stars has been recently outlined by Vincenzo & Kobayashi (2018), who stressed the importance of studying the yields of the CNO elements from AGB stars, in a paper focused on the reconstruction of the star formation history (SFH) of galaxies, based on the CNO trends observed in the interstellar medium. Finally, the determination of the amount of dust produced by AGB stars and the corresponding size distribution function is needed to determine the extinction properties associated with dust grains, which is a fundamental information to interpret the optical and near infrared data of high-redshift quasars and gamma ray burst spectra (Gallerani et al., 2010; Maiolino et al., 2004).

Assessing the role played by AGB stars in the physical contexts mentioned above requires an accurate modelling of the AGB phase, able to provide reliable gas and dust yields from stars of diverse mass and chemical composition. This has been the main motivation behind the choice of a few research groups to couple self-consistently the modelling of the AGB phase with the description of dust formation in the circumstellar envelope (Nanni et al., 2013, 2014; Ventura et al., 2014, 2012), based on the theoretical framework set up by the Heidelberg group (Ferrarotti & Gail, 2006; Gail & Sedlmayr, 1985, 1999; Zhukovska et al., 2008).

Despite these admirable efforts, the estimates of dust yields by AGB stars are still affected by several uncertainties, which can be broadly grouped into 3 distinct categories: a) the AGB evolution is strongly determined by the efficiency of two physical phenomena, still poorly known from first principles, namely convection and mass loss (Doherty et al., 2014; Karakas & Lattanzio, 2014; Ventura & D’Antona, 2005a,b); b) the dynamics of the wind is characterized by the formation of shocks, which cause significant deviations with respect to the isotropic, stationary schematization currently used (Bowen, 1988; Cherchneff, 2006); c) the dust production mechanism itself is still affected by several uncertainties, related to the scarce knowledge of the sticking coefficients of the molecules on the solid particles and

to the formation enthalpies of some solid compounds (Ferrarotti & Gail, 2006; Gail et al., 2013).

These uncertainties make the comparison with the observational evidence indispensable. Considering the difficulties associated with using the Milky Way stars, for reasons connected with the unknown distances, the vast majority of these investigations undertaken so far were based on the Magellanic Clouds (MCs), which have represented important laboratories to test theoretical predictions from stellar evolution theories, to derive information on the internal structure of AGB stars and on the efficiency of the mechanisms able to alter the surface chemical composition (Groenewegen & de Jong, 1993; Kamath et al., 2012; Karakas, 2011; Karakas et al., 2002, 2018; Marigo & Girardi, 2007; Marigo et al., 1999, 2008). Several dedicated large photometric surveys have made available to the community a plethora of observational data of AGB stars in the MCs. It is worth mentioning the Magellanic Cloud Photometric Survey (MCPS; Zaritsky et al., 2004), the Two Micron All Sky Survey (2MASS; Skrutskie et al., 2006) and HERschel Inventory of The Agents of Galaxy Evolution (HERITAGE; Meixner et al., 2010, 2013). Furthermore, the "Surveying the Agents of a Galaxy Evolution Survey" (SAGE-LMC; Meixner et al., 2006) and the Legacy program entitled "Surveying the Agents of Galaxy Evolution in the tidally stripped low metallicity Small Magellanic Cloud" (SAGE-SMC; Gordon et al., 2011), with the *Spitzer* Space Telescope, have provided spatially and photometrically complete infrared surveys of the evolved stellar populations of the MCs.

The data provided by *Spitzer* were the most notable for the studies on dust production by AGB stars. The study of the IR domain proves vital to improve the understanding of dust production by AGBs, because when dust is formed, a significant fraction of the overall energy released is at IR wavelengths. Furthermore, the mid-IR spectrum is characterized by various features, each associated to a specific dust species; this is important to infer the mineralogy of the dust formed. Indeed, the interpretation of IR observations of the MCs has received a strong push thanks to the great amount of spectroscopic data taken with IRS, the *Spitzer's* infrared spectrograph, because the fit of the IR spectra allows a more complete analysis of the various factors affecting the energy distribution, in comparison to the analysis based on photometric data (Groenewegen & Sloan, 2018; Jones et al., 2014).

The completeness of the *Spitzer* data allowed Dell'Agli et al. (Dell'Agli et al., 2015a, 2014b, 2015b) to characterize the evolved stellar population of the MCs, using the results from stellar evolution + dust formation modelling, to determine the mass, age and metallicity distribution of the AGB sources, and the dust mineralogy in their circumstellar envelope.

Recent studies attempted to extend the analysis applied to the MCs to other environments, characterized by different metallicities and star formation histories. These investigations were

mostly based on the mid-IR survey of DUST in Nearby Galaxies, with *Spitzer* (DUSTiNGS; Boyer et al., 2015a,b), which provided 3.6 and 4.5 μm *Spitzer* imaging of 50 dwarf galaxies within 1.5 Mpc. The availability of these data, complemented with *Hubble Space Telescope* HST and near-IR observations, was used to constrain the lifetimes of AGB stars in nearby galaxies (Girardi et al., 2010; Rosenfield et al., 2014, 2016) and to study dust production from AGB stars in the galaxies IC1613 (Dell’Agli et al., 2016), IC10 (Dell’Agli et al., 2018a) and Sextans A (Dell’Agli et al., 2019a).

We are now entering a new era for the studies of the evolution and dust production from AGB stars, thanks to the incoming launch of the *JWST* (Gardner et al., 2006). The *JWST* will allow an unprecedented exploration of the evolved stellar populations in the Local Universe, thus offering a unique opportunity to improving our understanding of AGB stars. Of particular interest will be the results obtained by MIRI (Rieke et al., 2015), the mid-IR camera mounted onboard the *JWST*, because the transmission curve of some of the 9 filters of the MIRI camera are overlapped with the spectral features related to the presence of specific dust species, which allows a detailed analysis of the dust mineralogy. The full exploitation of the *JWST* potentialities will allow the characterization of the evolved stellar populations observed in the galaxies of the Local Group, and possibly beyond.

To benefit from the results produced by *JWST* it is crucial to understand how dust formation works in the outflow of AGB stars and the path traced by the evolutionary tracks of AGB stars on the observational planes built with the combination of the magnitudes corresponding to the various MIRI filters.

The research presented in this work is aimed at supporting the scientific community with the ingredients required to make the most of the potential offered by the *JWST*, to follow the ideal path, which will eventually lead to an exhaustive comprehension of the properties of these still largely unknown objects and to the identification of their role as dust manufacturers in galaxies and across the Universe.

The present study, based on the pivotal role of the Large Magellanic Cloud (LMC), which harbours the most numerous sample of AGB stars, spanning a wide range of luminosities and infrared emission, has been developed along two main directions. The detailed comparison of the data-set provided by the *Spitzer* IRS instrument with the results from stellar evolution + dust formation modelling was used to shed further light on the dust formation mechanisms in the wind of AGB stars, and on the details of dust composition. The information obtained by the study of the vast sample of the evolved stars in the LMC was used to understand how AGB stars would populate the observational planes built with the MIRI filters magnitudes and, more important, the path traced by the evolutionary sequences of stars of different mass and metallicity as they evolve through the AGB.

The outcome of the present investigation was the identification of the MIRI filters most suitable to study AGB stars in galaxies, chosen on the basis of the opportunities offered to separate carbon stars from oxygen-rich objects and to characterize the individual sources based on the position on the observational planes. The results from this study, applied out of the LMC environment, will be useful to investigate the galaxies observed with *JWST*, in the attempt of characterizing their evolved stellar population, with the ultimate goal of reconstructing the star formation history and the age-metallicity relation.

The work is structured as follows. In Chapter 1, after a general description of the main points relative to the AGB evolution and to the dust production mechanism in the wind, we present and discuss the models calculated on purpose to interpret the observations, with a particular emphasis to the delicate interface between the evolution of the star and the dust formed in the circumstellar envelope; the sample of AGB stars used to study the evolved stellar population of the LMC and the modality with which we built the sequence of synthetic spectra used to interpret the combination of the spectroscopic and photometric data, are given in Chapter 2. Chapter 3 is dedicated to the description of peculiar classes of evolved stars which cannot be framed within the traditional distinction between carbon stars and oxygen-rich AGBs, for which we propose an alternative interpretation: we refer to the stars surrounded by iron dust (Marini et al., 2019a) and those with dual-dust chemistry (Marini et al., 2019b). The characterization of the individual stars investigated, with the indication of the MIRI filters most suitable for their study, are discussed in Chapter 4 and 5 for oxygen-rich (Marini et al., 2020a) and carbon stars (Dell’Agli et al., 2020; Marini et al., 2020b), respectively; the conclusions are given in Chapter 6.

1

The Asymptotic Giant Branch evolution

AGB stars can be considered as the most interesting laboratory for stellar evolution theories, as they are made up of different regions, which offer a unique variety of physical conditions, ranging from the strongly degenerate core to the tenuous envelope, which can be safely described by ideal gas laws.

The analysis developed and proposed in the present work requires an accurate description of the evolution of these stars, the variation of the overall energy release and of the surface chemical composition across the whole AGB phase. The modification of the spectral energy distribution of these objects, whose description is crucial for the interpretation of the observations, is extremely sensitive to the quantity, the mineralogy and the radial distribution of dust particles in their extended circumstellar envelope.

In the following sections we describe the most relevant stages of the evolution of these complex objects, paying particular attention to the nuclear channels most important for the determination of the total luminosity and to the efficiency of the physical mechanisms able to alter the surface chemical composition, a key factor to calculate the gas yields from these stars.

We discuss dust formation in the outflow of AGB stars, outlining how the variation of the physical and chemical properties of the star affects the dust mineralogy, the grain size distribution and the number density of the solid particles formed. These informations will be related to the infrared emission from the stars, the morphology of the spectral energy distribution, and the dust budget expected from these objects.

The role of mass and metallicity is discussed, with an accurate description of the results obtained in the present work, by means of stellar evolution and dust formation modelling, used to describe the AGB phase of stars characterized by the chemical compositions most suitable to characterize the stars nowadays evolving in the LMC.

To describe the chronology of the events occurring after the end of core helium burning we will follow the traditional approach, based on the separation between the initial, early AGB evolution and the thermally pulsating AGB phase.

1.1 Early-AGB evolution

The Asymptotic Giant Branch is the evolutionary phase which starts when the helium in the core is exhausted and the evolutionary tracks of the stars, on the HR diagram, rise up again along the Red Giant Branch (RGB). Generally speaking, AGB stars are energetically supported by two nuclear sources: a thin layer close to the CO core, where helium burning takes place, and a CNO burning shell near the base of the convective envelope (Iben & Renzini, 1983).

At the very beginning of the AGB evolution helium burning is the sole energy supply for the star. This is connected with the reaction of the star, as a whole, to the transition from core- to shell-helium burning. The consequent expansion of the stellar regions above the He-burning zone causes the general cooling of the outer layers and the temporary extinction of the H-burning activity. The exhaustion of the CNO shell and the expansion of the external envelope favour the inward penetration of the convective envelope, down to the regions enriched in helium. This phenomenon, called Second Dredge Up (SDU), occurs only for stars with $M \geq 4M_{\odot}$. In lower mass stars the gravitational energy reservoir of the envelope is not sufficient to allow the bottom of the envelope to reach the H-He discontinuity and favour the surface helium enrichment (Iben & Renzini, 1983).

As a reaction to the extinction of the H-burning nuclear activity, the surface regions contract, releasing gravitational energy, which is used to heat the outer zones of the star. This provokes the re-ignition of the CNO shell, while the CO core contracts and reach the condition of electron degeneracy. This point is traditionally assumed as the end of the early-AGB and the beginning of the thermally pulsating asymptotic giant branch phase (TP-AGB) (Herwig, 2005; Iben & Renzini, 1983).

1.2 The thermally pulsating AGB phase

The structure of an AGB star can be broadly schematized into five regions: a) a degenerate core, made up of carbon and oxygen¹; b) an internal shell, where 3α burning occurs; c) an intershell zone, whose chemistry is determined by past CNO nuclear activity; d) a more

¹We will generally refer to the central regions of AGB stars as the carbon and oxygen core, although stars in the narrow mass range $7 - 8M_{\odot}$ undergo an off-centre carbon ignition, with the development of a convective

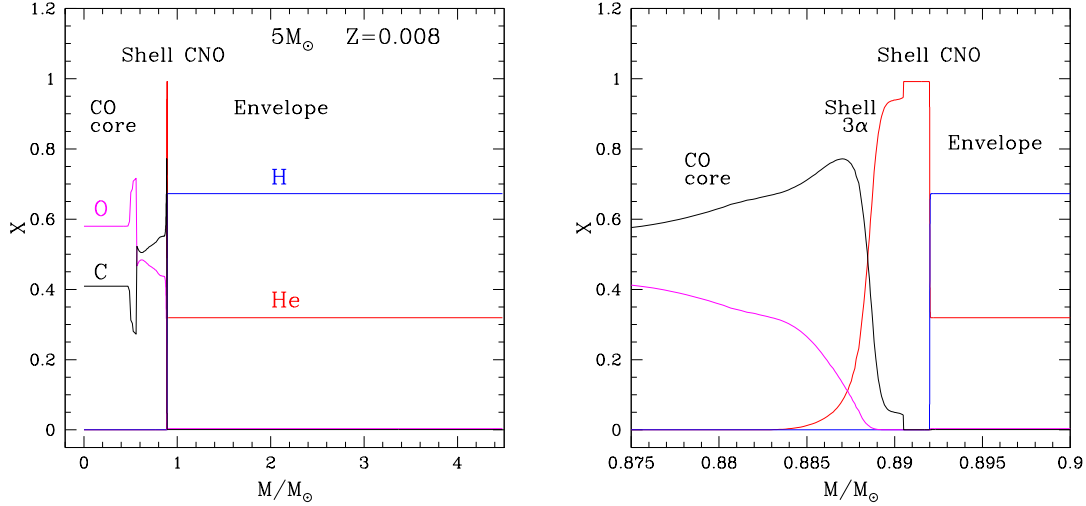


Figure 1.1 Left: internal chemical stratification of a star of initial mass $5M_{\odot}$ and metallicity $Z = 0.008$, during an interpulse phase. Right: zoom of the stratification shown in the left panel, in the intershell region.

external shell, where CNO cycling is active; e) the convective envelope. This is shown in Fig. 1.1, which reports the internal chemical stratification of an AGB star of initial mass $5M_{\odot}$ and metallicity $Z = 0.008$. The right panel of the figure displays a detail of the internal structure, corresponding to the intershell region, where is more clear how the internal chemical composition varies due to the progression of the various burning regions.

The core is the true driver of this evolutionary phase, because the degree of electron degeneracy inside it determines the temperature of the CNO shell and consequently the efficiency of hydrogen burning. The tight connection between core mass and energy release of the star was outlined in a classic paper by Paczyński (1970), who showed that if a radiative buffer separates the H-burning region from the convective envelope, the following relation holds:

$$L = 5.925 \times 10^4 \left(\frac{M_C}{M_{\odot}} - 0.52 \right) \quad (1.1)$$

The linear behaviour of luminosity with core mass can be explained by the peculiar structure of AGB stars. Indeed, owing to the presence of a degenerate core, there is a abrupt drop of the values of the thermodynamical variables at the edge between the core and the envelope, where the density decreases up to 10 orders of magnitudes. Under these conditions,

flame, that propagates inwards, causing the formation of a core made up of oxygen and neon (Doherty et al., 2010; García-Berro et al., 1997; Ritossa et al., 1996; Siess, 2006, 2007)

being the external envelope weakly bound from the gravitational point of view to the central regions, the core evolves almost completely independently of the rest of the star and the energy production within the H-burning zone is determined by the core conditions only.

1.2.1 Thermal Pulses

A distinguished feature of the AGB phase is the occurrence of the thermal pulses. They are related to the ignition of helium, which takes place under conditions of thermal instability. Indeed, a significant difference between the H- and He-burning shell is that the latter is much denser, thus, for mass conservation reasons, it has a much smaller geometrical extension. Nuclear burning in such a thin shell is thermally unstable (Schwarzschild & Härm, 1965, 1967), thus giving rise to periodic thermal pulses.

During each TP the energy released by the He-burning regions is between 10 and 10^4 stellar luminosities. Such a large energy flux favours a fast expansion of all the regions above and the consequent turning off of the H-burning activity. The reaction of the star to this unstable nuclear ignition is twofold: a) the luminosity decreases, as the main nuclear channel is extinguished; b) the surface regions contract as a reaction to H-burning extinction, until the CNO activity is restored. A long phase of stable H-shell burning follows, during which the mass of the intershell region grows, until the next thermal pulse occurs.

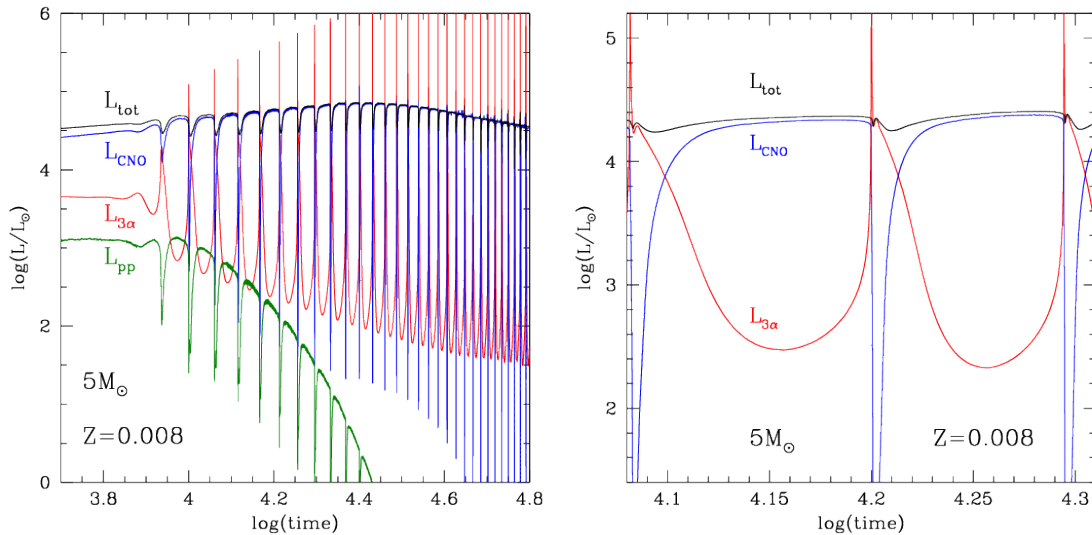


Figure 1.2 Left: evolution of the total luminosity (black) and of the CNO (blue), 3α (red) and pp (green) contributions as a function of time, during the evolutionary stage after ~ 5000 yr since the beginning of the TP-AGB phase. Right: same as the left panel, focused on two TPs in a row. Both panels refer to a $5M_{\odot}$ star with metallicity $Z = 0.008$.

The effect of TP ignition is shown in Fig. 1.2, which reports the AGB evolution of the overall stellar luminosity and of the individual contributions due to pp chain (L_{pp}), 3α reactions ($L_{3\alpha}$), and CNO cycle (L_{CNO}) of a $5M_{\odot}$ model star of metallicity $Z = 0.008$. In the left panel, which refers to the whole AGB lifetime, we see that CNO burning provides the whole energy supply to the star for $\sim 90\%$ of the AGB phase, while for the rest of the time the main contribution to the total luminosity is provided by 3α reactions. A non-negligible support from pp chain is limited to the first TPs.

The effect of the occurrence of TPs is more evident in the right panel of Fig. 1.2, which is focused only on two consecutive TPs: once the TP begins, the 3α luminosity increases, while the energy flux due to CNO cycling decreases rapidly; at the end of the thermal pulse L_{CNO} increases again. The overall luminosity is poorly affected by the TP ignition, showing up only a slight decrease, as a consequence of the extinction of CNO burning.

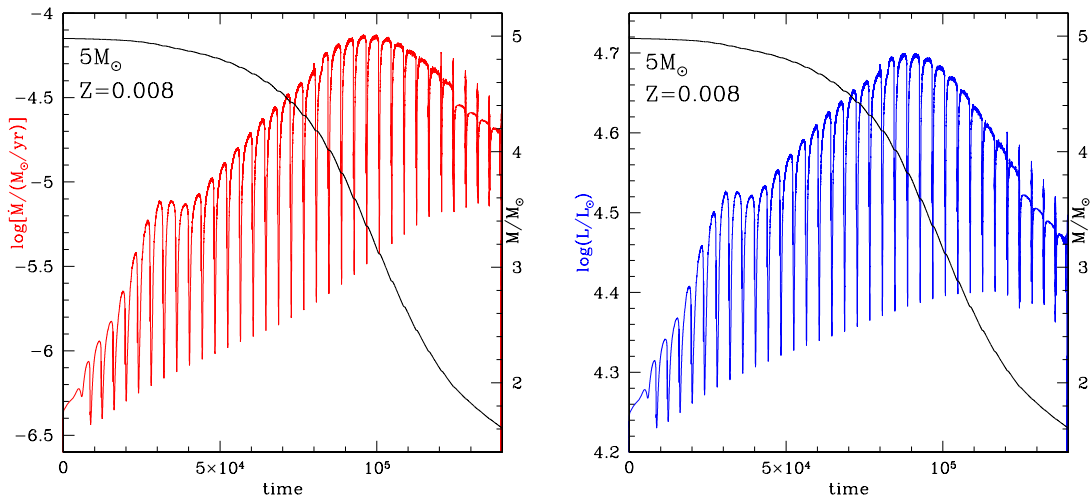


Figure 1.3 Left: Evolution of the total luminosity of the $5M_{\odot}$ star with metallicity $Z = 0.008$ shown in Fig. 1.1 and 1.2. Time is counted starting from the beginning of the TP-AGB phase. Right: variation of the mass loss rate for the same model shown in left panel. In both panels, the evolution of the mass of the star is indicated with a black line.

To have a better view of how the increase in the core mass and the gradual loss of the external mantle affect the overall energy release of the star and the time-scale of this peculiar evolutionary phase, we show in Fig. 1.3 the evolution of luminosity (left panel) and mass loss rate (right) of the $5M_{\odot}$ model star shown in Fig. 1.1 and 1.2, as a function of time, counted starting from the beginning of the TP-AGB phase. During the first part of the AGB phase the luminosity of the star increases, owing to the rise in the core mass, in turn connected with the effects of CNO nuclear burning, which increases the mass of the core; the overall luminosity

obeys to Paczynski's law (eq. 1.1) during these evolutionary phases. The increasing trend of the luminosity is reversed once a significant fraction of the envelope mass is lost, due to stellar winds: after each TP the gravitational energy budget stored in the envelope is not sufficient to resume the CNO burning rate, by contraction, at the same level as in the previous TP. The fate of AGB stars is to eventually lose their envelope, and evolve to the white dwarf stage.

The mass loss rate shown in the right panel of Fig. 1.3 follows the same trend. From the two panels of Fig. 1.3 it is clear that the general increase in both the luminosity and the mass loss rate is interrupted by periodical drops, attributable to thermal pulses. It is also noticeable that the maximum of both variables is reached almost simultaneously.

During the AGB evolution the surface chemical composition of the stars can be altered significantly, owing to the combination of nuclear activity and mixing processes, able to connect the surface regions of the star with more internal zones, currently or previously exposed to nuclear reactions.

These physical processes are extremely important for the spectroscopic identification of AGB stars and have relevant consequences for the variation of the main evolutionary properties. We believe therefore important to discuss the two main mechanisms, namely Third Dredge Up and Hot Bottom Burning, which modifies the surface chemistry of AGB stars.

1.2.2 The Third Dredge Up

Third Dredge Up (TDU) occurs shortly after the ignition of TPs, when the CNO shell is inactive (Herwig, 2005). The TDU consists in the inwards penetration of the outer convective envelope. In some cases convection can penetrate beyond the inactive H-burning shell, so that material from the intershell region is mixed in the outer envelope. As a consequence of TDU, the surface regions are enriched by the products of He burning, in particular ^{12}C .

Fig. 1.4 shows the change in the internal structure of a $3M_{\odot}$ and $Z = 0.008$ model star, reporting the variation of: a) the CO core mass, M_{core} ; b) the mass of the hydrogen-free region, M_{H} ; c) the base of the convective envelope, M_{bce} . During the interpulse phase both M_{H} and M_{bce} increase, because the CNO region moves outward in mass, while M_{core} is substantially unchanged, due to the inactivity of the 3α shell. We recognize the occurrence of TDU in the drop of M_{bce} and M_{H} , following each TP.

The most important effect of TDU is the formation of carbon stars (Iben & Renzini, 1983). The discovery of carbon stars raised an outstanding interest of the astrophysical community, because the stars form with an oxygen content significantly higher than carbon, and the mixing processes taking place during the RGB phase cause a further depletion of

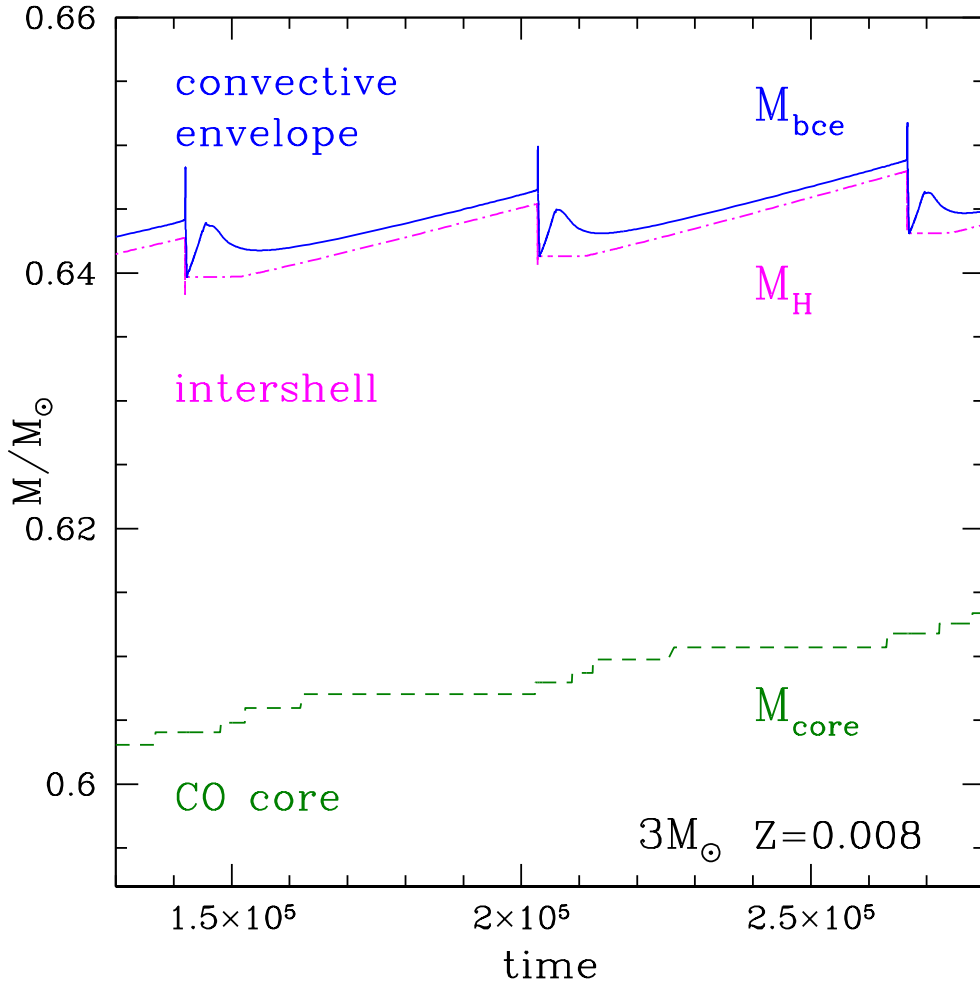


Figure 1.4 Internal structure of a $3M_{\odot}$, $Z = 0.008$, model star during two inter pulse phases. M_{core} (green, dashed line) and M_{H} (magenta, dotted-dashed line) indicate, respectively, the mass of the CO core and of the H-free region. M_{bce} (blue, solid line) refers to the base of the convective envelope. Time is counted from the beginning of the TP-AGB phase.

the surface ^{12}C , ruling out the possibility of reaching the $\text{C/O} > 1$ condition before the AGB evolution. On the other hand, repeated TDU events may cause the number of carbon nuclei in the surface regions to exceed that of oxygen ($\text{C/O} > 1$), thus favouring the formation of carbon stars.

On the physical side the carbon enrichment at the surface has strong effects on the evolution of carbon stars: as the surface of the star becomes more enriched in carbon, the

molecular opacities increase, favouring a more extended configuration of the star (Marigo, 2002; Ventura & Marigo, 2009, 2010), which evolves towards lower T_{eff} thus losing mass at larger rates (Wachter et al., 2008).

Only stars in a certain range of mass reach the carbon star stage, namely the stars with initial mass $M < 4M_{\odot}$; for stars of higher initial mass the formation of carbon star is inhibited by a different physical mechanism, Hot Bottom Burning, which will be described in the following section.

1.2.3 Hot Bottom Burning

In stars of mass $M \gtrsim 3M_{\odot}$ the temperature gradient in the regions between the edge of the degenerate core and the internal zones of the external mantle is so steep that the bottom of the convective envelope partly overlaps with the CNO burning shell. In these conditions the temperature at the base of the envelope exceeds ~ 30 MK, which favours the occurrence of an advanced proton-capture nucleosynthesis; the rapidity of convective motions makes the products of this nuclear activity to be transported to the surface, whose chemical composition will therefore reflect the effects of the nuclear reactions activated (Sackmann & Boothroyd, 1992, 1999).

The ignition of HBB leads to significant deviations from the Paczynski's law relating core mass and luminosity (Bloeker & Schoenberner, 1991), because of the partial overlapping between the envelope and the CNO burning shell, with no radiative buffer in the middle.

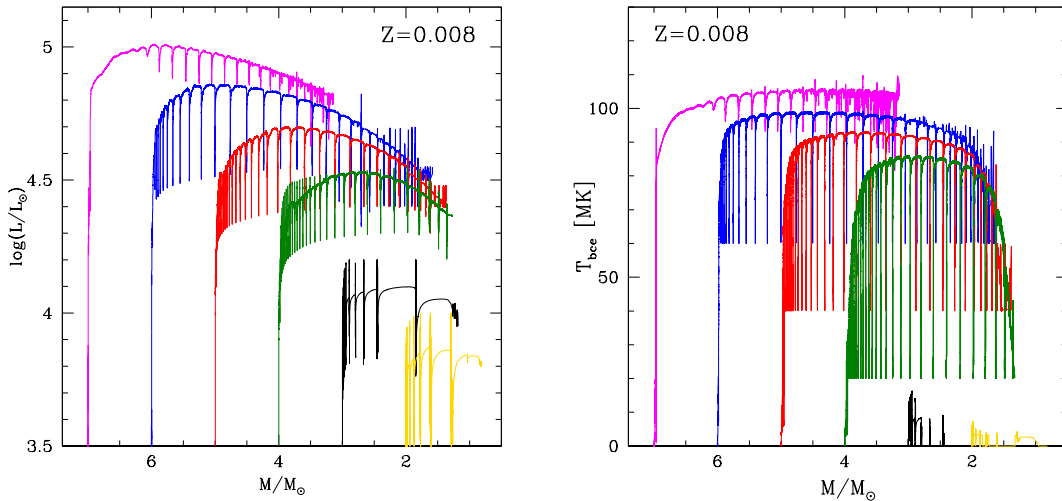


Figure 1.5 Evolution of the luminosity (left panel) and of the temperature at the base of the convective envelope (right), as a function of the current mass of the star, for stars with initial mass $7M_{\odot}$ (magenta), $6M_{\odot}$ (blue), $5M_{\odot}$ (red), $4M_{\odot}$ (green), $3M_{\odot}$ (black) and $2M_{\odot}$ (yellow), and metallicity $Z = 0.008$.

A global view of the evolution of stars experiencing HBB is shown in Fig. 1.5, reporting the variation of the luminosity (left) and of the temperature at the base of the convective envelope (right) of some model stars of initial mass $\geq 2M_{\odot}$. In this case we show the results as a function of the current mass of the star, which allows us to report all the evolutionary sequences in the same plot. Use of time would prevent this, considering the different evolutionary time-scales of stars of various mass.

As discussed in Section 1.2.1, the luminosity of the stars first increases, owing to the rise in the core mass, then decreases, due to the gradual loss of the envelope. The core mass during the AGB phase is higher the larger the initial mass of the star. The stars of higher mass thus experience conditions of stronger degeneracy, which favour steeper temperature and density gradients in the region extending from the border of the CO core to the inner layers of the external envelope. Such extreme conditions cause a higher energy release from the CNO burning shell, which reflects into a larger overall luminosity. This is the reason why the stars of higher mass are generally brighter, as shown in the left panel of Fig. 1.5. As a further confirmation that the luminosity is strongly influenced by the strength of the HBB experienced, we see in the right panel of Fig. 1.5 that the temperature at the base of the convective envelope follows the same trend of luminosity, both as a function of the initial mass of the star and for what concerns the variation with time during the AGB phase.

The high temperatures reached allow the ignition of the CN cycle in the envelope, which reprocesses, among the others, ^{12}C in ^{13}C and in ^{14}N , as clear from Fig. 1.6, which shows the variation of the surface mass fractions of the CNO elements related to the same model star shown in Fig. 1.1, 1.2 and 1.3. Therefore, HBB inhibits the formation of carbon stars because the carbon brought in the envelope is immediately converted into N, thus the C/O ratio remains below unity (Boothroyd et al., 1993). Two additional effects can be recognized in Fig. 1.6. First, the temporary, periodic rises in the ^{12}C surface mass fraction, due to TDU. Furthermore, HBB triggers the decrease in the surface ^{16}O , too, though at a lower extent than ^{12}C . The different behaviour of ^{12}C and ^{16}O is connected with the temperature required to deplete ^{16}O , ~ 80 MK, significantly hotter than for ^{12}C (~ 40 MK).

The metallicity of the star plays an important role on the HBB experienced. For a given initial mass, the lower the metallicity, the higher the temperature at the bottom of the convective envelope during the AGB phase, thus the degree of the nucleosynthesis experienced and the consequent modification of the surface chemistry (Dell’Agli et al., 2018b; Ventura et al., 2013). This reflects into the threshold mass required to ignite HBB, which is lower in $Z = 0.001$ stars ($\sim 3M_{\odot}$), compared to the $Z = 0.008$ metallicity ($3.5M_{\odot}$). We will return to this point in Section 1.3.

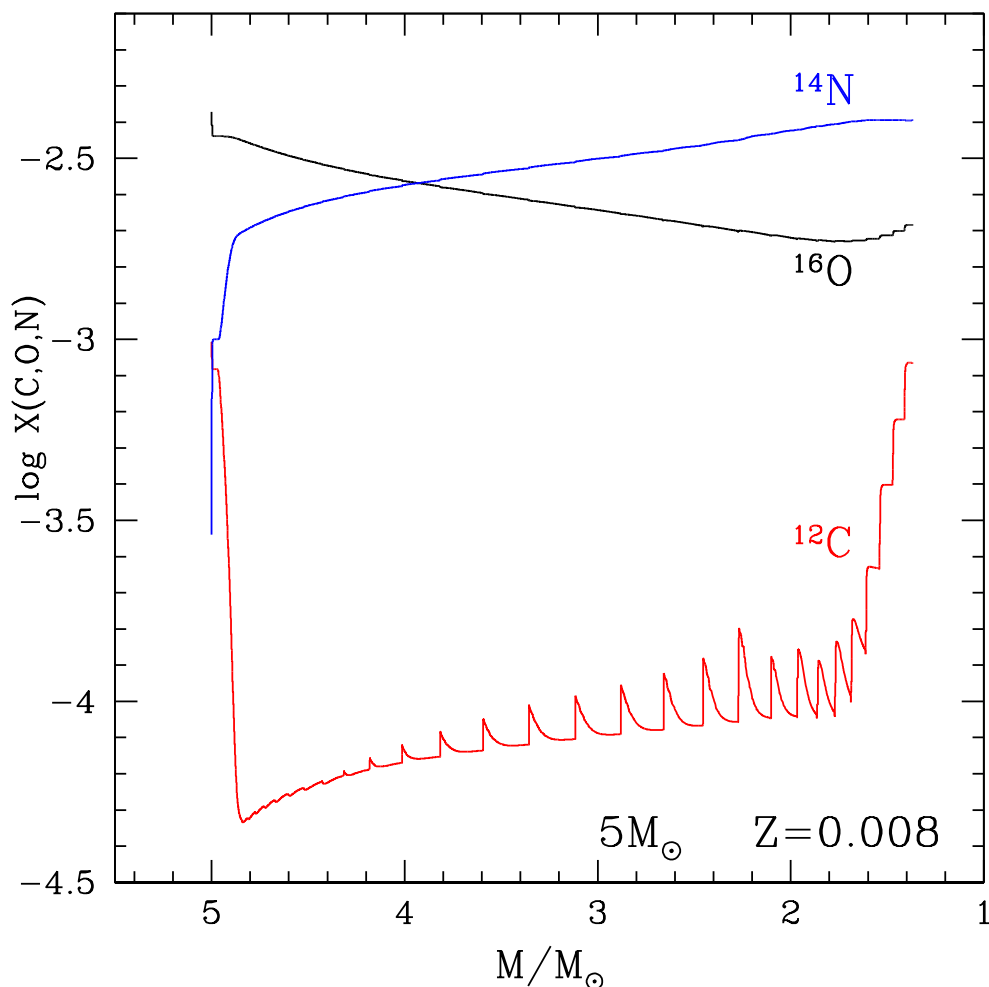


Figure 1.6 Variation of the surface mass fractions of ^{12}C , ^{16}O and ^{14}N during the AGB phase of a $5M_{\odot}$, $Z = 0.008$ model star. The results are shown as a function of the current mass of the star.

The relevant effect of metallicity on the strength of HBB is evident in Fig. 1.7, where we compare the variations of the surface mass fraction of oxygen of the same model stars shown in Fig. 1.5, with their $Z = 0.001$ counterparts. We decided to show ^{16}O , because its behaviour is more sensitive to the metallicity of the star with respect to ^{12}C . This figure clearly shows how the mass of the star affects the relative weight of TDU and HBB; we can notice a gradual transition from low-mass stars (which only experiment TDU), for which the surface ^{16}O increases during the AGB phase, to the higher mass counterparts, whose surface chemistry is affected exclusively by HBB, with the partial destruction of the surface ^{16}O .

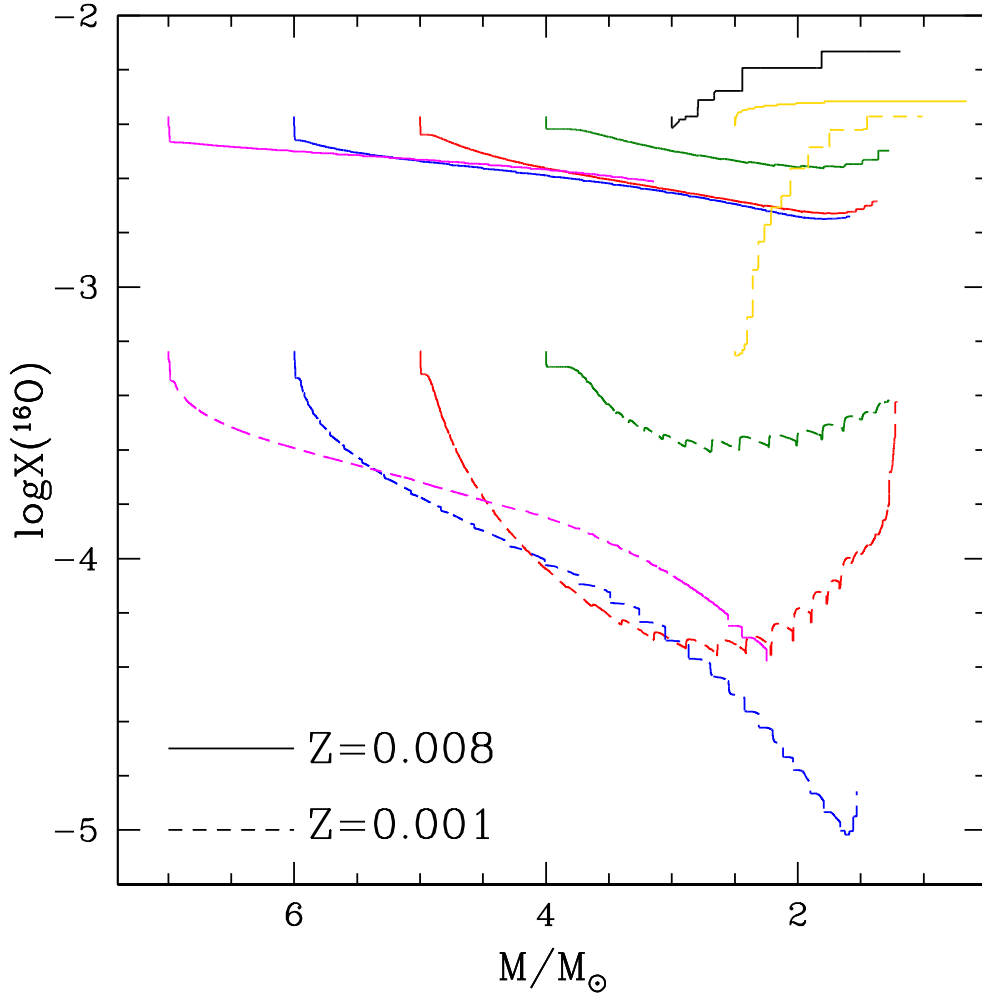


Figure 1.7 Variation during the AGB phase of the surface mass fraction of ^{16}O as a function of the current mass of the star, for the same $Z = 0.008$ model stars shown in Fig. 1.5 and for the lower metallicity, $Z = 0.001$, model star (dashed lines).

In the comparison between the behaviour of $Z = 0.001$ and $Z = 0.008$ model stars, it is clear that in the former the HBB is generally stronger and the depletion of the surface ^{16}O higher. The results shown in Fig. 1.7 outline that the relationship between the initial mass of the star and the overall extent of the ^{16}O destruction presents a turning point, with $M > 6M_{\odot}$ stars experiencing a softer nucleosynthesis with respect to their $5 - 6M_{\odot}$ counterparts, despite the higher temperatures reached at the bottom of the envelope (see right panel of Fig. 1.5). This is due to the very large mass-loss rate experienced, above $10^{-4}M_{\odot}/\text{yr}$ which makes the

star to lose the external mantle before a very advanced p-capture nucleosynthesis takes place; in other words, the time-scale of the envelope ejection becomes comparable with that of ^{16}O depletion in the $M > 6M_{\odot}$ domain.

1.3 AGB and post-AGB stars in the LMC: results from evolution modelling

As mentioned in the Introduction and addressed at the beginning of Chapter 2, one of the goals of this work is to characterize the population of AGB stars in the LMC, so far deeply explored with the *Spitzer* Space Telescope, with a view to the *JWST*. We base our analysis on models of mass in the $1M_{\odot} \leq M < 8M_{\odot}$ range and metallicity $Z = 0.008$, as it is the one shared by the majority of the stars in the LMC, now evolving through the AGB phase (Harris & Zaritsky, 2009). Furthermore, because the studies on the SFH and the age-metallicity relationship of the LMC indicate that metal-poor star formation took place, we also considered $Z = 0.001$ model stars.

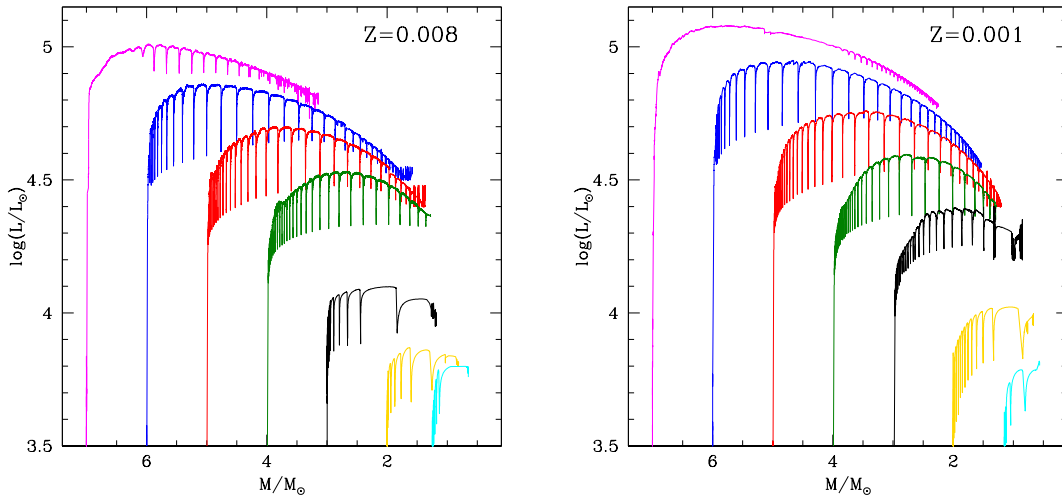


Figure 1.8 Variation during the TP-AGB phase of the luminosity as a function of the current stellar mass, of model stars with initial mass $7M_{\odot}$ (magenta), $6M_{\odot}$ (blue), $5M_{\odot}$ (red), $4M_{\odot}$ (green), $3M_{\odot}$ (black), $2M_{\odot}$ (yellow) and $1.25M_{\odot}$ (cyan), for the metallicities $Z = 0.008$ (left panel) and $Z = 0.001$ (right panel).

For the $Z = 0.008$ chemistry we preferred to replace previous models (Dell’Agli et al., 2016), used to provide an estimate of the gas yields and of the largest degree of obscuration reached by stars of different mass, with new evolutionary sequences, calculated with an

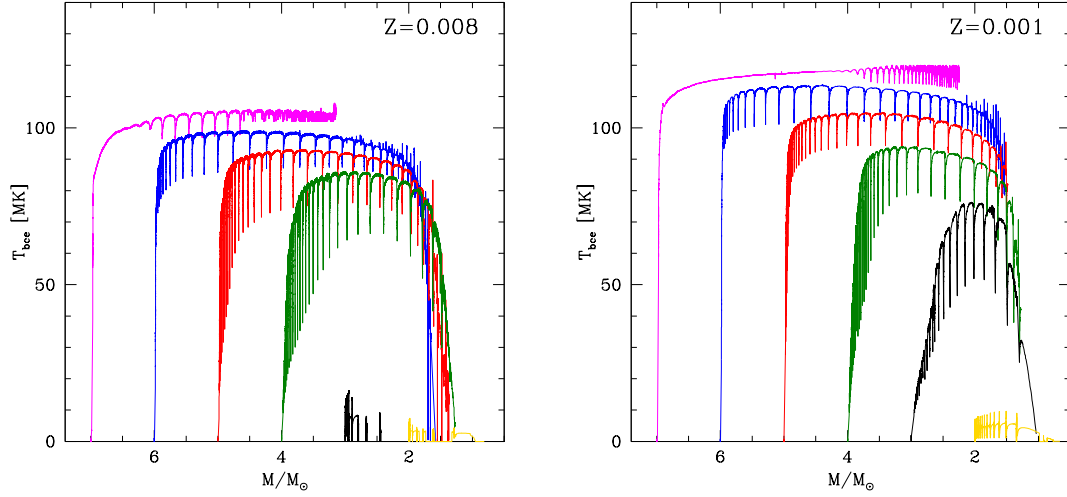


Figure 1.9 Variation during the TP-AGB phase of the temperature at the bottom of the convective envelope, as a function of the current stellar mass, of the same models shown in Fig. 1.8.

improved and more stable, on the numerical side, treatment of the TDU. This step, despite time consuming, was necessary for a detailed comparison between the theoretical evolutionary sequences and the distribution of the stars on the observational planes. A further reason to update the evolutionary models is the need to extend the computations to the post-AGB phase, considering that a few stars studied in the present work are evolving off the AGB.

In the following we discuss the main properties of the stellar models of the two above metallicities, which were calculated by means of the ATON code for stellar evolution (Ventura & D’Antona, 2009; Ventura et al., 1998). The numerical structure of the code and the physical and chemical ingredients used are presented in the Appendix. The main properties of the AGB models used in the present work are reported in Table 1.1.

Fig. 1.8 shows the variation of the luminosity during the AGB phase, for some of the model stars reported in Table 1.1, for the two metallicities considered. This figure confirms the increasing trend of the luminosity with the initial mass of the stars, M_{init} , discussed in Section 1.2.3. The luminosities of AGB stars cover a range of approximately one order of magnitude, extending from $L \sim 5 \times 10^3 L_{\odot}$ ($M_{\text{init}} \sim 1 M_{\odot}$), to $L \sim 10^5 L_{\odot}$ ($M_{\text{init}} \sim 7 - 8 M_{\odot}$). The tight relation between core mass and luminosity reflects into a difference in the duration of the whole AGB phase, according to the stellar mass (see Table 1.1). The present results indicate that the AGB phase of low-mass AGB stars lasts $\sim 1 \text{ Myr}$, whereas their counterparts of higher mass have an AGB lifetime of a few tens of kyr. Inspection of both panels of

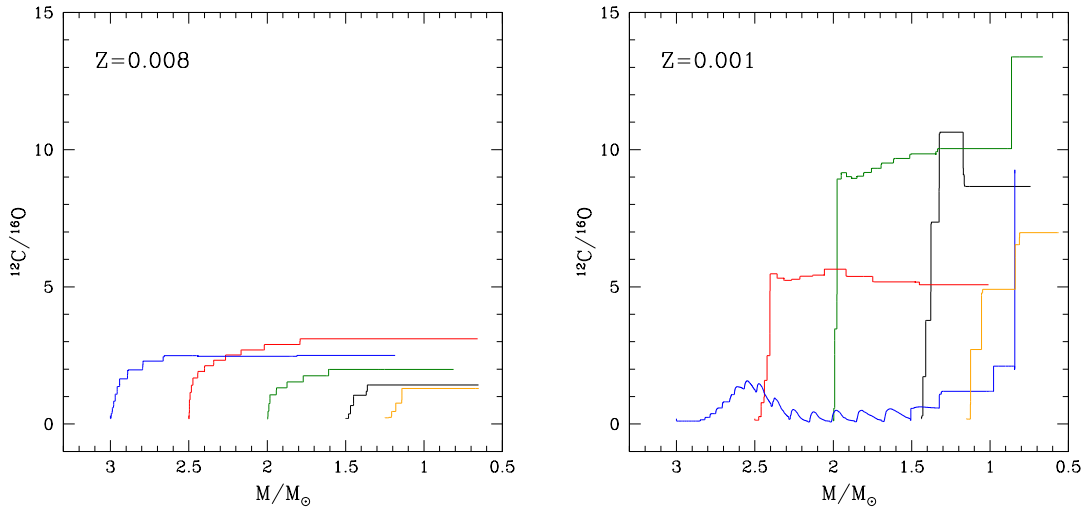


Figure 1.10 The evolution of the surface $^{12}\text{C}/^{16}\text{O}$ ratio, as a function of the current stellar mass, of model stars of $3M_{\odot}$ (blue), $2.5M_{\odot}$ (red), $2M_{\odot}$ (green), $1.5M_{\odot}$ (black) and $1.25M_{\odot}$ (yellow), with metallicity $Z = 0.008$ (left panel) and $Z = 0.001$ (right panel).

Fig. 1.8 shows that also the metallicity has an important effect on the luminosity: lower metallicity models reach larger luminosities.

In the previous sections we discussed the strong influence that TDU and the ignition of HBB have on the surface chemical evolution of AGB stars and how this reflects into a dichotomy between low- and high-mass AGB stars. We discuss this more in detail here.

Massive AGB stars, with initial mass $M > 3 - 4M_{\odot}$, remain oxygen-rich for the whole AGB phase, due to the effects of HBB. Fig. 1.9 shows the variation of T_{bce} during the AGB phase, for some of the model stars reported in Table 1.1, for $Z = 0.008$ (left panel) and $Z = 0.001$ (right panel). Inspection of Fig. 1.9 confirms the discussion in Section 1.2.3: the temperatures of the bottom of the convective envelope increase with the initial mass of the star. Moreover, a clear gap in temperature separates high-mass model stars from their lower mass counterpart ($M < 3M_{\odot}$), which do not experience HBB. On the other hand, the ignition of HBB in massive AGB stars favours a rapid increase in the luminosity (see Section 1.2.3).

Low-mass AGB stars, with initial mass $M < 3 - 4M_{\odot}$, evolve as carbon stars. These stars do not experience HBB, thus their surface chemistry reflects only the effects of TDU. The higher the number of TDU episodes experienced, the larger the surface enrichment in carbon, which consequently depends on the initial mass: model stars with initial mass $M \sim 2 - 3M_{\odot}$ achieve the largest surface abundances of carbon, as it is clear from Fig. 1.10, which shows the variation of the C/O surface ratio for model stars of different initial mass

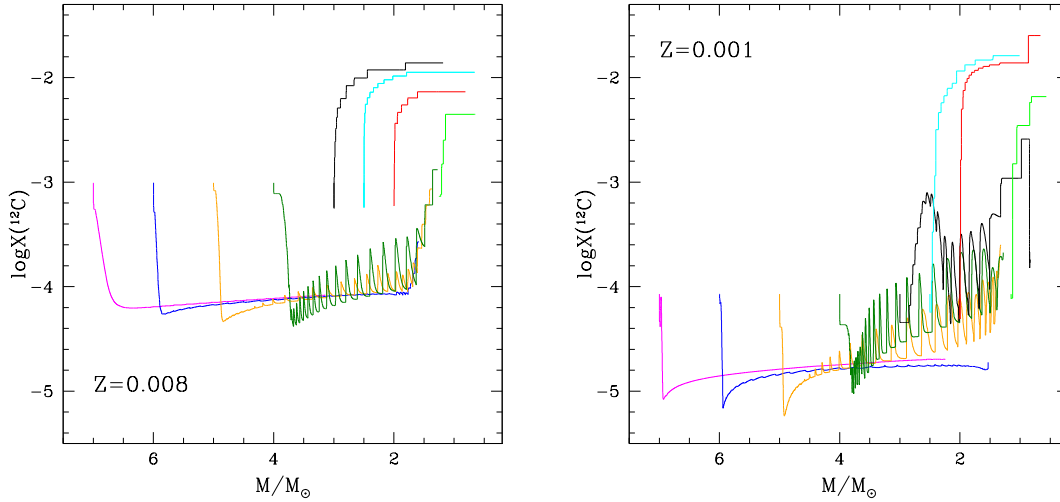


Figure 1.11 The evolution of the surface mass fraction of ^{12}C , as a function of the current stellar mass, of models with initial mass $7M_{\odot}$ (magenta), $6M_{\odot}$ (blue), $5M_{\odot}$ (yellow), $4M_{\odot}$ (green), $3M_{\odot}$ (black), $2.5M_{\odot}$ (cyan) and $2M_{\odot}$ (red), for the metallicities $Z = 0.008$ (left panel) and $Z = 0.001$ (right panel).

and for both metallicities. Inspection of this figure shows that the stars of mass below $2M_{\odot}$ and metallicity $Z = 0.008$ experience a last TP, after which they become C-stars, then start the post-AGB evolution, without experiencing further TPs. This is because after the $\text{C/O} > 1$ condition is reached a significant increase in the rate of mass loss speeds up the loss of the envelope (Lagadec & Zijlstra, 2008), thus preventing additional TPs.

To discuss how the surface chemistry of AGB stars is modified by the ignition of HBB and by the occurrence of TDU, and to investigate how the balance between these two mechanisms alters the mass fractions of the various chemical species, we show in Fig. 1.11 the variation of the surface ^{12}C for model stars of different initial mass and metallicity. We chose ^{12}C for this discussion, as it is the element most sensitive to the action of HBB and TDU, and because the effects of these two physical mechanisms on the surface abundance of ^{12}C are opposite. Therefore, the analysis of the variation of the surface ^{12}C proves the best indicator of the relative efficiency of HBB and TDU.

In the higher-mass regime ($M > 3 - 4M_{\odot}$), the activation of HBB favours the destruction of the surface carbon, exposed to proton fusion at the base of the envelope; this effect can be seen in the steep drop (by a factor ~ 20) in the surface ^{12}C during the initial AGB phases. For all the stars experiencing HBB it is evident the depletion of the surface carbon, independently of the chemical composition. The depletion of oxygen (see Fig. 1.7) takes place in more advanced phases, for the reasons discussed in Section 1.2.3. Other nuclear

reactions, e.g. proton captures by oxygen nuclei and the activation of the Ne-Na and Mg-Al-Si nucleosynthesis, demand temperatures close to 100 MK, that are reached only by low metallicity AGB stars ($Z \leq 5 \times 10^{-3}$, Dell’Agli et al. 2018a).

Turning to the low-mass domain, these stars experience TDU, which provokes a gradual increase in the surface carbon, evident in Fig. 1.11. As discussed in Section 1.2.2, repeated TDU events lead to the formation of carbon stars, with a surface C/O ratio above unity. Also in Fig. 1.11 is evident the mass threshold separating the model stars which become carbon stars from those which remain oxygen-rich, with HBB strongly depleting the surface carbon. The largest values of the surface carbon mass fraction, slightly above $\sim 1\%$, are reached by the stars of initial mass $\sim 2.5 - 3M_{\odot}$, that are exposed to a higher number of TDU episodes before they loose the external envelope, compared to their lower mass counterparts (Karakas, 2010; Karakas et al., 2018; Ventura et al., 2016b).

Before describing the final AGB phases that precede the beginning of the white dwarf (WD) cooling, we believe important to discuss the robustness of the results regarding the variation of the surface chemistry presented so far; this issue is particularly relevant for the present research, because the IR emission of evolved stars depends on the dust formed in the outflow, which, in turn, is extremely sensitive to the surface chemical composition of the star.

The surface carbon enrichment depends on the treatment of convective borders, particularly on the extension of the extra-mixed region: this zone is radiatively stable, based on the Schwarzschild criterium, yet it is reached by convective eddies, that cross the convective/radiative interface, pushed by inertia (Canuto & Mazzitelli, 1991; Chiosi, 2009; Mowlavi, 1999; Renzini & Voli, 1981; Ventura et al., 1998). The presence of extra-mixing favours the increase in the surface carbon, for two reasons: a) overshoot from the bottom of the convective envelope during the inwards penetration that follows the thermal pulse makes more carbon-rich matter to be mixed with the surface layers; b) extra-mixing from the borders of the convective shell that forms during each TP increases the strength of the pulse, in turn increasing the extent of the inwards penetration of the convective envelope (Herwig & Austin, 2004).

Previous investigations fixed the conditions for TDU to occur either by imposing the temperature of the innermost layer reached by the penetration of the convective mantle (Marigo et al., 1999), or by assuming a relation between the core mass at which TDU begins as a function of mass and metallicity (Izzard et al., 2004; Karakas et al., 2002; Marigo & Girardi, 2007). As it will be seen in Section 1.4.3, the quantity of dust that carbon stars form depends on the amount of ^{12}C transported by TDU from the internal regions to the convective envelope. In particular, the dust formed is sensitive to the time when the carbon star stage is reached and to the changes in the surface C/O. These quantities are extremely

Table 1.1 Main properties of the $Z = 0.008$ and $Z = 0.001$ models of various initial mass. Only the mass range of the stars which become carbon stars is reported in this table. The various columns report the following quantities: 1 - initial mass; 2 - formation epoch; 3 -duration of the TP-AGB phase; 4 - luminosity range of the inter-pulse phases; 5 - final surface C/O; 6/7 - largest \dot{M} (6) and optical depth (7) reached.

M/M_{\odot}	τ_{ev} [Myr]	τ_{AGB} [10^3 yr]	L/L_{\odot}	C/O	\dot{M} [M_{\odot}/yr]	τ_{10}
Z=0.008						
1.10	6530	1350	5000-5500	1.5	4.8×10^{-8}	0.60
1.25	4320	1310	6000-6300	1.3	2.9×10^{-8}	0.45
1.50	2234	1132	6000-6700	1.4	1.7×10^{-7}	1.89
2.00	1106	2400	6500-7300	2.0	5.1×10^{-7}	2.7
2.50	609	2520	8000-9200	3.0	1.5×10^{-6}	4.0
3.00	412	816	10500-12500	2.6	2.1×10^{-6}	4.9
3.30	313	450	15000-17000	2.3	1.1×10^{-6}	3.0
4.00	190	263	23100-33800	0.5	1.8×10^{-8}	0.45
5.00	111	135	30400-49800	0.08	4.8×10^{-9}	0.71
6.00	74	49	44200-75000	0.06	1.5×10^{-7}	1.22
7.00	53	16	61300-99100	0.05	4.6×10^{-7}	2.3
Z=0.001						
1.10	5400	1600	5400-6600	5.0	8.2×10^{-9}	0.10
1.25	2500	1550	6000-6500	8.8	9.8×10^{-9}	0.10
1.50	1480	1570	6000-8000	8.7	5.9×10^{-8}	0.30
2.00	700	2000	8000-9800	13.4	2.3×10^{-7}	0.54
2.50	410	868	13900-14800	5.4	2.5×10^{-7}	0.55
3.00	279	402	19300-21600	2.0	6.2×10^{-9}	0.07
3.50	196	307	23000-30900	0.5	4.5×10^{-9}	0.37
4.00	146	241	24200-39000	0.9	9.8×10^{-9}	0.64
5.00	92	84	45000-56800	0.4	9.5×10^{-9}	0.53
6.00	63	22	75000-87900	-	8.6×10^{-8}	1.84
7.00	47	14	73400-120000	-	1.9×10^{-7}	2.09

sensitive to the treatment of the convective borders, because a larger overshoot from the bottom of the convective mantle might favour the carbon enrichment, thus predicting an earlier achievement of the C-star stage and higher C/O ratios (Herwig, 2005). It is the high sensitivity to the modelling of convection close to the boundaries of both the external envelope and the pulse-driven convective shell which renders the predictions regarding the surface carbon enrichment particularly uncertain (Karakas & Lattanzio, 2014). However, the present context is an exception to the general picture, because the carbon stars population of the LMC has been traditionally used as a living laboratory to test the efficiency of TDU. Among others, we mention the works by Groenewegen & de Jong (1993); Kamath et al.

(2012); Karakas et al. (2002); Marigo et al. (1999), who provided robust calibrations of the extent of TDU, for stars of different mass, by looking for consistency with the observed luminosity function of carbon stars in the LMC and of the observations of AGB stars in LMC clusters. The treatment used in the models adopted here (see Appendix) is based on the same methods used in the afore mentioned investigations. For these reasons, the results given here can be considered as sufficiently robust.

On the other hand, regarding the high-mass domain, the efficiency of HBB was shown to be strongly dependent on the details of the convection modelling (Boothroyd & Sackmann, 1988; Renzini & Voli, 1981; Ventura & D’Antona, 2005a), in terms of the physical behaviour of the models and of the nucleosynthesis at the base of the external envelope. This discussion outlined that the treatment of the convective instability is the major uncertainty in the description of the evolutionary properties of AGB stars, which reflects on the gas and dust pollution from this class of objects.

1.3.1 Post-AGB evolution modelling

A few sources belonging to the sample analysed in the present work, that will be discussed in detail in Chapter 3, show the presence of cool dust in the circumstellar envelope, suggesting that dust production has stopped and that the dust currently observed was produced during earlier evolutionary phases. As it will be shown in Chapter 3, the SEDs of these stars present a peak in the optical that rules out the possibility that they are AGB stars. Based on these factors, we suggest that these stars have left the AGB and are evolving through the post-AGB phase.

The presence of these peculiar objects was the main motivation to extend the evolutionary sequences to include the post-AGB phase. This choice required a further numerical refinement of the architecture of the stellar evolution code used, considering the difficulties encountered when modelling AGB stars with the envelope mass reduced to below $\sim 0.01M_{\odot}$, the typical mass at which the excursion to the blue of the evolutionary tracks begins (Miller Bertolami, 2016).

For the stars not reaching the C-star stage ($M > 3M_{\odot}$) we modeled mass loss according to eq. 6 in Miller Bertolami (2016). For C-stars we chose, somewhat arbitrarily, to keep the description by Wachter et al. (2002, 2008). This choice will likely affect the timescale of the post-AGB evolution, but is not relevant for the determination of the excursion of the evolutionary track on the HR diagram.

The main properties of the post-AGB models are reported in Table 1.2. We only show model stars with $M \leq 2M_{\odot}$ and $Z = 0.008$, because the luminosities of the sources likely

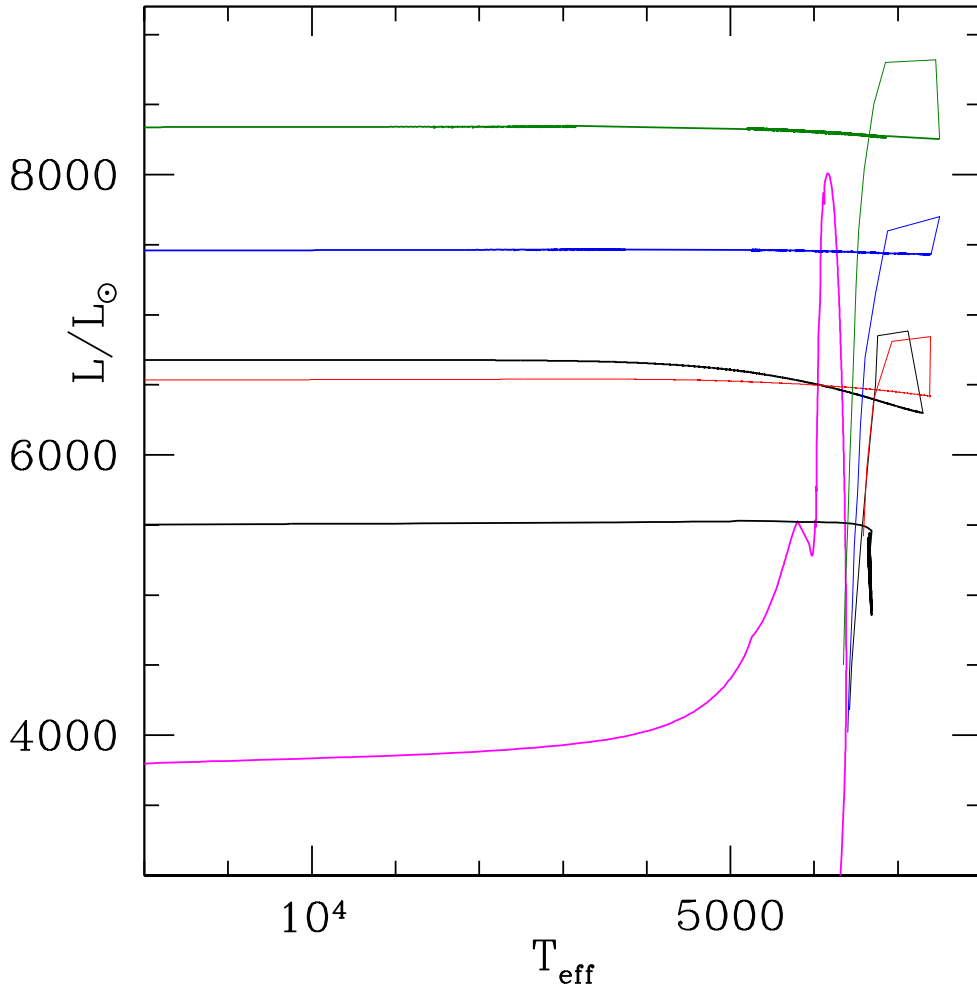


Figure 1.12 The path traced in the HR diagram by stars of initial mass $1M_{\odot}$ (magenta line), $1.1M_{\odot}$ (black), $1.25M_{\odot}$ (red), $1.4M_{\odot}$ (black), $1.6M_{\odot}$ (blue), $1.75M_{\odot}$ (green), during the latest AGB phases and the post-AGB phase.

evolving through the post-AGB phase are below $\sim 10^4 L_{\odot}$, which rules out $M > 2M_{\odot}$ progenitors.

As discussed by Miller Bertolami (2016), the definition of the start of the post-AGB phase is not rigorous, considering that the behaviour of the stars, particularly the beginning of the excursion of the evolutionary track to the blue, is dependent on the core mass. We assume that the AGB evolution ends when the mass of the envelope drops below 1% of the mass of the star and chose the point when the effective temperature is $\log T_{\text{eff}} = 3.85$ as the

Table 1.2 Main physical and chemical properties of the post-AGB models discussed in the text. Cols. 1 – 3 indicate the initial mass of the star, the mass at the beginning of the AGB phase and the final mass. The time scales reported in col. 4 and 5 indicate, respectively, the age of the star and the crossing time, defined as the time interval from the point when the mass of the envelope drops below 1% of the stellar mass and the time when the effective temperature becomes $\log T_{\text{eff}} = 3.85$. The last four cols. report the surface chemical composition, in terms of the mass fractions of helium, carbon, nitrogen and oxygen.

M/M_{\odot}	M_{AGB}/M_{\odot}	M_{f}/M_{\odot}	τ_{ev} (Gyr)	τ_{tr} (Kyr)	X(He)	X(C)	X(N)	X(O)
1.00	0.75	0.552	9.23	3.8	0.281	8.86e-4	4.72e-4	4.16e-3
1.10	0.90	0.575	6.52	8.8	0.281	9.74e-4	3.08e-4	4.24e-3
1.25	1.10	0.596	4.22	3.3	0.290	8.59e-4	3.24e-4	4.66e-3
1.40	1.25	0.590	2.91	4.2	0.284	3.91e-3	3.02e-4	4.39e-3
1.60	1.50	0.602	1.89	3.4	0.284	3.86e-3	2.99e-4	4.40e-3
1.75	1.75	0.622	1.42	2.9	0.285	4.84e-3	3.14e-4	4.62e-3
2.00	2.00	0.617	0.97	3.0	0.286	6.21e-3	2.97e-4	4.68e-3

intermediate stage between the post-AGB phase and the Planetary Nebula (PN) evolution. The time interval between these two evolutionary stages, proposed by Miller Bertolami (2016) as indicator of the transition time scale from the AGB to the post-AGB phase, is reported on column 5 of Table 1.2.

The path traced by the evolutionary tracks in the HR diagram of the models reported in Table 1.2 is shown in Fig. 1.12. Since the sources that will be discussed in Section 3.2 have $T_{\text{eff}} < 10^4$ K, we restrict our attention to effective temperatures below 1.2×10^4 K. For each mass we show a few points regarding the very final AGB phases and the whole post-AGB evolution.

These results will be used in Chapter 3 to discuss the aforementioned few stars in the sample that are most likely evolving through the post-AGB phase.

1.4 Formation of dust in the winds of AGB stars

AGB stars experience high rates of mass loss, up to a few $10^{-4}M_{\odot}/\text{yr}$, and they gradually lose their external envelope in the form of cold and dense winds, suitable for condensation of gas molecules into dust. AGB stars evolve with typical effective temperature around 3000 – 4000 K, which are not cool enough to allow the condensation of even the most refractory dust species in the photospheric layers of the stars. Therefore, a key role in the dust formation process is played by dynamical processes: shock waves generated by stellar pulsations propagate outwards through the atmosphere and lift the gas above the stellar surface, creating dense, cool layers, where solid particles may form. As the dust forms,

the radiation pressure accelerates the grains away from the star, which finally transfer the momentum acquired from the photons to the gas through collisions (Höfner, 2009), and therefore triggers the acceleration of the wind, favouring the mass loss in these structures (Fleischer et al., 1992).

The numerical treatment of physical phenomena of such complexity is beyond the current computation capabilities, particularly when these results must be interfaced with those from stellar evolution modelling, as in the present case. As of today, the most widely used model for dust formation in the outflow of AGB stars assumes that the wind expands isotropically from the surface of the star. The outflow of the wind is assumed to be stationary and spherically symmetric and the thermodynamical structure is determined following the schematization proposed by the Heidelberg group (Gail & Sedlmayr 1985, 1999; Ferrarotti & Gail 2002, 2003, 2006, hereinafter FG06; Zhukovska et al. 2008).

Dust grains grow by vapour deposition on some kind of seed nuclei, that are formed prior to the point where the different dust components start to condense, which then grow by accreting material to macroscopic grains. One of the most relevant open points connected with the dust formation in the wind of AGB stars is the nature and the density of the seed nuclei. In the formalism used by the Heidelberg group this quantity is expressed by n_d , the number densities of the seeds (Ferrarotti & Gail, 2001). n_d proves crucial to determine the density of the dust grains and the fraction f of the gas condensed into dust, defined as

$$f_i = \frac{4\pi(a_i^3 - a_{0,i}^3)}{3V_{0,i}} \frac{n_d}{\epsilon_k n_H} \quad (1.2)$$

In the equation above, a_i and $a_{0,i}$ are the current and initial grain sizes, V_0 is the volume of the nominal molecule in the solid, n_H is the number density of hydrogen atoms in the gas.

For each condensed species, it is defined a key element, whose abundance is the minimum among all the elements necessary to form the corresponding dust aggregate. For instance, silicon is the key element for silicates and silicon carbide, whereas carbon is the key elements for solid carbon. All the species considered in the present work, with the corresponding key elements, are listed in Table 1.3. In eq. 1.2 ϵ_k is the number density of free particles of the key element normalized to hydrogen.

The overall scattering coefficient, which is proportional to f , also depends on n_d (Ferrarotti & Gail, 2001). In the present computations we followed the suggestion by FG06, to adopt a constant value $n_d = 10^{-13} n_H$ for all the dust species considered, as determined observationally for oxygen-rich stars by Knapp & Morris (1985). However, alternative choices are possible, since the situation for carbon-rich and oxygen-rich stars of different metallicity could be different (see the discussion in Nanni et al., 2013). Because of the arbitrariness

Table 1.3 Dust species considered in the present work, their formation reaction and the corresponding key element (see the text).

Dust species	Reaction	Key element
Olivine	$2x\text{Mg}+2(1-x)\text{Fe}+\text{SiO}+3\text{H}_2\text{O} \rightarrow \text{Mg}_{2x}\text{Fe}_{2(1-x)}\text{SiO}_4+3\text{H}_2$	Si
Pyroxene	$x\text{Mg}+(1-x)\text{Fe}+\text{SiO}+2\text{H}_2\text{O} \rightarrow \text{Mg}_x\text{Fe}_{(1-x)}\text{SiO}_3+2\text{H}_2$	Si
Quartz	$\text{SiO}+\text{H}_2\text{O} \rightarrow \text{SiO}_2(s)+\text{H}_2$	Si
Corundum	$\text{Al}_2\text{O}+\text{H}_2\text{O} \rightarrow \text{Al}_2\text{O}_3+\text{H}_2$	Al
Silicon Carbide	$2\text{Si}+\text{C}_2\text{H}_2 \rightarrow 2\text{SiC}+\text{H}_2$	Si
Carbon	$\text{C} \rightarrow \text{C}(s)$	C
Iron	$\text{Fe} \rightarrow \text{Fe}(s)$	Fe

of this choice, the n_d/n_H ratio is kept as a free parameter. As a further initial condition, in agreement with FG06, we assume that the seed grains have an initial size $a_0 = 10^{-7}$ cm. Results from dust formation modelling in the wind show that the latter choice is less critical than the assumed value for n_d (Ventura et al., 2014).

The growth rate of each dust species depends on the competition between the formation and destruction rates (Ferrarotti & Gail, 2001, 2002; Gail & Sedlmayr, 1999). The latter is calculated via the difference between the formation enthalpy of the dust species and of the individual molecules concurring to the formation process, whereas the former is evaluated on the basis of the thermal velocity of the corresponding molecule and the number density of the key element.

The regions close to the central star are generally too hot to allow dust condensation, the destruction rate exceeding by far the production rate. At a distance of from the photosphere of the star that depends on the species which forms (typically $1 - 10 R_*$, see Sections 1.4.1 and 1.4.2), the temperature is low enough to allow the condensation of dust grains. The consequent increase in the opacity accelerates the wind via the strong radiation pressure and halts dust formation. We therefore expect the sizes of the different grain species and the terminal velocity of the wind to reach an asymptotic behaviour.

The mineralogy of the dust formed in the outflow is determined by the surface chemistry of the star, particularly the C/O ratio. This is because the CO molecule is extremely stable, then the less abundant between carbon and oxygen is entirely locked into CO, and is therefore unavailable to form dust. In O-rich ($C/O < 1$) environments the most stable dust species are silicates, alumina dust (Al_2O_3) and solid iron (Ferrarotti & Gail, 2001, 2002, 2006; Gail & Sedlmayr, 1999). Conversely, in the winds of carbon stars the most relevant dust species are silicon carbide (SiC), solid carbon and solid iron (Ferrarotti & Gail, 2002, 2006).

In summary, in oxygen-rich winds we consider the formation of silicates, under the form of olivine, pyroxene and quartz, of alumina dust and solid iron; in C-rich stars we

take into account the formation of SiC, solid carbon and solid iron. No further species are considered, because they form in small quantities, thus they are not expected to contribute to the acceleration of the wind and to the IR emission from the star.

The description of the equations of the wind structure and the thermodynamic quantities is demanded to the Appendix.

After having outlined which types of dust form in the wind of M and C stars, we will describe in more detail for each of the two classes of AGB stars the formation process of the solid grains of diverse species and at which distance from the star they form.

1.4.1 Oxygen-rich AGB stars

To explain the dust formation process in the winds of M-stars, we show in Fig. 1.13 the structure of the outflow of a $6M_{\odot}$ star, during an intermediate stage of the AGB evolution, when HBB is active. The quantities shown in the figure are the size of the olivine (the dominant silicate dust species) and Al_2O_3 grains along the circumstellar envelope. Iron grains are not shown, for clarity reasons. It is evident that alumina dust is by far the most stable compound, the formation of Al_2O_3 grains taking place at temperature as high as ~ 1500 K, at a distance from the photosphere of the star of $\sim 1 - 2 R_{\star}$. The formation of silicates occurs in a more external region, at a distance of $\sim 10 R_{\star}$ from the surface of the star, where the temperature is ~ 1100 K (Dell’Agli, 2012). Among the silicates, olivine is the most stable species, forming in larger quantities, followed by pyroxene and quartz. We note from Fig. 1.13 that the size reached by Al_2O_3 grains are smaller compared to that of olivine, despite forming in a more internal region: this difference is due to the higher availability of silicon with respect to aluminium in the stars.

The exact location of the condensation zone is mainly determined by the effective temperature of the star (see eq. 6.6 in the Appendix). Therefore, the trend with metallicity is straightforward: in higher metallicity models, owing to their lower T_{eff} , the growth of Al_2O_3 particles begins at $\sim 2 R_{\star}$ from the centre of the star, while at $Z = 0.001$ the Al_2O_3 condensation zone is in more external circumstellar regions, at $\sim 4 R_{\star}$. On the other hand, a change in the initial mass of the star does not strongly affect these results, because models with the same Z and different masses evolve at approximately the same T_{eff} (see Fig. 1 in Ventura et al., 2012).

The condensation of Al_2O_3 does not affect the formation of silicates, owing to its large transparency: the acceleration of the wind via radiation pressure starts further the formation of the alumina dust, where silicates begin to grow (Dell’Agli, 2012; Dell’Agli et al., 2014a).

The variation of the alumina dust grain size during the AGB evolution is different compared to silicates: alumina dust particles form in larger and larger dimensions as the

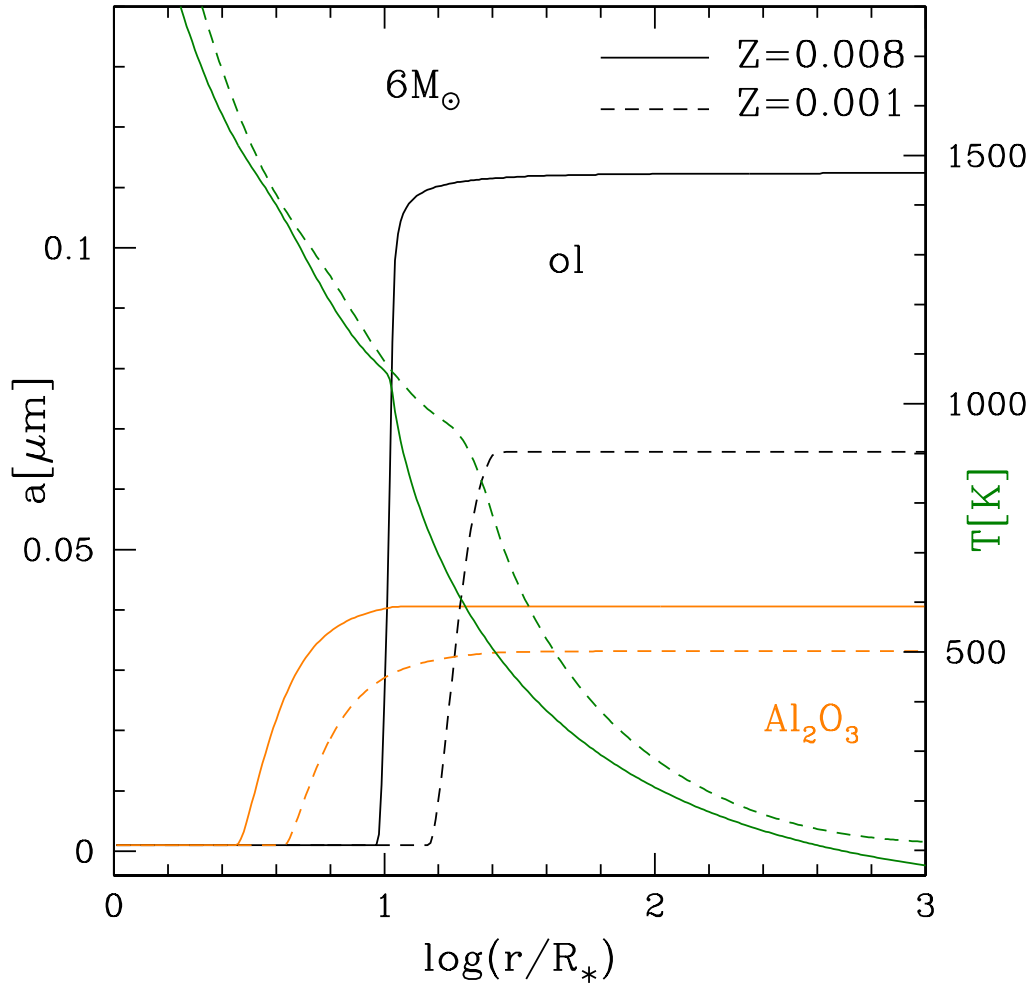


Figure 1.13 Size of the Al_2O_3 and olivine dust grains (orange and black lines, scale on the left axis) and the gas temperature (green line, right axis) as a function of the distance from the centre of the star, for a model star of initial mass $6M_\odot$ and metallicities $Z = 0.008$ (solid lines) and $Z = 0.001$ (dashed lines), during an intermediate stage of the AGB evolution, when HBB is active.

evolution proceeds, whereas the size of silicates follows the path traced by luminosity. This is an effect of HBB, which, via activation of the Mg–Al nucleosynthesis, favours a gradual aluminium enrichment of the surface layers (Ventura et al., 2013).

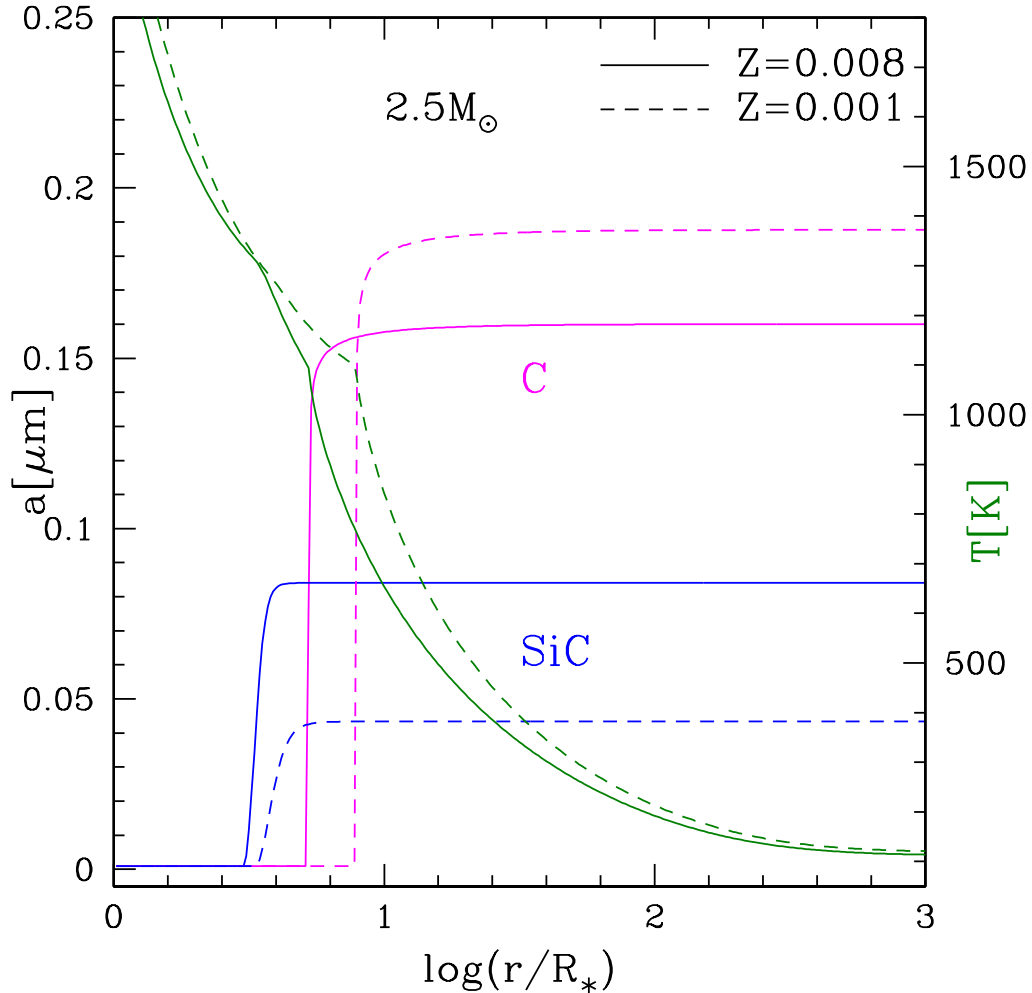


Figure 1.14 Size of the carbon and SiC dust grains (magenta and blue lines, scale on the left axis) and the temperature of the gas (green line, right axis) as a function of the distance from the centre of the star, for a star with initial mass $2.5M_{\odot}$. The figure refers to a late phase of the AGB evolution, before the beginning of the WD cooling.

1.4.2 Carbon stars

Stars with $M \leq 3M_{\odot}$ start their evolution on the AGB phase as oxygen-rich stars. They produce silicates in negligible quantities at the beginning of the AGB evolution, whereas in more advanced phases, after repeated TDU episodes, that lead to surface $C/O > 1$ (see Fig. 1.10), carbon dust is formed.

The structure of the wind of carbon stars shows us some similarities with the outflow of M-stars, with the formation of a more stable transparent dust species (SiC) in the internal regions, while the compound mostly responsible for the acceleration of the wind by action of radiation pressure (solid carbon) forms in a more external and cool zone of the circumstellar envelope. This is shown in Fig. 1.14, which represents the size of the carbon and SiC dust grains and the temperature of the gas as a function of the distance from the centre of the star. The figure refers to stars with initial mass $2.5M_{\odot}$ and metallicity $Z = 0.001$ and $Z = 0.008$, during a late phase of the AGB evolution, after large amount of ^{12}C ($X(^{12}\text{C}) \sim 1.1 \times 10^{-2}$ for $Z = 0.008$ and $\sim 1.6 \times 10^{-2}$ for $Z = 0.001$) have been transported to the surface by TDU events.

SiC, the most stable compound, forms at $\sim 4 R_{\star}$ from the central star, in a region where the temperatures are ~ 1300 K (Ferrarotti & Gail, 2002). Carbon, less stable, forms in regions with temperatures ~ 1100 K, at a distance from the photosphere of $\sim 8 R_{\star}$. Similarly to Al_2O_3 , SiC is extremely transparent to radiation, therefore the acceleration of the wind is determined essentially by carbon grains (Dell’Agli, 2012). On general grounds, the production of solid carbon is higher than SiC, because in the external region of carbon stars the availability of silicon is smaller with respect to the excess of carbon in relation to the oxygen².

The solid carbon grains formed grow bigger and bigger as the star evolve along the AGB, owing to the gradual accumulation of ^{12}C in the surface regions (see Fig. 1.10), which favours the increase of the density of carbon molecules in the wind. The present computation (but see also Dell’Agli 2012) shows that the size of carbon particles span the $0.07 - 0.2 \mu\text{m}$ range. The largest grains form in the wind of $2 - 3M_{\odot}$ stars, characterized by the largest ^{12}C mass fractions in the external regions (see discussion in Section 1.3).

While it is generally recognized that carbon dust is the primary source of extinction in the envelope of carbon stars, the debate is still open regarding the possibility that the dominant species is under the form of amorphous carbon or graphite. The discovery of pre-solar graphite grains from meteorites (Xu et al., 2016; Zinner, 2008) indicates that the graphite contribution is not negligible. Speck et al. (2009), based on results from radiative transfer modelling, suggested that graphite is the dominant dust species instead of amorphous carbon. On the other hand, Andersen et al. (2003) argued that the absence of the narrow band at $11.52 \mu\text{m}$ in most observed spectra, and the fact that the slope of infrared graphite spectra follows λ^{-2} , imply that graphite formation in AGB winds is unlikely. On general grounds, the physical conditions in AGB atmospheres seem to favour amorphous carbon dust,

²The only exception to this is when the transition from O-rich to carbon star occurs. In this case the production of SiC can exceed solid carbon.

since graphite formation requires temperatures that significantly limit the growth interval in a typical C-star. The stationary wind model adopted here allows the determination of the growth rate of carbon dust and the calculation of the extinction related to carbon grains; however, we cannot derive any indication on whether the carbon particles formed are under the form of amorphous carbon or graphite. The method we follow in order to derive the relative contribution from amorphous carbon and graphite is by looking for the best fit of the SED of carbon stars in the sample: first we derive the other parameters (e.g. luminosity, optical depth, percentage of SiC) and then we assume a variable percentage of graphite with respect to carbon, in order to reach the better agreement with the observation (see Chapter 5).

Unlike carbon, the amount of SiC produced is not tightly related to the mass of the star. SiC grains grow during the evolution until a threshold size in the range $0.05 - 0.09 \mu\text{m}$ is reached, after which no further growth occurs; the results are sensitive to the metallicity (Dell’Agli, 2012). This behaviour is connected with a saturation condition, in turn due to the lack of silicon particles in the wind. Owing to the stability of SiS molecule, in carbon-rich environments the number density of silicon molecules is given by $n_{Si} = [(1 - f_{SiC})\epsilon_{Si} - \epsilon_S]n_H$ (FG06), where f_{SiC} is the fraction of silicon condensed into SiC. This expression poses an upper limit on the amount of SiC that can form, corresponding to the value of f_{SiC} at which n_{Si} vanishes:

$$f_{SiC} = 1 - \frac{\epsilon_S}{\epsilon_{Si}} \quad (1.3)$$

Because in solar or α -enhanced mixtures $\frac{\epsilon_S}{\epsilon_{Si}} \sim 0.4$ (Grevesse & Sauval, 1998), f_{SiC} cannot exceed $\sim 60\%$.

While we may safely assume that SiC grains are the only solid particles formed in the internal part of the outflow, in the more external regions of the circumstellar envelope the presence of SiC could be associated with the formation of MgS (Zhukovska et al., 2008). Indeed, as it will be discussed in the following section, SiC is suited as a substrate for MgS precipitation, due to the obvious similarities of structure and bonding properties of SiC and MgS.

MgS

The spectrum of several carbon stars is characterized by a wide bump in the spectral region around the $25 - 30 \mu\text{m}$ region (see, e.g., bottom panels of Fig. 5.1). The presence of such a band was detected in the observations of carbon stars in the Milky Way (Hony et al., 2002; Volk et al., 2002) and in the Magellanic Clouds (Zijlstra et al., 2006). Goebel & Moseley (1985) first proposed that this feature can be associated to MgS, because the latter compound

has a feature in the same spectral region. The various possibilities proposed so far to explain the $30 \mu\text{m}$ bump were discussed in the recent review by Volk et al. (2020). Here we base on the analysis done by Sloan et al. (2014), who concluded that MgS is the best candidate to account for this spectroscopic evidence.

A significant step forward in the modelling of MgS production in the circumstellar envelope of carbon stars was done by Zhukovska et al. (2008), who included the growth of MgS grains in the description of the stellar wind. In the paper by Zhukovska et al. (2008) it is shown that the formation of pure MgS dust cannot account for the observed feature, because the formation of MgS is expected to take place at temperatures $\sim 900 \text{ K}$, after the wind has been accelerated by the formation of carbon dust, and the density has dropped to values too small to allow a significant growth of MgS particles. We did some tests after including the formation of MgS in the set of equations used here and confirmed the results by Zhukovska et al. (2008); the largest size reached by MgS grains is below $0.01 \mu\text{m}$, which corresponds to cross-sections far too small to account for the observed feature.

To model the MgS feature we considered the idea proposed by Zhukovska et al. (2008), that the growth of MgS occurs via precipitation on SiC grains. This choice opens the possibility of forming bigger size grains, because the SiC particles formed in the internal regions enter the MgS condensation zone with size in the $0.03 - 0.07 \mu\text{m}$ range (Nanni et al., 2013; Ventura et al., 2014). We find that precipitation of MgS on these already formed SiC grains would further increase the dimension of these particles by $\sim 0.02 \mu\text{m}$, if we assume that the deposition begins from the point where the pure MgS dust would start to form; this result is consistent with the analysis by Zhukovska et al. (2008).

1.4.3 The overall dust production by AGB stars

The methodology described earlier in this section allows the computation of the fraction of gaseous molecules condensed into dust. The knowledge of the latter quantity, combined with the estimate of the mass-loss rate of the star and of the surface chemical composition, allows the computation of the rate with which each individual dust species is produced during the various phases of the AGB evolution. All these rates concur to the determination of the global dust production rate, \dot{M}_d , which describes the efficiency with which AGB stars produce dust. The knowledge of this quantity proves crucial to evaluate the dust injection rate from evolved stars in the galaxies, an argument currently at the centre of a lively debate within the international astrophysical community (Schneider et al., 2016, 2014).

Integration over the whole AGB lifetime of the dust production rate allows the computation of the dust mass produced by AGB stars during their evolution. A summary of the

results obtained for the model stars used in the present work is shown in Fig. 1.15. For clarity sake we show the total dust mass of silicates, instead of the individual compounds.

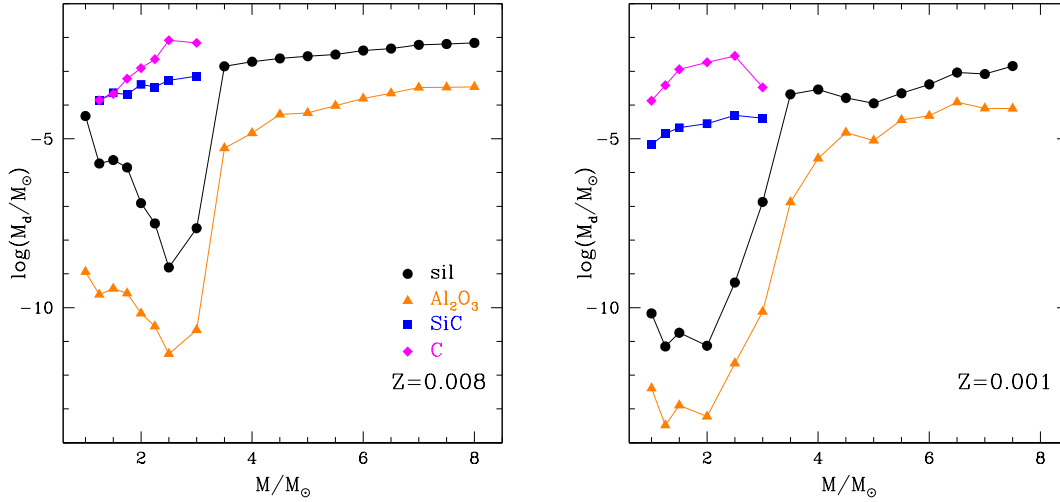


Figure 1.15 Dust mass produced during the AGB phase by the various species of dust considered in the present work, as a function of the current mass of the star. Left and right panels refer to stars of metallicity $Z = 0.008$ and $Z = 0.001$, respectively.

Fig. 1.15 confirms the dichotomy in mass previously discussed. Stars with initial mass below $3M_{\odot}$ produce mainly carbon dust and SiC. In these stars the production of silicates and Al_2O_3 takes place only in the phases prior to the formation of carbon star. $M < 1.5M_{\odot}$ stars (especially in the $Z = 0.008$ case) are characterized by a not negligible production of silicates and alumina dust with respect to the other low-mass stars which become carbon stars (Ventura et al., 2012). The reason is related to the fact that these stars evolve as M stars for most of their AGB life, reaching the C-star phase only in the very final AGB stages, when a significant fraction of the envelope is lost. During the end of the O-rich phase, before turning to C-stars, they evolve at cool effective temperatures, with mass loss rates $\sim 10^{-6}M_{\odot}/\text{yr}$.

The behaviour of the carbon dust produced with metallicity is more tricky, and changes according to the mass range considered. In $M < 2M_{\odot}$ stars production of carbon dust is favoured in $Z = 0.001$ objects with respect to their counterparts of metallicity $Z = 0.008$, because the former reach more easily the C-star stage, owing to the smaller quantity of ^{16}O in the star. In $2 - 3M_{\odot}$ stars this effect is not relevant, as the number of TP experienced is sufficiently high to favour the accumulation of large quantities of ^{12}C in the envelope. For stars within this mass range the most important factor is the lower effective temperatures

attained by $Z = 0.008$ stars, which thus produce larger quantities of carbon dust, than in the $Z = 0.001$ case (see discussion in Section 1.2.2). Indeed, the mass of solid carbon produced in the latter case ranges from $10^{-4}M_{\odot}$ to $\sim 5 \times 10^{-3}M_{\odot}$, whereas for $Z = 0.008$ stars it reaches the values of $10^{-2}M_{\odot}$ for the two masses $M = 2.5 - 3M_{\odot}$.

Inspection of Fig. 1.15 shows that the mass of SiC produced increases with the stellar mass, because the mass returned to the interstellar medium is higher the higher the initial mass of the star. Higher-metallicity models produce more SiC, owing to the larger amount of silicon present in the stars. The mass of SiC produced is in the $10^{-4}M_{\odot} - 10^{-3}M_{\odot}$ range for $Z = 0.008$, whereas for stars with metallicity $Z = 0.001$ it varies from $10^{-5}M_{\odot}$ to almost $10^{-4}M_{\odot}$ (Ventura et al., 2014).

For what concerns the high-mass domain, it is evident from Fig. 1.15 that the production of silicates increases with the stellar mass (Ventura et al., 2014, 2012). In the $Z = 0.008$ case the mass of silicates is in the range $10^{-3} < M_{\text{Sil}} < 10^{-2}$, whereas the $Z = 0.001$ models produce a smaller quantity of dust, owing to the scarcity of silicon available, but also because of the strong depletion of the surface oxygen: this is the reason for the dip around $\sim 5M_{\odot}$, that can be seen in the $Z = 0.001$ line in Fig. 1.15. The mass of alumina dust produced is also increasing with the stellar mass and varies from a few $10^{-6}M_{\odot}$ for $M = 3.5M_{\odot}$, to $\sim 10^{-6}M_{\odot}$ for $M = 7.5M_{\odot}$. The $Z = 0.001$ models produce a smaller amount of alumina dust, owing to the low surface mass fraction of aluminium (Dell'Agli et al., 2014b).

It is also evident from Fig. 1.15 that for $Z = 0.001$ models the significant formation of silicates begins at $\sim 3M_{\odot}$, whereas in the $Z = 0.008$ case at $\sim 3.5M_{\odot}$ (Ventura et al., 2014, 2012): this is because, as already mentioned in Section 1.2.3, lower-metallicity stars reach more easily HBB conditions.

1.4.4 Change in the optical depth of AGB stars

As discussed in Section 1.4, the rate of dust production in the winds of AGB stars generally increases during the AGB phase, thus the stars are characterized by a higher and higher IR emission as the AGB evolution proceeds. This reflects into a significant enhancement of the continuum emission and the spectrum gradually moves to IR wavelengths.

In the present work we quantify the degree of obscuration of the central star by the optical depth, at the wavelength $\lambda = 10 \mu\text{m}$, τ_{10} , which is determined by integrating along the radial direction the product of the number density of dust particle and the extinction cross section, based on the knowledge of the optical constants and the grain size, a . For the i -th species we have:

$$\tau_{(10\mu\text{m},i)} = \int n_d Q_{ext}(10\mu\text{m},i) \pi a_i^3 dr \quad (1.4)$$

where $Q_{ext}(10\mu\text{m},i)$ is the extinction coefficient at $10\mu\text{m}$ related to the i -th dust species.

Fig. 1.16 shows the variation during the AGB phase of the luminosity (left panel) and of the effective temperature (right panel) of stars of diverse initial mass and $Z = 0.008$ as a function of τ_{10} . Inspection of Fig 1.16 shows that carbon stars evolve at higher optical depths as the external layers cool (see discussion in Section 1.3 related to Fig. 1.11); carbon stars with the same T_{eff} have the same τ_{10} , independently of their previous history. From the left panel of Fig. 1.16 it is clear that the luminosity has only a minor effect on the optical depth variation of stars with initial mass $M < 4M_{\odot}$.

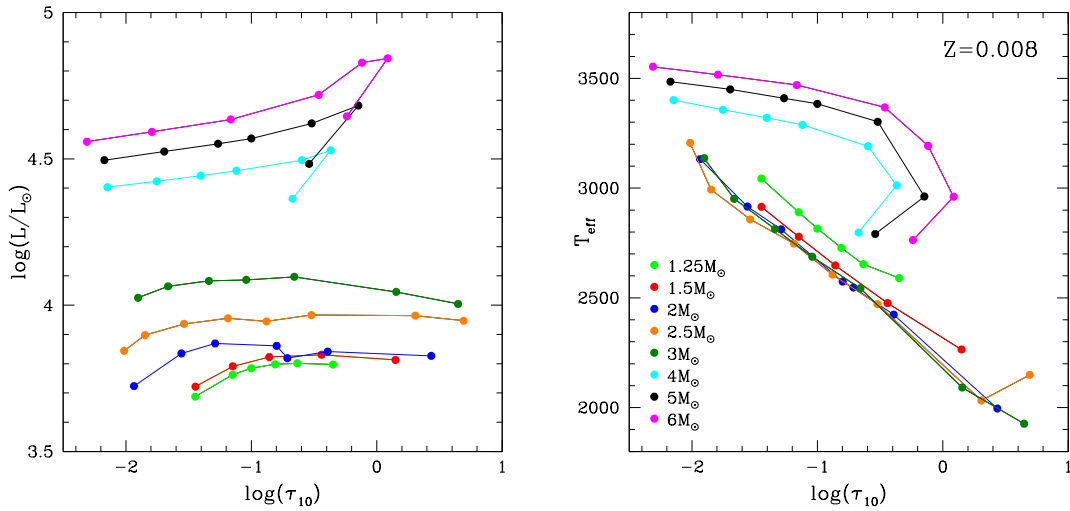


Figure 1.16 The evolution of carbon stars of diverse initial mass as a function of the optical depth τ_{10} . The left and right panels show the variation of the luminosity and of the effective temperature, respectively.

On the other hand, the evolution of stars with higher initial mass is driven by the temperature at the bottom of the envelope, which determines the luminosity, the mass-loss rate and consequently the quantity of dust formed. As shown in the left panel of Fig. 1.16, the luminosity undergoes significant variations during the AGB evolution: after the initial increase, due to the growth of the core mass, L decreases, owing to the gradual loss of the external mantle, as already described in Section 1.2.1. The phase of maximum dust production (with the highest τ_{10}) is in correspondence with the maximum L , when the mass-loss rate also reaches its largest values. Unlike the lower-mass counterpart, in the

high-mass domain the T_{eff} has a minor effect on τ_{10} , in agreement with the fact that dust production is mostly determined by the extent of the HBB experienced.

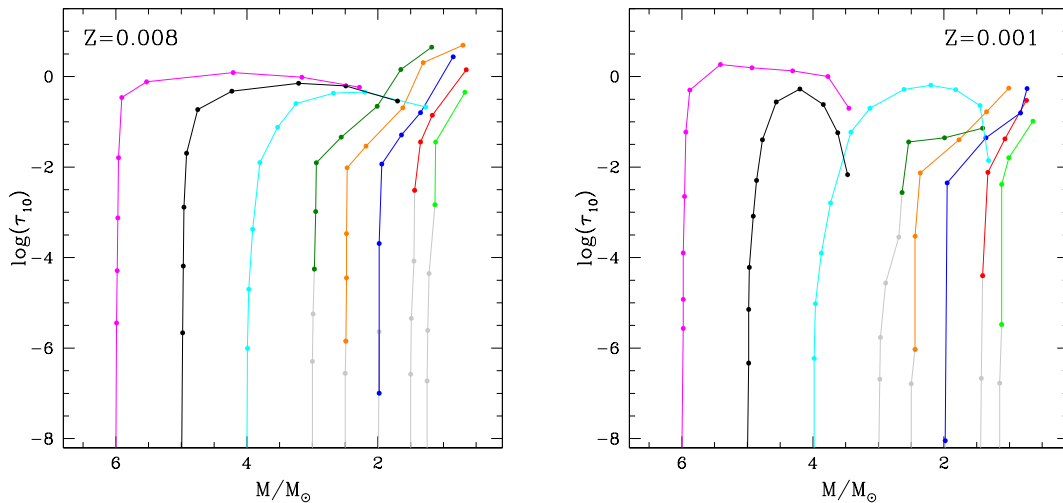


Figure 1.17 The variation of the optical depth at $10\mu\text{m}$ as a function of the current mass of the star, for model stars of different initial mass and metallicity $Z = 0.008$ (left panel) and $Z = 0.001$ (right). For $M \leq 3M_{\odot}$ stars the coloured part of the track corresponds to the C-star phase, while the M-type phase is indicated in light, grey.

Fig. 1.17 shows the evolution of τ_{10} for diverse initial masses, in the $Z = 0.008$ (left panel) and $Z = 0.001$ (right panel) cases. Low-mass stars evolve initially as oxygen-rich; the optical depth is extremely small during this phase, because of the small amount of silicate-dust in the envelope. After the carbon star stage is reached, τ_{10} increases because more and more carbon is accumulated at the surface of the star, owing to the effects of TDU, as previously mentioned. For stars of metallicity $Z = 0.008$ and $Z = 0.001$ the stars reaching the largest τ_{10} are those of initial mass $\sim 2.5 - 3M_{\odot}$ and $2 - 2.5M_{\odot}$ respectively. In both cases they reach the highest optical depth in the final evolutionary phases. The largest values of the optical depth, $\tau_{10} \sim 5$, are reached by the $Z = 0.008$ models, whereas low-mass AGB stars of $Z = 0.001$ evolve at optical depths below unity. As explained previously, higher- Z models evolve at lower effective temperatures, which favours dust formation, because the region where gas molecules condense into dust is closer to the surface of the star, in a region of higher density.

The stars with higher initial mass behave differently because they experience HBB. While in their counterparts of lower mass the optical depth depends strongly on the amount of carbon in the convective envelope, in massive AGB stars the dust formation process is mainly determined by the strength of HBB (Ventura et al., 2012). The phase with the highest infrared

emission and optical depth occurs during the phase of strongest HBB, when both luminosity and mass loss rate reach their maximum values. The luminosity in these stars peaks in an intermediate evolutionary stage (see left panel of Fig. 1.3), when τ_{10} is the highest shown. From Fig. 1.17 it is evident that oxygen-rich models of higher mass have a stronger infrared emission, because the strength of HBB increases with the initial mass of the star; this holds independently of the metallicity. For high-mass stars with metallicity $Z = 0.008$, the highest optical depth reached, $\tau_{10} \sim 1$, is smaller than in their lower-mass counterparts $\tau_{10} \sim 5$; this is due for two reasons: a) the content of carbon in low-mass AGB stars is larger compared to the silicon in the external regions of more massive AGB stars; b) the extinction coefficient of solid carbon dust is higher than the corresponding coefficients of silicates.

2

The *JWST*: a new perspective of the study of AGB stars in the Local Group galaxies

In this chapter we describe the state of the art of the studies focused on the characterization of the AGB populations in the Local Group, of their dust production, and the new perspectives that will be opened in the near future by the advent of the *JWST*. With the aim of maximizing the potentialities of this telescope for the study of these sources, we present our strategy to identify the MIRI filters most suitable for the characterization of the AGB stars and of the dust present in their circumstellar envelope. We introduce the two ingredients required to accomplish this goal, namely the sample of LMC stars used and the sequences of synthetic spectra representing the evolution of the stars across the AGB phase. Finally, we describe the methodology applied to the sample for the analysis of the individual sources.

2.1 Past, present and future of the AGB investigations in the Local Group galaxies

AGB stars are generally regarded as important dust manufacturers (Boyer et al., 2012; Gehrz, 1989; Riebel et al., 2012; Schneider et al., 2014; Srinivasan et al., 2009). It is now generally recognized that the contribution from AGB stars to dust production in the Universe cannot be neglected, even in early epochs (Valiante et al., 2017, 2009, 2011). A thorough comprehension of the dust formation process in their wind is crucial to assess the rate with which these stars eject dust into the interstellar medium of their host galaxy and, on more general grounds, their contribution to the overall dust budget of the Universe.

Theoretical modelling of dust formation in the outflow of evolved stars has made impressive steps forward in the last decade, during which some research groups have implemented a chemo-dynamical description of the stellar wind, self-consistently coupled with the modelling of the evolution of the star (Dell'Agli et al., 2019a; Nanni et al., 2013, 2014; Ventura

et al., 2014, 2013, 2012). However, considering the several uncertainties still affecting AGB evolution and dust formation modelling, it is mandatory to compare these predictions with the observations of evolved stars. Indeed, the IR emission of these sources, as also the shape of the spectral energy distribution, is entirely determined by the mineralogy and the amount of dust present in the circumstellar envelope. The synergy between IR observations and results from stellar evolution + dust formation modelling will prove decisive to characterize the evolved stars observed and to shed new light on the dust formation process in their wind.

The analysis of dusty AGBs in the Galaxy is not straightforward, owing to light absorption and scattering from its own interstellar medium and the unknown distances, which render uncertain the luminosity of the sources observed. This problem will be partially overcome for the less embedded objects by the *GAIA* data releases (Gaia Collaboration et al., 2016, 2018), while the extremely dusty ones will be too faint in the optical wavelengths to be detected. The difficulties encountered during the studies of Galactic AGB stars has been the main reason why the most used laboratories for investigating the life-cycle of dust in the interstellar medium (ISM), thus providing a fundamental benchmark to theoretical models, have been the Magellanic Clouds (Boyer et al., 2012; Groenewegen & Sloan, 2018; Groenewegen et al., 2009, 2007; Matsuura et al., 2009, 2013; Nanni et al., 2018; Riebel et al., 2012; Srinivasan et al., 2009; van Loon, 2006; van Loon et al., 2005, 1999).

This kind of studies have been possible thanks to several dedicated large photometric surveys, which made available a growing body of observational data. Among the others, the Magellanic Clouds Photometric Survey (MCPS; Zaritsky et al., 2004), the Two Micron All Sky Survey (2MASS; Skrutskie et al., 2006) and HERschel Inventory of The Agents of Galaxy Evolution (HERITAGE; Meixner et al., 2010, 2013) have provided catalogues of point sources as well as high-resolution maps of the emission by the warm and cold dust components in ISM.

The *Spitzer* Space Telescope provided the most complete exploration of the MCs. The Surveying the Agents of Galaxy evolution (SAGE-LMC; Meixner et al., 2006) (SAGE-SMC; Gordon et al., 2011) provided IR data of ~ 6.5 million sources, ~ 17000 out of which were classified as AGB stars by Riebel et al. (2010), taken with the InfraRed Array Camera (IRAC; 3.6, 4.5, 5.8, and 8 μm) and the Multiband Imaging Photometer (MIPS; 24, 70 and 160 μm) onboard the *Spitzer* Space Telescope.

Moreover, a plethora of complementary data has allowed to reconstruct the recent and past SFHs of these galaxies (see, among others, Bolatto et al., 2011; Cignoni et al., 2013; Harris & Zaritsky, 2004, 2009; Skibba et al., 2012; Weisz et al., 2013), such as their metal enrichment histories (see e.g. Carrera et al., 2008a,b; Piatti, 2012; Piatti & Geisler, 2013),

and their present-day global gas, stellar and dust content (see Meixner et al., 2013; Schneider et al., 2014).

The availability of this robust body of observational data has allowed the study of the dust enrichment from stellar sources in MCs from two different perspectives. Several authors used synthetic spectra, obtained by radiative transfer code available (DUSTY, Nenkova et al., 1999; 2DUST, Ueta and Meixner, 2003), to find the parameter combination giving the best fit of the various photometric data, to reproduce the position of the individual sources in the observation planes built with the IRAC and MIPS magnitudes (Riebel et al., 2012; Srinivasan et al., 2009, 2010, 2011). The results from these investigations were the determination of the luminosity, the dust mineralogy and the optical depth of the different stars; side results were the derivation of the mass loss rates.

A different and complementary approach was followed by Dell’Agli et al. (2015a, 2014b, 2015b), who studied evolved stars in the MCs, based on the comparison between results from mid-IR photometry and synthetic magnitudes, obtained by radiative transfer modelling. However, unlike the studies previously mentioned, the parameters of the stars allowing the best fit of the observations were not chosen based on a plain fitting procedure, rather they were selected based on results from AGB + dust formation modelling of stars of different mass and metallicity. The advantage of such an approach is that not only it allows the determination of the current evolutionary status of the stars and the description of the dust properties, but also their characterization in terms of mass, chemical composition and formation epoch of the progenitors.

An approach similar to Dell’Agli et al. (2015a, 2014b, 2015b) was followed by Nanni et al. (2019), who estimated the overall dust production rate by evolved stars in the MCs, by considering different observations in the infrared and optical data from *GAIA*, and derived important trends connecting mass loss rate, dust production rate, dust-to-gas ratio of the stars with the infrared colours, properly taken as indicators of the degree of obscuration.

While the combination of near-IR and mid-IR data to study the evolved stellar population has been so far successfully applied mainly to the MCs, recent investigations used IR data to derive information on the evolved population of environments beyond the MCs, e.g., M33 (Javadi et al., 2017), NGC 147 and NGC 185 (Hamedani Golshan et al., 2017).

The widest, systematic and most complete survey of AGB stars in the Local Group so far available in the literature is the DUSTiNGs survey (Boyer et al., 2015a,b, 2017; Goldman et al., 2019; McQuinn et al., 2017), a 3.6 and 4.5 μm imaging survey (with a follow-up that includes the filters F127M, F139M, and F153M on the HST) of 50 nearby dwarf galaxies, which searched for dusty evolved stars, spanning a large range in metal content (from about 0.2% to 8% of solar). By analysing the results from the DUSTiNGs survey, AGB stars in

the Local Group galaxies IC1613 (Dell’Agli et al., 2016), IC10 (Dell’Agli et al., 2018a) and Sextans A (Dell’Agli et al., 2019a) were studied, providing a characterization of the sources observed, in terms of mass, chemical composition and formation epoch of the progenitors; however, these studies, based on photometry results limited to wavelengths below $\sim 5 \mu\text{m}$, could not benefit of the information of the long-wavelength domain of the mid-IR flux.

While the availability of IR photometric data allows the derivation of the extent of the reprocessing of the radiation from the central star by dust particles, understanding the details of the dust mineralogy and the grain size distribution of the solid particles formed in the circumstellar envelope of the stars is possible only via the analysis of the spectral energy distribution. In the context of AGB stars in the MCs this kind of studies can benefit from the data collected with the *Spitzer*’s Infrared Spectrograph (IRS), which provided detailed mid-IR spectral distribution of more than 1000 point sources in the LMC. The fit of the IR spectra allows a wider and deeper exploration of the various factors affecting the spectral energy distribution, in comparison to the analysis based on the different magnitudes. Early attempts in this direction were presented by Jones et al. (2014) and Groenewegen & Sloan (2018).

The investigation of the evolved population in the galaxies of the Local Group, and possibly beyond, will receive a strong boost from the launch of the *JWST* (Gardner et al., 2006). It will provide extensive IR data for the AGB population in a variety of environments, different for SFH and age metallicity relation, thus revolutionizing our understanding of the evolved stellar population in the Local Universe. The large aperture (6.5 m) and the subarcsecond spatial resolution will allow the study of resolved dusty stellar populations at moderate and large distances, up to ~ 4 Mpc (Jones et al., 2017). MIRI (Rieke et al., 2015), mounted onboard the *JWST*, will provide spectroscopy in the $5 - 28.5 \mu\text{m}$ range (Bouchet et al., 2015), thus providing a unique opportunity to study the evolution of AGB stars and the dust formation process in their expanding wind, in a large variety of environments.

Compared to the *Spitzer*’s instruments IRAC and MIPS, MIRI will be more sensitive of a factor 50 with an improvement in the resolution of a factor 7 (from $5.8''$ at $24 \mu\text{m}$ with *Spitzer* to $0.7''$ at $21 \mu\text{m}$ with MIRI, Rieke et al., 2015), as shown in Fig. 2.1. MIRI will be equipped with 9 filters, with central wavelengths from $5.6 \mu\text{m}$ to $25.5 \mu\text{m}$, whose transmission curves are reported in Fig. 2.2. Some of these transmission curves are overlapped with the spectral features related to the presence of specific dust species, which allows a detailed analysis of the dust mineralogy. Therefore, it is essential to project the future works in a *JWST* perspective, exploring how the *JWST* space mission will allow the characterization of the evolved stellar populations of galaxies.

A first step in this direction was achieved by Jones et al. (2017), who provided the magnitudes of obscured M-stars in the LMC, that would be found if they were observed with the *JWST*, by convolving the IRS spectra with the corresponding transmission curves of the different filters.

Compared to previous works, which were based on an ad hoc fitting procedure (e.g. Jones et al., 2014), we are in the position of developing a deeper analysis here. Indeed, similarly to the afore mentioned studies by Dell’Agli et al. (2015a, 2014b, 2015b), we will use results from stellar evolution modelling, which will drive us through the determination of the stellar parameters. This will allow us to characterize the various sources considered and to derive the properties of their progenitors.

The main differences with respect to Dell’Agli et al. (2015a, 2014b, 2015b) are that we will focus on detailed SED fitting, not only on mid-IR photometry, and, more important, the analysis will be based on the expected magnitudes of the MIRI filters, complemented by IRAC and MIPS photometry.

In the following we present the sample of LMC AGB stars considered to compute this study, the synthetic spectra constructed for this analysis and we summarize the methodology applied in order to reach a complete characterization of the sources.

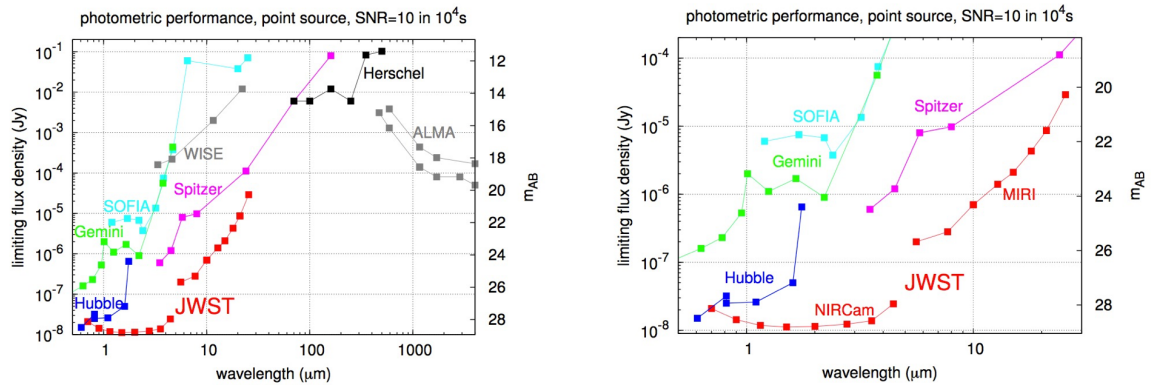


Figure 2.1 Left: faintest flux for a point source that can be detected at SNR= 10 in a 10,000s integration with *JWST*. Fluxes are given in Jy (scale on the left axis) and AB mag (right axis). Right: detail of the left panel, in the wavelength range $\lambda \leq 30 \mu\text{m}$ (<https://jwst.stsci.edu>)

2.2 Selection of the sample

In order to explore how the *JWST* space mission will allow the characterization of the evolved stellar populations of galaxies, we base the present work on the LMC sample of ~ 70 O-

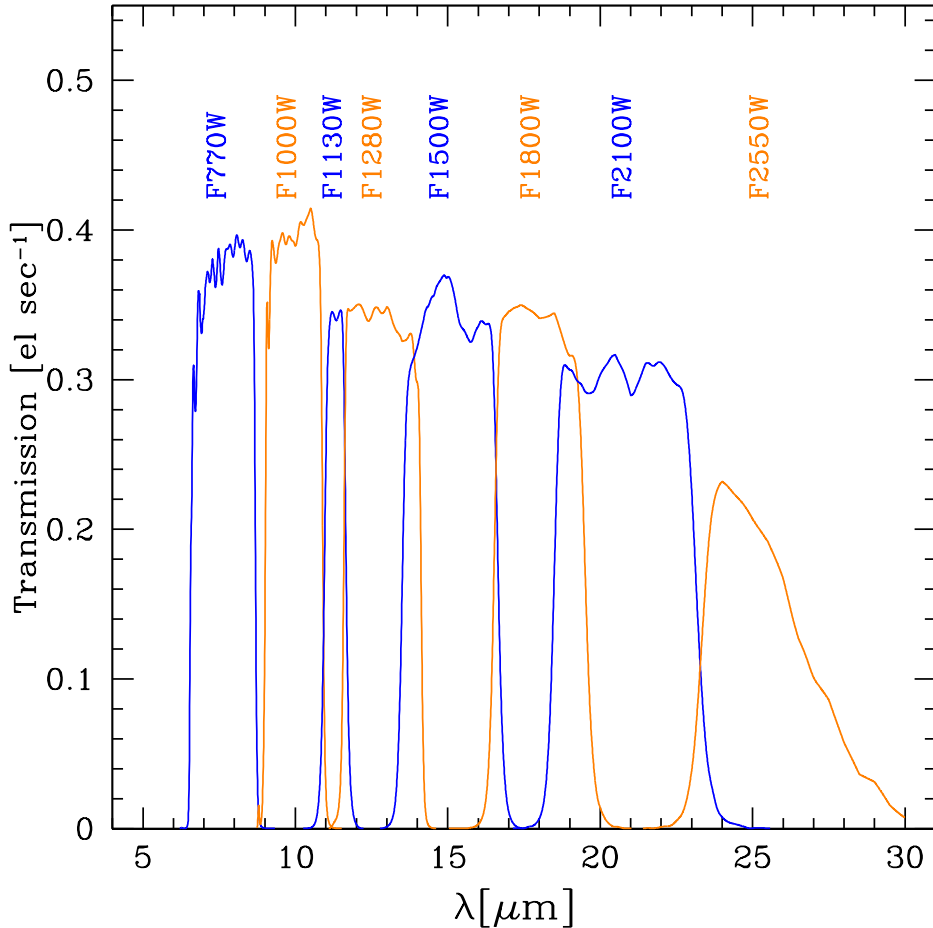


Figure 2.2 Transmission curves of the MIRI filters (Glasse et al., 2015)

rich and ~ 150 C-rich spectra from the SAGE-Spec database at the NASA/IPAC Infrared Science Archive, reduced by Jones et al. (2017), using the method discussed in Kemper et al. (2010). This database includes all staring-mode observations with the *Spitzer* IRS taken in the area of the sky covered by the SAGE survey (Meixner et al., 2006), which covers the LMC in its entirety. The sample includes point sources from the SAGE-Spec legacy survey of the LMC (Kemper et al., 2010), a spectroscopic follow-up to the SAGE-LMC project (Meixner et al., 2006) and has been supplemented from archival *Spitzer* IRS observation within the SAGE LMC footprint (Woods et al., 2011). The detailed description of the original target selection, the observing strategy and the techniques used in the data reduction for the SAGE-Spec legacy programme are discussed in Kemper et al. (2010). This sample satisfies

all the requirements needed for the present analysis: a) a large number of evolved stars (which allows to consider any other type of sources in the observational IR planes, e.g. PNe, RSG, post-AGB); b) a wavelength coverage in accordance with MIRI filters and the most interesting dust features; c) a well-known distance.

Jones et al. (2017) classified the sources of the sample by using the decision-tree classification method by Woods et al. (2011): the primary criterion for the classification was the *Spitzer* spectrum itself, but it also relied on the additional information provided by the SED, on the estimate of the bolometric luminosity and supplementary information from the literature. C-rich AGB stars are identified by molecular absorption features, particularly C_2H_2 (acetylene) at 7.5 and 13.7 μm , and by the dust features at 11.3 μm and 30 μm , whereas as long as the C/O ratio remains below unity, silicates are the dominant dust component in the spectra of AGB stars, with features at 10 and 18 μm , either in emission or absorption (silicate self-absorption at 10 μm indicates an extreme or optically thick O-rich AGB star). A molecular absorption at 8 μm , due to the fundamental vibrational mode of SiO, is used as a further indicator of oxygen-rich chemistry.

To study the expected distribution of the stars in the observational planes built with the magnitudes corresponding to the MIRI filters, we used the mid-IR magnitudes (F770W, F1000W, F1130W, F1280W, F1500W, F1800W, F2100W, F2550W) calculated by Jones et al. (2017), who integrated the IRS spectra of each source over the MIRI spectral response, shown in Fig. 2.2.

For all the sources the associated broadband photometry, including optical UBVI photometry from the Magellanic Clouds Photometric Survey (Zaritsky et al., 2004), 2MASS JHKS photometry (Skrutskie et al., 2006), mid-IR photometry from IRAC (3.6, 4.5, 5.8, 8.0 μm) and MIPS (24 μm), was compiled from the SAGE catalogue (Meixner et al., 2006).

The majority of the objects in the sample covers the 5 – 37 μm range of the low-resolution modules of the IRS, so the fluxes for the F560W filter are not available. For 27 out of the C-rich objects and 23 out of the O-rich sources the spectral coverage by the *Spitzer*-IRS is limited to the 5 – 14 μm range, therefore the mid-IR photometry beyond this wavelength is not available. While this limited spectral coverage does not represent an issue for the oxygen-rich stars, it does not allow the correct interpretation of the majority of C-rich spectra, which can reach such high values of optical depth that the peak of the SED shifts up to $\sim 13 \mu m$ (see Section 2.3). This led us to exclude the aforementioned 27 C-rich objects from our analysis. In addition, there are a paucity of C-rich sources, whose SED shows a steep rise starting from $\sim 20 \mu m$ and no decline up to the end of the spectra. We believe that these peculiar SEDs are affected by nearby background emission, as also suggested by Gładkowski

et al. (2019), and for this reason are not considered in the analysed sample. Therefore, the sample of analysed C-rich sources is actually made up of 110 stars.

In some cases the IRS data deviate significantly from the IRAC and MIPS photometry, which could be an effect of variability, considering that IRS, IRAC and MIPS data were collected in different epochs. On this regard, we share the criterion followed by Groenewegen & Sloan (2018), that variability can account for up to a 20% difference between the fluxes derived from the analysis of the IRS SED and those found via the IRAC and MIPS magnitudes. Otherwise, when this difference is above $\sim 20\%$, we can assume that the mismatch may be due to some issues in the data reduction. However, compared to the present work, which is mostly focused on the analysis of the IRS spectra, the study by Groenewegen & Sloan (2018) takes into account a more complete collection of photometric data, in terms of epochs and wavelengths considered. For this reason, we believe more accurate relying on Groenewegen & Sloan (2018) and scaling the IRS spectra to match the corresponding IRAC and MIPS photometry according to their interpretation. In the cases where the IRS spectrum was not scaled we left the MIRI magnitudes found by Jones et al. (2017) unchanged, otherwise we recalculated the corresponding MIRI magnitudes via convolution over the MIRI transmission curves.

The list of the stars analysed in this work is reported in Tables 4.1 and 5.1

2.3 Synthetic spectral energy distribution

For a correct understanding of the dust composition in the circumstellar envelope a detailed analysis of the spectral energy distribution is needed, considering that the morphology of the different spectral features is extremely sensitive to the type and the quantity of the dust formed in stellar winds.

As anticipated in the previous section, in order to characterize the individual AGB sources and derive the mass and formation epoch of the progenitor stars, it is crucial to interpret the IRS data via the comparison with the sequences of synthetic spectra obtained for each model star, corresponding to the evolutionary stages of AGB stars and to the dust formed in the circumstellar envelope. To build these sequences, we first select a few points along the AGB evolutionary sequences presented in Chapter 1, distributed among the various interpulse phases. Typically, we pick one evolutionary stage corresponding to the largest luminosity during the inter-pulse, before the ignition of the following TP. Towards the final evolutionary phases, when the mass-loss rate rises and a significant fraction of the envelope is lost during a single inter-pulse, we select one or two points more, in order to follow in more details the variation of the stellar properties as mass is lost from the envelope. For completeness, we

also considered a couple of stages following the extinction of each TP, when the contribution of the CNO burning shell accounts to 10% and 30% of the overall energy release of the star.

Based on the physical parameters attained by the star during these phases, particularly luminosity, effective temperature, current mass, mass loss rate and surface chemical composition, we model dust formation, which allows the determination of the amount of dust formed, the dust mineralogy, the size of the dust particles and τ_{10} (see Section 1.4 and the Appendix).

The last step consists in the calculation of the synthetic SED, which is done by means of the code DUSTY (Nenkova et al., 1999), which models the radiation from a source (a star, in this case) viewed after processing by a dusty region. The radiation from the sources is scattered, absorbed and reemitted by the dust, and the emerging processed spectrum often provides the only available information about the embedded objects. The code can handle both spherical and planar geometries and offers many options for input radiation, dust types and density distributions.

This allows us to determine the magnitudes in the various MIRI bands, via convolution with the corresponding transmission curves, shown in Fig. 2.2.

The synthetic spectra are calculated in two steps:

1. For carbon stars, we first consider the region from the photosphere to the beginning of the solid carbon formation zone. The only dust species considered in this region of the circumstellar envelope is SiC, based on the discussion in Section 1.4.2. As input radiation, we used the spectral energy distribution found by interpolation in surface gravity, effective temperature and C/O ratios among COMARCS atmospheres (Aringer et al., 2009) of the appropriate metallicity. An analogous procedure is followed for oxygen-rich stars (see Section 1.4.1), with the difference that the only species considered is alumina dust and the input spectrum is obtained by interpolating among NEXTGEN atmospheres (Hauschildt et al., 1999) of the same metallicity; in this case the computations are extended until the formation of silicates begins.
2. The spectral energy distribution obtained in step 1, emerging from the SiC or alumina dust layer for C stars or oxygen-rich stars respectively, is used as input for the second layer, where we consider the reprocessing of radiation by SiC and solid carbon for C stars or alumina and silicates for oxygen-rich stars. Solid iron is considered in both cases.

The inputs necessary to steps 1 and 2 are not assumed a priori; they are found via the description of dust formation in the wind, discussed in Section 1.4, which allows the determination of the dust grain size and composition, the temperature of the region where the various dust species form and the radial distribution of the gas density. The optical depth τ_{10} is determined

by the method discussed in Section 1.4.4. To compare the fluxes observed with those found via our spectral analysis, a distance to the LMC of 50 kpc (Feast, 1999) has been adopted. The extinction coefficients were found by using the optical constants from Zubko et al. (1996) (amorphous carbon), Pegourie (1988) (SiC), Draine & Lee (1984) (graphite) and Ordal et al. (1988) for solid iron.

While we postpone to the following sections the discussion on the evolutionary sequences of the stars in the observational planes, according to the initial mass and metallicity, we believe important to describe here the expected evolution of the IR emission of AGB stars, paying particular attention to the different shapes of the SED of M-type AGBs and carbon stars.

2.3.1 C stars

In the left panel of Fig. 2.3 we show the synthetic SEDs of a $2M_{\odot}$ star, corresponding to three evolutionary stages, from the initial AGB phases, when dust has just begun to form and $\tau_{10} = 0.03$, to the final phases, shortly before the post-AGB evolution, with $\tau_{10} = 2.7$.

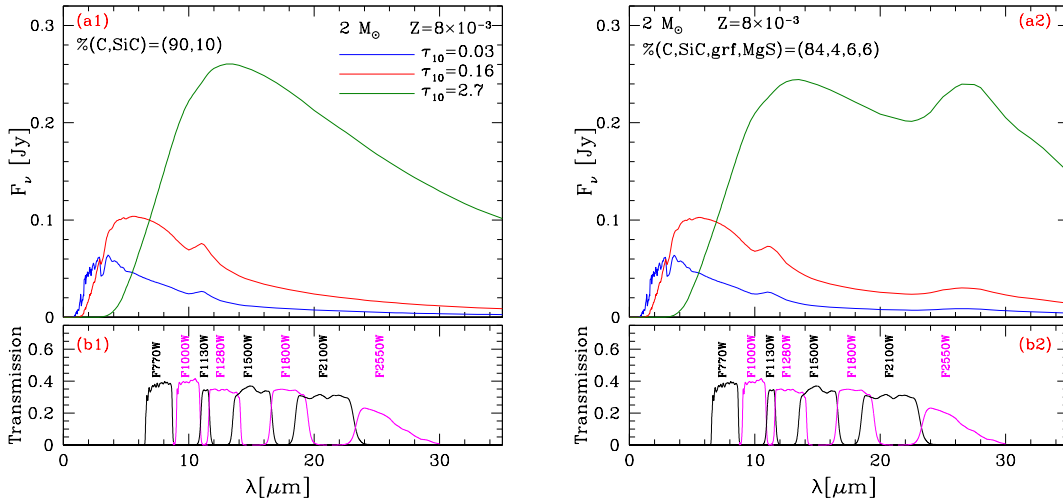


Figure 2.3 Variation of the expected SED during 4 different stages of the AGB evolution of a star of $2M_{\odot}$, when considering only solid carbon and SiC (left) and when also graphite and MgS are considered (right). The 4 phases are characterized by different optical depths, indicated in the three panels. In these examples the number density of the seeds of amorphous carbon dust relative to hydrogen is assumed 10^{-13} , whereas the density of the seeds of the other dust species are scaled with respect to amorphous carbon according to the percentages given in the two panels. Panels b1 and b2 show the transmission curves of MIRI filters in el. sec-1.

We observe the gradual shift of the peak of the SED, from $\sim 3 \mu\text{m}$ to $\sim 13 \mu\text{m}$, as a consequence of the rise in τ_{10} , in turn related to the accumulation of ^{12}C in the surface regions of the star (see Chapter 1). A further effect of the increase in the optical depth is the very large IR emission during the final AGB phases (note that the luminosity is not playing a role here, as it keeps approximately constant during the whole C-star lifetime).

The feature at $11.3 \mu\text{m}$ due to the reprocessing of radiation by SiC particles can be clearly seen, particularly in the lowest τ_{10} models. The SiC feature initially becomes more prominent as τ_{10} increases, because of the rise in the density of SiC grains in the outflow; in the $\tau_{10} = 2.7$ SED, shown in Fig. 2.3, the SiC feature is in absorption and can be hardly detected. The non-linear behaviour of the morphology of the SiC feature with τ_{10} prevents a straight use of the F1130W flux as a τ_{10} indicator, as will be discussed in the following chapters.

The right panel of Fig. 2.3 shows how the results shown in the left panel change when small quantities of graphite and MgS are introduced in the dust mixture. While a detailed discussion on the formation of these species in the wind of carbon stars is postponed to the following chapters, we note the significant bump in the $\sim 25 - 30 \mu\text{m}$ spectral region, connected with the presence of MgS.

2.3.2 M stars

From the discussion in Section 1.4 we know that in the context of M stars significant dust quantities are produced by $M \leq 2M_{\odot}$ stars, in the phases previous to the achievement of the C-star stage, and by massive AGB stars, after the beginning of HBB. We discuss these two cases separately.

Low-mass stars evolve as M-type for most of their AGB life, until they become carbon stars. \dot{M}_d becomes higher and higher during the AGB phase, because the gradual loss of the envelope and the general cooling of the external regions favour the increase in the mass loss rate (see Section 1.2.2). The infrared emission in the SED of these objects thus increases during the M-stage. This is shown in panel a1 of Fig. 2.4, that shows the expected evolution of the SED of a star of initial mass $1.5M_{\odot}$ during the M-phase; the different lines correspond to four evolutionary stages, from the initial AGB phases, when dust formation is inefficient, to the phases immediately before the achievement of the C-star phase, when the optical depth is $\tau_{10} \sim 0.1$. The increase in the amount of dust formed makes the SED of the star to exhibit two prominent features, at $9.7 \mu\text{m}$ and $18.7 \mu\text{m}$, associated to the presence of silicates. Furthermore, the SED in the whole mid-IR region of the spectrum is lifted. Panel a2 of Fig. 2.4 shows a sequence of SEDs of the same $1.5M_{\odot}$ model star, taken during the phases after the carbon star stage is reached. As already seen for the

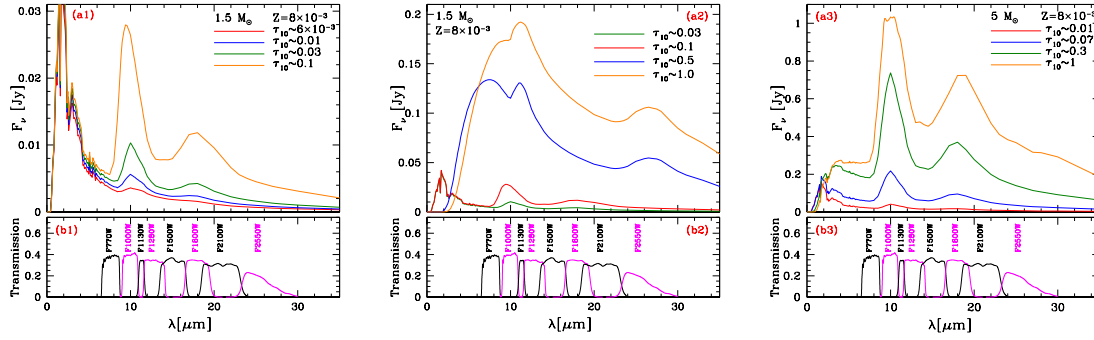


Figure 2.4 The expected variation of the SED during 4 evolutionary phases of the AGB evolution of a star of initial mass $1.5M_{\odot}$ (a1 and a2) and $5M_{\odot}$ (a3). For clarity's sake, a1 shows only the M-star stage of the $1.5M_{\odot}$ model star, whereas the phases after the carbon star stage is reached are shown on a2. The 4 phases are characterized by different optical depths in the three panels. Panels b1 b2 and b3 show the transmission curves of MIRI filters in el. sec-1.

stars represented in Fig. 2.3, we can notice that: a) the peak of the SED gradually shifts to longer wavelengths, with a significant enhancement of the continuum emission owing to the increasing production of carbon dust; b) the silicates features disappear, giving way to those associated to carbonaceous dust¹.

The stars that reach the highest \dot{M}_d during the M-stage are those that experience HBB (see Fig. 1.15), the progeny of $M > 4M_{\odot}$ stars. As shown in the right panel of Fig. 1.3, \dot{M}_d of this class of objects increases during the first part of the AGB evolution, until the maximum luminosity and mass loss rate is reached, then decreases when the efficiency of HBB starts to diminish. According to our modelling the largest optical depths attained are of the order of $\tau_{10} \sim 1$ (Dell'Agli et al., 2015b). Panel a3 of Fig. 2.4 shows the expected evolution of the SED of a $5M_{\odot}$ star, from the beginning of the AGB phase (red line), until the point of the highest obscuration, reached in conjunction with the largest luminosity (orange).

It is clear from bottom panels of Fig. 2.3 and 2.4 that mid-IR *JWST* filters cover spectral regions partly or fully overlapped with the afore mentioned features.

As it will be discussed in detail in Chapters 3-5, the changes in the SED of these three classes of objects, namely carbon stars, massive and low mass M-stars, allow the determination of the general obscuration patterns traced by these sources in the different observational planes, that are useful to characterize the evolved stars in the LMC and in other galaxies.

¹Note that in this case we took into account both MgS and graphite

2.4 Characterizing the sample: a methodology to determine the AGB stars progenitors and their dust production in the *JWST* diagrams

To determine the *JWST* observational diagrams most suitable for the analysis of the AGB populations we need to characterize the individual sources distributed in these planes. To this aim we adopt a two steps methodology, based on the AGB + dust modelling and on a detailed analysis of SED morphology.

We first characterize the individual sources based on the comparison between their position in the observational planes and the path traced by the evolutionary tracks, calculated by convolving the synthetic SEDs, presented in the previous section, with the transmission curves of the MIRI filters. The identification of the synthetic SED that best reproduces the IRS spectrum leads to a robust derivation of the luminosity and of the optical depth of each source, which are essential ingredients to deduce the mass of the progenitors and the current AGB phase they are evolving through. The availability of the photometric data, in particular for the near-IR wavelengths, co-operates in the determination process, further constraining the slope of the SED and its reddening. Moreover, the comparison with the periods, when available, with the theoretical estimates based on the expected variation of the mass and luminosity of the model stars, provides a further check to make the characterization of the single source more robust.

The second step consists in a refinement of the details of the dust mineralogy by the tight comparison between the IRS spectra and the synthetic SEDs, corresponding to the individual points along the tracks. From the analysis of the slope of the SED and the shape of the spectral features, we derive crucial information on the dust composition in the outflow, which, in turn, allows a better understanding of the dynamics of the wind and of the dust formation process. Moreover, the interpretation of the observations from *JWST* requires the knowledge of the dust species in the circumstellar envelope, since most of the mid-IR *JWST* filters cover spectral regions partly or fully overlapped with the afore mentioned features (see Fig. 2.3 and 2.4).

The search for the parameters allowing the best fit of the SED of the individual sources was done by eye for each star. We did not use any automatic procedure, despite being less time-consuming, because in the present context the priority is the correct reproduction of the whole SED.

Applying this methodology to the entire sample, we provide a full characterization of the individual sources and their dust production with an unprecedented accuracy. The results

obtained from the detailed inspection computed with this procedure are presented in the following chapters, starting from two groups of peculiar objects identified in this study for the first time

3

Peculiar sources in the LMC: from their SEDs to their origins

The launch of the *JWST* will undoubtedly open new exciting opportunities to the research focused on AGB stars, on their evolutionary properties, on the gas and dust yields, on the role which they play in the evolution of their host system.

Taking benefit of this important opportunity demands the capability of interpreting the *JWST* observations, being able to characterize the evolved stars detected on the basis of their colours and magnitudes, in order to reconstruct their past history, primarily mass and formation epoch of the progenitors, and to derive relevant information, such as the current dust production rate.

As described in Chapter 2, such a study is made possible by the combination of the results from stellar evolution and dust formation modelling and of the huge dataset of spectra of AGB stars collected in the last decades, which leads to the setting of a decision-tree, presented by Woods et al. (2011), commonly adopted to disentangle C- from M-stars and, more generally, to identify AGB stars with different properties in relation to the mineralogy of the dust in their circumstellar envelope.

Before entering the general discussion on the expected distribution of stars of different mass and evolutionary status on the observational planes built with the mid-IR magnitudes of the MIRI filters, we believe important to discuss the properties of some stars in the sample described in Section 2.2 characterized by a spectral energy distribution that cannot be framed in the scheme proposed by Woods et al. (2011).

These peculiar objects, identified in the present work, can be broadly classified into two distinct groups: AGB sources surrounded by iron dust and stars with dual-dust chemistry composition.

In the following we will discuss their origin, the properties of their progenitors, the possible criterion for their identification and the information we can draw from their presence about the SFH of the host system.

3.1 Stars surrounded by iron dust in the LMC

A few M-stars in the LMC exhibit a peculiar SED, which cannot be explained within the commonly assumed framework, discussed in Section 1.4, that silicates are the dominant dust species formed in the wind of M stars.

Our analysis of these objects is driven by the changes in the surface chemical composition of AGB stars, particularly the evolution of the surface abundance of the chemical species involved in the formation of the main dust compounds produced in the wind of M stars. Based on the behaviour of silicon, magnesium and oxygen, we offer an innovative interpretation, suggesting that the dust in the circumstellar envelope of these objects corresponds to a rather unusual mineralogy, where solid iron is the dominant dust species.

The formation of dust mainly composed by solid iron particles in the winds of metal-poor, evolved stars finds support from independent observational evidences: McDonald et al. (2010, 2011) studied 14 metal-poor ($[\text{Fe}/\text{H}] = -1.91$ dex to -0.98 dex) giant stars (including AGB stars) in the Galactic globular cluster ω Centauri and found that metallic iron dominates dust production in metal-poor, oxygen-rich stars; Kemper et al. (2002) found that metallic Fe is supposedly dominating the near-infrared flux of the M star OH 127.8+0.0. Taken together, theory and observations seem to create a picture where metallic Fe is a natural constituent of AGB winds. The results presented in this chapter reinforce this picture.

We find that the conditions required to produce such a peculiar dust composition are achieved only by stars within a narrow range of ages and metallicities; therefore, the results presented here, if confirmed, can be used as an independent identifier of chemical composition and formation epoch of the sources observed. These findings will be important for the analysis of the soon-to-be results from the *JWST* mission, particularly when studying galaxies dominated by a metal poor stellar component.

3.1.1 Iron dusty AGB stars in the LMC

Fig. 3.1 shows the distribution of the M stars in the sample described in Section 2.2 in the colour-magnitude ($F770\text{W}-F2550\text{W}$, $F770\text{W}$) plane (hereafter in this chapter CMD). We will see that the position of the stars in this plane allows the best discrimination of the mineralogy of the dust present in the circumstellar envelope, as the relative distribution of the various dust species mostly affects the details of the shape of the SED in the region covered by the MIRI filter centred at $7.7 \mu\text{m}$. In this plane we show the evolutionary AGB sequences of stars of initial masses $4M_{\odot}$ and $6M_{\odot}$, with $Z = 0.008$, the metallicity shared by the majority of the stars in the LMC younger than 200 Myr (Harris & Zaritsky, 2009). The evolutionary

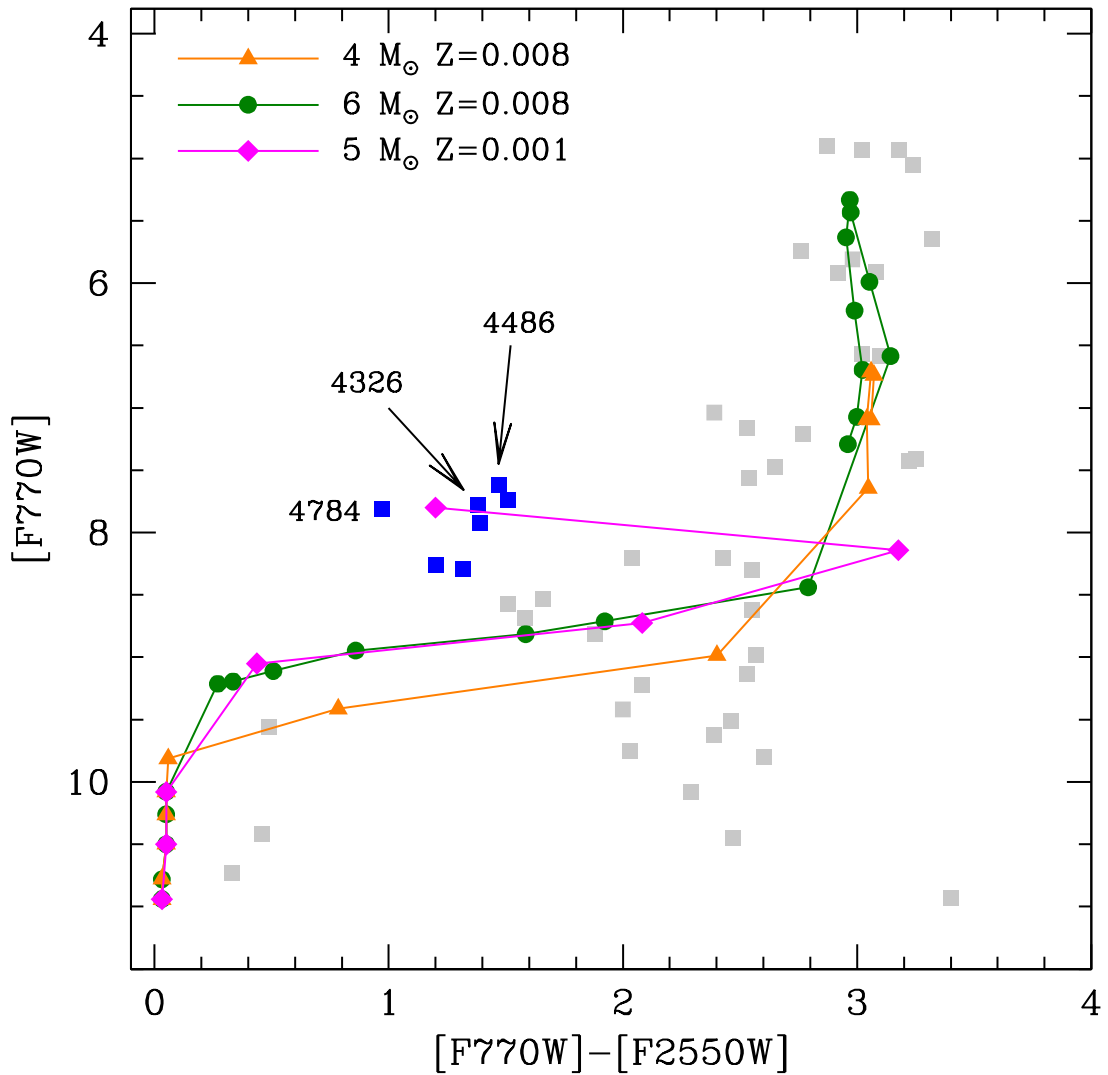


Figure 3.1 The distribution of the M-stars sample described in Section 2.2, indicated by grey squares, in the colour-magnitude ($F770W-F2550W$, $F770W$) plane. Blue squares refer to the group of stars discussed in the present chapter. Green points and orange triangles indicate the synthetic colours assumed by stars of metallicity $Z = 0.008$ and mass, respectively, $4M_{\odot}$ and $6M_{\odot}$, during the AGB evolution. Magenta diamonds refer to the evolution of a $5M_{\odot}$ star of metallicity $Z = 0.001$ before the achievement of the C-star stage.

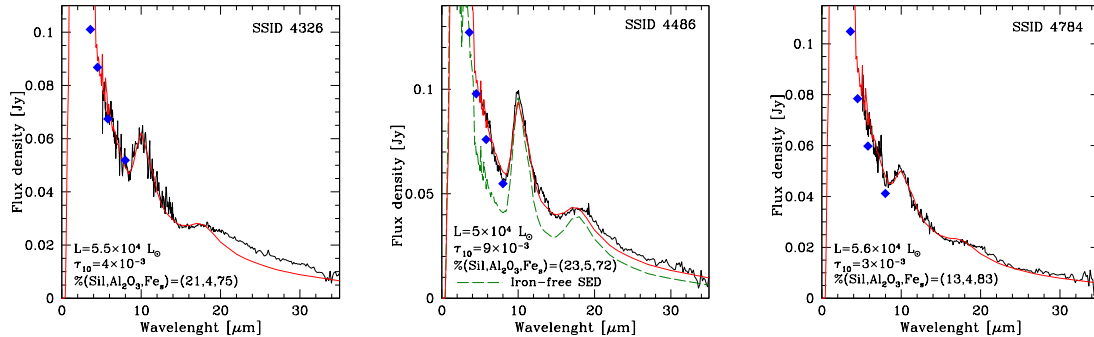


Figure 3.2 The comparison between the observed IRS spectra (in black) and the synthetic SED (in red), obtained by assuming different luminosities and percentages of the various dust species, for three stars in the LMC, interpreted as low-metallicity massive AGBs (see text for discussion). Blue diamonds refer to IRAC [3.6], [4.5], [5.8], [8.0] photometry. The green, dashed line in the middle panel refers to a synthetic SED, calculated assuming iron-free dust around the star.

paths in the figure can be explained by the significant production of silicates which starts after the beginning of HBB (Dell’Agli et al., 2015b; Ventura et al., 2012). The tracks first move to the red, almost horizontally, owing to the gradual rise of the mid-IR flux as the circumstellar envelope becomes more and more opaque. The progressive increase in the rate of dust production eventually favours the formation of a prominent silicate emission feature at $9.7 \mu\text{m}$, which lifts the flux in the $7.7 \mu\text{m}$ region, thus provoking a vertical upturn in the tracks (see Fig. 2.4)

Here we focus on the group of stars populating the left region of the CMD, located at $F770W-F2550W \sim 1.4$, $F770W \sim 7.5 - 8$, not covered by the tracks of $Z = 0.008$ stars. These objects, indicated with blue squares in Fig. 3.1, exhibit a very peculiar SED; Fig. 3.2 displays three illustrative examples. The $9.7 \mu\text{m}$ feature in the SED indicates the presence of silicate type dust. On the other hand, the steep rise of the SED for wavelengths shorter than $8 \mu\text{m}$ cannot be reproduced if we assume that most of the dust is composed of silicates. This is shown in the middle panel of Fig. 3.2, where we report the SED obtained assuming the same luminosity of the best-fit model, an optical depth chosen to reproduce the morphology of the silicate feature, and iron-free dust: the comparison with the observed SED clearly shows that the overall SED, both in the spectral region $\lambda < 8 \mu\text{m}$ and at the mid-IR wavelengths $\lambda > 12 \mu\text{m}$, does not match the observations.

Before presenting our interpretation on the evolutionary status of these objects, we deem appropriate to briefly recall the most relevant physical and chemical properties of stars with metallicity $Z = 0.001$ evolving through the AGB phase, already discussed in Section 1.3, with a specific look at the analysis presented in this chapter.

3.1.2 Evolution and dust production of metal-poor, massive AGB stars

Considering stars of initial mass $M > 3M_{\odot}$, which experiment HBB, we showed in Section 1.2.3 that, on general grounds: a) the higher the mass the stronger the HBB activated; b) the strength of HBB is extremely sensitive to the metallicity, with lower Z stars experiencing a more advanced nucleosynthesis at the base of the envelope (Dell’Agli et al., 2018b; Ventura et al., 2013).

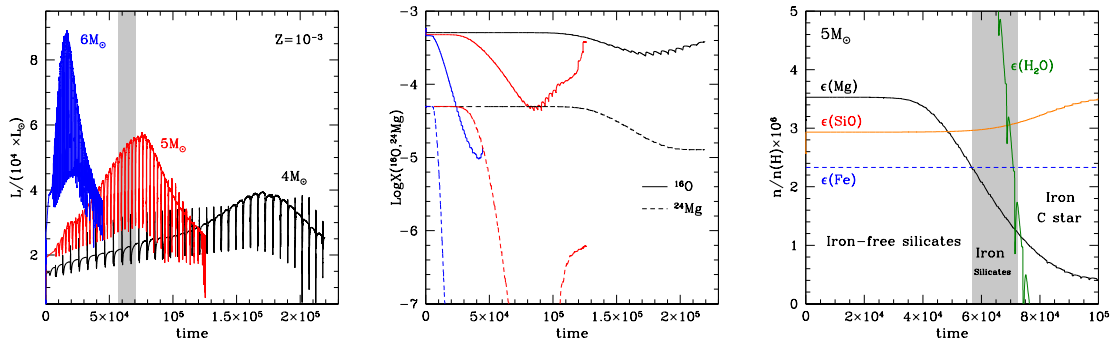


Figure 3.3 The variation of the main physical and chemical properties of stars of metallicity $Z = 0.001$ and initial mass $4M_{\odot}$ (black lines), $5M_{\odot}$ (red) and $6M_{\odot}$ (blue), during the AGB phase. Times on the abscissa are counted since the beginning of the thermally pulsating phase. The left and middle panels show, respectively, the variation of the luminosity and of the surface mass fractions of ^{16}O (solid) and ^{24}Mg (dashed). The right panel, which refers to the $5M_{\odot}$ model, shows the AGB variation of the main quantities relevant to dust production, namely the number densities of silicon (red), magnesium (black), iron (blue, dashed) and water molecules (green), the latter being given by the oxygen excess with respect to carbon and silicon; all the four quantities are normalized to the number density of hydrogen. We mark the three AGB phases during which dust in the circumstellar envelope has the following composition: a) mainly silicates; b) a dominant solid iron contribution with traces of silicates and alumina dust; c) no silicates formation is possible, due to lack of water molecules. Grey shading in the left and right panels indicate the AGB phases of the $5M_{\odot}$ star corresponding to phase (b).

Fig. 3.3 shows the evolution of the luminosity (left panel) and of the surface mass fractions of ^{16}O and ^{24}Mg (middle panel) of AGB stars of mass 4, 5 and $6M_{\odot}$ and metallicity $Z = 0.001$. The ignition of HBB is witnessed by the drop in the surface abundances of oxygen and magnesium, a signature of the activation of full CNO cycling and of the Mg-Al-Si nucleosynthesis. As showed in Section 1.2.3, the strength of HBB is sensitive to the mass of the star. Indeed, the $4M_{\odot}$ star experiences only a soft HBB, with the depletion of oxygen being limited to a factor of ~ 2 , occurring only during the very late AGB phases; conversely, in $5 - 6M_{\odot}$ stars, a significant depletion of both oxygen and magnesium takes place since the early AGB phases.

The ignition of HBB provokes the destruction of the surface carbon, leaving no space for the formation of carbonaceous particles. This was discussed in Section 1.4.1, where we also showed that under these conditions the most stable dust species are alumina dust and silicates. We showed in Section 1.4.1 that in the wind of M stars, in addition to the more stable species, alumina dust and silicates, also solid iron particles can form in modest quantities, in more external and less dense environments (FG06).

Among silicates, we only take into account olivine, whose formation occurs via a reaction involving SiO and water molecules and magnesium atoms (see Table 1.3); consequently, the amount of Mg_2SiO_4 which can be formed is constrained by the number densities of silicon and magnesium, and by the excess of oxygen with respect to carbon and silicon (FG06). As far as there are magnesium and oxygen available, silicates are the most abundant dust species, because the surface content of silicon and magnesium are higher than aluminium and iron.

The right panel of Fig. 3.3 shows the variation of the three aforementioned number densities and iron during the AGB evolution of the $5M_{\odot}$ star. All the quantities are normalized to the hydrogen density. We can distinguish 4 phases.

1. In the initial AGB phases the surface magnesium is in excess of silicon, thus the rate of formation of silicates is constrained by the silicon abundance; in this regime the least abundant among the species involved in the formation reaction of olivine are the SiO molecules.
2. The ignition of HBB provokes the depletion of the surface Mg, thus the key species for the formation of silicates is magnesium; the dust formed is still dominated by silicates.
3. The action of HBB eventually makes the Mg/Fe ratio to drop below unity; in these conditions the formation of silicates is severely reduced, thus leaving room for the formation of solid iron dust.
4. During the final AGB phases the surface oxygen mass fraction becomes so small that the star becomes a C-star. The surface C is so low that iron dust is expected to be the dominant species anyway.

These results show that dust production in low-Z, massive AGB stars can deviate from the common assumption that silicates is the dominant species, rather indicating that during the advanced AGB phases, after the effects of HBB have severely modified the surface chemical composition, there is wide room to the formation of iron grains.

Formation of metallic Fe in AGB atmospheres seems plausible from the expected condensation temperature (similar to that of silicates) at gas pressures typical of circumstellar environments (Gail & Sedlmayr, 1999, FG06).

Laboratory experiments have shown that metallic Fe condenses almost ideally under high supersaturation conditions, and evaporates nearly ideally in vacuum (Tachibana et al., 2011). However, metallic Fe does not necessarily nucleate homogeneously in circumstellar environments, but likely through heterogeneous nucleation on pre-existing dust, e.g., the highly stable Al_2O_3 . For a supersaturation ratio $S > 1$, the condensation and evaporation efficiencies are almost equal (Tachibana et al., 2011), which means that $S > 1$ is in principle sufficient to grow metallic Fe. Thus, if silicate formation is suppressed due to low Mg abundance, metallic Fe can form and grow since efficient evaporation is essentially prevented in the presence of metallic iron vapour.

3.1.3 Understanding iron-dusty stars

Fig. 3.1 shows that the position of most M stars in the sample is reproduced by the evolutionary AGB tracks of stars of initial masses $4M_\odot$ and $6M_\odot$, with metallicity $Z = 0.008$: therefore, they can be explained within the traditional understanding, that dust formation around O-rich AGB stars is mainly composed by silicates, with little traces of alumina dust. On the other hand, the colours and magnitudes of the peculiar stars, indicated with blue squares in Fig. 3.1, are not reproduced by the $Z = 0.008$ tracks. As discussed previously, and shown in Fig. 3.2, their SED cannot be reproduced if we assume that silicates are the main dust species.

We propose that the dust formed in the wind of these peculiar objects is mainly composed by iron grains. Indeed, Fig. 3.2 shows that a highly satisfactory fit of the observed SED is obtained by assuming $\sim 70 - 80\%$ of solid iron, with smaller percentages of silicates ($\sim 15 - 20\%$) and alumina dust ($\sim 5\%$). We suggest that these stars descend from metal-poor progenitors with initial masses $\sim 5 - 6M_\odot$, formed ~ 100 Myr ago. We already pointed out in Section 1.3 that the presence of a recent low- Z star formation activity is compatible with the SFH and the age-metallicity evolution of the LMC computed by Harris & Zaritsky (2009). The particular mineralogy of the dust in the envelope of these objects is determined by the action of HBB, which, as described in the previous section, partly inhibits the production of silicates.

The evolutionary track of the $5M_\odot$ star discussed in Fig. 3.3 is shown in Fig. 3.1. During the first part of the evolution, corresponding to the phases 1 and 2 above, the path followed is similar to the higher- Z , massive AGBs: the track moves to the red, owing to the formation of silicates in the circumstellar envelope. However, when iron takes over as the dominant dust species (point 3 above, grey-shaded region in Fig. 3.3) the track moves to the left, entering the region populated by the stars analysed in the present investigation. According to these

results, all the stars in the regions of the CMD at $F770W < 7$ are massive AGBs of metallicity $Z \geq 0.004$.

Only low- Z stars of mass $M > 4M_{\odot}$ evolve through a phase dominated by iron dust, because the HBB experienced by lower mass objects is not sufficiently strong to trigger a significant decrease in the surface Mg and O (see middle panel of Fig. 3.3). The constraint on the initial mass is fully consistent with the luminosities required to reproduce the overall SED, of the order of $50000L_{\odot}$ (see grey-shaded areas in the left and right panels of Fig. 3.3).

This interpretation is confirmed by the observed periods of the sources discussed, which are in the range 600 – 640 d (Fraser et al., 2008; Groenewegen & Sloan, 2018): these are the same periods expected for the $5M_{\odot}$ star when evolving through the phase dominated by iron dust (grey-shaded regions in Fig. 3.3), calculated by applying eq. 4 in Vassiliadis & Wood (1993).

We rule out that the metallicity of the sources considered here is above $Z > 0.002$ because the HBB experienced is not sufficiently strong to allow a significant O and Mg depletion in the surface regions (Ventura et al., 2014). $Z \sim 0.001$ represents the lowest metallicity that dust around M stars is currently observed to be forming at (Boyer et al., 2017).

The stars discussed here populate a specific region in the CMD; this opens the way to the definition of a criterion to identify metal-poor stars exposed to HBB in samples of AGB sources, which will be extremely important to interpret the data from the *JWST* space mission. The inhibition of silicate production, which is related to the lack of magnesium, confirms that very low- Z , massive AGB stars experience strong HBB at the base of their envelope, thus suggesting that convection is extremely efficient in those physical conditions, far in excess of what is required to reproduce the evolution of the Sun.

3.2 Dual-dust evolved stars in the LMC

The sample of LMC stars analysed in the present work encompasses a further group of sources that, similarly to the stars surrounded by iron dust, are characterized by a peculiar spectral energy distribution that shows up the presence of a featureless dust species, in addition to silicates. Unlike the objects discussed in the previous section, we will rule out that they are surrounded by iron dust.

Indeed, while the $9.7 \mu\text{m}$ feature arises from silicate particles, the whole infrared data suggest they are characterized by a dual-dust chemistry, surrounded by an internal dust layer and an external shell, populated, respectively, by carbonaceous particles and silicate grains.

The idea that AGB stars with dual-chemistry exist was proposed independently by Willems & de Jong (1986) and Little-Marenin (1986), after the detection of objects that

showed clear absorption bands from carbon-rich molecules in their optical and near-IR spectra while showing silicate emission in the mid-IR. The possible presence of such systems is challenged by the expansion of the outer silicate-rich layer, to the point where the silicate feature is no longer detectable (Chan & Kwok, 1988). On the other hand, the formation of a disc, possibly related to the presence of a companion, might prevent the escape of the external silicate shell (Lloyd Evans, 1990). Here we try to identify the physical conditions and the evolutionary phases allowing the formation of this class of objects.

These findings will be also important to identify dual dust chemistry stars in samples of evolved stars in galaxies.

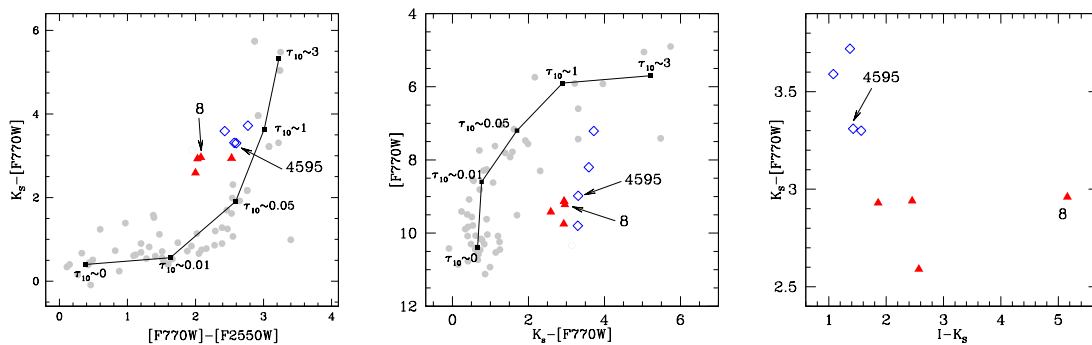


Figure 3.4 Distribution of the sample of M-stars in the LMC described in Section 2.2, indicated by grey points, in the colour-colour (left panel) and in the colour-magnitude diagrams (middle panel). Blue open diamonds and red full triangles indicate the two groups of stars discussed in the present paper. The black lines indicate a theoretical reddening sequence of M-stars, assuming a dust composition made up of silicates, alumina dust and solid iron. Typical values of the optical depth at $1 \mu\text{m}$ and the position of the sources SSID 8 and SSID 4595 are indicated. In the right panel is shown a diagram with a colours combination able to clearly separate the stars among the two groups described in Sections 3.3 and 3.4. Magnitudes come from (Zaritsky et al., 2004).

The left panel of Fig. 3.4 shows the distribution of the stars in the sample considered in this work in the colour-colour ($F770W-F2550W, K_S-F770W$) plane. The stars trace a reddening sequence, up to colours $F770W-F2550W \sim 3$ and $K_S-F770W \sim 6$. A reddening path is also present in the colour-magnitude ($K_S-F770W, F770W$) diagram (see middle panel of Fig. 3.4).

The stars highlighted with coloured symbols fall off the reddening sequences. This is particularly evident in the middle panel, where these sources define a vertical sequence below the main reddening pattern, at $K_S-F770W \sim 2.5 - 3.5$.

As for the stars discussed in Section 3.1, the peculiar position of these objects in the observational planes is due to their SED: while the $9.7 \mu\text{m}$ feature indicates the presence

of silicates, the continuum in the $\lambda < 8 \mu\text{m}$ region suggests the presence of a featureless dust species. The two most plausible options are solid iron and amorphous carbon, given the low stability and the small abundances of other species. A dominant contribution from solid iron to the overall extinction was explored in Section 3.1 in the context of low- Z , massive AGB stars, in which strong HBB inhibits the formation of silicates, via the destruction of the surface oxygen and magnesium. This possibility can be ruled out in the present case, because the luminosities of the stars analysed here, below $10^4 L_{\odot}$, are much smaller than those typical of the stars undergoing HBB, above $2 \times 10^4 L_{\odot}$ (see left panel of Fig. 3.3). Therefore, we will base our analysis on the hypothesis of the presence of a dust layer composed by amorphous carbon. In the following we divide these stars into two groups, according to the morphology of their SED, derived from IRS and photometric data. This classification can be appreciated in the colour-colour diagram ($I - K_S, K_S - F770W$) shown in the right panel of Fig. 3.4, in which these two groups clearly separate from each other.

3.3 A class of post-AGB stars

The sources plotted with blue open diamonds in Fig. 3.4 exhibit a short-wavelength peak, at $\sim 0.4 - 0.6 \mu\text{m}$, and two features, at $9.7 \mu\text{m}$ and $18 \mu\text{m}$, that reveal the presence of silicates. An example is shown in the right panel of Fig. 3.5. The SED indicates a post-AGB nature, because the effective temperatures deduce from SED fitting are above $\sim 5000 \text{ K}$.

We propose that these post-AGB stars descend from $1.2 \leq M/M_{\odot} < 2$ progenitors. A nice fit of the observed SED (see right panel of Fig. 3.5) is obtained by assuming the presence of two dusty layers: the more internal is composed by carbon dust, whereas the more external hosts mainly silicate particles. A similar explanation was invoked by Bunzel et al. (2009) to interpret the SEDs of Galactic O-rich post-AGB stars (heavily obscured and showing strong silicate absorption) although their peculiar SEDs could be fitted with pure silicate dust when including very large and cold grains (R. Szczerba 2019, priv. comm.); a possibility that we rule out for the significantly less obscured stars discussed here.

Based on the discussion in Section 1.3, we believe that the two dust layers formed just before and after the last TP, when the transition from M-star to C-star occurred. Indeed, these stars produce oxygen-rich dust for most of their life on the AGB, but the phases following the last TP, when they produce carbonaceous dust. The change in the dust mineralogy associated with the occurrence of the TP set the conditions for the presence of two dusty shells, with amorphous carbon and silicate dust. These results indicate that the hypothesis that a late TP converts an M-star into a C-star, proposed by Perea-Calderón et al. (2009) to explain the dual

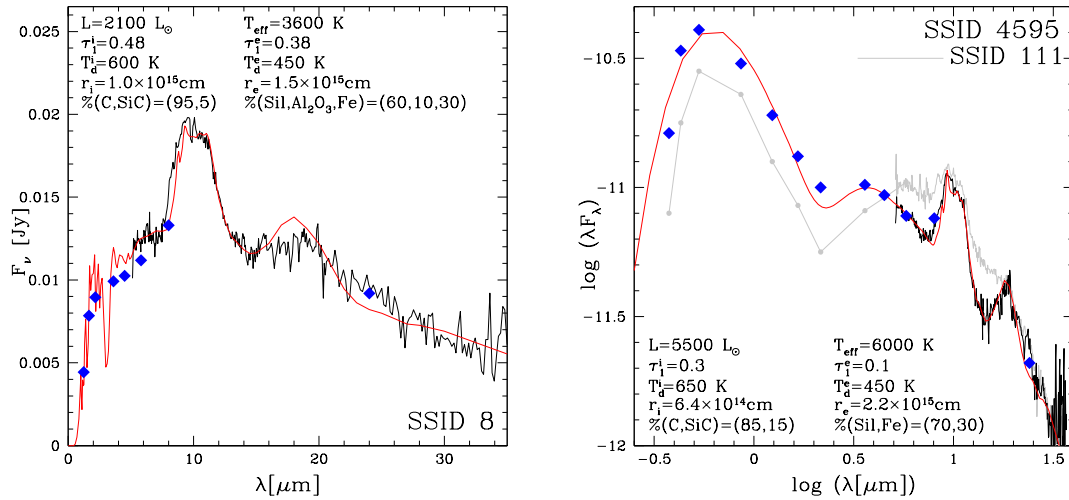


Figure 3.5 The comparison between the observed IRS spectra (in black) and the synthetic SED (in red) of the stars in the LMC sample described in 2.2: SSID 8 (left panel, see Fig. 3.4) and SSID 4595 (right). Blue diamonds show *Spitzer* photometry from Meixner et al. (2006) and optical + near IR data, available in the literature. The grey line in the right panel refers to SSID 111, classified as a post-AGB stars from Woods et al. (2011). In both panels we report the luminosity and effective temperature of the star, and the following parameters for the internal and outer dust shells: optical depth (at $10 \mu\text{m}$), dust temperature, dust composition and distance from the central star. For SSID 8 we modelled the emission from the central star with a COMARCS atmosphere corresponding to the best-fit effective temperature, while for SSID 4595 we used a black body spectrum.

chemistry phenomenon in Galactic bulge planetary nebulae, is indeed a common behaviour of all the stars formed between 1 and 4 Gyr ago.

This interpretation is supported by the luminosities required to reproduce the SED, in the range $5 - 10 \times 10^3 L_{\odot}$, in agreement with the post-AGB luminosities reported in Fig. 1.12. This understanding is in agreement with the fact that only one source shows a 90-day period, and the other 7 show no signs of variability (Jones et al., 2017). A further probe for this interpretation comes from the presence of a weak PAH-like emission feature at $6.3 \mu\text{m}$ in a post-AGB star in our sample (SSID 4547), confirming the presence of C-rich material and the classification as post-AGB stars¹.

The presence of these stars in the AGB sample is due to the criterion followed to distinguish AGB from post-AGB stars, discussed by Woods et al. (2011) (see their Fig. 3). Post-AGB stars are commonly identified by the presence of two distinct peaks in the SED,

¹A few PNe with a similar dual-dust chemistry (i.e., PAHs + amorphous silicates) have been observed in our Galaxy (e.g. Perea-Calderón et al., 2009). Curiously, their $6.3 \mu\text{m}$ feature is always the strongest one, as seen in our star SSID 4547

located in the $\lambda < 1 \mu\text{m}$ portion of the spectrum and at $9.7 \mu\text{m}$, separated by a clear minimum in the SED at $\sim 2 \mu\text{m}$. The presence of carbon dust affects significantly the shape of the SED in the $1 - 8 \mu\text{m}$ region, preventing the appearance of a minimum, making the SED very similar to a M-type AGB.

The Milky Way is known to host dual chemistry PNe (García-Hernández & Górný, 2014; Gutenkunst et al., 2008; Guzman-Ramirez et al., 2011) and post-AGB stars (Cerrigone et al., 2009; Molster et al., 2001; Waelkens et al., 1996); however, no dual chemistry PNe or post-AGB stars have been previously detected in the MCs (Bernard-Salas et al., 2009; Stanghellini et al., 2007), which could pose a problem to the present suggestion of the existence of dual chemistry post-AGBs. However, this might be just a consequence of small-number statistics given the low number of PNe that has been observed in the MCs in the infrared compared with the number of AGBs stars.

3.4 Faint, dusty AGB stars

The SED of the stars indicated with red full triangles in Fig. 3.4 show evidence of cool dust, with a peak at $9.7 \mu\text{m}$, revealing the presence of silicate grains. The left panel of Fig. 3.5 shows an example of these spectra. The luminosities deduced from SED fitting fall in the range $2 - 4 \times 10^3 L_{\odot}$.

Obscured M stars are produced either from $M > 3M_{\odot}$ stars experiencing HBB or to low mass stars (initial masses below $\sim 1.5M_{\odot}$) evolving through advanced AGB phases, before becoming carbon stars. Both explanations are not plausible in this case, because the luminosities would be much in excess of those observed. Furthermore, we have not found a way of reproducing the SED in the $4 - 8 \mu\text{m}$ region, without assuming significant amounts of carbon dust.

As it is noticeable in Fig. 3.6, which shows the evolution of the luminosity of the $1.2M_{\odot}$, $1.5M_{\odot}$ and $2M_{\odot}$ stars during the AGB evolution, the luminosities given above are compatible with the post-TP phases of low-mass stars. During these phases dust formation stops, because the drop in the mass loss rate provokes a significant decrease in the density of gaseous particles available to condensation.

We propose that these stars have reached the C-star stage via a TDU episode that followed the previous TP, and are currently evolving through a post-TP, low-luminosity phase. Similarly to the post-AGB stars discussed earlier in this section, we reproduce their SED by two dusty layers, with a more internal zone, populated by carbonaceous particles, and an outer region, with silicate grains. As shown in the left panel of Fig. 3.5, the synthetic SED obtained with these assumptions reproduces the IRS and photometric data well. Both dusty

layers are cool, in agreement with the expectation that dust formation is halted during these low-luminosity phases.

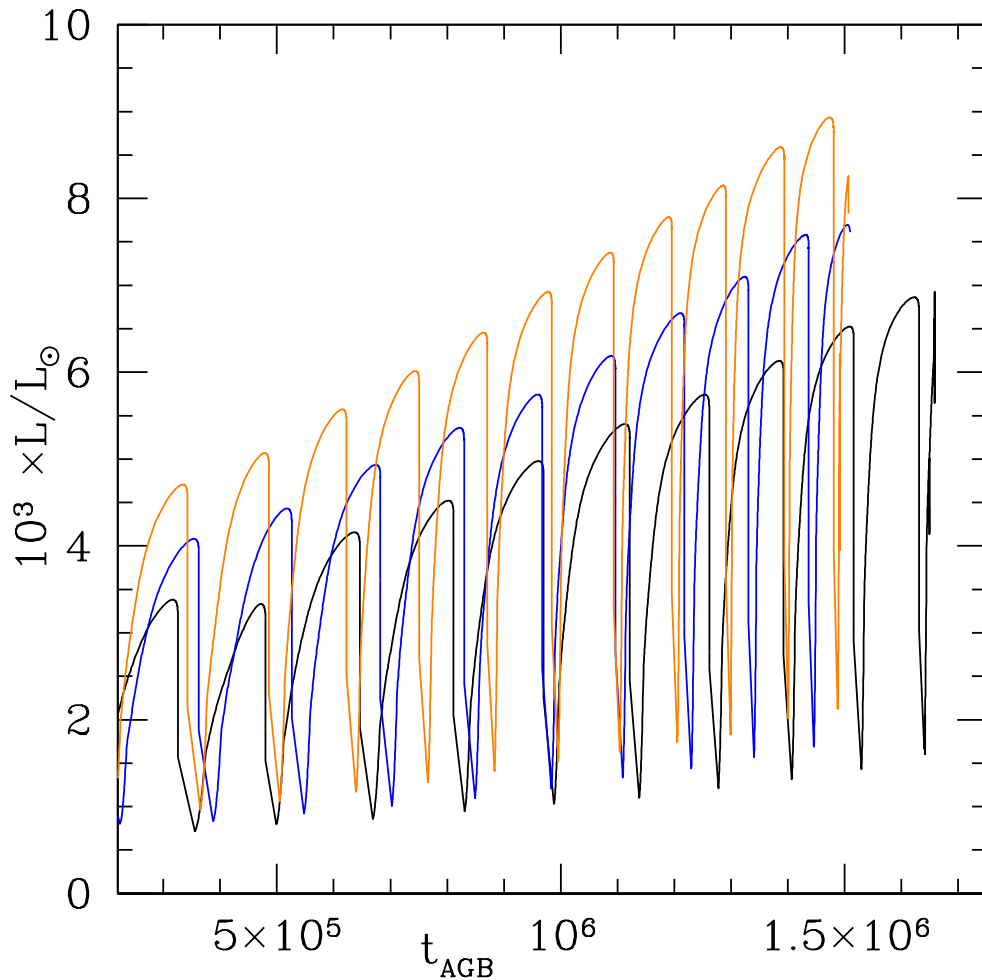


Figure 3.6 The evolution of the luminosity during the AGB evolution of stars of initial masses $1.2M_{\odot}$ (black line), $1.5M_{\odot}$ (blue) and $2M_{\odot}$ (orange).

The source shown in the left panel of Fig. 3.5 was studied by Groenewegen & Sloan (2018), who tried to fit its SED by adopting a single silicate dust shell. As shown in the two bottom left panels on page 77 of that paper, some significant differences between the observed SED and the best fit exist. The dual-dust chemistry model, compared to the single silicate dust shell, agrees better, particularly in the location of the primary peak and in the flux in the $\lambda > 15 \mu\text{m}$ domain.

According to our interpretation the two groups of stars discussed in Section 3.3 and 3.4 have a common origin, as all of them descend from progenitors of mass $1M_{\odot} < M < 2M_{\odot}$,

consistent with the episode of star formation that the LMC experienced 3 – 5 Gyr ago (Bertelli et al., 1992). They are characterized by a dual dust chemistry, being surrounded by a dust layer composed of carbonaceous particles, and a more external zone, harbouring silicates, alumina dust and solid iron.

The presence of amorphous carbon, a featureless species, renders the SED of these objects significantly different from stars of similar optical depth and luminosity surrounded by O-bearing dust species only.

We believe that the dual-dust chemistry originates from the transition to a C-rich photosphere during the final phase of life on the AGB. If this understanding is correct, we would expect these stars are C-rich, with a surface C/O not far in excess of unity.

Optical and/or NIR high-resolution spectroscopy would be valuable to confirm or disregard the present interpretation. If confirmed, the results presented in this paper suggest that evolved stars with dual chemistry are expected to be found in galaxies where significant star formation in the epochs 1 – 4 Gyr ago occurred. Their identification will be possible in the context of the *JWST* mission, considering that they occupy specific regions in the various observational planes.

With this results we completed the revision of the sample of AGB stars in the LMC, giving a new classification of the stars showing some peculiarities in their spectrum. After the two main groups of AGB stars, M-stars and carbon stars, have been redefined, it is now possible to carry out the overall characterization of the sample of AGB stars in the LMC, which will be discussed in the following chapters, the first dedicated to the oxygen-rich sources, while the final one is focused on the interpretation of the carbon-rich stars.

4

M-type stars: a *JWST* perspective

The discussion presented earlier in the present work outlined that stars begin the AGB phase as M-type stars, then, in a way that depends on the initial mass and chemical composition, they can become carbon stars.

The differences between these two classes of AGB stars concerns not only the molecular species formed in the surface regions, which affect the spectral energy distribution in the optical and near-IR wavelengths, but, more important, the mineralogy of the dust formed in the outflow, which reflects into the IR emission in the mid-IR, and the dust features characterizing the SED.

Important differences also distinguish the evolutionary properties of M- and C-stars, considering the reaction of the external regions of the stars to the achievement of the C-stage, discussed in Chapter 1, and the consequences for the evolution of the star in the following phase.

Based on these arguments, we decided to discuss separately the characterization of the stars and the choice of the observational planes most suitable to their study for either groups. In this chapter we focus on the oxygen-rich AGB sources in the sample presented in Section 2.2, listed in Table 4.1.

A detailed care is devoted to understand the planes where the different classes of the sources observed can be easily distinguished and where the obscuration trends for oxygen-rich stars are most clearly defined. This step is crucial to set up a methodology that will be extended to the galaxies in the Local Group, once the *JWST* data will become available. The discussion presented here are based on the AGB evolution models described in Chapter 1, which include the description of dust formation in the circumstellar envelope.

As a starting point we consider three observational planes proposed by Jones et al. (2017), obtained by combination of the MIRI F770W, F1000W, F1500W and F2100W magnitudes. To explore the potentialities offered by the combination of near-IR and mid-IR photometry,

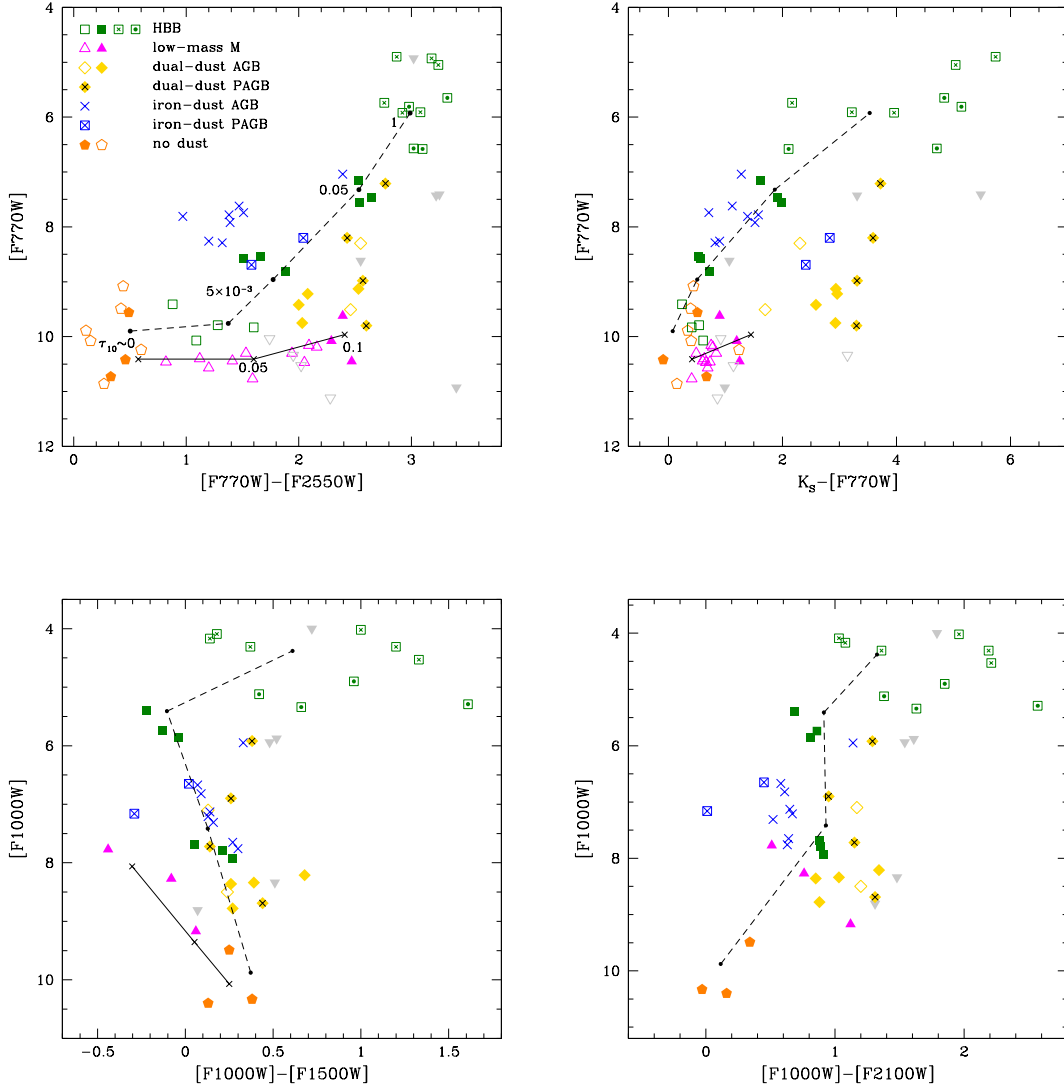


Figure 4.1 The distribution of the LMC stars belonging to the sample described in Section 2.2 in various observational planes, built with different combinations of the filters of the MIRI camera and 2MASS K_S filter. The values of the magnitudes have been obtained by convolving *Spitzer* IRS data with the transmission curves of the various filters. For the stars indicated with open points, the IRS data were truncated to $\sim 14.2 \mu\text{m}$; in these cases we used the MIPS [24] magnitude, when available, as a rough estimate of F2550W, as the difference between them is only a few hundredth of magnitudes. The different symbols refer to the various classes of objects, according to the legend reported in the top, left panel. Among these, grey triangles indicate sources for which we could not provide a reliable interpretation on the basis of their SED. The solid and dashed lines indicate the reddening sequence of low-mass, oxygen-rich AGB stars and of massive AGBs experiencing HBB, respectively (see Section 4.2 and 4.3 for details). The black points along the two sequences refer to typical values of the optical depth τ_{10} , which are indicated in the top, left panel.

we also consider the (K_S -F770W, F770W) plane (see Dell’Agli et al., 2016, 2019a, 2018a, for a discussion on the advantages of using near- and mid-IR photometry).

The distribution of M-type AGBs in the 4 planes is shown in Fig. 4.1.

We follow the approach described in Section 2.4 to characterize the individual sources and the details of the dust present in their surroundings. To make our conclusions more robust, we will compare the OGLE periods of the stars (Soszyński et al., 2009), when available, with the theoretical estimates, based on the expected variation of the mass and luminosity of the model stars. The distribution of the AGB sources in the OGLE period vs luminosity plane is shown in Fig. 4.2.

In the following sections we present our interpretation of the M-type AGB sample, with the different sources grouped into various sub-samples, each characterized by a specific combination of evolutionary and dust properties and by the quantity and mineralogy of the dust particles in the circumstellar envelope.

4.1 Scarcely obscured, dust-free stars

The stars indicated with orange pentagons in Fig. 4.1 show no trace of dust in their surroundings. The SED of these objects can be safely reproduced by assuming optical depths close to zero, indicating a negligible degree of obscuration. Based on the luminosities obtained by SED fitting, we deduce that this group of sources is mainly composed by low-mass stars, that have not reached the C-star stage. In the (F770W-F2550W, F770W) plane they populate the region within $0 < F770W-F2550W < 0.7$, separated from the other sources.

In the (F1000W-F1500W, F1000W) and (F1000W-F2100W, F1000W) planes these stars can be identified by means of the low F1000W fluxes, consistent with the scarce presence of silicates in the circumstellar envelope, that prevents the formation of the $9.7 \mu\text{m}$ feature. In the (K_S -F770W, F770W) plane their identification is more tricky, because they mix with obscured stars with optical depths $0.005 < \tau_{10} < 0.1$. This is because when $0.005 < \tau_{10} < 0.1$: a) the formation of silicates increases the flux in the spectral region around $10 \mu\text{m}$, provoking at the same time a dip around $\sim 8 \mu\text{m}$, that decreases the F770W flux (see e.g. the blue line in the right panel of Fig. 2.4); b) there is no significant shift of the SED towards mid-IR wavelengths, thus the K_S flux is only scarcely affected by dust reprocessing. Therefore, the stars with low optical depths are characterized by K_S -F770W colours and F770W magnitudes not significantly different from those exhibited by the unobscured stars discussed here.

In the planes shown in the top panels of Fig. 4.1 the stars with no dust span a F770W range of approximately 2 mag. This reflects the different luminosities, which we find (by SED fitting) to be in the range $5 \times 10^3 - 3 \times 10^4 L_\odot$, consistent with the heterogeneity in the

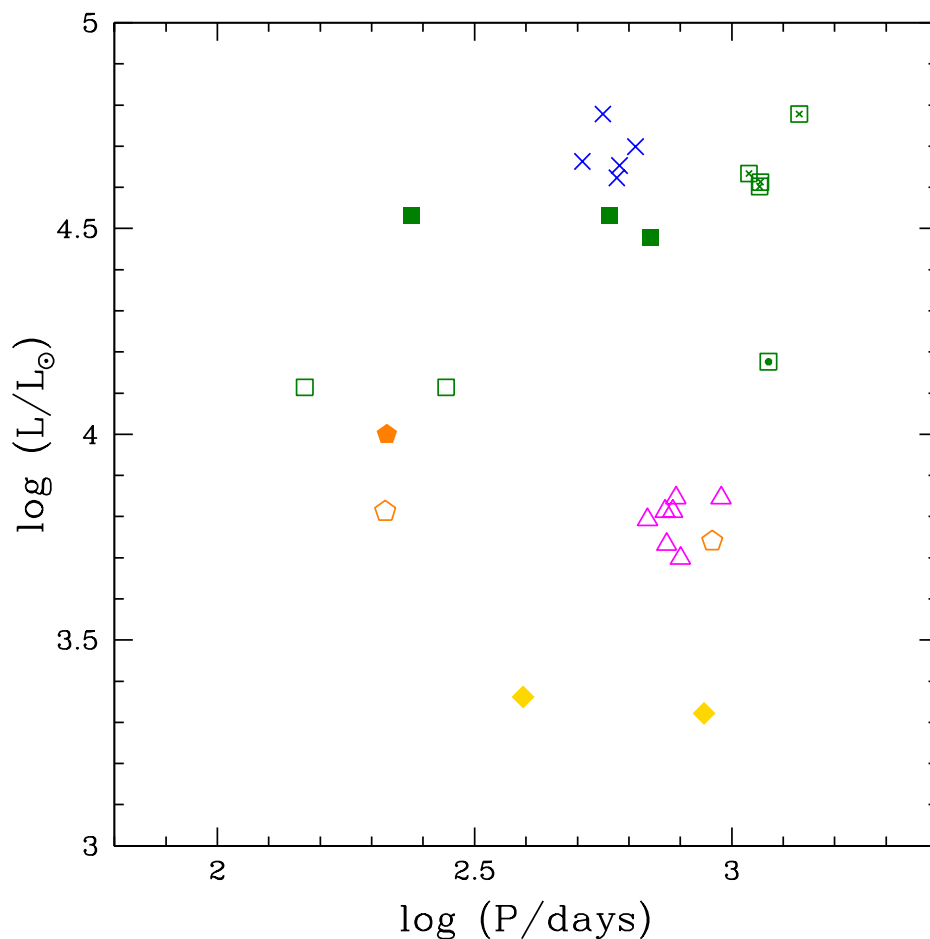


Figure 4.2 Period - Luminosity diagram of the LMC M-type stars in the sample presented in Section 2.2, for which OGLE periods are available. Luminosities are those reported in Table 4.1. Symbols are the same used in Fig. 4.1.

mass and formation epoch of the progenitors of these sources. This same analysis cannot be done in the planes shown in the bottom of the figure, because the lack of the *Spitzer* IRS data at wavelengths $\lambda > 14.2 \mu\text{m}$ prevents the determination of F1000W-F1500W and F1000W-F2100W for the majority of these objects (those indicated with open pentagons in the top panels).

4.2 Low-mass dusty M-type AGB stars

The magenta triangles in Fig. 4.1 indicate stars that we interpret as low-mass dusty stars. The evolutionary tracks of these objects (discussed in Chapter 2) in the different observational planes overlap substantially, mainly because of the similar luminosities, favoured by the occurrence of core electron degeneracy for $M \leq 2M_{\odot}$ progenitors. The redwards extension of the tracks depends on both the initial mass and the metallicity. Stars of initial mass $M \lesssim 1.5M_{\odot}$ reach higher optical depths during the phases preceding the C-star stage, compared to their $2 - 3M_{\odot}$ counterparts (see discussion in Section 1.4.4). The lower the metallicity the shorter the redwards extension of the evolutionary tracks, owing to the lower amounts of silicon present in the envelope of low- Z stars. This behaviour with mass and chemical composition is discussed in detail in Dell’Agli et al. (2015b, Fig. 8).

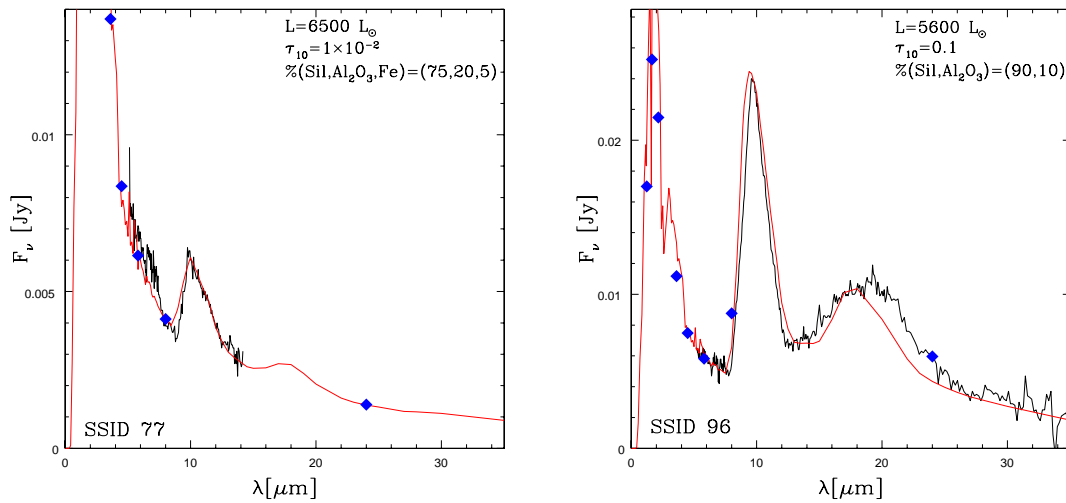


Figure 4.3 The *Spitzer* IRS spectra (black line) of two stars, selected among those interpreted as low-mass AGBs, taken along the obscuration sequence of low-mass stars shown in Fig. 4.1. The photometry is indicated with blue diamonds. The best fit, indicated with the red line, is obtained by assuming the luminosity, dust composition and optical depth indicated in the two panels.

The position of this class of objects in the various planes is mainly determined by the optical depth, which allows us to draw theoretical reddening sequences (see Chapter 2), indicated with solid lines in Fig. 4.1. The SED of the stars indicated with magenta triangles confirms the theoretical expectations, as it is reproduced by assuming a majority (70 – 90%) of silicate grains, with lower percentages of alumina dust and solid iron and luminosities in the range $5 \times 10^3 - 10^4 L_{\odot}$ (see Table 4.1 for details).

We report in Fig. 4.3 two examples of these objects, for which we show the *Spitzer* IRS data, the photometry available in the literature and the best fit model obtained in the present analysis. These two cases exhibit significantly different degrees of infrared emission that cover almost the whole range of the optical depths derived.

The range covered by the luminosities and the position of the magenta triangles in the PL plane shown in Fig. 4.2 suggests that these sources form a homogeneous group, made up by objects that descend from low-mass progenitors (in agreement with Trabucchi et al., 2018), the progeny of $M \leq 1.5M_{\odot}$ stars, older than ~ 2 Gyr. Indeed, stars of mass $2M_{\odot} \leq M \leq 3M_{\odot}$ form negligible quantities of dust during the M-stage (see discussion in Chapter 2).

In summary, we base the characterization of the stars in this sub-sample on the following points: i) the luminosities are below $\sim 10^4 L_{\odot}$; ii) dust is mainly composed of silicates; iii) the optical depths are in the range $0.005 < \tau_{10} < 0.1$.

The range of optical depths and dust composition required to reproduce the SED are in agreement with the low-mass model stars discussed in Dell’Agli et al. (2015b). The fraction of silicates is found to increase across the reddening sequence, ranging from $\sim 70\%$ to $\sim 90\%$. This trend is connected with the fact that alumina dust, as discussed in Chapter 1, is more stable than silicates, thus it forms at larger rates, in a more internal region of the circumstellar envelope, whereas silicates form in a more external zone. The increase in wind density triggers a higher formation rate of both species; however, this has a larger effect on the amount of silicates formed, as alumina dust is so stable that it forms in quantities close to saturation, thus being less sensitive to variations in the thermodynamics of the wind.

The reddest objects of this group along the sequence in the (F770W-F2550W, F770W) plane, with $F770W-F2550W > 2$ and $\tau_{10} \sim 0.1$, are evolving through the final phases as M stars, before becoming carbon stars. This hypothesis was proposed by Dell’Agli et al. (2015b) to explain the O-rich stars studied by Blum et al. (2006), that define a prominent finger in the colour-magnitude ([8.0]-[24],[24]) diagram. The present interpretation might be tested by measuring the surface C/O ratio in these stars (e.g. via near-IR spectroscopy), that is expected to increase across the sequence, until becoming slightly below unity for the sources exhibiting the largest infrared emission.

In this context, the sources SSID 22 and SSID 130, indicated with yellow open diamonds, represent an ideal prosecution of this evolutionary path, because we interpret them as stars that have only recently reached the C-star stage, with the circumstellar envelope hosting a more internal, hot, dusty layer, populated by solid carbon particles, and a cooler zone, where silicate dust formed during previous evolutionary phases is expanding away from the star. The details of the best fit obtained for SSID 22 are shown in Fig. 4.4.

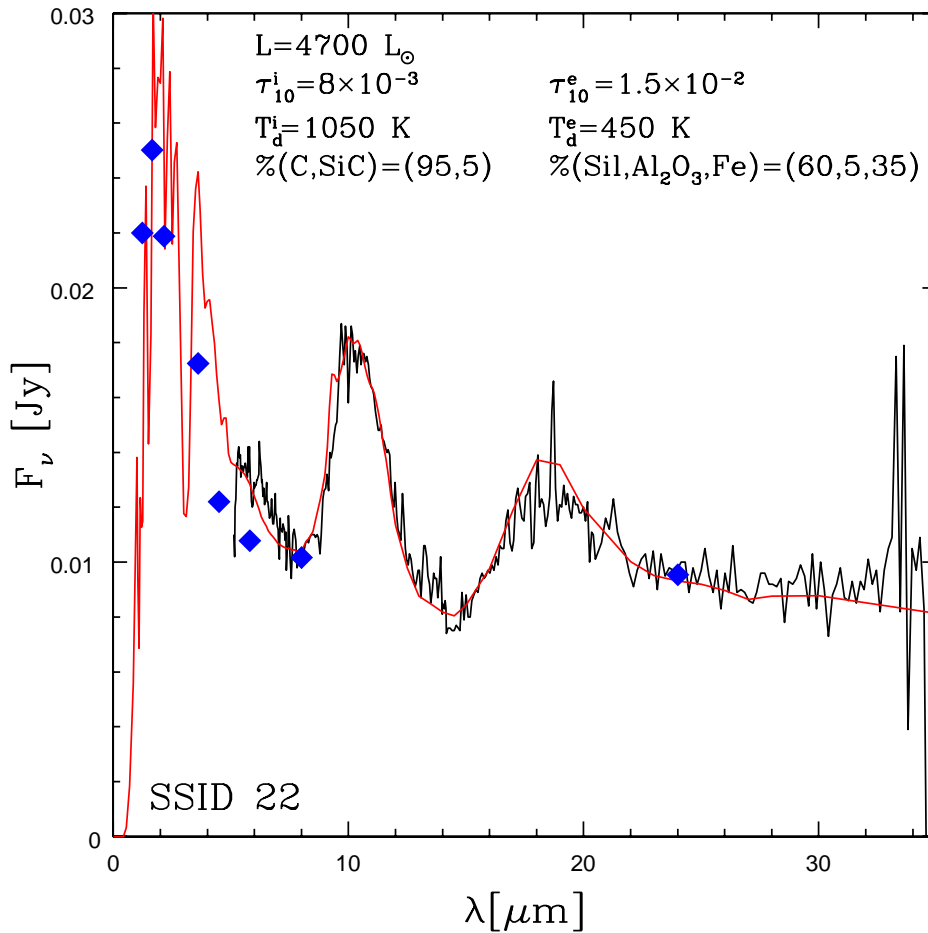


Figure 4.4 Best-fit model for the source SSID 22 (same symbols and colours as in Fig. 4.3 are used), interpreted as a low-mass star that has just reached the C-star stage (see text for details). The values of the overall luminosity and of the parameters of the internal and external dust layers are indicated.

The track in the (F770W-F2550W, F770W) plane is approximately horizontal; this behaviour is connected with the evolution of the shape of the SED of low-mass stars with τ_{10} , shown in the left panel of Fig. 2.4. With increasing optical depth the height of the silicate feature and the overall spectrum in the $\lambda > 10 \mu\text{m}$ region increase, whereas the F770W flux keeps approximately constant, owing to the reasons explained in the previous section, related to the shape of the silicate feature.

Inspection of Fig. 4.1 shows that (F770W-F2550W, F770W) is the only plane where the evolutionary sequence of these objects has a significant extension and does not overlap with different kind of stars. In the (K_S -F770W, F770W) plane they lay very close to the dust-free sources, for the reasons given in Section 4.1. In the (F1000W-F1500W, F1000W) plane these sources populate a diagonal band, reported in the bottom, left panel of Fig. 4.1,

with the most obscured stars located in the bluer and brighter region. This is due to the increasing prominence of the $10\ \mu\text{m}$ feature, that rises the F1000W flux. The colour range, $\Delta(\text{F1000W-F1500W}) \sim 0.5\ \text{mag}$, is less extended than in the previous cases, because the increase in the flux in the $10\ \mu\text{m}$ spectral region is accompanied by the rise of the flux in the whole region at wavelengths $\lambda > 10\ \mu\text{m}$ (see the left panel of Fig. 2.4).

In the (F1000W-F2100W, F1000W) diagram the identification of these stars is even harder, because the percentage increase in the flux as the optical depth increases are very similar in the spectral regions where the two filters are centred, i.e. 10 and $21\ \mu\text{m}$.

4.3 Stars undergoing hot bottom burning

We turn the attention to the stars indicated with green squares in Fig. 4.1. A few examples of the SED of these objects are shown in Fig. 4.5, where we present the observations and the corresponding theoretical SED. Unlike low-mass stars, massive AGBs span a wide range of luminosities, extending by a factor ~ 5 (see discussion in Chapter 1 and Fig. 1.5). The position of each model in the various planes is determined by the values of the luminosity and optical depth. Therefore the tracks of stars of different mass are practically overlapped, the only difference being that the higher the mass of the progenitor the larger the maximum luminosity and the optical depth reached (see Chapter 1), and the wider the excursion of the evolutionary track in the planes. The dashed lines shown in Fig. 4.1, connecting points characterized by different optical depths and luminosities, can be considered as a reddening sequence of massive AGBs.

The extension of the theoretical sequences is at first order independent of metallicity. On the other hand, on the statistical side, we must consider that for lower metallicities the range of masses that reach the largest τ_{10} values is narrower and, more important, the largest optical depths are experienced only during a small fraction of the AGB life (see Fig. 2 in Dell’Agli et al., 2015a, for the metallicity effects on the obscuration of massive AGBs).

The luminosities deduced from the analysis of the SED of the stars in this sub-sample are in the $2 - 8 \times 10^4 L_{\odot}$ range and the optical depths span the interval $\tau_{10} \sim 0.005 - 3$. The SED of these sources can be nicely interpreted by assuming a "standard" dust mineralogy for obscured M stars: a dominant contribution from silicates, with percentages in the range $60 - 100\%$, completed by smaller fractions of alumina dust and solid iron. As for the low-mass counterparts, the higher the required fraction of silicates the larger the optical depth.

These results, compared with the theoretical models discussed in Chapter 1 (see left panel of Fig. 1.5) and the sequence of SEDs in the right panel of Fig. 2.4, indicate that these stars

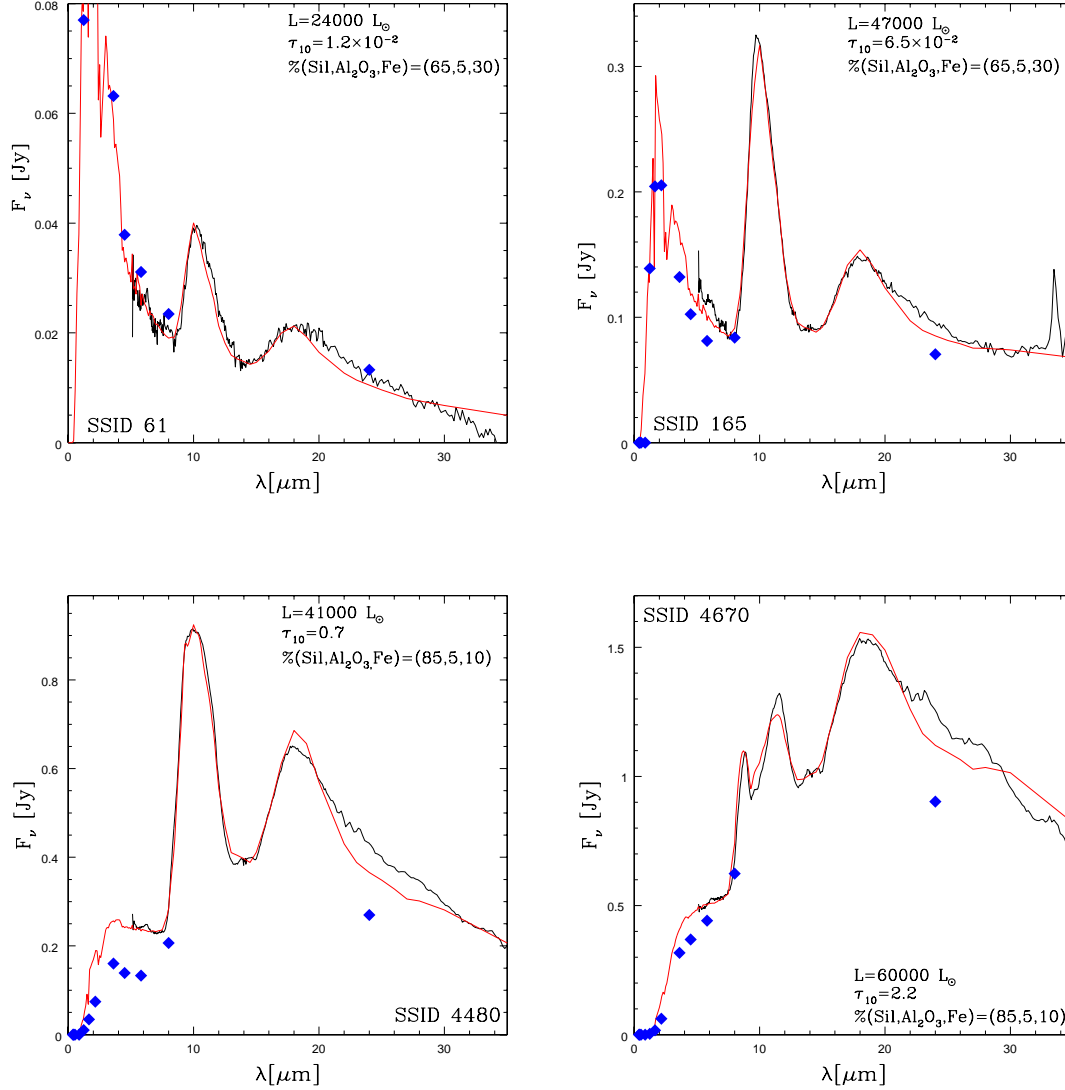


Figure 4.5 The *Spitzer* IRS spectrum (black line) of 4 stars, selected among those interpreted as massive AGBs, currently experiencing HBB, taken along the obscuration sequence indicated with a dashed line in Fig. 4.1. The photometry and the best-fit (red line) are shown, with the parameters adopted.

descend from progenitors of mass above $3M_{\odot}$, formed not earlier than $\sim 250 - 300$ Myr ago. This interpretation is also confirmed by their position in Fig. 4.2: their PL relation is in agreement with Trabucchi et al. (2018) models for massive AGB stars ($> 3M_{\odot}$).

The significant amount of dust present in the circumstellar envelope rules out the possibility that these stars are metal poor and suggests that their metallicity is $Z = 4 - 8 \times 10^3$; this hypothesis is supported by the mass-metallicity relation of the LMC, according to which

star formation in the last 1 Gyr is dominated by a $Z = 0.008$ stellar population (Harris & Zaritsky, 2009).

4.3.1 Massive AGB stars in the colour-magnitude planes

The reddening sequence defined by massive AGB stars, discussed in the previous section, can be used to attempt their characterization.

Indeed, on general grounds, we find that the optical depths increase across the sequences in the different planes: the sources indicated with open and full green squares are characterized by $5 \times 10^{-3} < \tau_{10} < 0.1$, whereas dotted and crossed green squares correspond to $\tau_{10} > 0.5$.

In the (F770W-F2550W, F770W) plane (see top, left panel of Fig. 4.1) the region populated by these objects extends over ~ 2 mag in F770W-F2550W and almost 4 mag in F770W. Unlike the lower mass counterparts, discussed in Section 4.2, the luminosity is generally correlated with τ_{10} , the brighter stars being on the average more obscured (see Chapter 1). The stars indicated with green, dotted squares are an exception to this rule, as they are fainter than their counterparts with similar optical depth, indicated with green, crossed squares. We will discuss these sources later in this section.

Both the F770W and F2550W fluxes rise with increasing τ_{10} , as shown in the right panel of Fig. 2.4 and in the examples in Fig. 4.5. On the other hand, it is clear from Fig. 2.4 that the increase of the flux in the spectral region around $25.5 \mu\text{m}$ is percentually larger when compared to the $\lambda \sim 7.7 \mu\text{m}$ domain, thus making F770W-F2550W to increase with τ_{10} , provoking a rightwards trend of the theoretical sequence.

The stars discussed here trace a diagonal pattern in the (K_S -F770W, F770W) plane. With the excursion in the F770W magnitude discussed before, K_S -F770W spans a range of almost 6 mag, due to the gradual shift of the whole SED towards mid-IR wavelengths and the decrease in the near-IR flux, particularly relevant for $\tau_{10} > 0.1$. This allows for a higher sensitivity to τ_{10} , although the measurement of the near-IR flux could be critical for the most obscured stars. Indeed, one out of the 3 brightest stars are not reported in this plane, owing to the lack of the K_S flux.

Regarding the (F1000W-F1500W, F1000W) diagram, shown in the bottom, left panel of Fig. 4.1, the path traced by the reddening pattern presents a turning point: the initial trend towards the blue, down to F1000W-F1500W ~ -0.2 , is followed by a redwards excursion. The first part is due to the appearance of the feature at $9.7 \mu\text{m}$, that rises the $10 \mu\text{m}$ flux and diminishes the emission in the wavelength region around $15 \mu\text{m}$ (see Fig. 2.4). When τ_{10} exceeds ~ 0.1 this trend is reversed, because the whole mid-IR flux is lifted. The most obscured stars distribute approximately horizontally on this plane, because for $\tau_{10} > 2$ the

silicate feature turns into absorption, thus no further increase in the 10 μm flux occurs. The stars with the highest optical depths that correspond to the brightest and youngest objects discussed previously, are located in the right, upper region of the plane.

In the (F1000W-F2100W, F1000W) diagram the sequence of the stars discussed here follows a slightly different behaviour compared to the (F1000W-F1500W, F1000W) plane. The reddening pattern extends towards higher F1000W fluxes; however, no clear turning point is found, because the rise of the SED in the 10 and 21 μm spectral regions occurs with similar percentages. The stars with $\tau_{10} > 0.5$ populate the brightest region of this plane, at F1000W-F2100W > 1.

4.3.2 Stars undergoing soft HBB

The stars indicated with green, open squares in Fig. 4.1 harbour little amounts of dust in their circumstellar envelope. The optical depths are a few 10^{-3} . According to our interpretation, they have just started the HBB activity. We expect that only a modest depletion of the overall surface carbon has occurred and that the $^{12}\text{C}/^{13}\text{C}$ ratio has dropped to values close to the equilibrium abundances, of the order of ~ 4 . No meaningful depletion of the surface oxygen is expected.

Following the theoretical reddening pattern, we analyze the sources indicated with green, full squares in Fig. 4.1, that have $0.01 < \tau_{10} < 0.1$ and luminosities covering the interval $2 - 4.5 \times 10^4 L_{\odot}$. The sources SSID 61 and SSID 165, reported in the top panels of Fig. 4.5, belong to this group. The luminosities and τ_{10} s given above suggest that these objects are the progeny of $4 - 5 M_{\odot}$ stars formed 100 – 300 Myr ago, currently experiencing HBB. As shown in Chapter 1, the surface carbon should be $\sim 10 - 20$ times smaller than in their less obscured counterparts, the surface nitrogen enhanced by one order of magnitude and the surface $^{12}\text{C}/^{13}\text{C}$ ratio should be very close to the equilibrium value, i.e. 3 – 4. Furthermore, these stars are expected to be experiencing the Cameron & Fowler (1971) mechanism, thus they should be enriched in lithium.

4.3.3 Highly obscured O-rich AGBs

The objects indicated with crossed and dotted green squares in Fig. 4.1 are producing dust at a high rate, as confirmed by the large optical depths, $\tau_{10} > 0.5$.

In the (F770W-F2550W, F770W) and (K_S -F770W, F770W) planes the obscuration patterns are most easily distinguished. The stars with F770W > 5.5 (all the crossed and dotted, green squares, but the 3 brightest objects) have luminosities below $\sim 5 \times 10^4 L_{\odot}$; an example is the source SSID 4480, reported in the bottom, left panel of Fig. 4.5. Based on the

results regarding $Z = 0.008$ metallicity shown in Chapter 1 (see Fig. 1.5), we deduce that they descend from progenitors of mass in the range $3.5 - 5M_{\odot}$, formed between 100 Myr and 300 Myr ago. The optical depths, $0.5 < \tau_{10} < 1.5$, are consistent with this conclusion.

The 3 brightest sources, with $F770W < 5.5$, are characterized by a very large mid-IR emission, with $\tau_{10} \sim 2 - 3$, and luminosities above $5 \times 10^4 L_{\odot}$, that, based on the results shown in Chapter 1, indicate progenitors of mass above $\sim 5M_{\odot}$, younger than ~ 100 Myr.

A word of caution regarding dust formation modelling in the winds of these peculiar objects is needed here. While AGB models reproduce both the luminosities and the periods of these sources, the optical depths required, in the range $2 < \tau_{10} < 3$ are higher than the largest theoretical values predicted, shown in Chapter 1, of the order of $\tau_{10} \sim 1^1$. This outlines some tension between models and observations. Recent radiation-hydrodynamic (RHD) models of winds of M-type AGB stars (see, e.g., Höfner et al., 2016; Höfner & Olofsson, 2018) indicate that dust formation will indeed start deeper inside the atmosphere (at smaller condensation radius), but this result was obtained at solar metallicity (not typical LMC metallicity). However, the difference in condensation radii in the simple stationary outflows of the stellar evolution models and the more sophisticated RHD models, is likely a result of the different levels of detail of the two types of models. First, the RHD models are known to produce different results due to the dynamics (pulsation) and time dependence. Second, frequency-dependent radiative transfer (RT) changes the energy balance and temperature structure compared to the atmospheric structures obtained in the stellar evolution models. That is, the simplistic atmosphere models we employ probably do not predict correct condensation radii.

4.3.4 A class of massive AGBs in the very late AGB phases?

A second issue of the present understanding is the interpretation of the stars indicated with dotted, green squares in Fig. 4.1. These sources have luminosities of the order of $2 \times 10^4 L_{\odot}$, significantly smaller than those of their brighter counterparts, indicated with crossed, green squares. These luminosities are compatible both with those of stars evolving through the initial TPs, or at the end of their AGB life, after HBB was turned-off. Their periods (we refer to the OGLE period for SSID 4007 and those from Groenewegen & Sloan 2018 for the other sources in this group) are close or above 1000 d. Because in the first case we should expect periods below ~ 500 d (see Fig. 4.2), we believe more plausible that these stars are experiencing the latest AGB phases.

The main drawback of this interpretation is that their degree of obscuration is also expected to be low (see the bottom, left panel of Fig. 4.1), whereas their optical depths are

¹We do not consider here the SAGB models ($6M_{\odot} < M \leq 8M_{\odot}$), which reach higher values of τ_{10} , because the extreme short duration of their AGB life, of the order of ~ 10 kyr.

$\tau_{10} > 1$. A possible solution is that during the very final AGB phases the formation of a disc favours the accumulation of the dust produced during earlier phases, such that the overall dust density is significantly higher than predicted by the simplified description of the wind used in the present analysis. We leave this problem open.

The surface chemical composition of the stars indicated with crossed and dotted, green squares is expected to show the imprinting of proton-capture processing, in analogy with the less obscured counterparts, indicated with open and full, green squares. These stars are also expected to have started the Ne-Na nucleosynthesis, with a sodium enrichment by a factor of ~ 5 (Ventura et al., 2013). If this small sample includes stars of lower metallicity, of the order of $Z = 0.004$ then we would observe the results of oxygen burning and of Mg-Al nucleosynthesis, with a surface Al enhancement by a factor $5 - 10$ and oxygen depletion by a factor ~ 2 (Ventura et al., 2016a).

4.4 Iron-dust stars

4.4.1 Massive AGB stars with iron dust

The sample studied in the present work includes a paucity of bright objects, showing peculiar SEDs, indicated with blue crosses in Fig. 4.1. We have discussed this group of stars in Chapter 3, interpreting them as the progeny of metal-poor ($Z \sim 10^3$), $M > 4M_{\odot}$ stars, formed ~ 100 Myr ago. Moreover, we showed that the mineralogy of the dust around these objects is dominated by solid iron, which accounts for $\sim 80\%$ of the total dust, with smaller percentages of silicates ($\sim 15\%$) and alumina dust $\sim 5\%$. Unlike the bright stars undergoing HBB, discussed earlier in Section 4.3.3, the optical depths are not particularly large, being $\tau_{10} < 0.01$.

As shown in Fig. 4.1, in the (F770W-F2550W, F770W) plane these objects populate the region at $1 < F770W-F2550W < 1.5$ and $F770W \sim 8^2$. The colours of these sources are not extremely red, consistently with the low optical depths. The F770W fluxes are higher than those exhibited by the more metal rich counterparts of similar colours. This is due to the peculiar shape of their SED (see Fig. 3.2 in Chapter 3), because the low percentage of silicates prevents the depression of the flux in the spectral region around $8 \mu\text{m}$, thus lifting the F770W emission (see Chapter 3 for the detailed discussion).

²The only exception is the source SSID 4098, with $F770W-F2550W \sim 2.4$, which is evolving through a less advanced evolutionary phase, when oxygen in the envelope has not been completely burnt, so that $\sim 40\%$ of dust is made up of silicates.

In the (K_S -F770W, F770W) and (F1000W-F1500W, F1000W) planes (see Fig. 4.1) the iron dust stars cannot be easily identified, as they lie along the reddening sequence of their counterparts of higher metallicity, close to those indicated with full, green squares.

In the (F1000W-F2100W, F1000W) plane these sources populate a zone ~ 0.2 mag bluer than the stars with similar optical depths and higher metallicity: this is because the higher fraction of iron dust affects the SED by decreasing the relative height of the secondary silicate feature, at $\sim 20 \mu\text{m}$, which diminishes the F2100W flux, rendering the F1000W-F2100W colours bluer (see Fig. 3.2 in Chapter 3).

4.4.2 Post-AGB stars with iron dust

In the family of stars surrounded by iron dust we also consider the sources SSID 4267 and SSID 6, indicated in Fig. 4.1 with open, blue squares filled with crosses. The *Spitzer* IRS and photometric data and the best-fit model for SSID 4267 are shown in Fig. 4.6.

We find that these two objects have effective temperatures in the range $T_{\text{eff}} \sim 7000 - 8000$ K, luminosities $\sim 2 - 2.5 \times 10^4 L_{\odot}$ and are surrounded by dust, mainly composed by solid iron. These parameters point to an evolutionary nature that is more evolved than that of stars in the AGB phase, suggesting that they are post-AGBs; this is also consistent with the large IR excess observed (Kamath et al., 2014, 2015; van Aarle et al., 2011; van Winckel, 2003) and with the predicted post-AGB luminosities of metal-poor massive AGBs (Miller Bertolami, 2016). SSID 4267 is classified as a post-AGB candidate in the photometric study to search for post-AGB stars in the LMC by van Aarle et al. (2011). Additionally, in the *Spitzer* and TIMMI2 study by Gielen et al. (2011) of post-AGB disc sources, SSID 6 is classified as a post-AGB star with atypical dust chemistry, because it shows no strong evidence for the expected crystalline features in their spectra. A combination of amorphous silicate dust and alumina was required to fit the spectral features in the $5 \mu\text{m} < \lambda < 40 \mu\text{m}$ region. Since we find that SSID 4267 and SSID 6 are surrounded by iron dust, we classify these two objects as iron-dust post-AGB stars.

Iron dust post-AGB stars are characterized by optical depths $\tau_{10} \sim 1 - 5 \times 10^{-3}$, smaller than their counterparts evolving through the AGB phase. This is because dust formation stops when the stars leave the AGB and the dust layer currently observed is expanding away from the central star, in a lower density region. The dust temperatures required, of the order of 700 – 900 K, support this interpretation. In the study by Woods et al. (2011) these objects have been classified as M-type AGB stars. This is because Woods et al. (2011) identify post-AGB stars based on the presence of a distinguished double peak in the SED, separated by a clear minimum at $\lambda \sim 2 \mu\text{m}$; the SEDs of SSID 4267 and SSID 6 do not show such an expected minimum. Our interpretation for the lack of the minimum is that

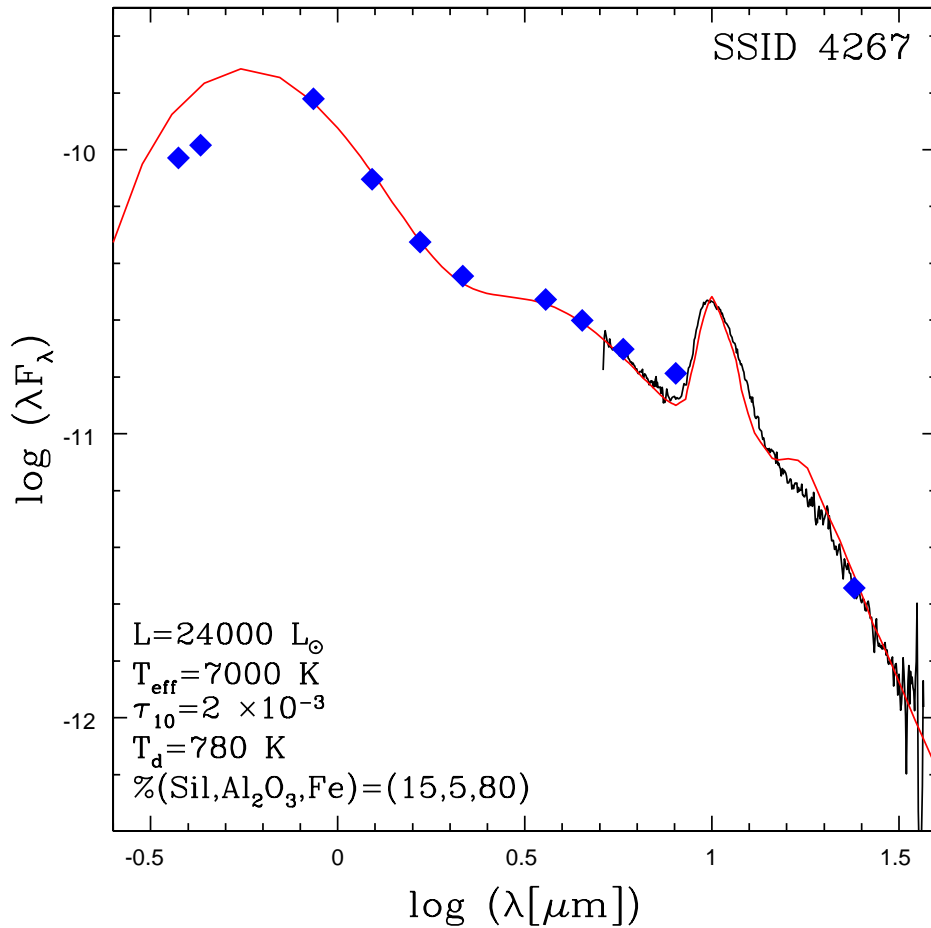


Figure 4.6 IRS, photometry results and best-fit models for SSID 4267, interpreted as a post-AGB star surrounded by dust, whose composition is dominated by iron grains, evolving through the AGB and the post-AGB phase, respectively. We report the flux in the $\log(\lambda F_{\lambda})$ scale, to better understand why this object was misclassified as an AGB star (see text for a discussion on this point).

the presence of iron dust makes the minimum in the SED to vanish almost completely, thus rendering the spectrum similar to a scarcely obscured M-type AGB star. As discussed in Chapter 3 for the dual-dust post-AGB stars, such a modification of the SED is the typical effect of the presence of significant quantities of a featureless dust species (like solid iron is). Furthermore, a meaningful difference between the SED of AGB and post-AGB stars surrounded by iron dust is the peak in the spectral emission, located at shorter wavelengths in the latter case (see Fig. 4.6). As a consequence, AGB stars have lower F770W magnitudes than their post-AGB counterparts, and their (F770W-F2550W) colours are bluer. This can be

seen in the relative position of the two groups of stars in the (F770W-F2550W, F770W) plane. (K_S -F770W, F770W) is the plane where iron dust AGB and post-AGB stars can be separated more easily. This is because the SED of AGB stars generally peaks at wavelengths around $\sim 2 \mu\text{m}$, that renders their K_S -F770W colours significantly bluer than in the post-AGB case. In the (F1000W-F1500W, F1000W) and (F1000W-F2100W, F1000W) planes iron dust stars populate the same regions.

4.5 Dual dust chemistry AGB stars

We discussed in Chapter 3 the stars indicated with yellow diamonds in Fig. 4.1, proposing for them a dual-dust chemical composition. Despite according to our interpretation yellow crossed diamonds and full diamonds indicate two groups of stars that are evolving through different evolutionary phases, we discuss them in the same context, owing to the similarities in the mass and formation epoch of the progenitors and in the mineralogy of the dust in their circumstellar envelope.

The yellow, crossed diamonds (see Fig. 4.1) indicate the sources SSID 4054, SSID 4245, SSID 4547, SSID 4595, that we interpreted in Chapter 3 as post-AGB stars descending from low-mass (below $2M_\odot$) progenitors, with a dual-dust composition. They are characterized by effective temperatures above 5000 K and luminosities in the range $5 \times 10^3 - 10^4 L_\odot$.

Full, yellow diamonds in Fig. 4.1 point refer to faint stars with luminosities in the range $2 - 4.5 \times 10^3 L_\odot$, which we previously interpreted as dual-dust chemistry stars that are evolving through a post-TP phase, during which the CNO nuclear activity is temporarily extinguished (which accounts for the low luminosities found), and no dust is being formed (see Chapter 3 for the detailed discussion).

4.5.1 Dual-dust stars in the colour-magnitude planes

Among the different observational planes shown in Fig. 4.1, the diagram where dual-dust chemistry objects can be identified most easily is the (K_S -F770W, F770W) plane. Indeed, we discussed these sources relating to this colour-magnitude diagram in Chapter 3. Here we recall that the presence of carbon dust makes the F770W flux higher and the K_S -F770W colour bluer than in stars of similar optical depth. Therefore, the colours of these stars in this plane are comparable with those of the largely obscured stars discussed in Section 4.3, that are much brighter. In the same K_S -F770W colour range is located also SSID 130, that, on the other hand, is characterized by a dual dust chemistry as well (see Section 4.2).

In the (F770W-F2550W, F770W) plane they lie slightly above the stars with similar optical depth, again for the peculiar shape of the SED in the $\lambda \sim 8 \mu\text{m}$ spectral region; however, their identification is more tricky than in the (K_S -F770W, F770W) plane.

In the (F1000W-F1500W, F1000W) and (F1000W-F2100W, F1000W) planes the dual chemistry stars populate the same region where we find the sources with low τ_{10} .

4.6 M-type evolved stars in the colour-colour diagrams

The distribution of the various classes of M-type evolved stars, in the colour-colour diagrams can be used to identify the different reddening sequences and to select those planes where the various groups can be distinguished more clearly. In this case we lack the information on the luminosity of the individual sources, but we obtain a more reliable indication on the optical depth of the circumstellar envelopes. We show here the population of the stars in the sample considered in the present chapter on the (F770W-F2550W, K_S -F770W), (K_S -F770W, F1500W-F1800W), (F1000W-F1280W, F1500W-F1800W), (F770W-F1000W, F1500W-F2550W) planes. We base the discussion on the results commented in the previous section.

As shown in the top, left panel of Fig. 4.7, in the (F770W-F2550W, K_S -F770W) plane, low-mass stars (magenta triangles, Section 4.2), and massive AGBs (green squares, Section 4.3), follow similar reddening patterns, the latter extending to redder colours, because they reach higher optical depths. The two locii overlap in this case, because the main factor affecting the position of the stars is the optical depth itself; this allows us to draw a unique reddening line. The trend is approximately horizontal up to $\tau_{10} \sim 0.1$, F770W-F2550W ~ 2 ; this behaviour is consistent with the arguments presented in Section 4.2, related to the modification of the shape of the SED, when the main silicate feature appears. For higher τ_{10} , as shown in the bottom panel of Fig. 2.4, the SED is shifted to the mid-IR, which diminishes the flux in the near-IR, thus triggering a significant reddening of the K_S -F770W colours: the sequences turn upwards in the diagram.

The stars with iron dust, both AGB and post-AGB, and those with dual-dust chemistry (see Sections 4.4 and 4.5 and Chapter 3), are located in a diagonal sequence above the two afore mentioned reddening sequences. This is once more due to the particular morphology of their SED, which does not exhibit a clear minimum in the $8 \mu\text{m}$ region. The link between the position of the individual sources and the degree of obscuration of the circumstellar envelope is clear also in the (K_S -F770W, F1500W-F1800W) plane, shown in the top, right panel of Fig. 4.7. Low-mass and massive AGB stars describe obscuration sequences that extend to the red, with K_S -F770W and F1500W-F1800W spanning a range of ~ 6 mag and ~ 1 mag, respectively.

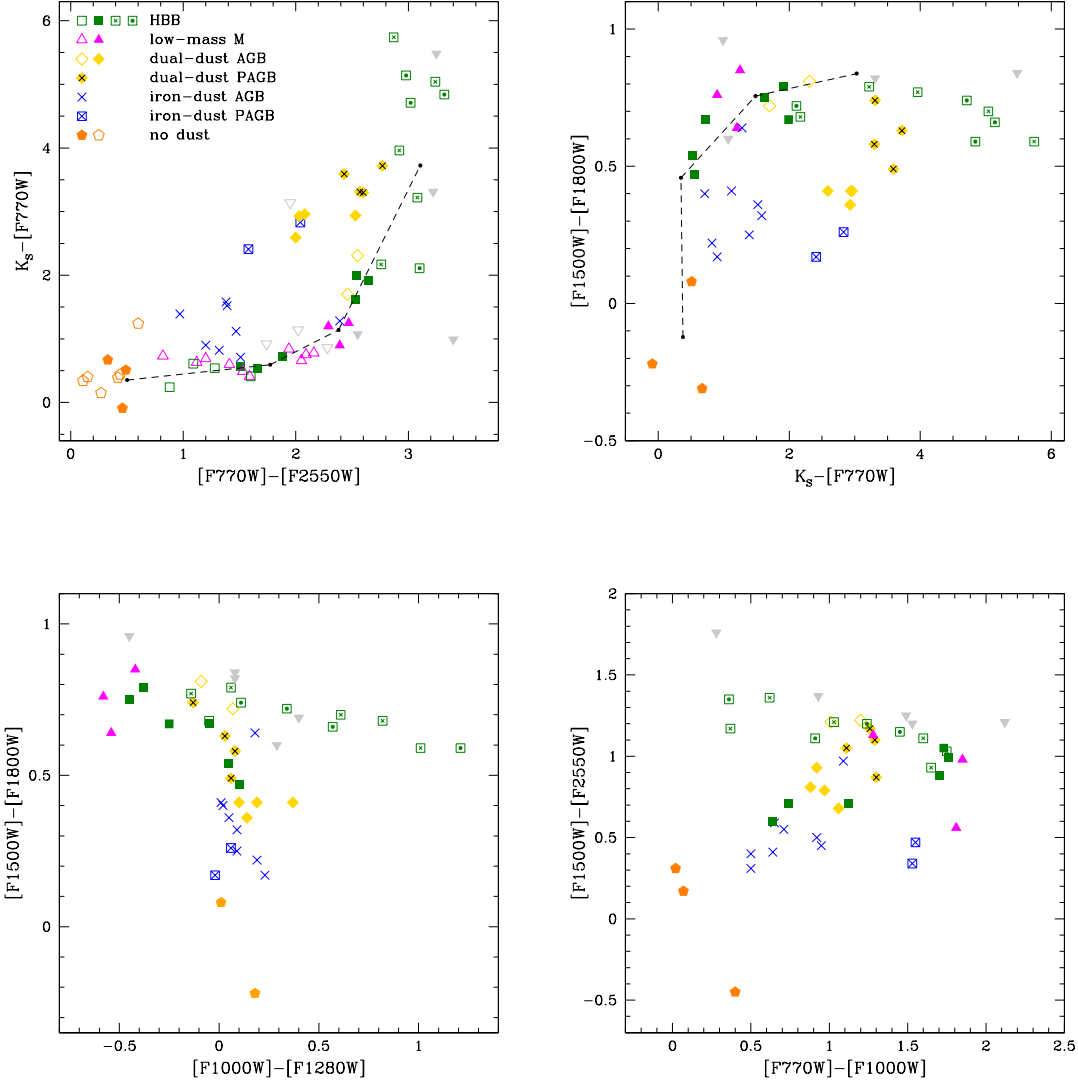


Figure 4.7 The evolved, M-type stars in the sample considered in this study in the various colour-colour planes, obtained by using MIRI filters.

Among the colours considered so far, $F1500W-F1800W$ is the least sensitive to τ_{10} , because, as shown in Fig. 2.4, the presence of the secondary silicate feature at $18 \mu\text{m}$ is accompanied by a general increase in the stellar flux in all the spectral region between 10 and $25.5 \mu\text{m}$: both the $F1500W$ and $F1800W$ fluxes increase when a prominent secondary silicate feature is present in the spectrum. This is the reason why $F1500W-F1800W$ never exceeds the maximum value, $F1500W-F1800W \sim 0.8$, reached for $K_S-F770W \sim 2$.

The peculiar shape of the SED in the $8 \mu\text{m}$ region makes iron dust and dual dust chemistry stars populate regions of the plane below the main obscuration pattern. In particular, AGB stars surrounded by iron dust are clearly separated from post-AGB stars and low-luminosity objects, with $K_S\text{-F770W} \sim 1$, $\text{F1500W-F1800W} \sim 0.3$. This is due to the steep rise of the SED at $\lambda \leq 8 \mu\text{m}$ of the iron dust AGB sources respect to their post-AGB counterparts and stars with dual-dust chemistry. An additional colour where iron post-AGB stars are clearly isolated is the F1280W-F2550W . This is due to the absence of the silicates secondary feature. This colour in combination with $K_S\text{-F770W}$, separates this group of sources from the obscuration sequence traced by the rest of the sample.

The bottom panels of Fig. 4.7 show the distribution of the stars in the sample considered here in two additional planes proposed by Jones et al. (2017) to discriminate AGB stars from other sources, e.g. young stellar objects and planetary nebulae. (F1000W-F1280W , F1500W-F1800W) is also useful to separate O-rich from C-rich AGB stars, while (F770W-F1000W , F1500W-F2550W) is efficient in distinguishing between galactic and non-galactic sources. Nevertheless, unlike the upper panels diagrams, the trend of the colours of the O-rich stars with the optical depth in this plane is not straightforward, since it presents turning points and deviations, which prevent a straight understanding of the results. This is because the F1000W and F1280W flux depend on the particular way with which the shape of the main silicate feature changes with τ_{10} , thus making these filters to be of little help in the interpretation of the observations.

In the (F1000W-F1280W , F1500W-F1800W) plane the position of the individual stars does not allow a clear identification of the reddening properties, but the peculiar groups of stars discussed in Chapter 3 can be distinguished more clearly here with respect to the other colour-colour diagrams: indeed their F1500W-F1800W colours are bluer for a given F1000W-F1280W , because the depression of the flux at $15 \mu\text{m}$ is lower in comparison to the stars whose main dust component is made up of silicates (see Chapter 3).

In the (F770W-F1000W , F1500W-F2550W) plane the different classes of stars presented in the previous sections partly overlap and the separation among the various groups is not straightforward.

4.7 Studying oxygen-rich AGB stars with *JWST*

A summary of the interpretation of the sources analysed in this chapter is reported in Table 4.1. For each source we report the luminosity, coordinates, periods (when available) obtained by the OGLE collaboration (Soszyński et al., 2009), τ_{10} , dust mineralogy and evolutionary characterization. In the case of stars with dual-dust chemistry, we also report the optical

depth and the percentages of solid carbon and SiC of the inner layer. The details of the SED fitting of the IRS spectra are shown in the Appendix.

A clear results from this study is that the use of the F1000W and F1800W filters, whose transmission curves largely overlap with the two silicate features, are extremely useful to deduce the presence of silicates and to confirm that the stars are oxygen-rich, but their use in a global characterization of the individual sources is not straightforward. The same holds for the F1500W and F2100W filters, which are also partly affected by the presence of the silicates features in the spectrum. The difficulties encountered when using observational planes built with the combination of these filters are connected with the non-linear behaviour of the shape of the silicate features with the optical depth.

On general grounds, we find that the best planes to study M-type AGB stars are the colour-magnitude (F770W-F2550W, F770W) and (K_S -F770W, F770W) planes, and the colour-colour (K_S -F770W, F770W-F2550W) diagram.

These planes are the only ones in which the excursion of the reddening sequences follows a monotonic trend with the optical depth, thus providing a direct information on the dust reprocessing of the radiation from the central star. The peculiar stars discussed in Chapter 3 and in the present chapter can be also easily distinguished, based on their position in these diagrams. Furthermore, the two colour-magnitude planes involving the K_S , F770W and F2550W filters allow disentangling low-mass, oxygen-rich AGBs from their higher mass counterparts, experiencing HBB.

Table 4.1 The interpretation of the sample of M-type stars analysed in the present work. The different columns report the SSID of the star (1), OGLE period (2), estimated luminosity (3), dust mineralogy (4), optical depth τ_{10} (5), evolutionary characterization (6). In the case of stars with dual-dust chemistry, we also report the optical depth and the percentages of solid carbon and SiC of the inner layer.

SSID	Period [d]	L/L_{\odot}	%(Sil,Al ₂ O ₃ ,Fe)	τ_{10}	Type
1	-	7000	(60,40,0)	4.5×10^{-3}	Low-mass M
6	-	18000	(15,0,85)	2×10^{-3}	Iron-dust PAGB
8	883.7	2100	(60,10,30)	3.2×10^{-2}	Dual-Dust AGB
		C 95, SiC 5	1.5×10^{-2}		
13	916.3	5500	-	-	No dust
22	-	4700	(60,5,35)	1.5×10^{-2}	Dual-dust AGB
			C 95, SiC 5	8×10^{-3}	
38	577.2	34000	(65,5,30)	6.7×10^{-2}	HBB

54	-	4300	(55,30,15) C 100	1.8×10^{-2} 6×10^{-3}	Dual-dust AGB
58	-	10000	-	-	No dust
61	-	24000	(65,5,30)	1.2×10^{-2}	HBB
63	-	7000	(85,15,0)	3×10^{-2}	Low-mass M
67	741.8	6500	(80,20,0)	1.2×10^{-2}	Low-mass M
68	-	13000	-	-	No dust
72	794.9	5000	(85,15,0)	1.5×10^{-2}	Low-mass M
77	767.7	6500	(75,20,5)	1×10^{-2}	Low-mass M
82	-	34000	(60,10,30)	8×10^{-3}	HBB
89	685.9	6200	(60,40,0)	6×10^{-3}	Low-mass M
91	779	7000	(100,0,0)	2×10^{-2}	Low-mass M
93	-	7300	(100,0,0)	0.1	Low-mass M
96	-	5600	(90,10,0)	0.1	Low-mass M
121	-	55000	(90,0,10)	2.5	HBB
124	213.5	10000	-	-	No dust
130	-	6500	(65,0,35) C 75; SiC 25	6.2×10^{-2} 2.2×10^{-2}	Dual-dust AGB
142	-	20000	(30,70,0)	2×10^{-3}	HBB
143	147.9	13000	(60,40,0)	6×10^{-3}	HBB
148	953.3	7000	(80,20,0)	1.7×10^{-2}	Low-mass M
152	747.6	5400	(90,10,0)	2.8×10^{-2}	Low-mass M
159	-	7000	(100,0,0)	3.8×10^{-2}	Low-mass M
165	-	47000	(65,5,30)	6.5×10^{-2}	HBB
166	392.6	2300	(65,5,30) C 95; SiC 5	2.6×10^{-2} 1×10^{-2}	Dual-dust AGB
173	-	27000	-	-	No dust
176	278.4	13000	(80,20,0)	9×10^{-3}	HBB
178	-	19000	-	-	No dust
180	238.7	34000	(50,15,35)	6×10^{-3}	HBB
197	-	10000	(80,20,0)	7×10^{-3}	HBB
4007	1179	15000	(75,5,20)	1.3	HBB
4038	1080	43000	(80,5,15)	0.7	HBB
4054	-	2100	(60,5,35) C 95; SiC 5	1.4×10^{-2} 8×10^{-3}	Dual-dust PAGB
4075	-	40000	(100,0,0)	3	HBB

4081	693.9	30000	(60,10,30)	7×10^{-2}	HBB
4098	561.8	60000	(40,10,50)	2×10^{-2}	Iron-dust AGB
4149	-	16000	(90,0,10)	1.2	HBB
4159	-	2400	(55,10,35)	1×10^{-2}	Dual-dust AGB
			C 90; SiC 10	7×10^{-3}	
4205	597.8	42000	(20,10,70)	3×10^{-3}	Iron-dust AGB
4245	-	10000	(65,10,25)	1.6×10^{-2}	Dual-dust PAGB
			C 95; SiC 5	6×10^{-3}	
4254	-	18000	(80,5;15)	1	HBB
4267	-	24000	(15,5,80)	2×10^{-3}	Iron-dust PAGB
4326	-	55000	(20,5,75)	4×10^{-3}	Iron-dust AGB
4368	-	5000	(90,10,0)	4.5×10^{-2}	Low-mass M
4449	512.2	46000	(20,10,70)	2×10^{-3}	Iron-dust AGB
4462	212.1	6500	-	-	No dust
4467	-	8500	-	-	No dust
4468	604.9	45000	(25,5,70)	9×10^{-3}	Iron-dust AGB
4480	1137	41000	(85,5,10)	0.7	HBB
4483	-	20000	-	-	No dust
4486	650.1	50000	(25,5,70)	9×10^{-3}	Iron-dust AGB
4530	-	25000	(85,0,15)	2.2	HBB
4535	-	55000	(90,0,10)	3	HBB
4547	-	16000	(60,15,25)	3.8×10^{-2}	Dual-dust PAGB
			C 95, SiC 5	7×10^{-3}	
4595	-	5500	(70,0,30)	1×10^{-2}	Dual-dust PAGB
			C 85; SiC 15	1×10^{-2}	
4670	1352	60000	(85,5,10)	2.2	HBB
4777	-	46000	(20,5,75)	5×10^{-3}	Iron-dust AGB
4784	-	56000	(10,5,85)	3×10^{-3}	Iron-dust AGB
4791	1133	40000	(95,5,0)	1.2	HBB

5

Understanding carbon stars in the LMC with a look at the *JWST*

In order to complete the characterization of the AGB stars in the LMC we extend the analysis done in Chapters 3 and 4 to the C-rich stars sample. This step is important in the general context of dust production by stars in galaxies, because the overall dust production rate from AGB sources is dominated by carbonaceous species in the Magellanic Clouds (Nanni et al., 2019, 2018; Schneider et al., 2014), particularly in metal poor environments (Boyer et al., 2013; Cioni & Habing, 2003). Furthermore, while in solar-metallicity environments the dust return to the ISM is dominated by O-rich stars (Javadi et al., 2013), recent studies have shown that in lower-metallicity environments the dust production rate (DPR) is dominated by carbon dust (e.g. Boyer et al., 2012; Dell’Agli et al., 2016, 2019a; Schneider et al., 2014), with a relevant contribution from the most obscured stars.

Similarly to M-stars, to understand the distribution of carbon stars and the evolutionary sequences in the observational planes (colour-colour and colour-magnitude diagrams obtained with the *JWST* filters) we need to characterize the individual sources. To this aim, we follow the same procedure used in the previous analysis, discussed in Section 2.4.

5.1 An overall view of carbon stars in the LMC

The stars analysed in this chapter are reported in Table 5.1.

A few examples of this analysis are shown in Fig. 5.1, reporting the interpretation of the SED of stars of various L and τ_{10} . The main deviations of the synthetic SED from the observed spectrum are in correspondence of the C_2H_2 molecular bands in the regions $6.6 - 8.5 \mu\text{m}$ (centred at $\sim 7.5 \mu\text{m}$) and $13.5 - 13.9 \mu\text{m}$ (Matsuura et al., 2006) and the $CO+C_3$ band in the region $5.0 - 6.2 \mu\text{m}$ (Jørgensen et al., 2000). The properties of these features have been widely analysed in the past (e.g. Sloan et al., 2016) and references therein) but, unfortunately, they are poorly or not reproduced by model atmospheres available

in the literature, owing to the scarce knowledge of the opacities of such molecules. The $\sim 7.5 \mu\text{m}$ feature affects the flux in the $6 - 9 \mu\text{m}$ spectral region, the effect becoming smaller and smaller as τ_{10} increases, eventually vanishing for $\tau_{10} > 1$. On the other hand the $\text{C}_2\text{H}_2 \sim 13.7 \mu\text{m}$ feature, which affects the emission in the $12 - 16 \mu\text{m}$ domain, is present in the spectra of carbon stars characterized by different τ_{10} , even in those with very large infrared emission. The $\text{CO}+\text{C}_3$ band is the most tricky to handle in the present analysis, because it is spread across a spectral region only partially covered by IRS, which poses some problems in the extrapolation of the flux in the optical and near-IR domains. For the stars where this ambiguity is most relevant, we will consider the combination of the IRS data with results from photometry, following an approach similar to Groenewegen & Sloan (2018). Fortunately the analysis of the most obscured stars is not affected by the $\text{CO}+\text{C}_3$ band, as the SED of these sources peaks at longer wavelengths.

The result of the interpretation of the observations of the carbon stars analysed here is shown in Fig. 5.2, where we report the distribution of the individual sources on the τ_{10} versus luminosity plane. Overimposed to the points indicating the stars are the tracks, corresponding to the evolution of the AGB stars discussed in Chapter 1. Green squares in Fig. 5.2 indicate stars with luminosities below $7500L_\odot$: these are the oldest objects in the sample, descending from stars of initial mass below $2M_\odot$, formed in epochs earlier than one Gyr ago. Red triangles indicate objects younger than 1 Gyr, descending from stars of initial mass above $2M_\odot$. In particular, those with luminosities above 10^4L_\odot are interpreted as the progeny of stars of initial mass $2.5 - 3.3M_\odot$, formed during the peak in the SFH of the LMC, between 300 and 600 Myr ago (Harris & Zaritsky, 2009). Magenta crosses refer to bright stars, with luminosities above $20000L_\odot$.

The distribution of the stars in Fig. 5.2 is determined by the mass distribution of the progenitors (luminosity) and the amount of carbon accumulated in the surface regions, which affects the dust formation in the outflow, thus the optical depth (see discussion in Chapter 1). The stars on the right side of the diagram are those producing dust at higher rates. We find that the gas-to-dust ratio, Ψ , decreases when moving to higher τ_{10} , ranging from $\Psi \sim 700$, for the stars with little dust, to $\Psi \sim 100$, for the most obscured sources. These results are fully consistent with those obtained by Nanni et al. (2019), who correctly warned against the choice of assuming a constant Ψ when fitting the observed SED. The gas and dust mass loss rates also increase with τ_{10} , until reaching $\dot{M} \sim 1.5 \times 10^{-4}M_\odot/\text{yr}$ and $\text{DPR} \sim 10^{-6}M_\odot/\text{yr}$. In the $\tau_{10} < 1$ domain the \dot{M} and DPR values derived here are consistent with Nanni et al. (2019), whereas for the stars with the largest degree of obscuration the present results are similar to Gullieuszik et al. (2012).

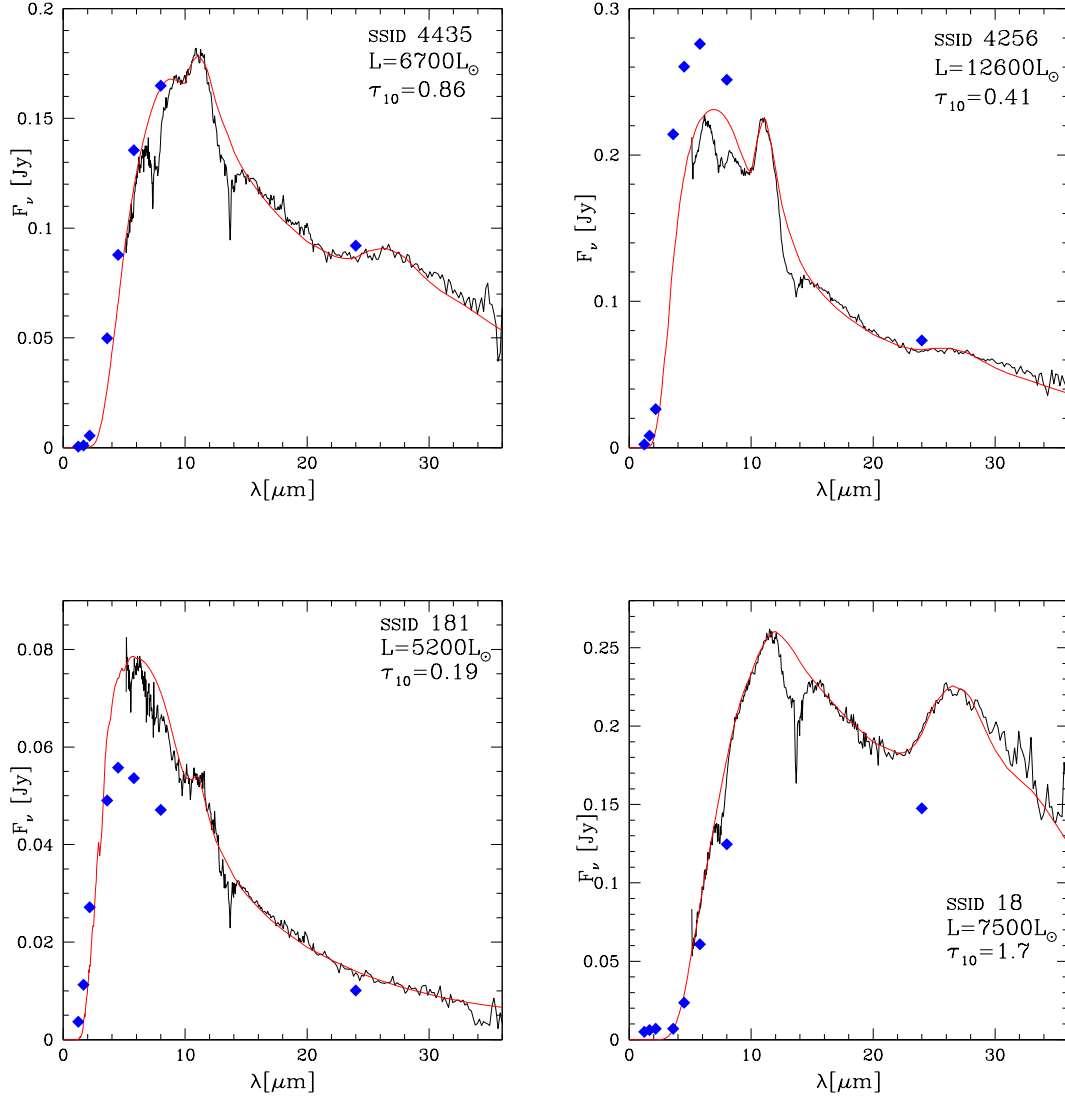


Figure 5.1 Comparison between the IRS (black lines) and the synthetic (red) spectra of a few sources in the LMC sample of carbon stars, with various luminosities and degrees of obscuration. The values of luminosities and τ_{10} reported in each panel are those allowing the best fit, corresponding to the red lines.

The tracks reported in Fig. 5.2 nicely reproduce the distribution of the sources on the plane, with the exception of a few groups of stars, for which the derivation of the main physical and evolutionary properties is not straightforward. In particular, we refer to: a) the stars with luminosities below $5000L_\odot$, indicated with orange asterisks, which are too faint when compared to the evolutionary tracks; b) the stars on the right part of the figure, at $\tau_{10} > 3$, indicated with blue diamonds, whose optical depth is in excess of the theoretical

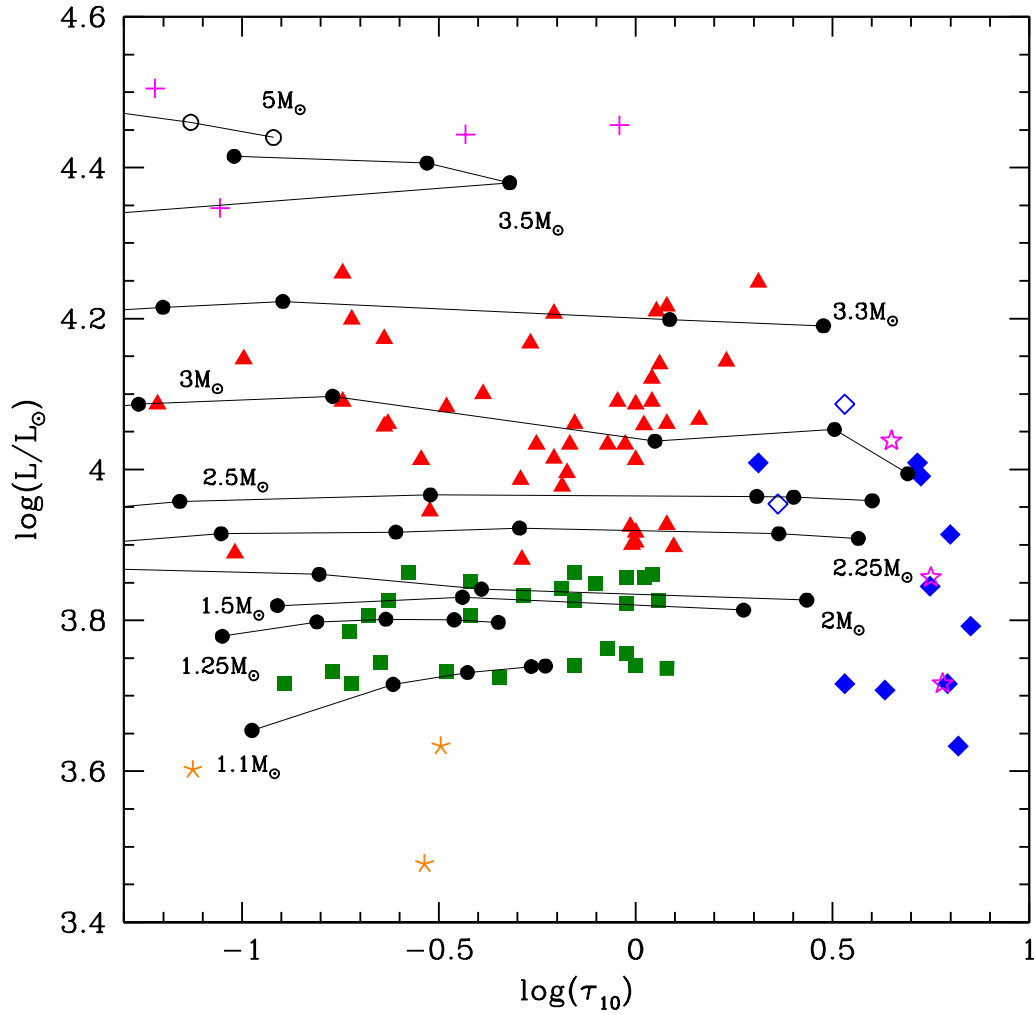


Figure 5.2 Luminosities and optical depths derived for the stars in the sample analysed in the present work. Green squares and red triangles indicate the progeny of $M < 2M_{\odot}$ stars and the higher mass counterpart, respectively; orange asterisks refer to stars with luminosities below $5000L_{\odot}$; magenta crosses indicate stars brighter than $20000L_{\odot}$; blue diamonds indicate extremely obscured objects, taken from Gruendl et al. (2008), plus the source SSID 9; the stars indicated with open diamonds are SSID 125 and SSID 190. The black lines and points in the figure refer to the evolution of models discussed in Chapter 1; the initial masses are indicated next to the corresponding track. Magenta stars indicate the results obtained by artificially increasing the mass loss rate of the stars of initial mass $1.1M_{\odot}$, $2.5M_{\odot}$, $3M_{\odot}$, after reaching the C-star stage.

expectations (see the largest τ_{10} values expected for stars of different mass and luminosity, reported in Table 1.1).

In the following, before the general discussion on the wind structure and the distribution and the distribution of carbon stars in the observational planes, we discuss separately the stars outlined in point (a) and (b) and the bright stars, indicated with magenta crosses in Fig. 5.2.

5.2 Stars in the thermal pulse phase

The sources SSID 3, SSID 66, SSID 103 and SSID 141 are characterized by luminosities below $5000L_{\odot}$. The IRS spectrum of the latter star, with our best-fit interpretation, is shown in the left panel of Fig. 5.3. These energy fluxes are at odds with the results shown in Fig. 5.2, which reports the luminosities of the stars during the sequence of interpulse phases, when the CNO burning activity is fully recovered, after the temporary extinction owing to the ignition of the thermal pulse. On the other hand the re-ignition of the CNO shell after the TP is extinguished is not immediate, thus the luminosity undergoes a series of periodic variations, with temporary dips in conjunction with the ignition of TPs. The right panel of Fig. 5.3 shows the variation with time of the luminosity of stars of initial mass $1.5; 2; 2.5M_{\odot}$, during the C-star phase. We see that at the ignition of each TP the luminosity drops below $3000L_{\odot}$, then increases as CNO burning is gradually re-activated. The rise of the luminosity following each TP is sufficiently slow that the possibility of observing stars in such low-luminosity phases is statistically not negligible. This holds particularly for the lowest mass stars considered. Therefore, we propose that the low-luminosity stars identified in the IRS sample are carbon stars that have recently experienced a TP, and are evolving through a phase when the H-burning shell has not fully recovered its efficiency. This interpretation is consistent with the small optical depths which we derived for these stars ($\tau_{10} \sim 0.1 - 0.3$), because during these evolutionary phases the stars assume a compact configuration, which prevents the formation of large quantities of dust. While a robust estimate of the mass of the progenitor is not possible in this case, arguments related the mass distribution of the stars, based on realistic mass functions, lead us to consider more likely that these sources descend from $1.2 - 1.5M_{\odot}$ stars, formed $2 - 4$ Gyr ago.

5.3 A signature of hot bottom burning?

The sources indicated with magenta crosses in Fig. 5.2 (SSID 4109, 4451, 4540, 4776) are characterized by luminosities above $20000L_{\odot}$, significantly higher than the other stars in the sample and above the upper limit expected for carbon stars ($\sim 17000L_{\odot}$), given in Table

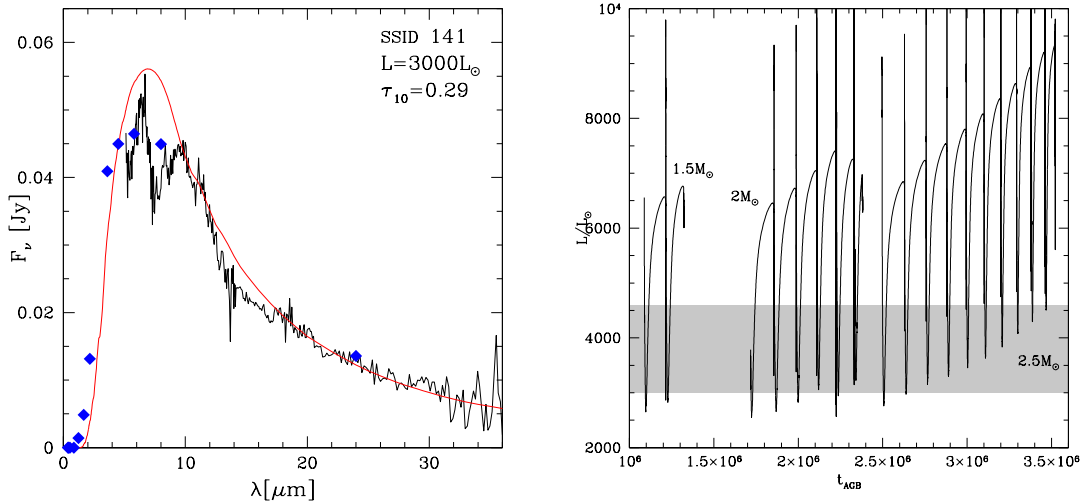


Figure 5.3 Left: IRS SED of the source SSID 141, compared with our interpretation, based on synthetic modelling. Right: AGB evolution with time of the luminosity of 1.5, 2, 2.5 M_{\odot} stars; the O-rich phase was omitted for readability. The sequence of the 2.5 M_{\odot} was artificially shifted by 1 Myr for readability. The grey shaded region indicates the luminosity range of the low-luminosity stars SSID 3, SSID 66, SSID 103 and SSID 141.

1.1 and shown in Fig. 1.5. These luminosities indicate that the cores of these stars are more massive than their counterparts discussed in Section 1.2.2, which translates into higher mass progenitors. The mass threshold given in Section 1.2.2 was based on the fact that higher mass stars experience HBB, which destroys the surface carbon, thus preventing the stars from becoming carbon stars. Indeed, stars within a narrow mass range, clustering around $3.5M_{\odot}$, experience a series of TDU events before HBB is activated. These stars reach the C-star stage and evolve as carbon stars for a few TPs, until the beginning of HBB.

An example of this behaviour is shown in the right panel of Fig. 5.4, reporting the evolution of a $3.5M_{\odot}$ star, in terms of the surface C/O and of the luminosity. The effects of TDU can be seen in the rise of C/O after each TP, whereas HBB causes a drop in C/O after each TDU event. In this specific case HBB starts after 12 TPs and the star evolves as C-star during 4 inter-pulse phases, before the surface C/O drops below unity. The ignition of HBB is accompanied by the fast rise in the luminosity of the star, which increases from $\sim 17000L_{\odot}$ to above $20000L_{\odot}$. During the C-star phase we find $L \sim 25000L_{\odot}$, in agreement with the luminosities derived for SSID 4109 and 4451 (see the comparison of the IRS spectra with the synthetic models in the left and middle panel of Fig. 5.4).

We propose that the latter two sources descend from $3.5 - 4M_{\odot}$ progenitors, formed ~ 250 Myr ago, that have reached the C-star phase and that are currently experiencing HBB

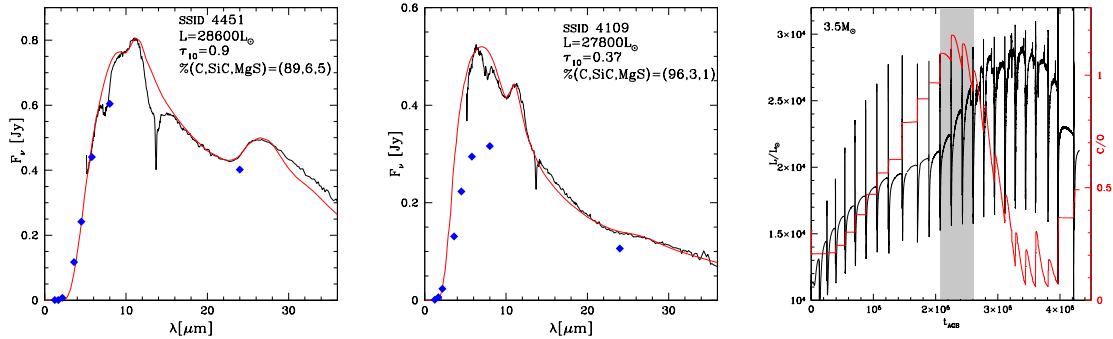


Figure 5.4 IRS and best-fitting SED for the sources SSID 4451 (left panel) and SSID 4109 (middle). Right: evolution with time (counted since the beginning of the TP-AGB phase) of luminosity (black) and surface C/O (red track, scale on the right) of a $3.5M_\odot$ star. The grey-shaded area indicates the phase during which the star is carbon-rich.

at the base of the envelope. According to this interpretation, they are evolving through the C-star phase, before becoming again oxygen-rich. If this understanding is correct, these stars are characterized by a surface C/O slightly above unity and they are enriched in lithium, because the time elapsed since the start of HBB is not sufficient to destroy the surface ^3He , which allows the Cameron & Fowler (1971) mechanism to operate. These sources would be examples of the lithium-rich, carbon stars, which Ventura et al. (1999) proposed as independent distance indicators, based on the robust estimate of the luminosities at which we expect this mechanism to occur. We rule out the possibility that the progenitors are higher mass stars formed more recently, because stars of initial mass above $4M_\odot$ experience HBB since the early AGB phases, thus the formation of C-stars is inhibited.

The scenario invoked to explain the IRS spectrum of SSID 4109 and 4451 could potentially work also for SSID 4776. However, the SED of the latter star is peculiar, since we find no evidence of the $11.3 \mu\text{m}$ SiC feature and of the $30 \mu\text{m}$ bump: this suggests that the dust is composed exclusively of solid carbon.

The situation regarding SSID 4540, whose SED is shown in the left panel of Fig. 5.5, is even more tricky, because the estimated luminosity, $32000L_\odot$, is higher than the largest luminosity attained by the $3.5M_\odot$ model, shown in the right panel of Fig. 5.4. The large luminosity and the SiC- and MgS-free dust mineralogy lead us to consider the alternative possibility that the progenitors of SSID 4540 and SSID 4776 are metal-poor, massive AGB stars. These stars experience for most of the AGB lifetime vigorous HBB at the base of the external mantle, which causes the depletion of the surface carbon and, unlike their higher metallicity counterparts, a strong reduction of the surface oxygen. During the final AGB phases, when HBB is turned off by the loss of the external envelope, the very low amount of

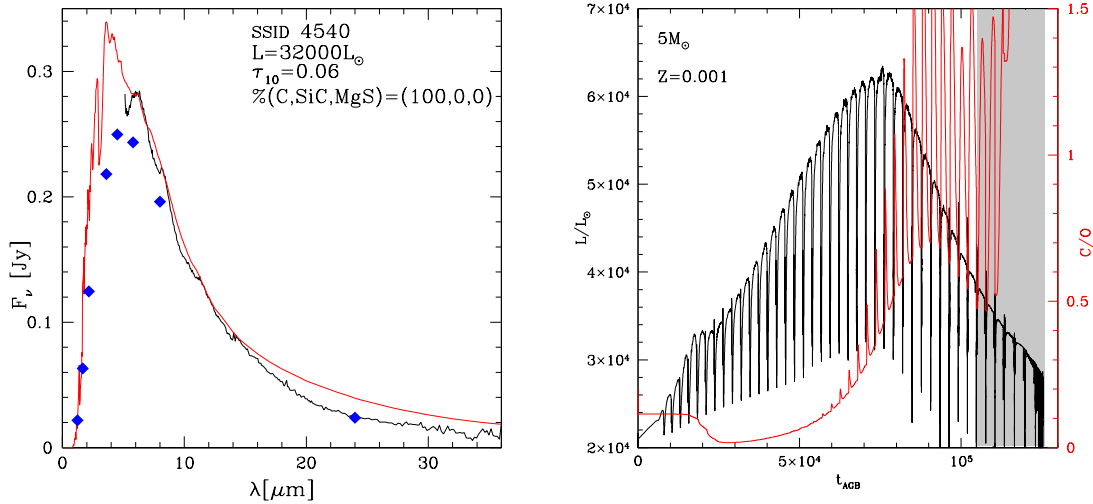


Figure 5.5 Left: IRS SED of the source SSID 4540, compared with our interpretation, based on synthetic modelling. Right: AGB evolution with time of the luminosity (black line, scale on the left) and of the surface C/O ratio (red line, scale on the right) of a $5M_{\odot}$ model with metallicity $Z = 0.001$. The grey-shaded area indicates the evolutionary phase during which the star evolves as a carbon star.

oxygen residual in the external regions allows a few TDU episodes to turn the stars into a C-star. This is shown in the right panel of Fig. 5.5, reporting the evolution of the luminosity and of the surface C/O of a $5M_{\odot}$, $Z = 0.001$ model star. The luminosities at which this transition occurs are in the $25000 - 35000L_{\odot}$ range, consistent with the estimate done for SSID 4540 and SSID 4776.

If this interpretation is correct, these stars share the same origin with the O-rich objects in the LMC which we discussed in Chapter 3, identified as metal-poor stars, in which the significant destruction of the surface oxygen, caused by HBB, makes the dust in their surroundings to be dominated by solid iron grains.

According to this hypothesis SSID 4540 and SSID 4776 are currently evolving through the stages immediately following those of the stars considered in Chapter 3, after becoming a C-star. They would be the youngest object in the carbon stars sample considered in this chapter, with an age of ~ 100 Myr. An important difference with respect to the origin invoked for SSID 4109 and 4451 is the surface chemical composition, which should exhibit an extremely poor oxygen content and no evidence of lithium.

These stars are not expected to produce great quantities of dust, because the carbon excess with respect to oxygen is low, given the effects of HBB experienced during the earlier evolution. This is consistent with the small optical depths, $\tau_{10} = 0.06 - 0.08$, deduced from

the analysis of the SED, and with the shape of the IRS spectrum (see left panel of Fig. 5.5), which shows no significant IR emission.

5.4 Extreme carbon stars

The existence of LMC stars with extremely red mid-IR colours was first discussed by Gruendl et al. (2008), who used IRAC and MIPS photometry and IRS follow-up to identify 7 objects as extreme carbon stars. The authors introduced the terminology ERO ("extremely red object") to refer to these peculiar stars. Gruendl et al. (2008) underlined the peculiarities of the EROs, especially the derived mass loss rates, which span the $(5 \times 10^{-5} - 2 \times 10^{-4}) M_{\odot}/\text{yr}$ range, significantly higher than those deduced for carbon stars, when radiative transfer modelling is used to reproduce their photometric properties (van Loon et al., 1999).

In Fig. 5.2 the EROs, on the right side of the $\tau_{10} - L$ plane, are indicated with blue diamonds. We use the same symbol to identify SSID 9, which we also consider extreme, as it lies on the same region of the diagram populated by the Gruendl et al. (2008) sources.

Fig. 5.6 shows the IRS spectra of 4 out of these stars, with the parameters required to reproduce the details of the observed SED. In all cases, with the only exception of SSID 4299, a clear SiC absorption feature is visible, indicating an extremely thick dusty region. Note that the interpretation of the spectra of the EROs is not affected by the presence of the molecular bands discussed in the first part of this chapter. The sources SSID 125 and SSID 190, belonging to the Gruendl et al. (2008) sample, are indicated in Fig. 5.2 with open, blue diamonds; these stars are extremely red and show up a peculiar SED, peaking at wavelengths $\lambda > 20 \mu\text{m}$. An example is shown in Fig. 5.7.

The possible nature of the EROs was discussed by Sloan et al. (2016) and Groenewegen & Sloan (2018), who stressed the difficulty in fitting the data of these stars, particularly in the context of modelling dust formation in radial outflows, departing from the surface of single carbon stars. An interesting overview of the critical issues to face when modelling stars with a very large infrared excess is found in Nanni et al. (2019), who explored the role of the mass loss rate, carbon excess, optical constants of solid carbon dust.

We confirm here that the interpretation of these objects, based on the standard modelling so far used to describe the other stars analysed, is extremely hard. The results presented in Fig. 5.2 and 5.6 outline that the optical depths required to reproduce the observations, which span the $3 < \tau_{10} < 7$ range, are significantly higher than the majority of the largest τ_{10} expected on the basis of theoretical modelling, reported in Table 1.1. Indeed the synthetic SEDs shown in the 4 panels of Fig. 5.6 and the parameters corresponding to these stars reported in Table 5.1 were obtained by artificially increasing the optical depth of the most

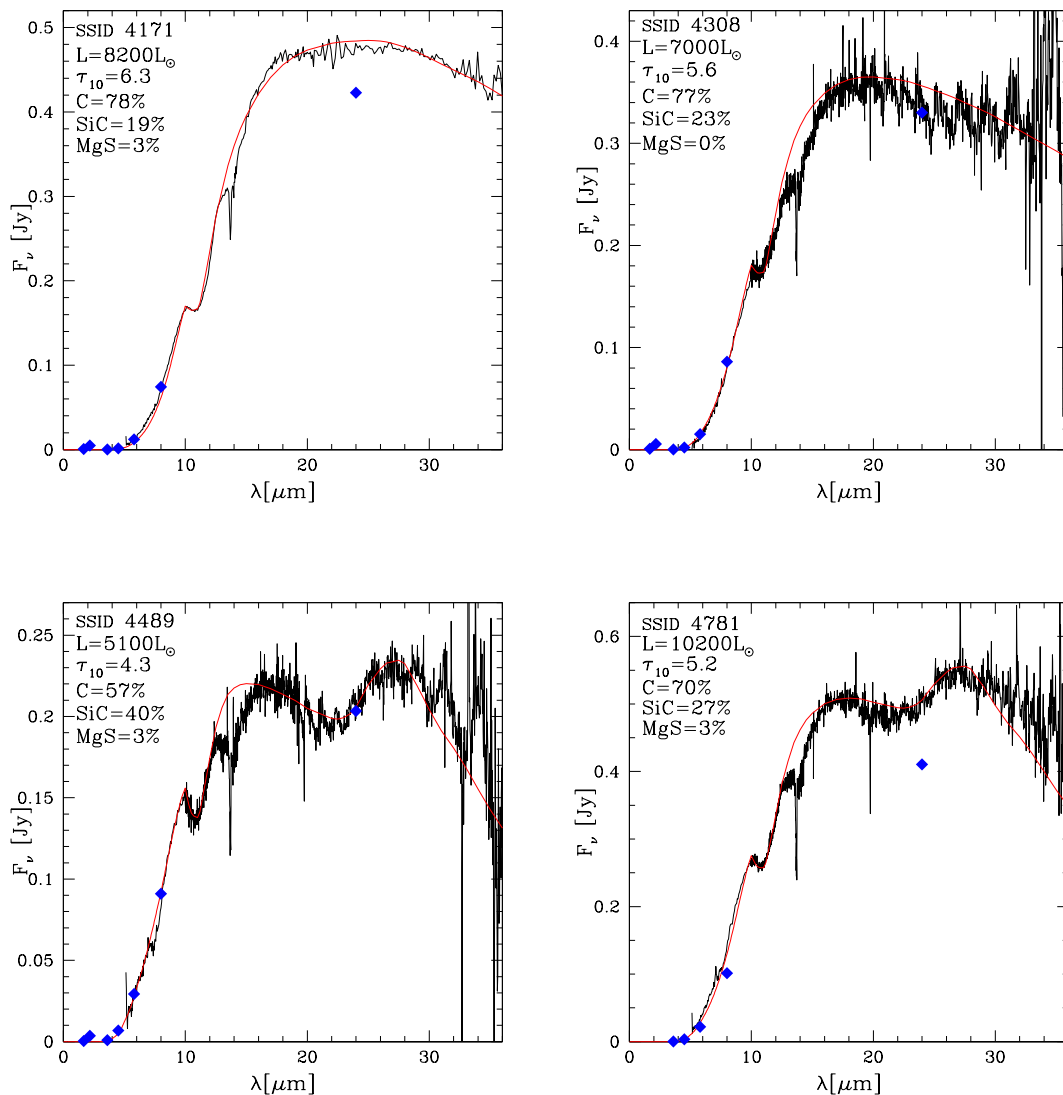


Figure 5.6 SED fitting of 4 out of the extremely red objects studied by Gruendl et al. (2008)

obscured model, taken among the points of the evolutionary sequences used to characterize all the other stars in the sample. The left panel of Fig. 1.17 shows that optical depths $\tau_{10} \sim 5$ are reached during the latest AGB phases of $2 - 3M_{\odot}$ stars.

These largely obscured models might partly explain, as far as the degree of obscuration is concerned, the SSID 4299 and SSID 4781 data (see bottom-right panel of Fig. 5.6), the brightest sources in this group, for which we estimate a luminosity around $10000L_{\odot}$. However, there is no way to account for the observations of the fainter objects, particularly those with estimated luminosities in the $L < 6000L_{\odot}$ range: these energy fluxes indicate

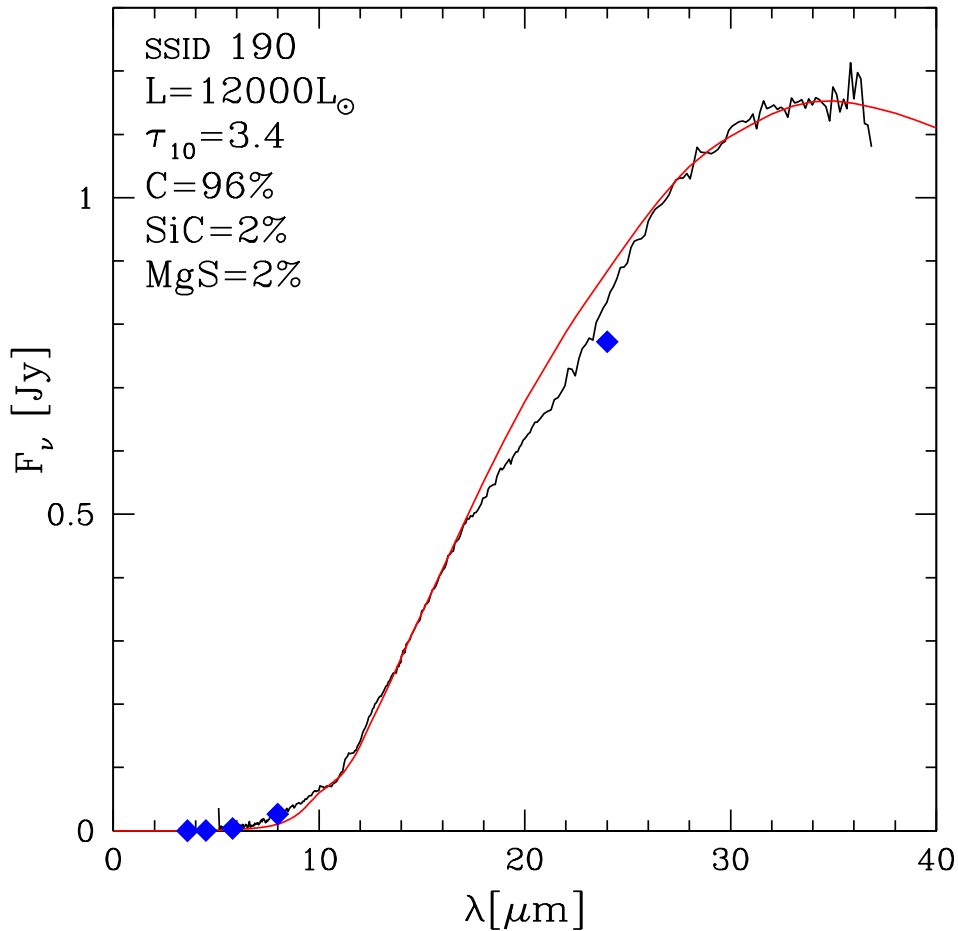


Figure 5.7 The IRS (black) and synthetic (red) spectra of the source SSID 190.

$M \sim 1.1 - 1.5 M_{\odot}$ progenitors, which are not expected to evolve to such extreme τ_{10} , owing to the relatively low carbon excess reached (see Fig. 1.11 in Chapter 1).

Regarding the possible reasons for such a significant difference between the theory and the observations, we cannot rule out that the stationary wind model used in the present investigation to model dust formation might underestimate the amount of dust formed in the wind of AGB stars. As discussed in Section 1.4, the present model neglects the effects of pulsations and the pulsation-induced shocks, which might drive dense gas clouds into external regions of the outflow, where dust condensation would be favoured by the cool temperatures. Furthermore, here we do not account for gas-to-dust drift, which might affect the structure of the wind and cause higher dust yields. Sandin & Mattsson (2020) have

recently performed unique state-of-the-art simulations of C-star wind formation, confirming that drift is significant at low mass loss rates and becomes less and less important as the rate goes up. This means we cannot firmly conclude that the dust yields should be significantly higher unless we redo the stellar evolution modeling including a correction for drift. The effect on the integrated DPR depends on the evolution of the mass loss rate, which in turn depends on how the stellar parameters and carbon excess evolve.

Despite the above uncertainties, we believe that there is no room to obtain τ_{10} values significantly higher than those reported in Table 1.1 and shown in Fig. 1.16. This is definitively impossible in case of $M < 2M_{\odot}$ stars, for the reasons given above. For what attains the stars of mass above $2M_{\odot}$, the large values of τ_{10} reached are mainly caused by the high mass loss rates experienced during the latest AGB phases, which are slightly below $\sim 2 \times 10^{-4}M_{\odot}/\text{yr}$. We consider these rates as upper limits, because their calculation is based on the description by Wachter et al. (2002, 2008), which might overestimate the true mass loss rates (Bladh et al., 2019).

A possible reason for the discrepancy between the τ_{10} obtained by modelling and the optical depth derived from the analysis of the spectra is that the winds are significantly denser than predicted by the theoretical modelling, suggesting that dust is formed at higher rates than predicted by stellar evolution calculations. To test this hypothesis we reconsidered the C-star phase of the models presented in Chapter 1, and artificially increased the mass loss rate to be used in the modelling of dust formation, until obtaining the values of τ_{10} required to fit the IRS spectra. We found consistency with mass loss rates of the order of $\dot{M} \sim 5 \times 10^{-4}M_{\odot}/\text{yr}$.

Based on these findings, we suggest that the EROs are part of binary systems composed of a carbon star and a low-mass companion, with the primary star that filled the Roche lobe, giving origin to a common envelope phase (Dell’Agli et al., 2020).

The large mass-loss rates required to increase the gas density of the outflow, and to produce the amounts of dust compatible with the optical depths deduced from the SED, are connected with the instability of the mass-loss phenomenon when the carbon star fills the Roche lobe.

Fig. 5.8 shows the AGB variation with time of the radius and the surface C/O of stars of different initial mass. We see that in all cases the stars undergo a phase of rapid expansion, soon after they become carbon stars. The fast increase in the stellar radius enhances the probability that the Roche lobe is overfilled, giving the start to a phase of strong mass loss, which we artificially impose starting from the corresponding evolutionary points, indicated with green arrows in Fig. 5.8. As previously discussed, use of $\dot{M} = 5 \times 10^{-4}M_{\odot}/\text{yr}$ leads to

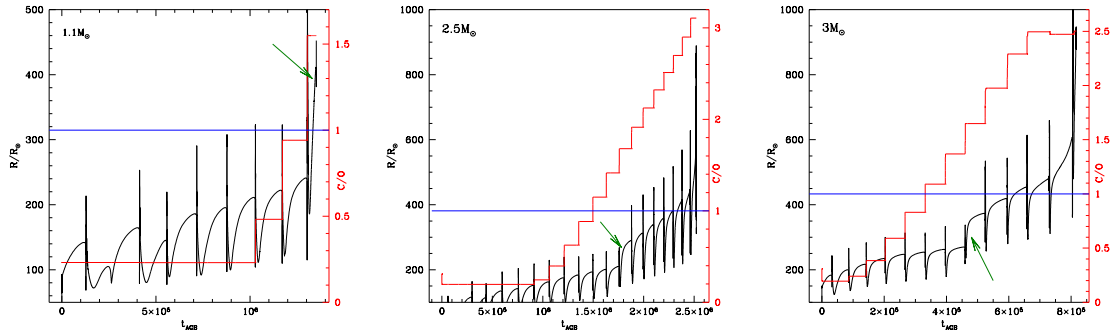


Figure 5.8 Evolution of the radius (black lines, scale on the left) and surface C/O ratio (red, scale on the right) during the AGB phase of stars of initial mass $1.1M_{\odot}$ (left panel), $2.5M_{\odot}$ (middle) and $3M_{\odot}$ (right). The thin, blue horizontal lines indicate the C=O condition, whereas the green arrows indicate the phase of rapid expansion of the star, as a consequence of the surface carbon enrichment.

efficient formation of dust, in quantities sufficiently large to reconcile the optical depth of the envelope with the degree of obscuration indicated by the observations.

As shown in Fig. 5.2, the results obtained, indicated with magenta stars, are in substantial agreement with the τ_{10} and luminosity values of the extreme stars derived from the analysis of the IRS spectra.

For SSID 125 and SSID 190, we propose a slightly different interpretation, based on the cool dust temperature required to fit the IRS spectra, of the order of ~ 350 K, which might indicate that the dust layer is moving away from the system; this is also consistent with the derived optical depths, $\tau_{10} \sim 2 - 3$, among the lowest in the extreme stars sub-sample, which might be due to the decrease in the gas densities, caused by the expansion. These findings suggest that these systems have recently moved away from the AGB and have started the post-AGB phase (Dell’Agli et al., 2020); this understanding would be consistent with the interpretation proposed by Groenewegen & Sloan (2018).

In all cases, the interpretation based on the fact that these stars are evolving through, or have recently crossed a common envelope phase is consistent with the relative small fraction of solid carbon dust, deduced from the analysis of the SED, in most cases below 80%, because the fast loss of the external envelope prevents the accumulation of large quantities of carbon in the surface regions.

5.5 The winds of carbon stars: what we learn from IRS spectra?

We discussed in Chapter 2 that the luminosity and the optical depth of the individual sources can be safely derived by comparing the observed spectrum with the synthetic SED, calculated on the basis of a basic wind model, which assumes that the dust is composed only of carbon and SiC.

On the other hand we know that other dust species form in the winds of carbon stars; furthermore, it is possible that not all the solid carbon forms in the amorphous state, but that a fraction of it might be in other aggregates, such as graphite. As discussed in Section 2.4, the comprehension of the details of the dust formation process demands the knowledge of the mineralogy of the dust formed, which consists into the determination of the percentages of the different species considered, or, equivalently, the individual contributions to the overall cross-section. This ambitious task requires the interpretation of the whole SED, including the details of the features and the slopes of the stellar spectra, in the whole wavelength interval covered by IRS.

We now discuss in detail the dust species other than solid carbon, and how their presence reflects onto the SED.

5.5.1 Silicon carbide

SiC is by far the second most abundant species beyond carbon. The presence of SiC dust was used by several authors (Groenewegen & Sloan, 2018; Groenewegen et al., 2009, 2007; Srinivasan et al., 2009, 2010) to reproduce the spectra of carbon stars, based on the observation of the well distinguished SiC feature, centred at $11.3 \mu\text{m}$. This can be seen in the synthetic SEDs reported in Chapter 2 and in the IRS spectra shown in Fig. 5.1. While we may safely assume that SiC grains are the only solid particles formed in the internal part of the outflow, in the more external regions of the circumstellar envelope the presence of SiC could be associated with the formation of MgS (Zhukovska et al., 2008). Indeed, as it has been discussed in Chapter 1, SiC is suited as a substrate for MgS precipitation, due to the obvious similarities of structure and bonding properties of SiC and MgS.

5.5.2 MgS

We discussed in Chapter 1 that we interpret the wide bump in the $25 - 30 \mu\text{m}$ spectral region, which characterize the spectrum of several carbon stars, with the presence of MgS,

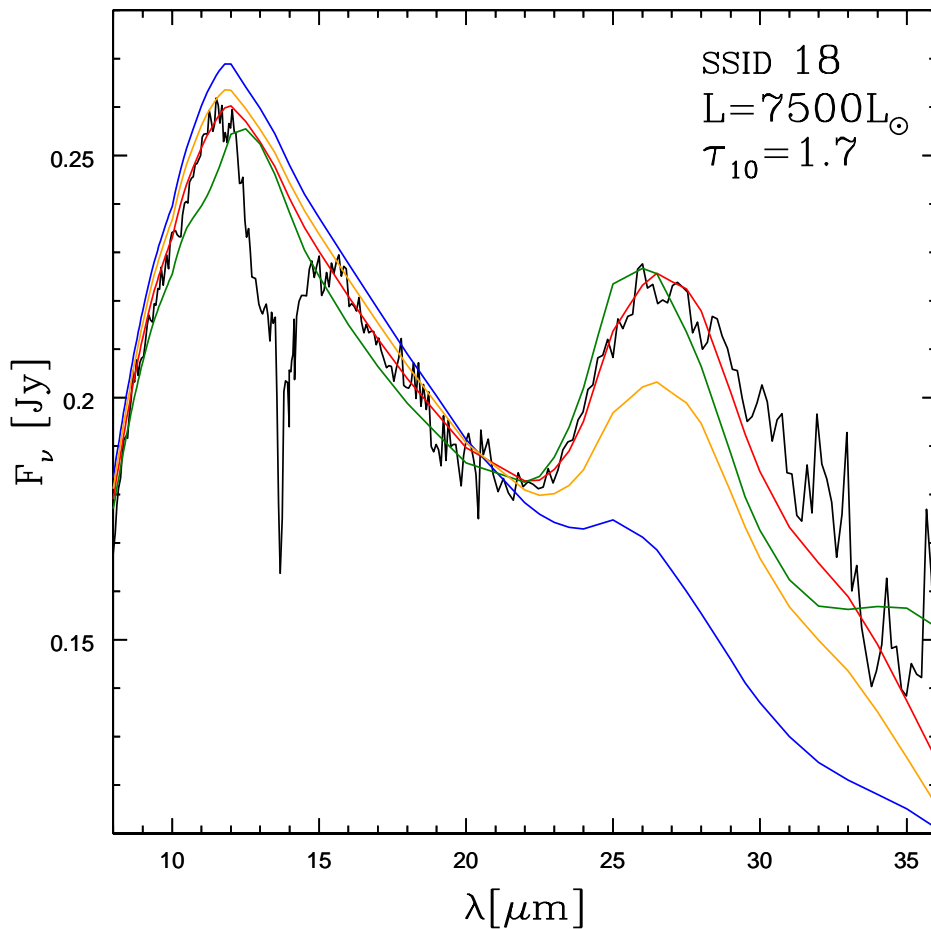


Figure 5.9 IRS spectrum of SSID 18 (black line) compared with synthetic SEDs, corresponding to the same luminosity and τ_{10} , and different percentages of SiC+MgS and of the relative width of the MgS mantle (a_{man}) on top of SiC core. The various lines correspond to the following: red - our best-fit model, with SiC+MgS= 9% and $a_{man} = 0.05 \mu\text{m}$; green - SiC+MgS= 35% and $a_{man} = 0.02 \mu\text{m}$; blue - SiC+MgS= 9% and $a_{man} = 0.02 \mu\text{m}$; orange - SiC+MgS= 6% and $a_{man} = 0.05 \mu\text{m}$.

in the form of mantle covering SiC grains cores. To better understand how the presence of SiC+MgS dust affects the SED of carbon stars, we calculated a series of synthetic SEDs, where the condensation point and the percentage contribution of this compound were allowed to vary within reasonable ranges. The detailed fit of the MgS feature in the SED allows the determination of the percentage of the SiC+MgS particles with respect to the total dust formed, and of the fractional width of the MgS mantle with respect to the total dimension of the SiC+MgS grains. The latter quantity is related to the condensation point, as a larger mantle is formed when the condensation zone is more internal. An example of this kind of analysis is shown in Fig. 5.9, where the effects of changing the percentage of SiC+MgS dust and of the size of the MgS mantle are indicated.

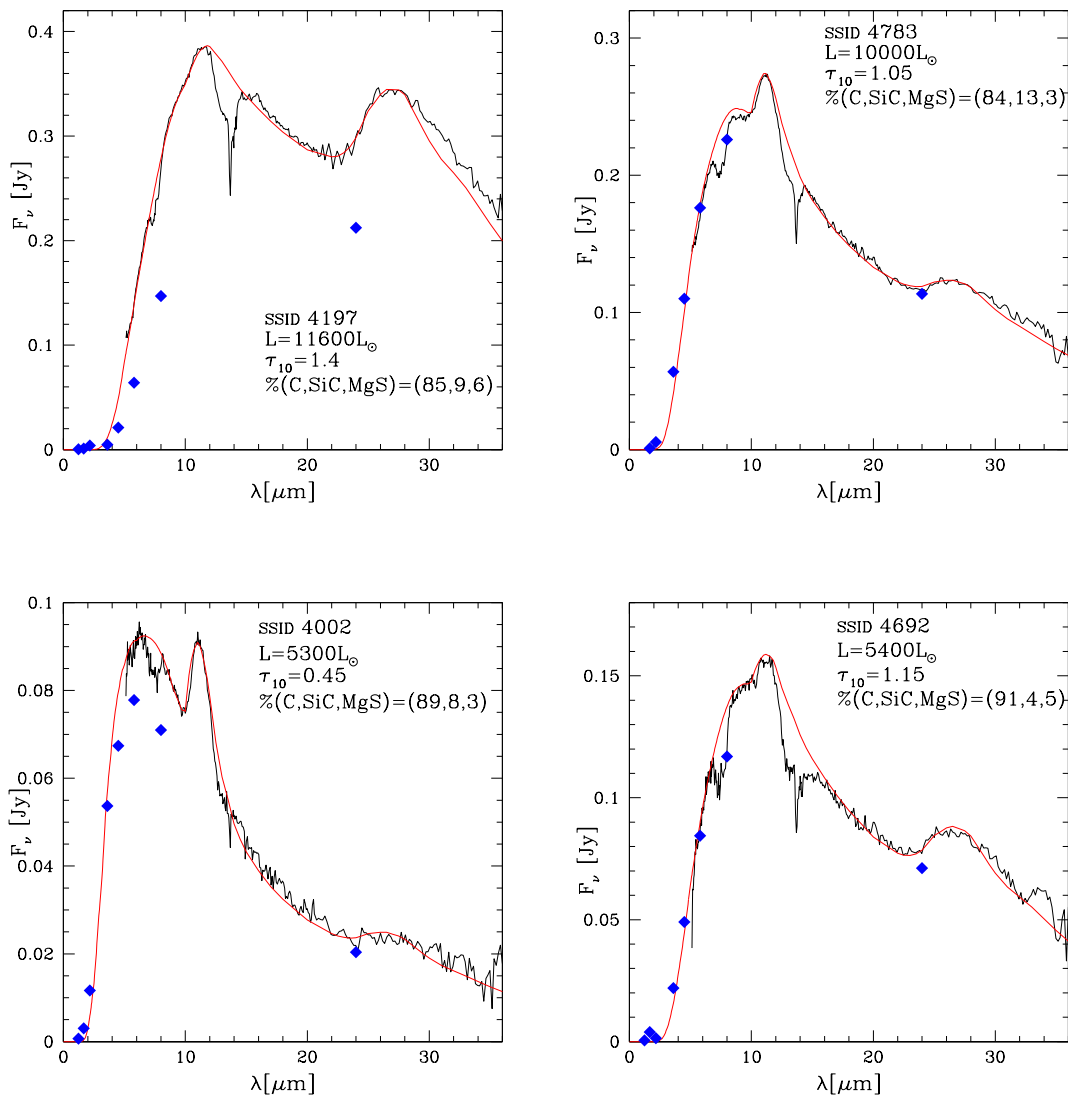


Figure 5.10 IRS spectra of the sources SSID 4197 (top-left panel), SSID 4783 (top-right), SSID 4002 (bottom-left) and SSID 4692 (bottom-right), with the best fit models, obtained with the luminosities, optical depths and dust mineralogy indicated in the individual panels

We find that in the majority of the sources analysed the fraction of MgS+SiC particles is around 5%, of the same order of pure SiC grains. The detailed fit of the morphology of the 25 – 30 μm feature demands that the width of the MgS mantle accounts for 30 – 40% of the overall size of the SiC+MgS grains, which is consistent with assuming that precipitation of MgS onto SiC cores begins in a more internal region of the outflow than found for pure MgS dust. A few examples of stars with SED characterized by SiC and MgS features are shown in Fig. 5.10.

The conclusions we draw for the present analysis are the following:

1. A fraction around 50% of the SiC particles formed in the internal regions of the circumstellar envelope act as seeds for the deposition of MgS. This is consistent with the study of the 30 μm feature in carbon stars published in Messenger et al. (2013), who found a tight correlation between the 11.3 μm and the 30 μm features in the spectra of Galactic carbon stars, concluding that the carriers of these features are strongly related to each other. SiC and SiC+MgS dust make up around 10% of the total dust, this result being substantially independent of the degree of obscuration of the star
2. Formation of SiC+MgS particles takes place in the same region of the circumstellar envelope where solid carbon condensation occurs.

5.5.3 Graphite

As anticipated in Section 1.4.2, the presence of carbon dust in the form of graphite is taken into account in the present work. Our choice is to derive the relative contribution from amorphous carbon and graphite by looking for the best fit of the SED of carbon stars in the sample examined here. The approach we followed is the following: we first derived the luminosity, optical depth and percentages of SiC and MgS according to the method so far discussed, then assumed a variable percentage of graphite with respect to carbon, until reaching full consistency with the observed SED.

An example of the analysis done is shown in Fig. 5.11, where we show the interpretation of the SED of the source SSID 4722, whose spectrum exhibits a fairly large level of infrared emission, with τ_{10} slightly below unity. Changing the fraction of graphite with respect to the total of carbon dust (hence amorphous carbon + graphite) does not sensitively alter the morphology of the SED in the wavelength region close to the emission peak (in the example shown in Fig. 5.11), but has a strong effect on the $\lambda > 20 \mu\text{m}$ domain, which is lifted by the presence of graphite.

Other results, where a not negligible fraction of graphite is required to reproduce the observed SED of the stars in the $\lambda > 20 \mu\text{m}$ spectral region, can be seen in Fig. 5.12, which shows the comparison between the IRS and the synthetic spectra, for stars of various luminosities and τ_{10} .

From the analysis of the sources examined, we deduce that amorphous carbon is the dominant dust component in the winds of carbon stars. Graphite is formed in the circumstellar envelope of $\tau_{10} > 0.1$ stars, in percentages growing with τ_{10} , ranging from a few percents to $\sim 20\%$.

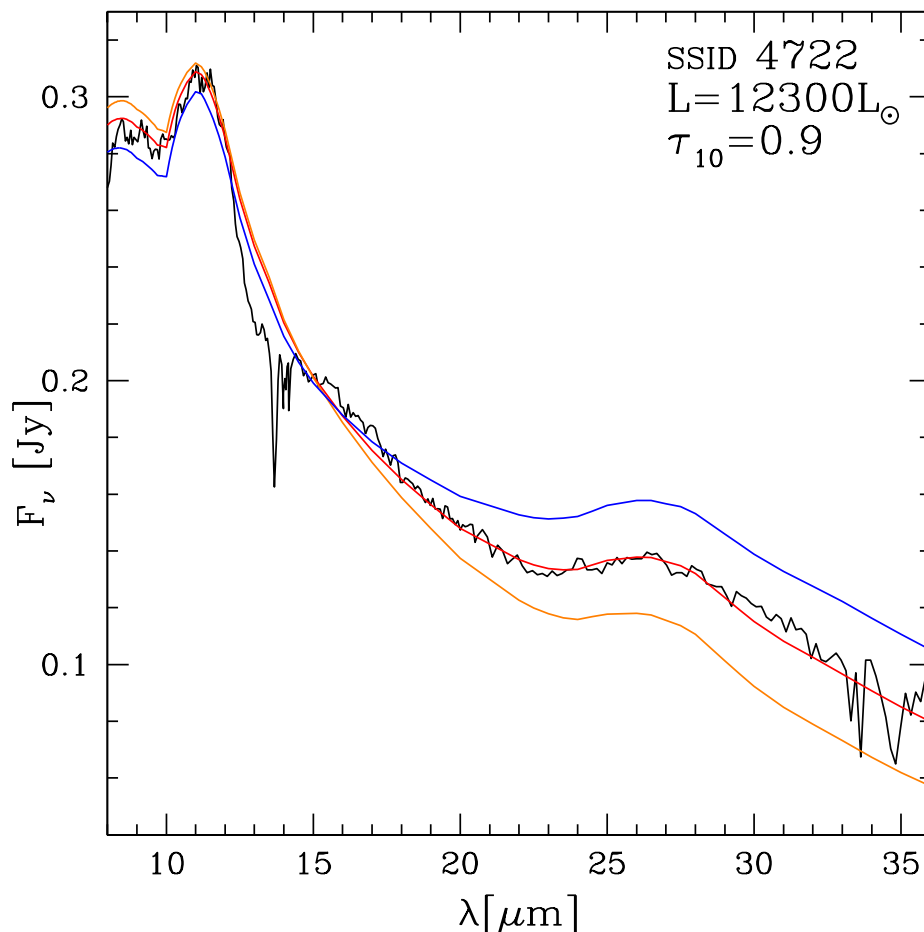


Figure 5.11 IRS spectrum of SSID 4722 compared with synthetic SED, differing for the percentage of graphite. The different lines refer to percentages of 0% (orange), 15% (red), 30% (blue).

5.6 Carbon stars in the *JWST* observational planes

As well as for the M-type stars, whose characterization is discussed in the previous chapter, it is extremely important to understand how carbon stars are expected to distribute on the observational planes that will be built with the mid-IR filters of the MIRI camera. This will be crucial to interpret the data collected by *JWST* and to select the combination of filters allowing the best determination of the degree of obscuration and of the mineralogy of the stars, and the identification of the progenitors, in terms of formation epoch and chemical composition.

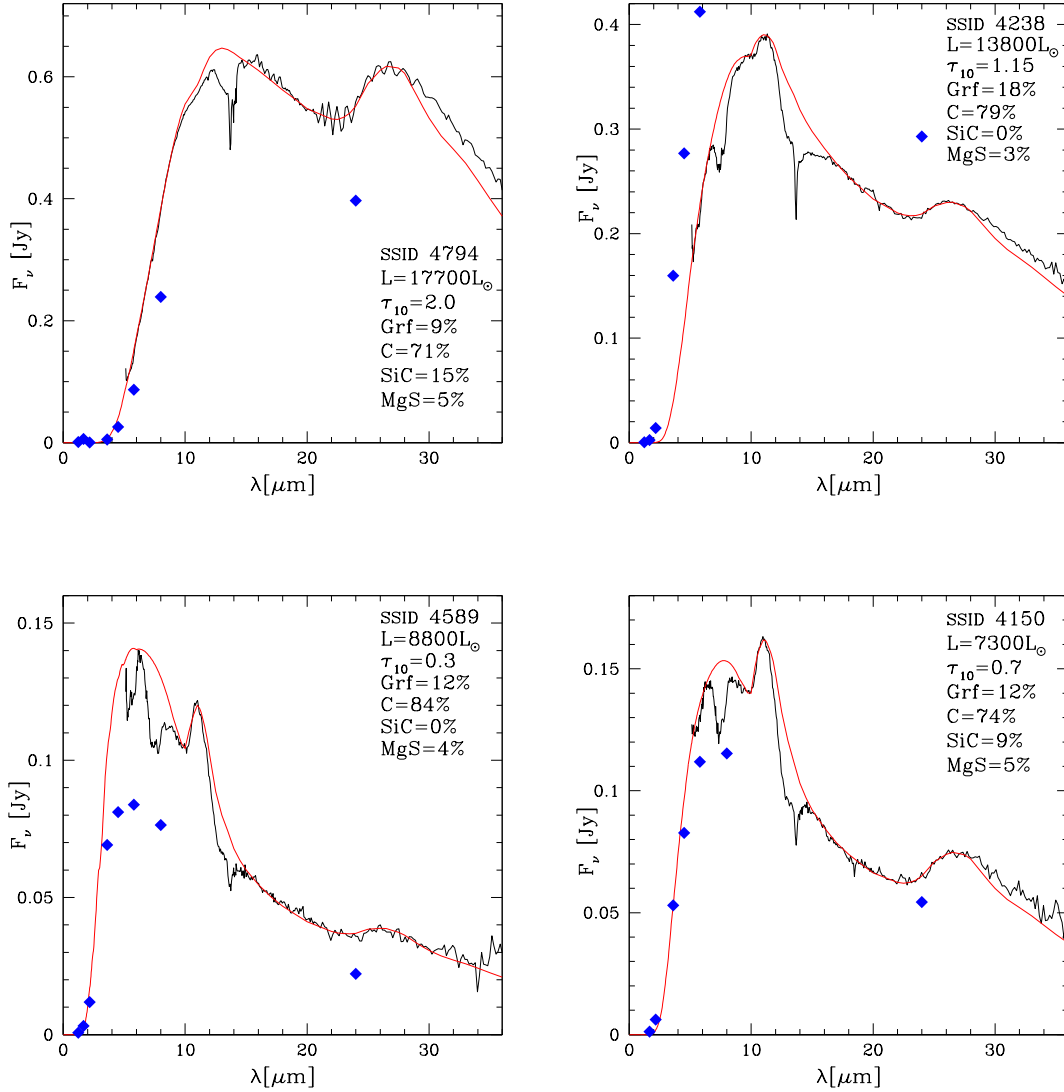


Figure 5.12 IRS spectra of the sources SSID 4794 (top-left panel), SSID 4238 (top-right), SSID 4589 (bottom-left) and SSID 4150 (bottom-right), with the best fit models, obtained with the luminosities, optical depths and dust mineralogy indicated in the individual panels.

We discussed in Chapter 2 the spectral features in the SED of carbon stars, the most important being the $11.3 \mu\text{m}$ feature and the bump at $\sim 30 \mu\text{m}$. These spectral features can also be seen in the synthetic spectra shown in Fig. 2.3 in that chapter (the $30 \mu\text{m}$ feature is not present in the left panel, because in that simulations only amorphous carbon and SiC were considered), to which we will refer in the following analysis. We outlined that the dust species responsible for the presence of these features do not provide any significant contribution to the overall optical depth of the circumstellar envelope of the star, which is

mainly given by absorption by solid carbon grains. On the other hand, reprocessing of the radiation by SiC and MgS particles affects the morphology of the SED in regions of the spectrum which fall inside the transmission curves of the majority of the MIRI filters. As clear in Fig. 2.3 and 5.1, the MIRI filters covered by the IRS spectral range and falling in a wavelength interval substantially clear of features associated to dust are F770W, F1000W and F1800W.

F770W is affected by the molecular band centred at $7.5 \mu\text{m}$, which becomes less and less deep as the degree of obscuration increases, and has no relevance in the spectra of the stars with the largest IR emission. This behaviour can be seen, e.g., in the sequence of spectra in Fig. 5.1, where we note the little incidence of this feature in the interpretation of the spectrum of the most obscured source SSID 18, shown in the bottom-right panel. According to the present analysis, we find that in the $\tau_{10} > 1$ domain the acetylene $7.5 \mu\text{m}$ feature is not relevant in the determination of the main properties of the stars, whereas the impact on the analysis of the poorly obscured objects can be safely managed by introducing a correction factor to account for the depression of the flux in that spectral region. We will return to this point shortly.

The wavelength interval covered by F1000W is only partially overlapped on the SiC feature, provided that the latter is very prominent. We will see that this does not affect the general colour- τ_{10} trend while, on the other hand, use of this filter allows drawing information on the metallicity of the stars.

The spectral region covered by the transmission curve of F1800W (see Fig. 2.3) is not affected by molecular or dust features. This suggests using the F1800W flux in the interpretation of the SED of carbon stars. The only caution to take into account is that the reprocessing of the radiation by MgS and graphite particles makes the SED flatter in the $12 - 20 \mu\text{m}$ region, which reflects into a higher F1800W flux. This is clear from the comparison between the synthetic SED shown in Fig. 2.3. The F1800W fluxes based on synthetic models where the presence of MgS and graphite dust is neglected are slightly underestimated.

Based on these arguments, we consider the colour-magnitude (F770W-F1800W, F1800W) and (F1000W-F1800W, F1800W) planes as the most suitable to study the reddening sequences of carbon stars, where the characterization of the individual objects is fairly independent of the details of the dust mineralogy and scarcely affected by the details of the morphology of the most relevant spectral features.

The left panel of Fig. 5.13 shows the distribution of the sample of carbon stars described in Chapter 2 on the (F770W-F1800W, F1800W) plane. The sources within the subsample that we analysed in detail in the present investigation are shown with different symbols. In

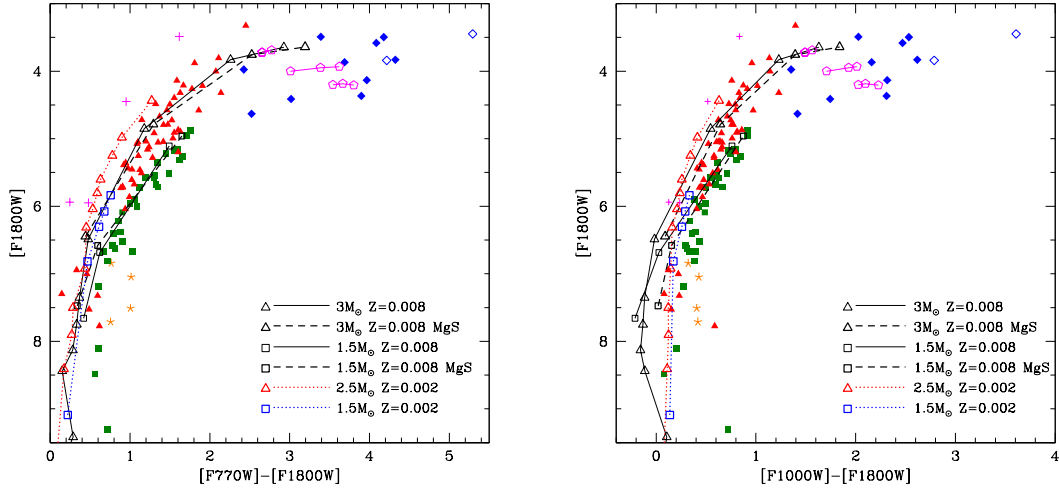


Figure 5.13 Left: Stars in the sample described in Section 2.2 are shown in the colour-magnitude (F770W-F1800W, F1800W) plane. Same symbols of Fig. 5.2 were adopted. Black squares and triangles indicate the expected evolution of stars of metallicity $Z = 0.008$ and initial mass $1.5M_{\odot}$ and $3M_{\odot}$, respectively. Dashed lines refer to the expected evolution of $1.5M_{\odot}$ and $3M_{\odot}$ stars, when the presence of SiC+MgS and graphite grains are considered in the computation of the synthetic SED. Blue squares and red triangles, connected with dotted tracks, refer to the evolution of $Z = 0.002$ stars of initial mass $1.5M_{\odot}$ and $2.5M_{\odot}$, respectively. Magenta pentagons indicate the tracks of $1.1M_{\odot}$, $2.5M_{\odot}$ and $3M_{\odot}$ (from fainter to brighter) models, obtained by artificially increasing the mass loss rate after the jump in the stellar radius caused by the increase in the surface carbon, according to the discussion in Section 5.4. Right: distribution of stars in the colour-magnitude (F1000W-F1800W, F1800W) plane.

the figure we show as solid lines the tracks corresponding to the sequences of synthetic SED of $Z = 0.008$ stars of initial mass $1.5M_{\odot}$ and $3M_{\odot}$, which were calculated by assuming a dust composition made up only of solid carbon and SiC. The dashed lines indicate the tracks of the same stars, recalculated to account for the presence of SiC+MgS and graphite grains, in quantities consistent with the discussion in Section 5.5. The dashed lines connecting the blue squares and red triangles refer to the evolution of $1.5M_{\odot}$ and $2.5M_{\odot}$ stars of metallicity $Z = 0.002$ (Dell’Agli et al., 2016, 2019b), taken as a representative of a metal-poor population. In this case we do not show the corresponding tracks which consider SiC and MgS, because little formation of these species is expected in the wind of metal-poor stars.

The evolutionary tracks provide a nice fit of the observations, except for the stars discussed in Section 5.4. For the latter objects we followed the indications given in Section 5.4, i.e. we modelled dust production by assuming a higher mass loss rate since the phase during which the stars experience a fast expansion, owing to the carbon enrichment of the surface regions.

The results obtained, shown with magenta stars on the plane, are in fair agreement with the colour and magnitudes of the extreme stars.

The ~ 0.2 mag colour shift between the synthetic and the observed colours of the bluest stars in the sample, characterized by little dust in the circumstellar envelope, is connected with the absorption C_2H_2 feature at $7.5 \mu\text{m}$, discussed earlier in this section. This is the correction to be applied to the synthetic (F770W-F1800W) colour of carbon stars with little dust in the circumstellar envelope.

The stars on this colour-magnitude plane define a well distinguished obscuration sequence, spanning the colour range $0 < \text{F770W-F1800W} < 4.5$ and the magnitude interval $3.5 < \text{F1800W} < 8.5$. (F770W-F1800W) is a reliable indicator of the degree of obscuration of the stars: we find a tight correlation between this colour and the optical depth, which extends from $\text{F770W-F1800W} \sim 0.5$, $\tau_{10} \sim 0.1$, to the objects with the largest infrared emission, with $\text{F770W-F1800W} \sim 4.5$ and $\tau_{10} \sim 7$.

Roughly, we have

$$\log \tau_{10} \sim -0.1 \times (\text{F770W} - \text{F1800W})^2 + 0.9 \times (\text{F770W} - \text{F1800W}) - 1.2 \quad (5.1)$$

For a given (F770W-F1800W) the observed distribution exhibits a ~ 1 mag spread in F1800W, which is due to differences in the luminosity of the stars, which cover the $5000 - 17000 L_{\odot}$ range (see Fig. 5.2). The position on the plane is connected with the formation epoch of the sources, the stars formed more recently being in the upper part of the diagram.

The bright sources discussed in Section 5.3, which we associate either to stars currently experiencing HBB or to metal-poor, massive AGB stars during the late AGB phases, make a sort of upper envelope of the distribution of the stars on this plane.

The tracks based on models that consider SiC+MgS and graphite are slightly redder than those which take into account only solid carbon and SiC. This difference, which is visible only for the most obscured stars, is related to the increase in the F1800W flux, consistently with the discussion done at the beginning of the present section.

The tracks corresponding to metal-poor stars are bluer than the $Z = 0.008$ tracks. This difference is visible only for the stars characterized by optical depths $\tau_{10} > 0.1$, whereas they are substantially overlapped in the low τ_{10} domain. This is explained by the lower rate of dust formation in metal-poor stars, related to the absence of SiC and to the higher effective temperatures, which inhibits the formation of great quantities of dust (Ventura et al., 2014). The scarcity of stars in the region of the plane covered by the track of the metal-poor, $2.5 M_{\odot}$

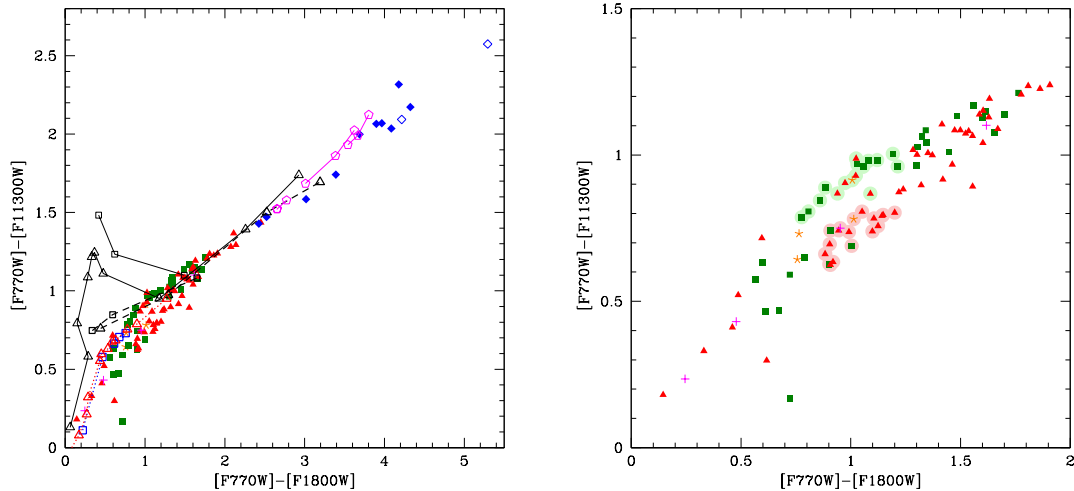


Figure 5.14 Left: position of the stars in the sample presented in Section 2.2 in the colour-colour ($F770W-F1800W$, $F770W-F1130W$) plane. The symbols for the stars and the evolutionary tracks are the same as in Fig. 5.13. Right: zoom of the same plane shown in the right panel, to outline the bifurcation between stars of different metallicity.

indicates the poor star formation of metal-poor stars occurred in the LMC in the last 1 Gyr, in agreement with the studies on the star formation in the LMC (Harris & Zaritsky, 2009).

The distribution of the sample stars in the colour-magnitude ($F1000W-F1800W$, $F1800W$) plane is shown in the right panel of Fig. 5.13, with the same evolutionary tracks reported in the left panel. The trend traced by the observations is similar to the one in the ($F770W-F1800W$, $F1800W$) diagram, with the difference that the colour range is in this case ~ 2.5 mag wide: as expected, ($F770W-F1800W$) is more sensitive to τ_{10} in comparison to ($F1000W-F1800W$). The relationship between ($F1000W-F1800W$) and τ_{10} can be approximated by

$$\log \tau_{10} \sim -0.2 \times (F1000W - F1800W)^2 + 1.13 \times (F1000W - F1800W) - 0.75 \quad (5.2)$$

In the lower-left side of the plane, populated by stars with little dust, the low-metallicity tracks are bluer than their $Z = 0.008$ counterparts: this is connected with the SiC feature, present in the SED of $Z = 0.008$ objects and absent in that of metal-poor stars, which causes a slight lift of the $F1000W$ flux. We note that the metal-poor tracks are overlapped on the observations, suggesting that a significant fraction of stars with little or no dust in the circumstellar envelope belong to a low-metallicity population. We will return to this point later in this section.

Fig. 5.14 shows the distribution of the stars in the colour-colour (F770W-F1800W, F770W-F1130W) plane. The same tracks as in Fig. 5.13 are shown.

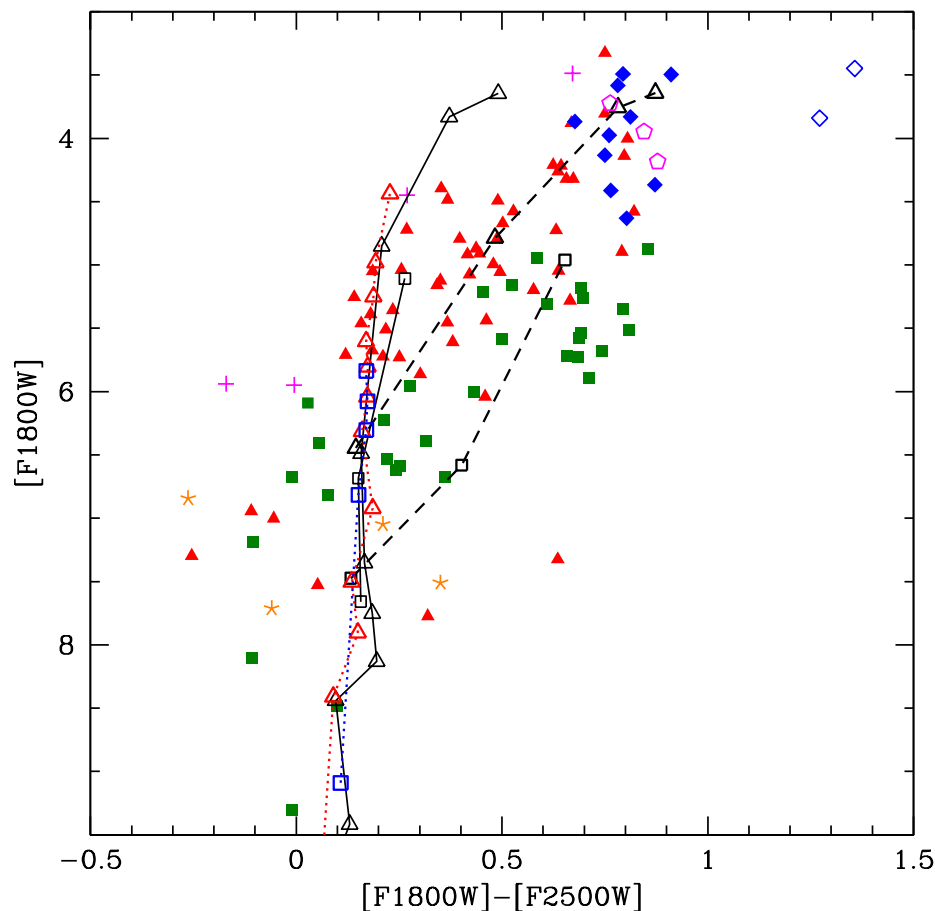


Figure 5.15 Position of the stars in the sample presented in Chapter 2 in the colour-magnitude (F1800W-F2550W, F1800W) plane. The symbols for the stars and the evolutionary tracks are the same as in Fig. 5.13.

The obscuration pattern traced by the sample stars is clear in this plane, and can be roughly approximated by a straight line, with slope 0.5. Generally speaking, (F770W-F1130W) gets redder and redder as τ_{10} increases. For $\tau_{10} < 1$ this trend is mostly due to the presence of the SiC feature in the SED, which increases the flux in the $11.3 \mu\text{m}$ region (see the blue and red lines in of Fig. 2.3). For higher τ_{10} the increase in (F770W-F1130W) is related to the shift of the SED towards the mid-IR part of the spectral range, the peak being at wavelengths $\lambda > 10 \mu\text{m}$ (see green line in Fig. 2.3).

The tracks of metal-poor models are below those of the more metal-rich stars, because the F1300W flux is smaller, owing to the little (or no) quantity of SiC in the circumstellar envelope. The difference between the $Z = 0.002$ and $Z = 0.008$ tracks are negligible at large τ_{10} , because under those conditions the SiC feature becomes less prominent and the SED shifts to longer wavelengths.

The evolutionary tracks in this plane reproduce the extension of the trend traced by the stars in the sample. The EROs are once more an exception on this side, their colours being reproduced only by invoking higher mass loss rates, according to the discussion in Section 5.4. In the region of the plane at $F770W-F1130W < 0.8$ there is an offset between the $Z = 0.008$ tracks and the observations, even when the correction for the presence of MgS+SiC and graphite is considered. The $Z = 0.002$ tracks are in much better agreement with the observational evidence in this region of the colour-colour plane, which is populated by stars with little dust in their surroundings, with $\tau_{10} < 0.5$. Most of these stars descend from low-mass progenitors, with initial mass below $\sim 1.5M_{\odot}$, formed in epochs older than 2 Gyr. In the spectrum of the majority of these stars there is no evidence for the SiC feature, which is the reason why their position is better reproduced by $Z = 0.002$ models. While we cannot rule out that some unknown mechanisms inhibits the formation of SiC particles under particular circumstances, the most plausible explanation for this result is that the low-mass stars with little dust in the outflow are mostly metal-poor stars; this is consistent with the age-metallicity relationship of the LMC, studied in Harris & Zaritsky (2009), and with the study by Dell’Agli et al. (2015b), who claimed the presence of a significant fraction of low-metallicity objects in the LMC stars descending from $M < 2M_{\odot}$ progenitors. The right panel of Fig. 5.14 shows a zoom of the colour-colour plane in the $0 < F770W-F1800W < 2$ region. Here we note a clear dichotomy in the distribution of the stars, which we interpret as a metallicity spread: the stars painted in pink, with no SiC, correspond to the metal-poor population, whereas the green counterparts represent the more metal-rich stellar component. These spread vanishes for $0 < F770W-F1800W < 1.5$, because metal-poor stars are not expected to evolve to such red colours.

We now turn our attention to the colour-magnitude (F1800W-F2550W, F1800W) diagram, shown in Fig. 5.15, with the same symbols used in Fig. 5.13 and Fig. 5.14.

In this plane, as expected, use of the tracks that consider the formation of SiC+MgS is mandatory, because the transmission curve of the F2550W filter is entirely overlapped to the $30 \mu\text{m}$ bump. The significant discrepancy between the tracks calculated with or without SiC+MgS can be understood by confronting the synthetic SEDs shown in Fig.2.3: especially in the higher τ_{10} cases the SEDs are noticeably different, particularly in the F2550W flux. This despite the assumed MgS percentage is only 5% of the total dust. We see in Fig.5.15

that the tracks which consider MgS are in much better agreement with the observations and are overlapped with most of the stars with $F1800W < 6$.

The colour range of the sample stars in the (F1800W-F2550W, F1800W) plane is ~ 1 mag. This is significantly smaller than in the (F770W-F1800W, F1800W) plane (see Fig.5.13), where the colour difference between the stars with no dust and the most obscured ones is ~ 4 mag. This difference is explained by the saturation of (F1800W-F2550W) for $\tau_{10} > 3$, because the SED becomes approximately horizontal in the $\lambda > 20 \mu\text{m}$ domain.

The low-metallicity tracks shown in Fig.5.15 define an approximately vertical trend, which is because there is no $30 \mu\text{m}$ bump in the spectra of these stars and the slope in the $15 - 30 \mu\text{m}$ spectral region is practically unchanged. The latter point is linked to the fact that low-metallicity carbon stars are not expected to evolve at $\tau_{10} > 1$, as shown for $Z = 0.001$ in Chapter 1 (see Fig. 1.17). We note that the $Z = 0.002$ tracks nicely reproduce the position of the stars with $F1800W-F2550W \sim 0.1 - 0.2$ and $4 < F1800W < 6$. These sources are the same located in the $F770W-F1130W < 0.8$ region in the colour-colour plane shown in Fig.5.14, which we identified as low-metallicity stars. This conclusion is further reinforced by the present analysis, suggesting a criterion to disentangle stars of different chemical composition in the (F1800W-F2550W, F1800W) diagram.

The summary of the interpretation of the C-rich stars in the LMC is shown in Table 5.1, which gives the derived values of L , τ_{10} and dust mineralogy for each source investigated, whereas all results of the SED fitting of the IRS spectra are shown in the Appendix.

Table 5.1 The interpretation of the sample carbon stars analysed in the present work. The different columns report the SSID of the star (1) estimated luminosity (2), dust mineralogy (3) and optical depth τ_{10} (4).

SSID	L/L_{\odot}	%(C,SiC,MgS)	τ_{10}
3	4100	(87,13,0)	0.1
7	7900	(99,1,0)	0.05
9	5200	(81,14,5)	3.4
18	7500	(83,8,9)	1.7
51	13000	(100,0,0)	0.04
55	7700	(97,2,1)	0.1
60	3300	(93,4,3)	0.54
65	6200	(78,21,1)	7.1
66	4300	(100,0,0)	0.32
80	5400	(90,10,0)	0.024

98	5400	(97,2,1)	0.33
103	4000	(89,11,0)	0.075
125	8800	(86,12,2)	2.3
126	12200	(100,0,0)	0.06
140	8500	(87,6,7)	1.2
141	3000	(100,0,0)	0.29
145	6100	(100,0,0)	0.19
156	5200	(90,10,0)	0.13
167	10200	(74,19,7)	2.0
181	5200	(95,3,2)	0.19
190	12000	(96,2,2)	3.4
4000	7500	(90,9,1)	0.79
4001	7900	(78,15,7)	1.25
4002	5300	(89,8,3)	0.45
4003	5500	(92,4,4)	1.0
4004	9900	(91,7,2)	0.67
4012	7100	(99,0,1)	0.38
4016	11500	(95,4,1)	0.7
4021	15500	(100,0,0)	0.6
4034	11500	(100,0,0)	0.23
4037	18200	(99,1,0)	0.18
4052	6900	(87,7,6)	0.65
4062	11500	(92,5,3)	1.05
4067	10500	(94,5,1)	0.27
4093	5600	(92,5,3)	0.58
4100	13200	(87,7,6)	1.1
4109	27800	(96,3,1)	0.37
4150	7300	(86,9,5)	0.7
4154	14700	(93,4,3)	0.54
4155	10800	(89,9,2)	0.85
4171	8200	(78,19,3)	6.3
4185	5200	(74,25,1)	6.2
4197	11600	(85,9,6)	1.45
4206	8900	(81,16,3)	1.06
4211	8900	(96,4,0)	0.41
4225	14900	(95,3,2)	0.23

4228	9500	(97,2,1)	0.65
4238	13800	(97,0,3)	1.15
4240	8300	(97,1,2)	1.0
4241	10800	(92,4,4)	0.94
4244	9700	(95,5,0)	0.51
4246	13900	(85,7,8)	1.7
4251	10400	(100,0,0)	0.62
4252	8000	(95,3,2)	1.0
4256	12600	(87,11,2)	0.41
4293	7200	(83,10,7)	0.95
4299	9800	(100,0,0)	5.3
4308	7000	(77,23,0)	5.6
4309	11500	(96,0,4)	1.2
4334	6500	(97,2,1)	0.38
4339	5500	(84,9,7)	0.9
4385	5500	(89,10,1)	0.22
4391	10800	(93,4,3)	0.56
4401	6700	(87,7,6)	1.14
4402	7200	(91,5,4)	1.05
4408	9300	(88,7,5)	0.6
4411	15800	(97,2,1)	0.19
4415	4700	(80,20,0)	6.6
4421	10800	(94,5,1)	0.68
4432	5700	(100,0,0)	0.005
4435	6700	(94,3,3)	0.86
4442	7300	(95,5,0)	0.26
4447	7600	(97,2,1)	0.51
4448	5800	(100,0,0)	0.03
4451	28600	(89,6,5)	0.91
4463	6400	(92,7,1)	0.21
4469	6700	(97,3,0)	0.23
4476	14000	(100,0,0)	0.1
4478	7100	(93,4,3)	0.79
4479	5500	(82,16,2)	0.61
4481	6700	(89,5,6)	0.7
4488	11600	(90,10,0)	0.035

4489	5100	(57,40,3)	4.3
4491	8000	(97,0,3)	0.98
4510	10300	(96,4,0)	0.28
4513	16100	(94,5,1)	0.62
4519	6800	(88,6,6)	0.52
4540	32000	(100,0,0)	0.06
4556	12200	(82,16,2)	1.0
4562	8400	(89,6,5)	0.97
4565	5000	(96,2,2)	0.75
4575	12100	(99,1,0)	0.33
4589	8800	(96,0,4)	0.3
4593	5700	(83,10,7)	0.95
4600	5800	(93,4,3)	0.85
4604	11400	(94,5,1)	0.23
4692	5500	(91,4,5)	1.2
4717	10300	(91,5,4)	1.0
4722	12300	(90,8,2)	0.9
4736	8800	(97,2,1)	0.28
4758	7500	(88,11,1)	0.85
4759	7200	(87,6,7)	1.1
4776	22200	(100,0,0)	0.09
4779	16500	(79,17,4)	1.2
4780	10500	(93,6,1)	0.52
4781	10200	(70,27,3)	5.2
4783	10000	(84,13,3)	1.05
4794	17700	(80,15,5)	2.0
4811	16200	(87,6,7)	1.13
4812	12300	(96,0,4)	1.1

Conclusions

We studied the evolved stellar population of the Large Magellanic Cloud, with the double aim of shedding new light on the dust formation mechanism in the circumstellar envelope of AGB stars and to support the astrophysical community to benefit from the opportunities which will soon be offered by the incoming launch of the *James Webb* Space Telescope, in the study of the evolved stars in Local Group galaxies. We focused in particular on the results which will be obtained by the MIRI camera (Rieke et al., 2015), mounted onboard the *JWST*, with 9 filters covering the mid-IR spectral region, whose transmission curves are largely overlapped with the spectral features which characterize the spectra of stars surrounded by dust particles.

The analysis developed in the present investigation is mainly based on the data obtained by the IRS instrument onboard the *Spitzer* Space Telescope, because the determination of the dust mineralogy of the stars with a large infrared emission demands the detailed analysis of the morphology of the spectral energy distribution. This is an important step forward with respect to previous explorations of evolved stars in the Magellanic Clouds, based on near- and mid-IR photometric data.

To this aim, we calculated ad hoc AGB evolutionary sequences of metallicity $Z = 0.008$, suitable to study LMC stars, complemented with $Z = 0.001$ models, to account for the presence of a metal poor stellar component currently evolving in the LMC (Harris & Zaritsky, 2009). With respect to previous calculations, the new models are based on an improved numerical treatment of the convective borders and are extended until the post-AGB phase. An important effort was devoted to the modelling of dust formation in the wind, which was used to calculate a library of synthetic SED, allowing to describe the variation of the infrared emission of stars of various mass and metallicity as they evolve across the AGB. This is the tool which we used to interpret the IRS data.

The detailed analysis of the SED of evolved stars in the LMC classified as AGB sources led to the identification of a group of stars, whose current main dust component is solid iron, and of a few sources, which we propose to be surrounded by two dusty layers. We suggest

that the former are the progeny of metal-poor, massive AGB stars, formed ~ 100 Myr ago (Marini et al., 2019a), in which the formation of silicates is partly inhibited by the effects of strong HBB, which caused a significant depletion of the surface oxygen and magnesium, leaving room to the formation of dust dominated by solid iron grains. The second group of stars are older (3 – 5 Gyr) objects, descending from low mass ($\sim 1 - 2M_{\odot}$) progenitors, which have recently become carbon stars (Marini et al., 2019b). They are surrounded by a more internal, recently formed dusty layer, composed by carbonaceous particles, and a more external silicate dust shell, formed just before the occurrence of the last thermal pulse.

Other than these two peculiar groups of stars, the use of the synthetic library of SED allowed an extensive characterization of the AGB stars in the LMC, an analysis which was divided among M-type AGBs and carbon stars.

For what concerns the oxygen-rich sample, we could separate the progeny of low-mass stars from massive AGBs, currently experiencing HBB. In the former group, the formation of silicates and alumina dust increases during the AGB phase, until they become carbon stars, thus starting the production of carbonaceous dust. Massive AGBs were identified by means of their large luminosities and the large optical thickness of their circumstellar envelope, which according to our modelling is strictly connected with the strength of the HBB experienced.

The MIRI filters whose transmission curves overlap with the two silicate features centred at $\sim 10 \mu\text{m}$ and $\sim 18 \mu\text{m}$, i.e. F1000W, F1800W and F2100W, can be hardly used for the characterization of oxygen-rich AGB stars, owing to the non linear behaviour of the two features with the optical depth. The plane allowing the best study of M-type AGB stars, with the identification of the evolutionary status and of the dust quantity and mineralogy formed in the outflow, is the (F770W-F2550W, F770W) diagram. Indeed the F770W flux proves extremely effective in the study of these stars, because it is not sensitive to the modification of the SED with the optical depth; on the other hand it is affected by the presence of featureless dust species, such as solid iron, thus it can be efficiently used to identify such peculiar objects.

The study of carbon stars confirmed earlier investigations, that the dust mineralogy is largely dominated by amorphous carbon and silicon carbide grains. However, the present study demonstrates that for optical depths $\tau_{10} > 0.1$ part of the carbon dust forms as graphite, in percentages up to 20%. The study of the clear bump present in the SED of carbon stars in the 25 – 30 μm spectral region indicated that a possible origin of this feature emission is the growth of MgS grains via precipitation of SiC particles formed in more internal regions of the outflow. As for the SiC case, the prominence of this bump is sensitive to the metallicity of the star.

The observational planes allowing the best analysis of the carbon star population are the colour-magnitude (F770W-F1800W, F1800W) and (F1000W-F1800W, F1800W) diagrams. The former allows a better evaluation of the optical depth of the envelope, thus the amount of dust formed in the outflow; the distribution of the stars in the latter diagram is more sensitive to the metallicity of the stars, owing to partial overlapping of the transmission curve of the F1000W filter with the SiC feature, which, in turn, is sensitive to the silicon content. In both cases the F1800W flux turns out a reliable luminosity indicator, because it is not overlapped with any important feature characterizing the spectra of carbon stars. For this class of stars the use of the F1800W flux is preferable to F2550W, because the latter is influenced by the bump in the $25 - 30 \mu\text{m}$ associated to MgS, which is different from star to star.

We conclude this study with a recommendation for the future observations aimed at characterizing the AGB population in the Local Universe with *JWST*. Other than the F770W filter, we notice that the MIRI filter combinations allowing the best investigation of oxygen-rich AGBs and carbon stars differ, thus not allowing the identification of an optimal solution, of general validity. Despite these difficulties, the combination of the F770W, F1000W, F1800W and F2550W magnitudes will definitively allow an exhaustive analysis of the AGB population of galaxies.

6

6.1 ATON

The AGB evolutionary sequences presented here were computed by means of the ATON code for stellar evolution (Ventura & D’Antona, 2009; Ventura et al., 1998). We recall here the main physical inputs, most relevant for the topic of the present investigation.

The arguments presented in this work outline how relevant the description of convection is for the AGB phase, in terms of the evolution of the main physical quantities, number of thermal pulses experienced, change in the surface chemical composition due to HBB and TDU. In agreement with other investigations by our group, the temperature gradient within convective regions is found by the FST model, developed by Canuto & Mazzitelli (1991). Mixing of chemicals and nuclear burning were coupled with a diffusive approach, according to the scheme suggested by Cloutman & Eoll (1976). The overshoot of convective eddies into radiatively stable regions is described by an exponential decay of velocities beyond the formal border found via the Schwarzschild criterium. The relation used is

$$v = v_b \times \exp P/\zeta P_b \quad (6.1)$$

where v_b and P_b are the values of velocity and pressure at the formal boundary. The extent of the overshoot is given by the free parameter ζ . For the convective cores that form during the hydrogen and helium burning phases, and generally for the phases previous the AGB evolution, we followed the calibration given in Ventura et al. (1998), and assumed $\zeta = 0.02$. For what concerns the AGB phase, we calibrated the extent of the extra-mixing from the base of the convective envelope and from the borders of the shell that forms at the ignition of each thermal pulse based on the luminosity function (LF) of carbon stars in the Large Magellanic Cloud (Groenewegen 2004). We find that adopting $\zeta = 0.002$ leads to a

satisfactory agreement between the observed and the predicted LFs. With this assumption we recover the relation between initial mass and luminosity of the transition from oxygen-rich to carbon-rich surface chemical composition given in Marigo & Girardi (2007).

In agreement with previous explorations focused on the AGB evolution, mass loss was modeled according to the formulation by Bloeker (1995). The Blocker formula is suitable to describe the steep increase with luminosity that characterizes massive AGB stars; the Blocker description is based on a steep dependence of \dot{M} on luminosity, $\dot{M} \sim L^{4.7}$, in agreement with dynamical models of AGB envelopes by Bowen (1988). For M stars, with masses $M > 4M_{\odot}$, evolving at large luminosities, the mass-loss rates used here are substantially larger than other treatments in the literature, such as the classic recipe by Vassiliadis & Wood (1993), or the empirical relation by van Loon et al. (2005); this difference will result in a smaller number of TPs. For models of smaller mass, the comparison between the Blocker formula and the treatment for C-star winds by Wachter et al. (2002, 2008) is mainly determined by the strong sensitivity to the effective temperature ($\sim T_{eff}^{6.81}$) of this latter. In this mass interval the mass-loss rates used here are smaller, although a comparison with other investigations in the literature is not trivial, because the effects of the mass-loss treatment are strongly related to the way convection is modelled, which is relevant for the effective temperature of the models.

The radiative opacities for temperatures above 10^4 K were calculated using the OPAL on line tool (Iglesias & Rogers, 1996); for smaller temperatures we used the AESOPUS tool described in Marigo & Aringer (2009). This choice allows accounting for the increase in the opacity associated with the change in the surface chemistry determined by TDU. The pioneering study by Marigo (2002) shows how the modelling of AGB stars experiencing TDU is sensitive to the set of opacities adopted; detailed discussions on this argument can be found in Ventura & Marigo (2009, 2010). The nucleosynthesis computation follows the evolution of 30 elements, from hydrogen to alluminum, with the most relevant isotopes entering the pp and 3α chains, and the CNO cycle. The nuclear cross sections are taken from the NACRE compilation (Angulo et al., 1999), with a few exceptions, the most relevant for this study being the rate of the proton capture reaction by nitrogen nuclei, taken from Formicola et al. (2004). The metallicities investigated are: $Z = 0.008$ and $Z = 0.001$. The mixtures follow the relative abundances of the elements according to Grevesse & Sauval (1998), with α -enhancement $[\alpha/Fe] = +0.2$ (for $Z = 0.008$) and $[\alpha/Fe] = +0.4$ (for $Z = 0.001$). This corresponds to an iron content $[Fe/H] = -0.5$ and $[Fe/H] = -2$.

6.2 The equations of the wind structure and dust formation

In the models used in the present work we determine the structure of the wind following the schematization by Ferrarotti & Gail (2006, hereinafter FG06).

The wind is assumed to expand isotropically from the surface of the star, characterized by mass M , luminosity L , radius R , and effective temperature T_{eff} . The outflow is assumed to be stationary and spherically symmetric. The velocity of the wind is determined from the equation for momentum conservation in which the pressure forces are neglected¹:

$$v \frac{dv}{dr} = - \frac{GM_{\star}}{r^2} (1 - \Gamma) \quad (6.2)$$

Where M_{\star} is the current mass of the star. The quantity

$$\Gamma = \frac{kL}{4\pi cGM_{\star}}. \quad (6.3)$$

is the ratio between the radiative pressure on the dust and the gravitational pull of the star, where k is the flux-averaged mass extinction coefficient of the gas-dust mixture, which is dominated by the dust formed in the outflow, which we approximate by (as FG06):

$$k = k_{gas} + \sum_i f_i k_i \quad (6.4)$$

where $k_{gas} = 10^{-8} \rho^{2/3} T^3$ (Bell & Lin, 1994). The sum in eq. 6.4 is extended to all the dust species considered: the f_i terms give the degree of condensation of the key element for each dust species, whereas k_i is their corresponding extinction coefficients.

The density structure in the wind is calculated from the equation of mass conservation

$$\dot{M} = 4\pi r^2 \rho v \quad (6.5)$$

and the temperature profile is calculated according the approximation of Lucy (1976) for a spherically symmetric grey circumstellar dust shell from

$$T^4 = \frac{1}{2} T_{eff}^4 \left[1 - \sqrt{1 - \frac{R_{\star}^2}{r^2} + \frac{3}{2} \tau} \right], \quad (6.6)$$

where the optical depth is defined by

¹Since in this model the shock structure of the outflow is neglected, it would make no sense to retain the pressure forces in this equation

$$\frac{d\tau}{dr} = -\rho k \frac{R_\star^2}{r^2} \quad (6.7)$$

with the limiting condition that $\tau \rightarrow 0$ for $r \rightarrow \infty$ (for numerical reasons, this condition is reached at a distance of $10^4 R$ from the centre, where the asymptotic behaviour of all the quantities is definitively reached).

The equations of the wind structure are solved from the point where the first dust species becomes stable, commonly located 3 – 4 stellar radii away from the centre of the star. This is expected to coincide with the region where $\Gamma > 1$ and the wind is accelerated to supersonic velocities. Similarly to FG06, we keep the velocity of the gas constant from the surface of the star to the region where dust forms. The equations presented above are integrated out to a radial distance of $10^4 R_\star$ (R_\star is the stellar radius), far beyond the point where all the relevant quantities reach their asymptotic behaviour.

The temporal variation of the dust grain size for the i th dust species, a_i , depends on the competition between the growth rate, J^{gr} , and the destruction rate, J^{dec} , that is:

$$\frac{da_i}{dt} = V_{0,i} \left(J_i^{gr} - J^{dec} \right) \quad (6.8)$$

where $V_{0,i}$ is the volume of the nominal molecule in the solid.

The growth rate is evaluated on the basis of the number density of the key element, n , and the thermal velocity of the corresponding molecule, v_{th} :

$$J_i^{gr} = \alpha_i n_i v_{th,i} \quad (6.9)$$

where α_i is the sticking coefficient of the species i .

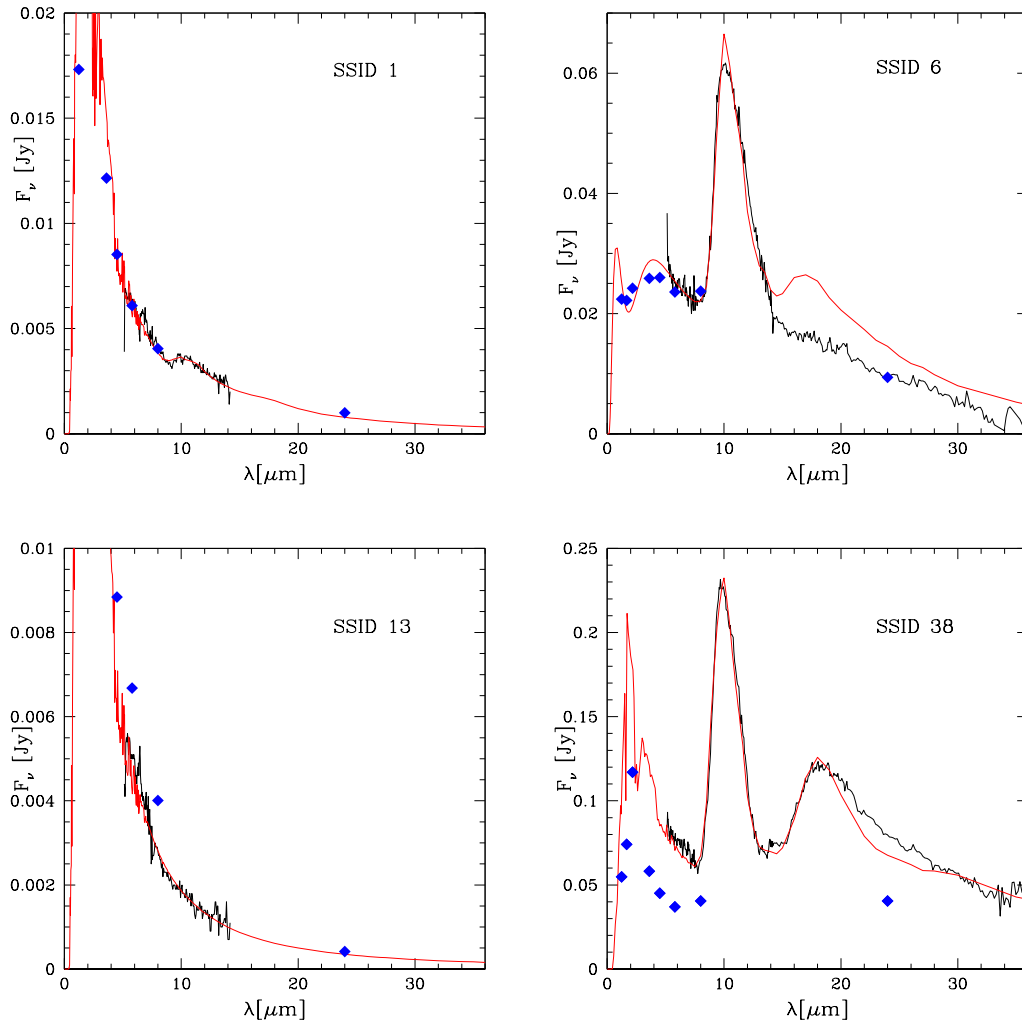
Whereas the destruction rate is calculated via the difference between the formation enthalpy of the dust species and of the individual molecules concurring to the formation process:

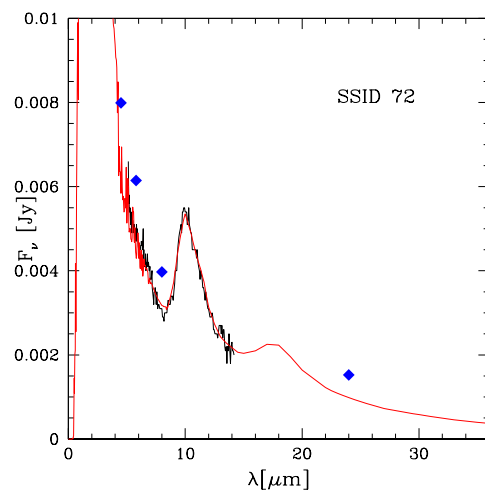
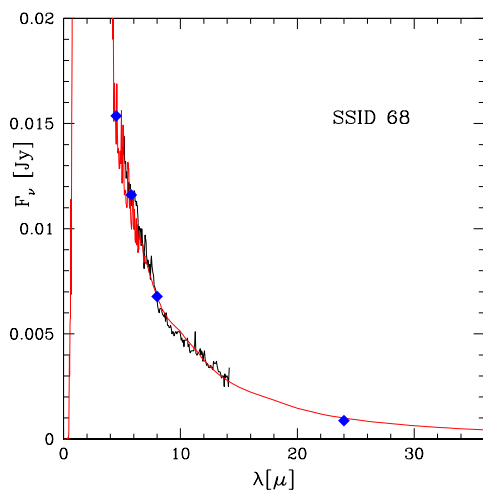
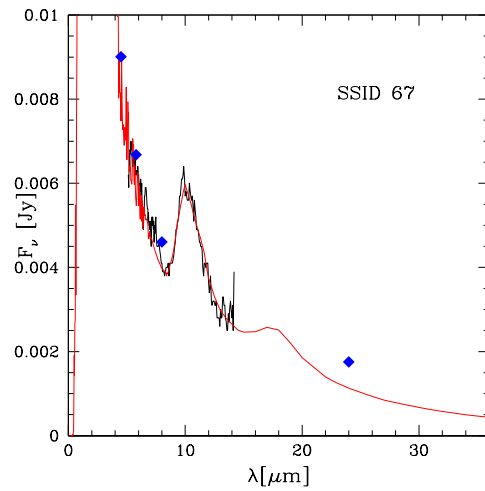
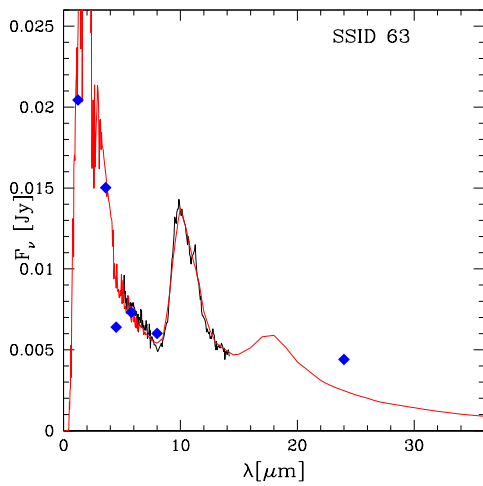
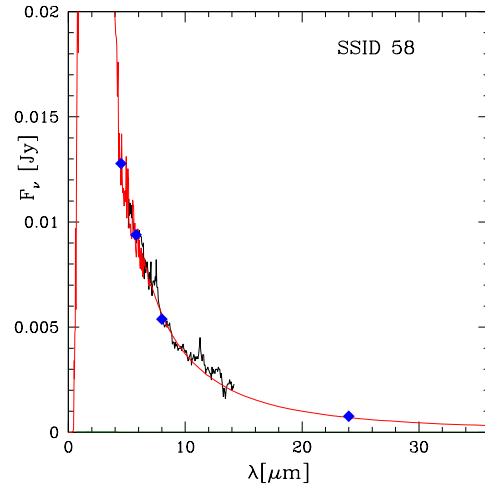
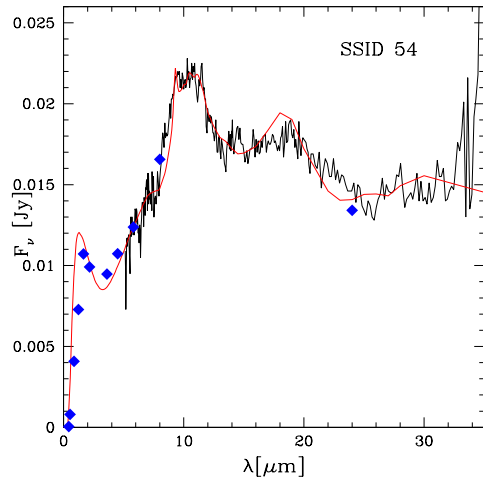
$$J_i^{dec} = \alpha_i v_{th,i} \frac{p_{v,i}}{kT} \quad (6.10)$$

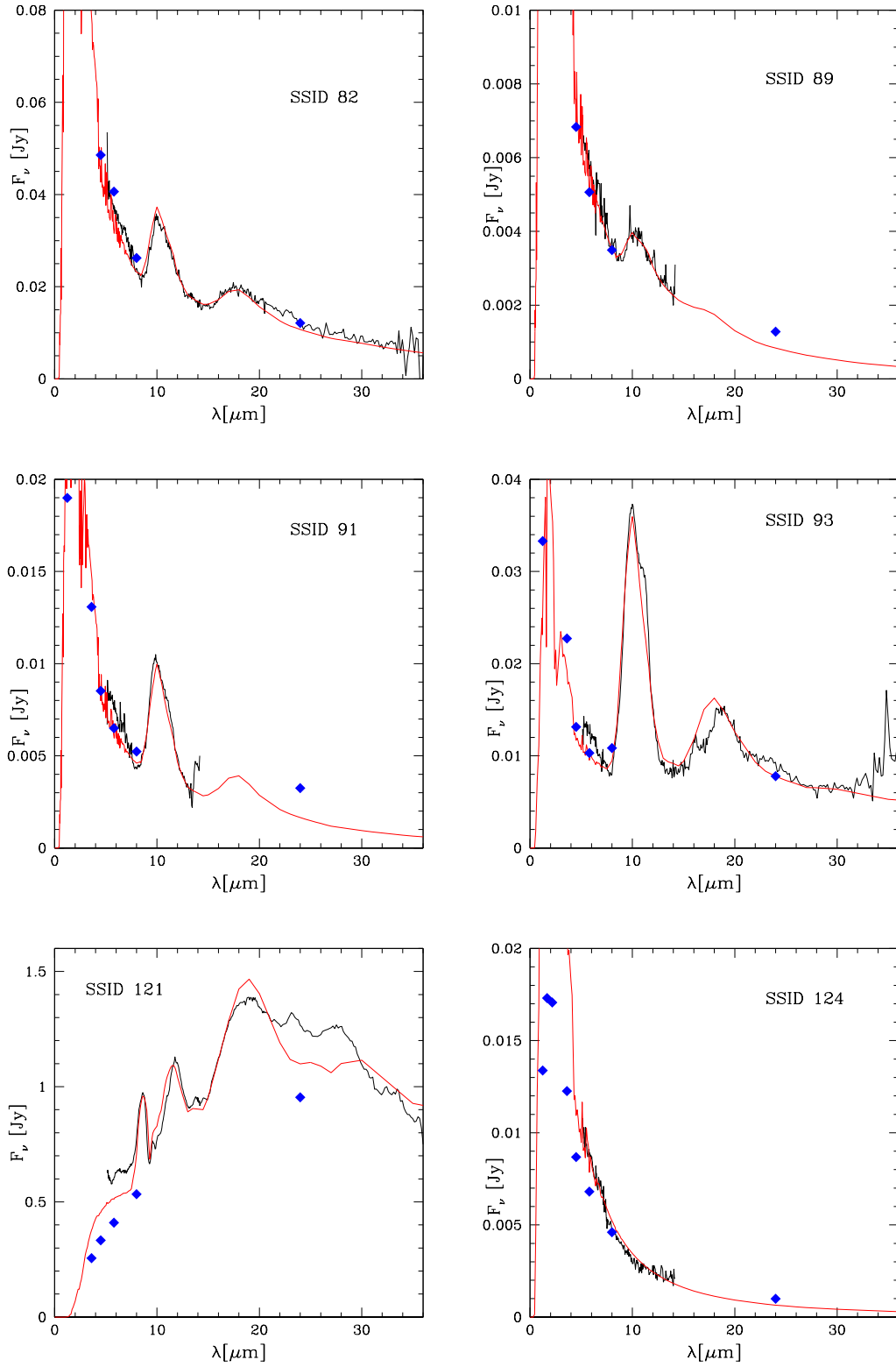
where $p_{v,i}$ is the vapour pressure of the key species over the solid state.

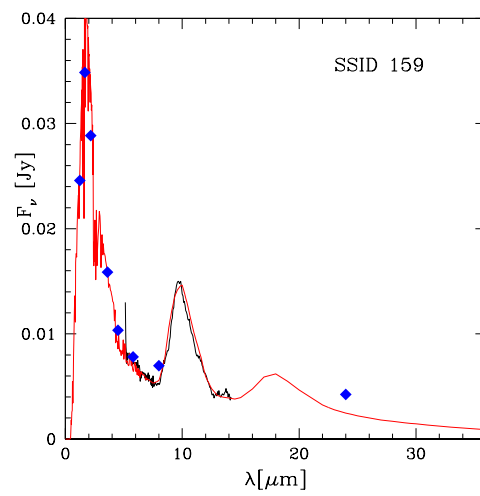
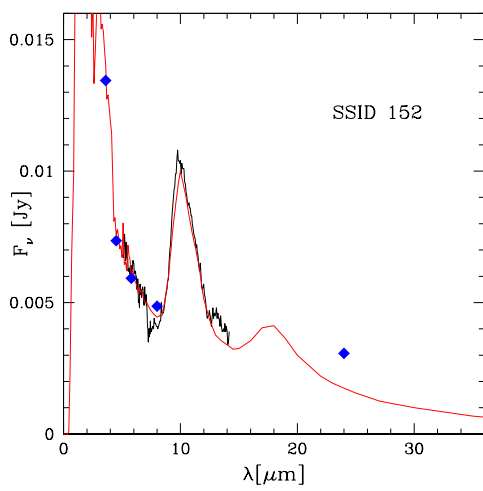
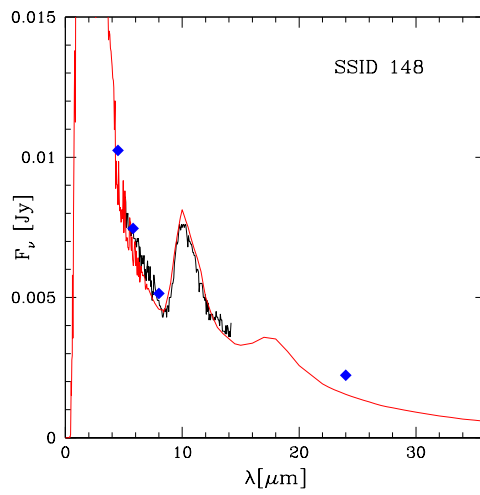
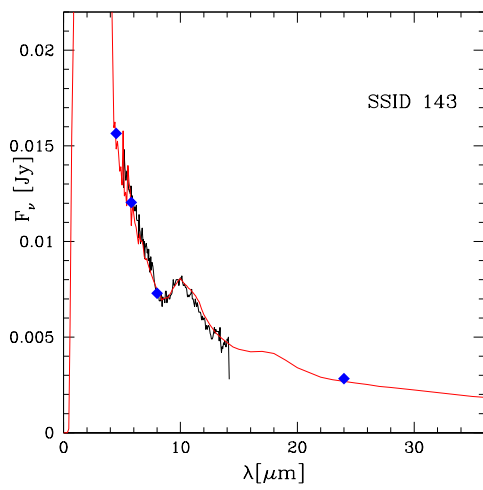
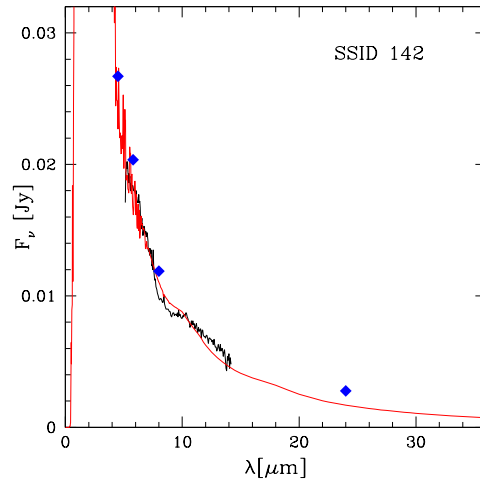
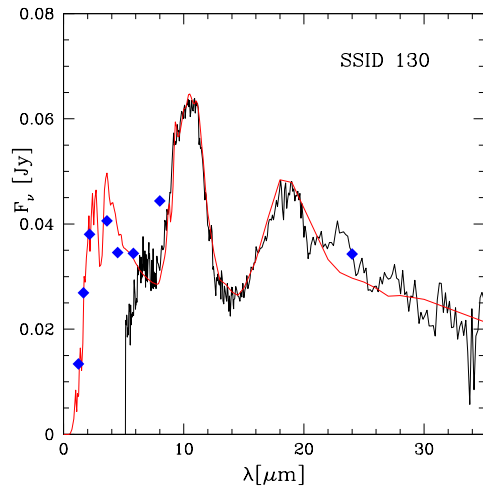
For carbon, based on the discussion in FG06, it is assumed that condensation begins at a temperature of 1100 K and that the destruction term is negligible. An exhaustive description of the methodology followed to estimate the individual vapour pressures can be found, for example, in Ferrarotti & Gail (2001).

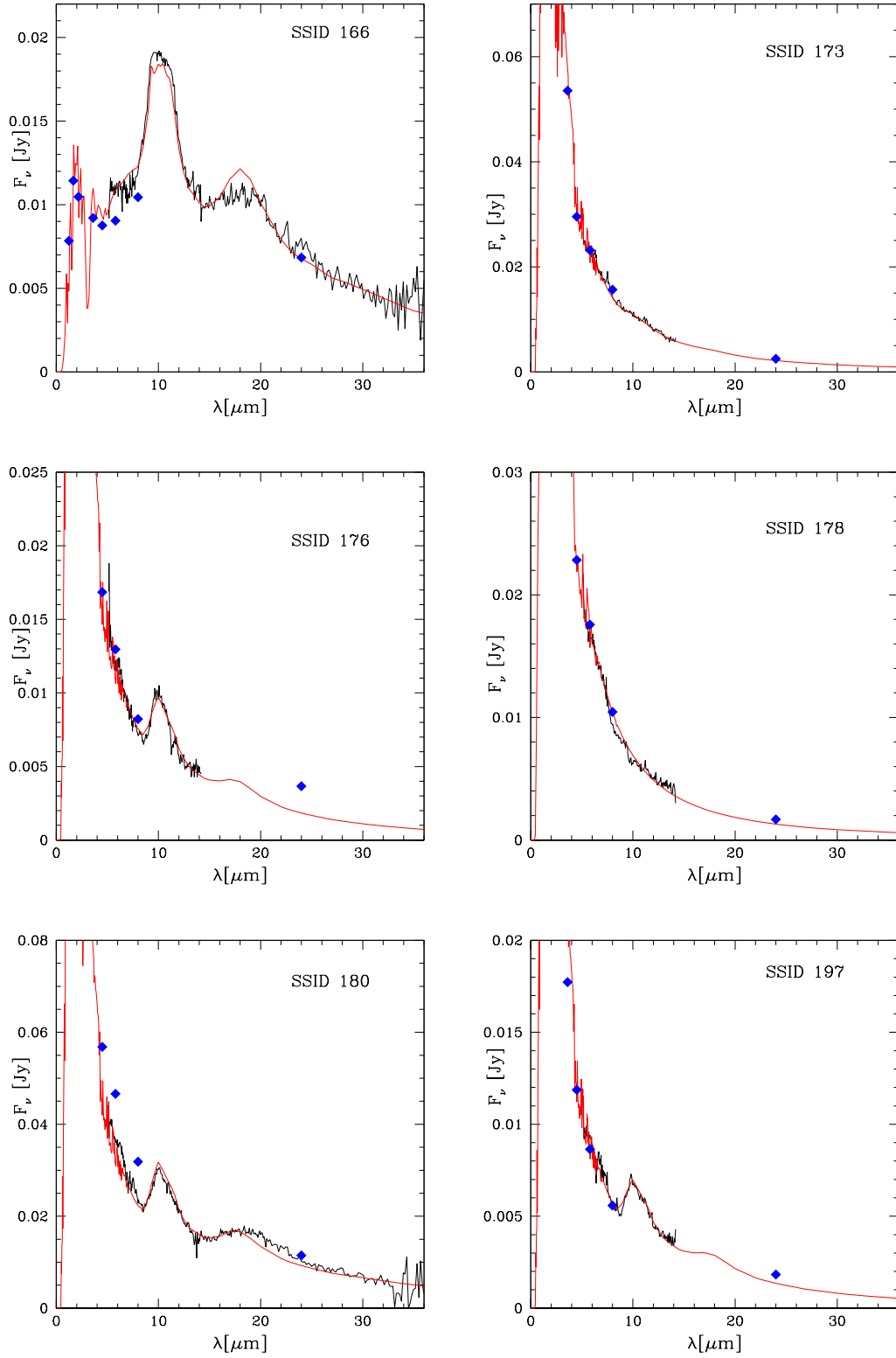
6.3 Fit results of the LMC AGB sample

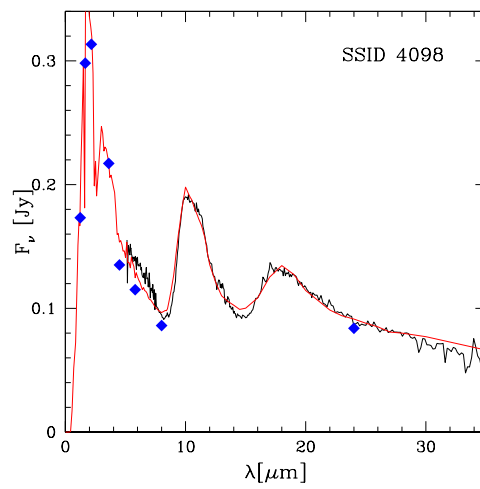
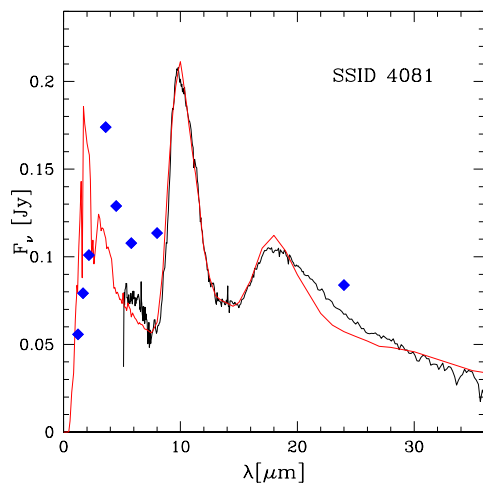
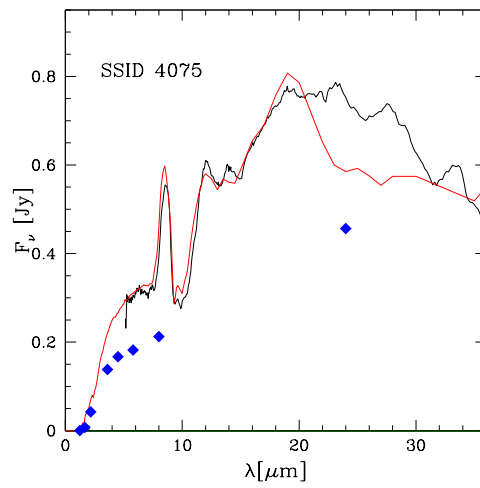
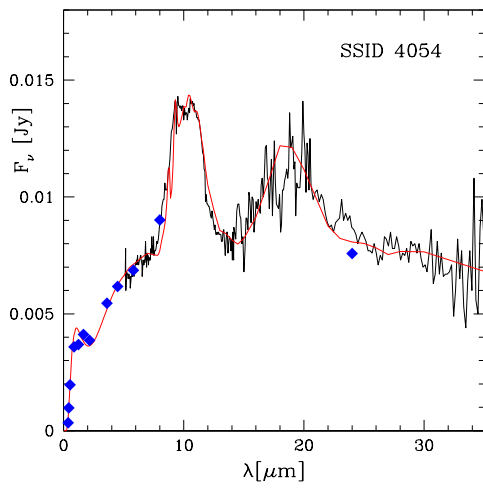
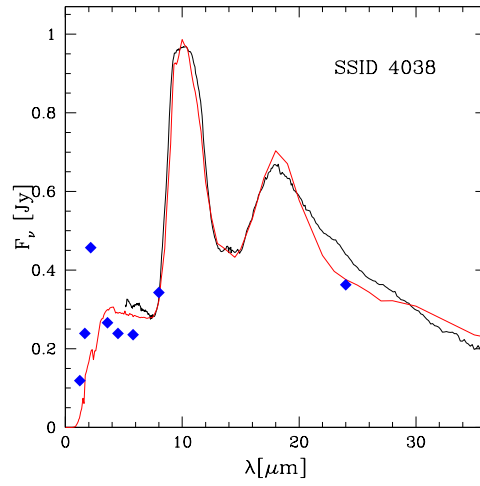
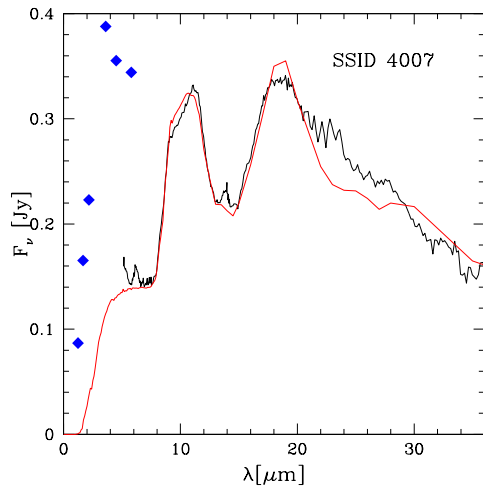


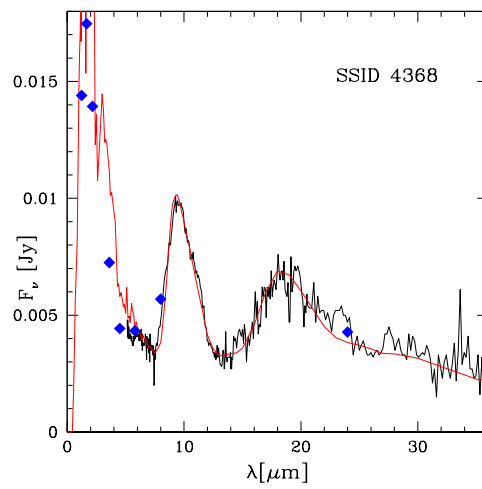
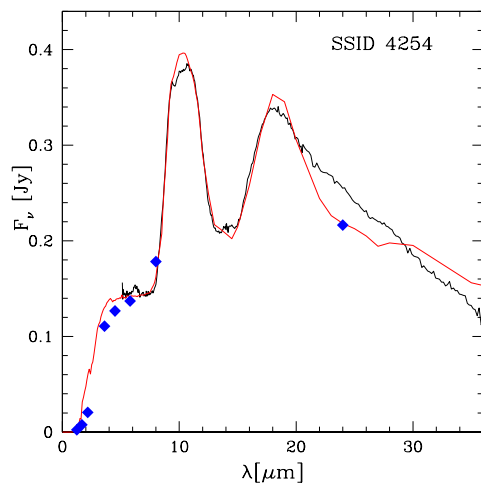
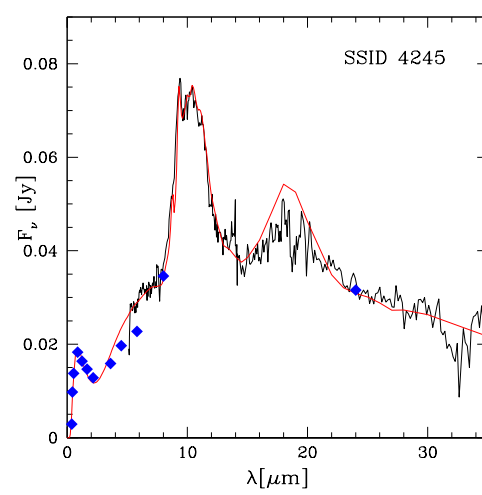
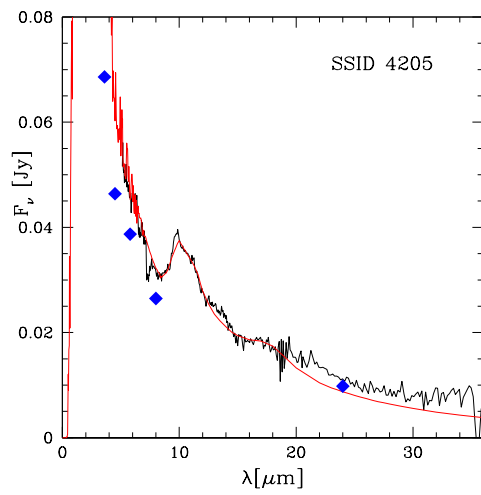
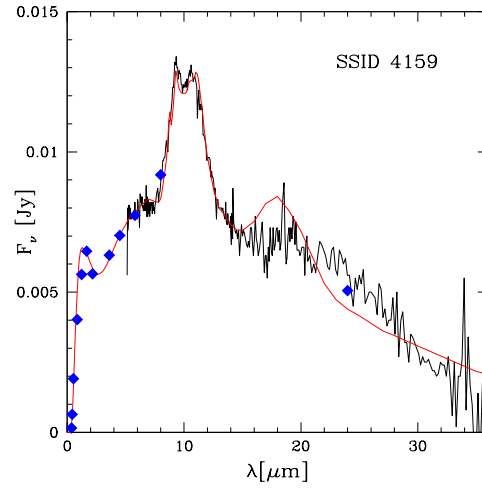
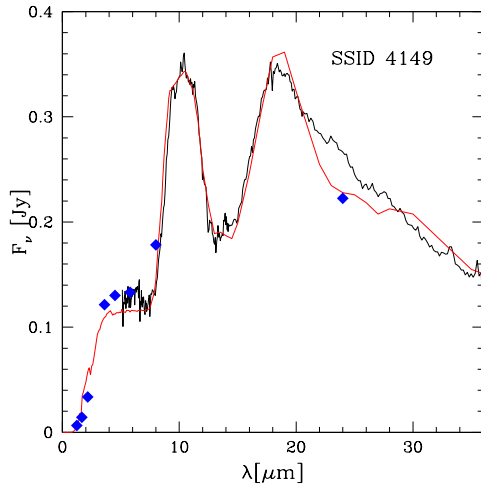


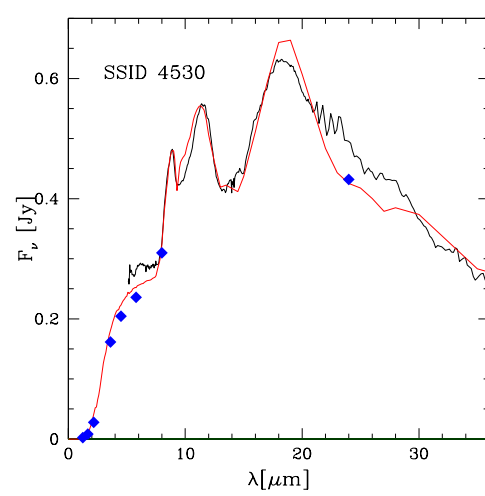
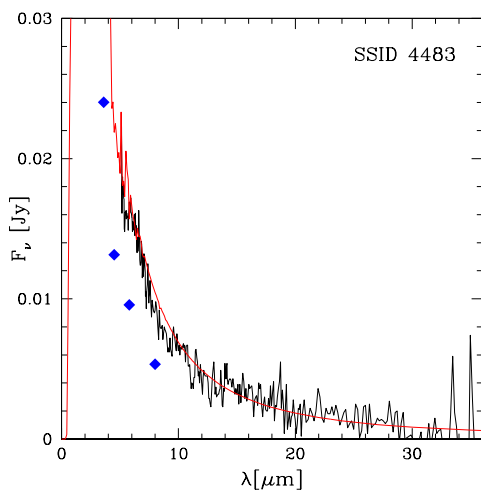
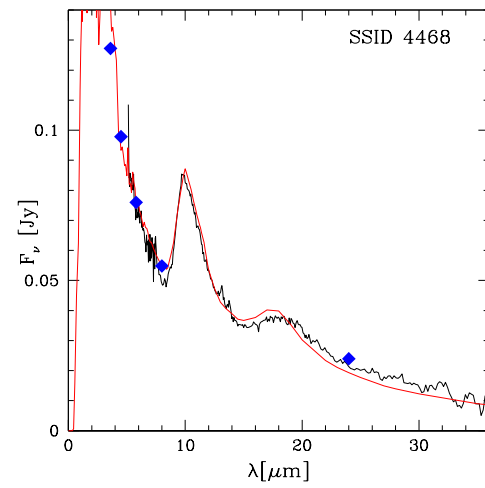
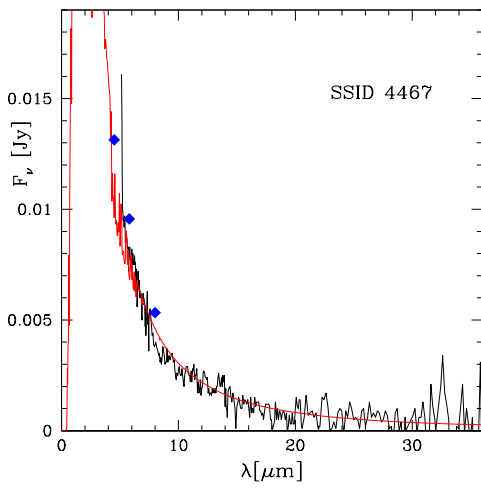
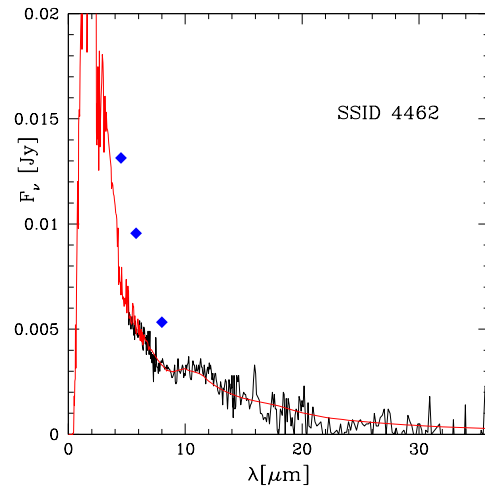
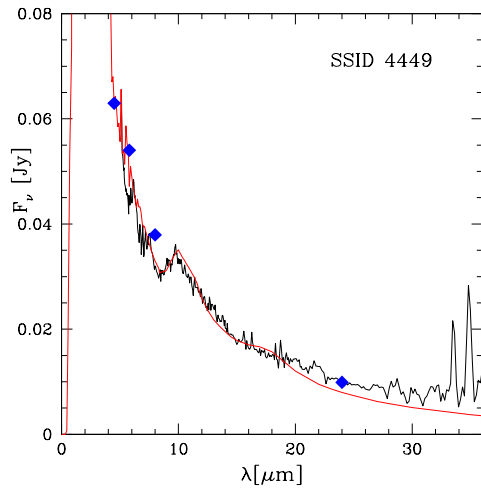


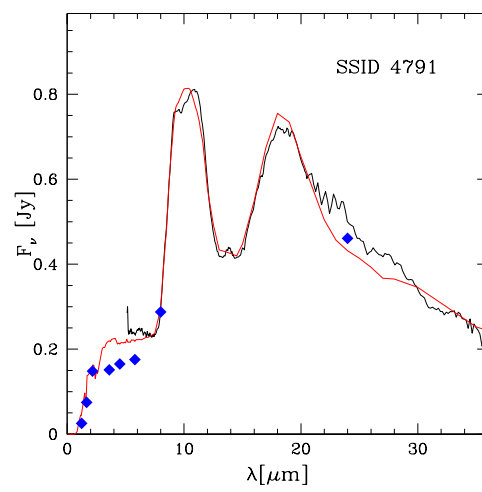
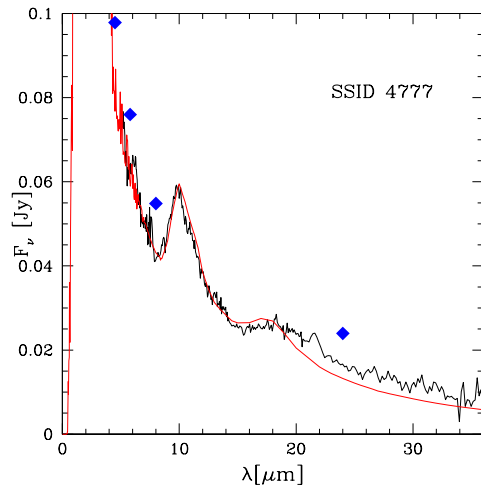
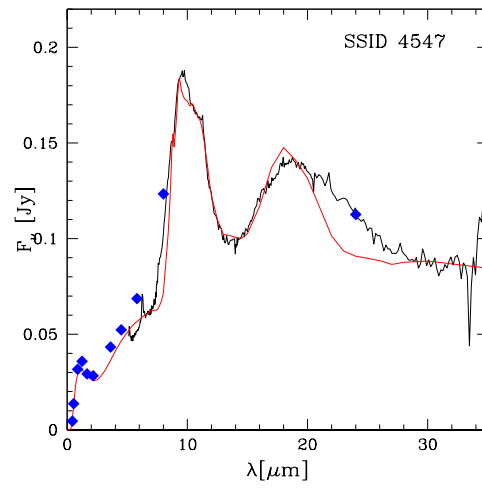
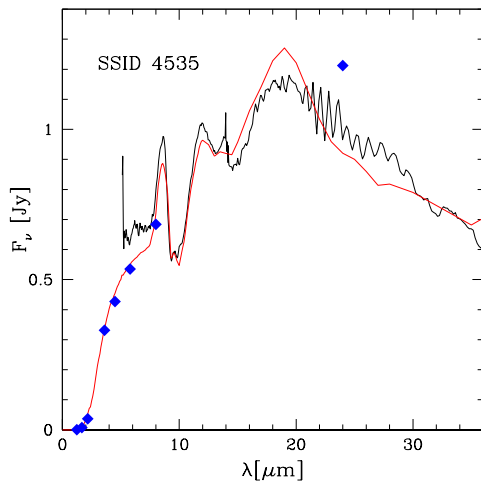


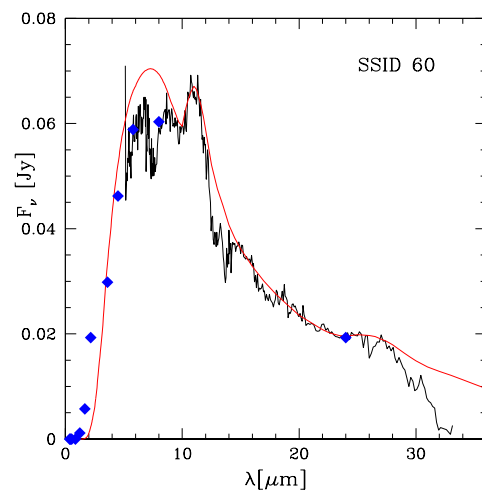
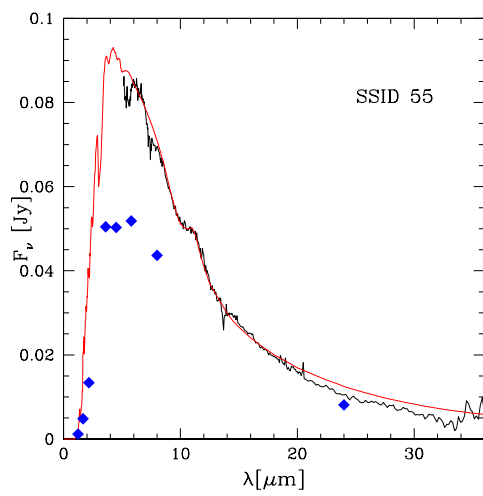
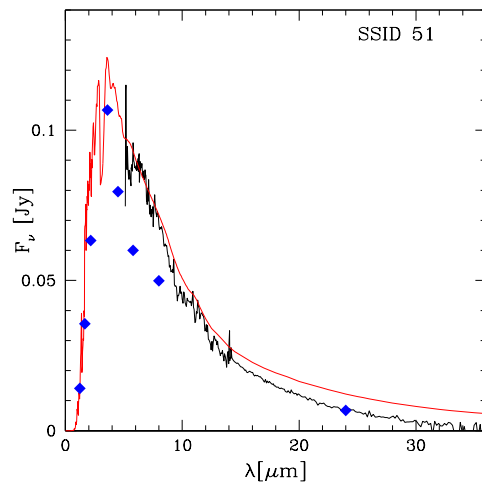
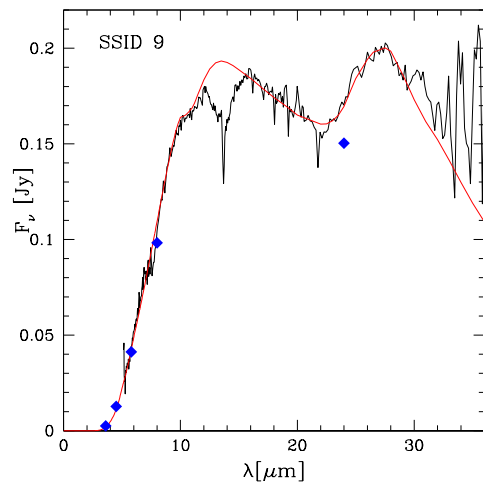
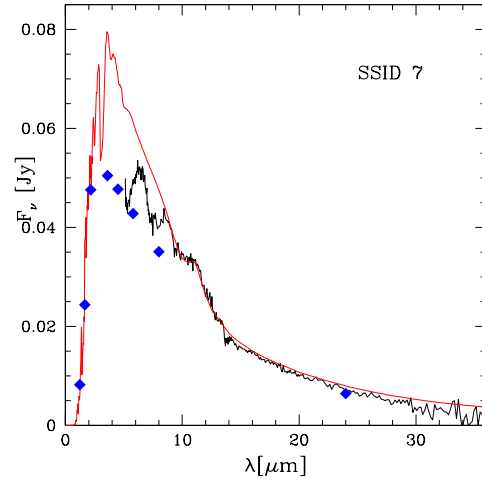
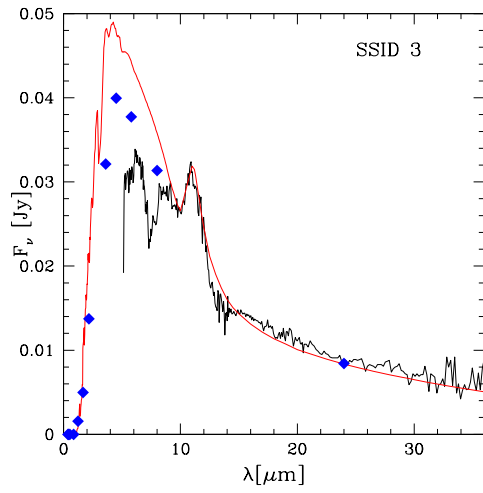


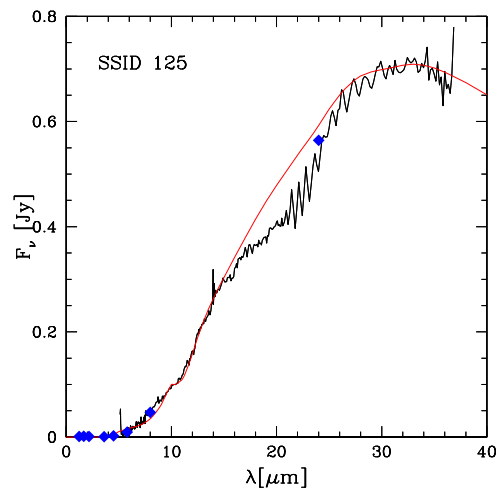
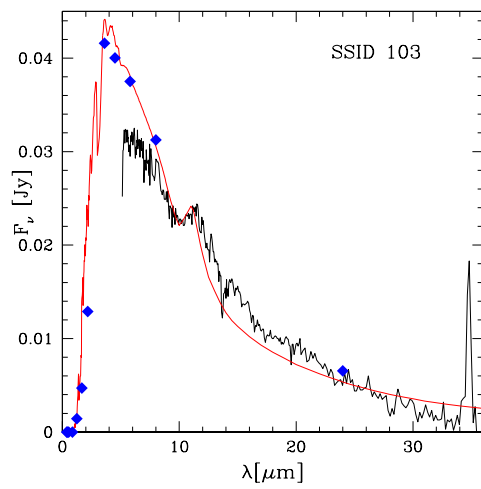
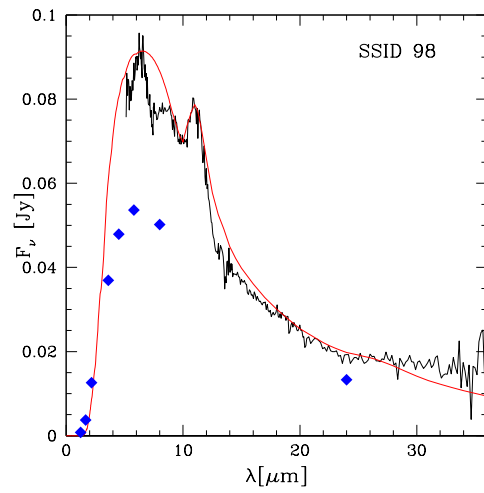
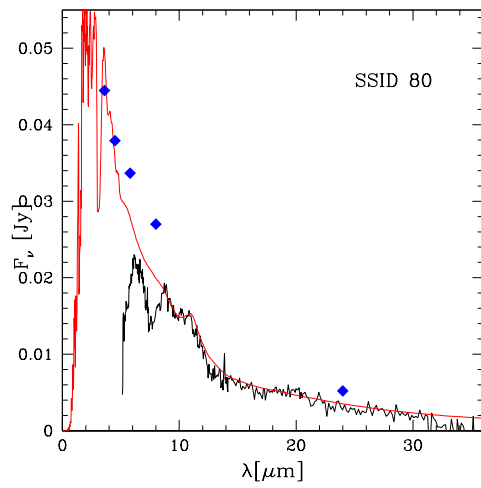
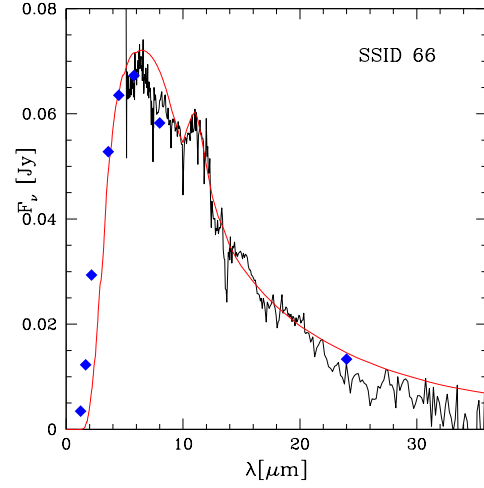
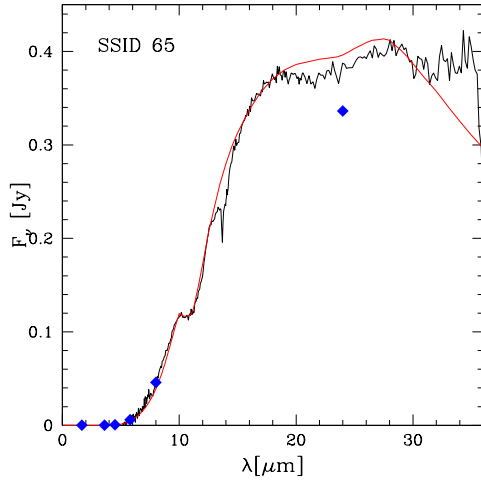


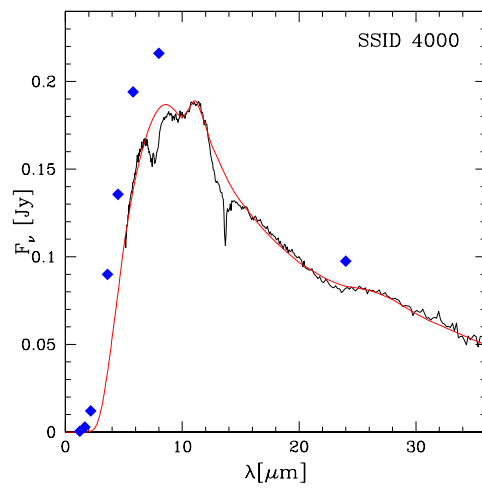
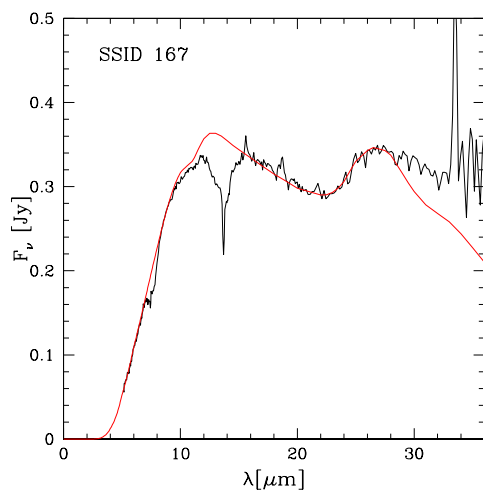
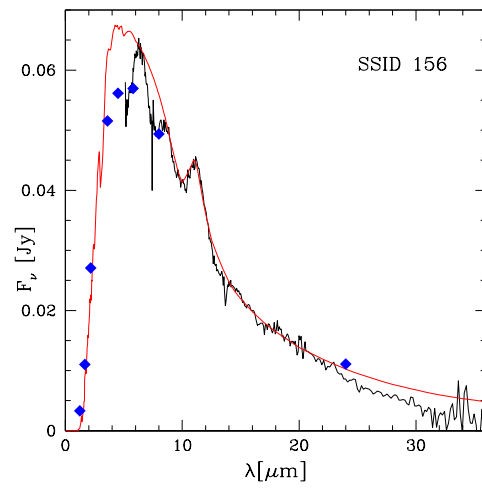
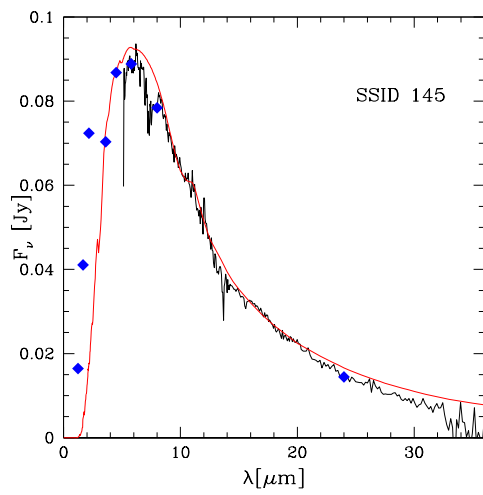
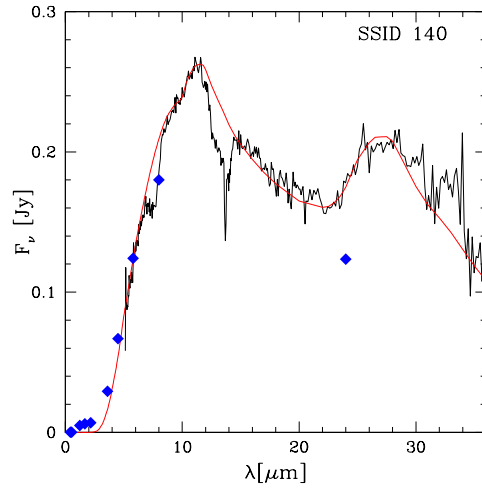
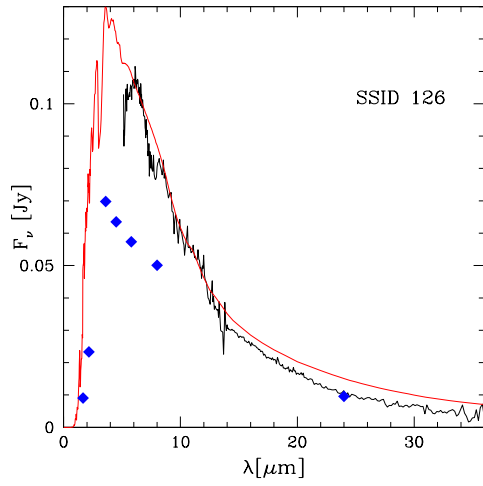


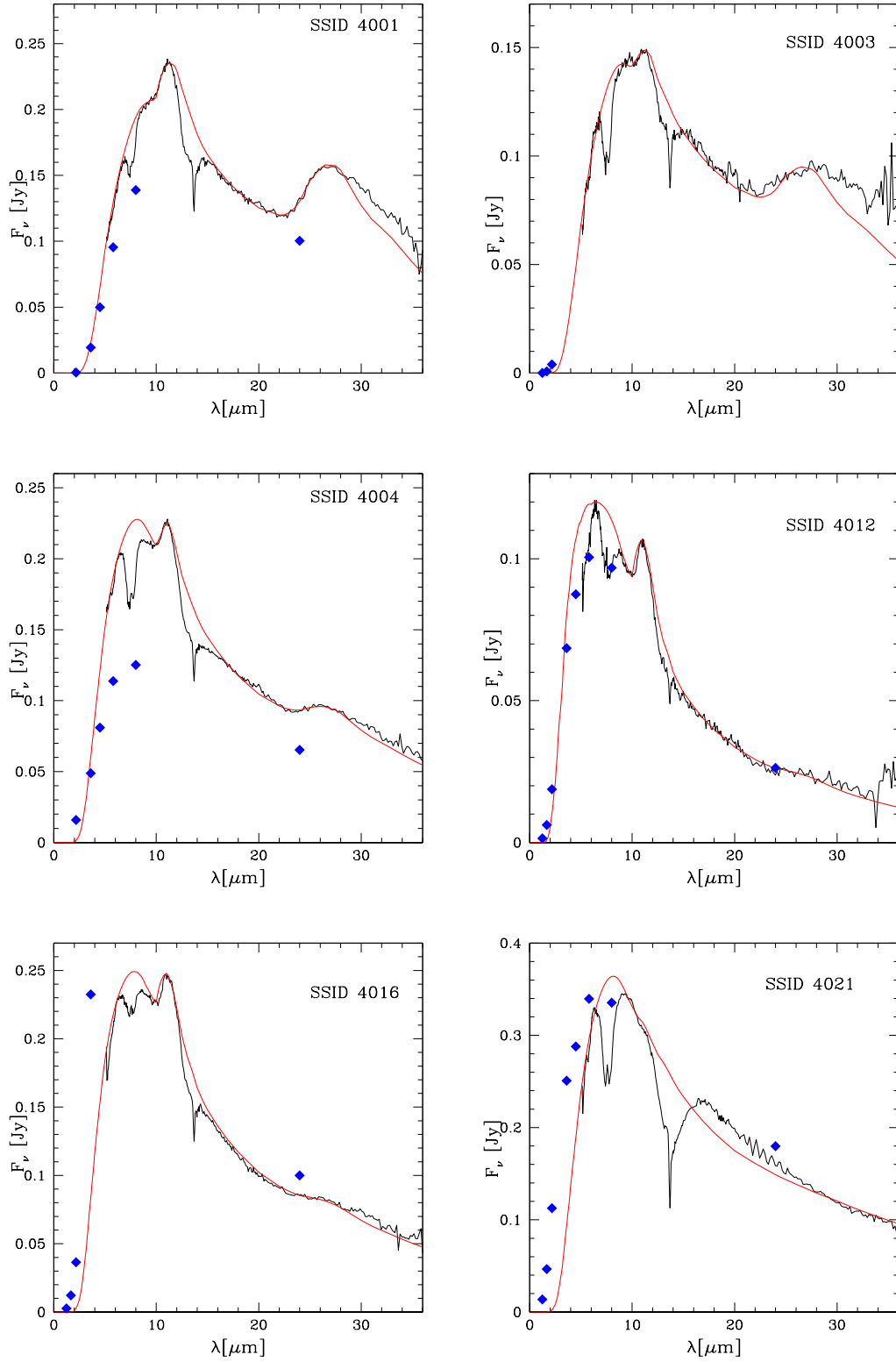


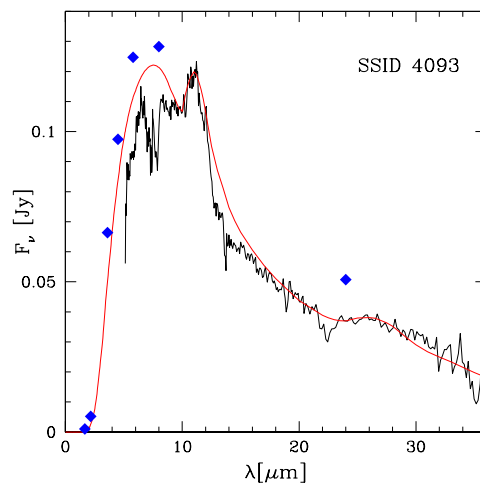
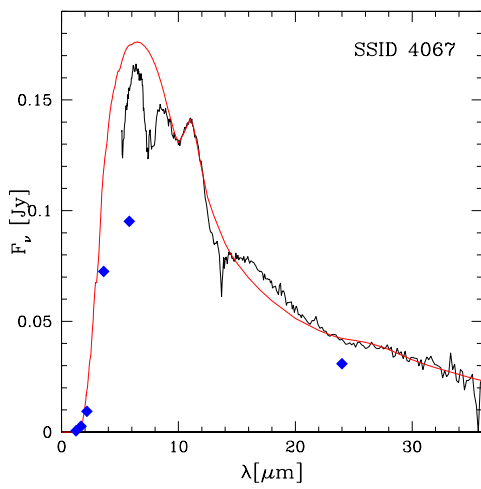
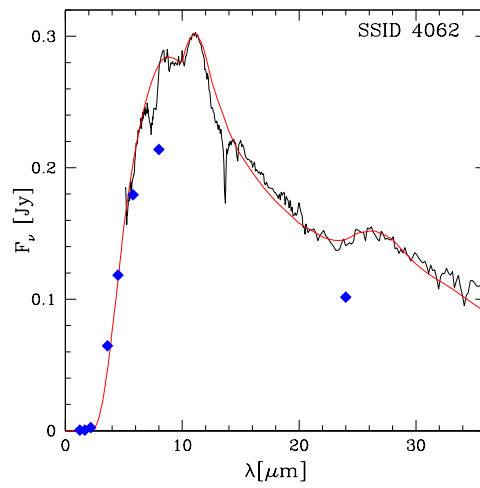
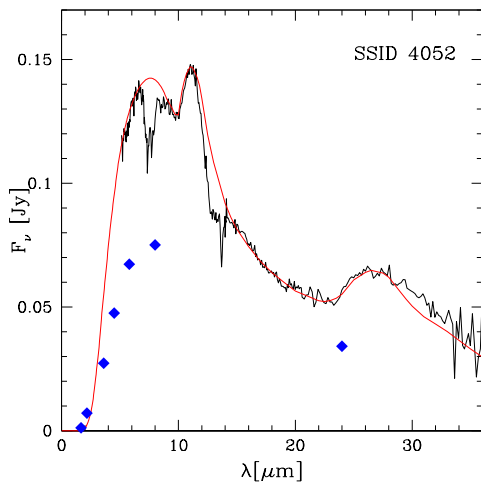
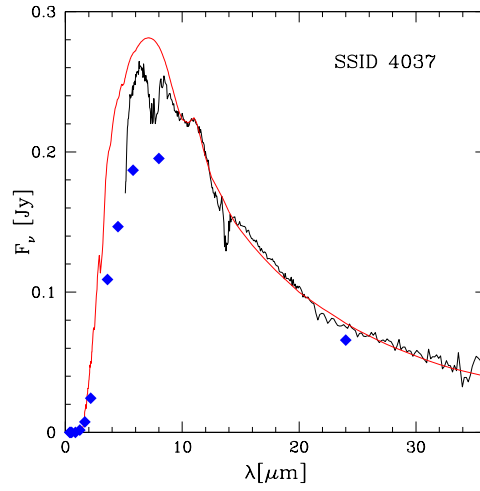
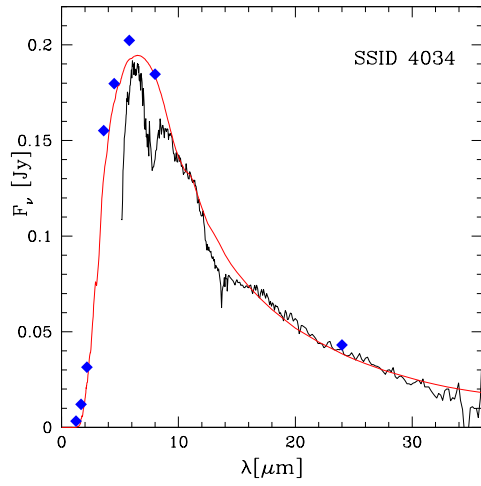


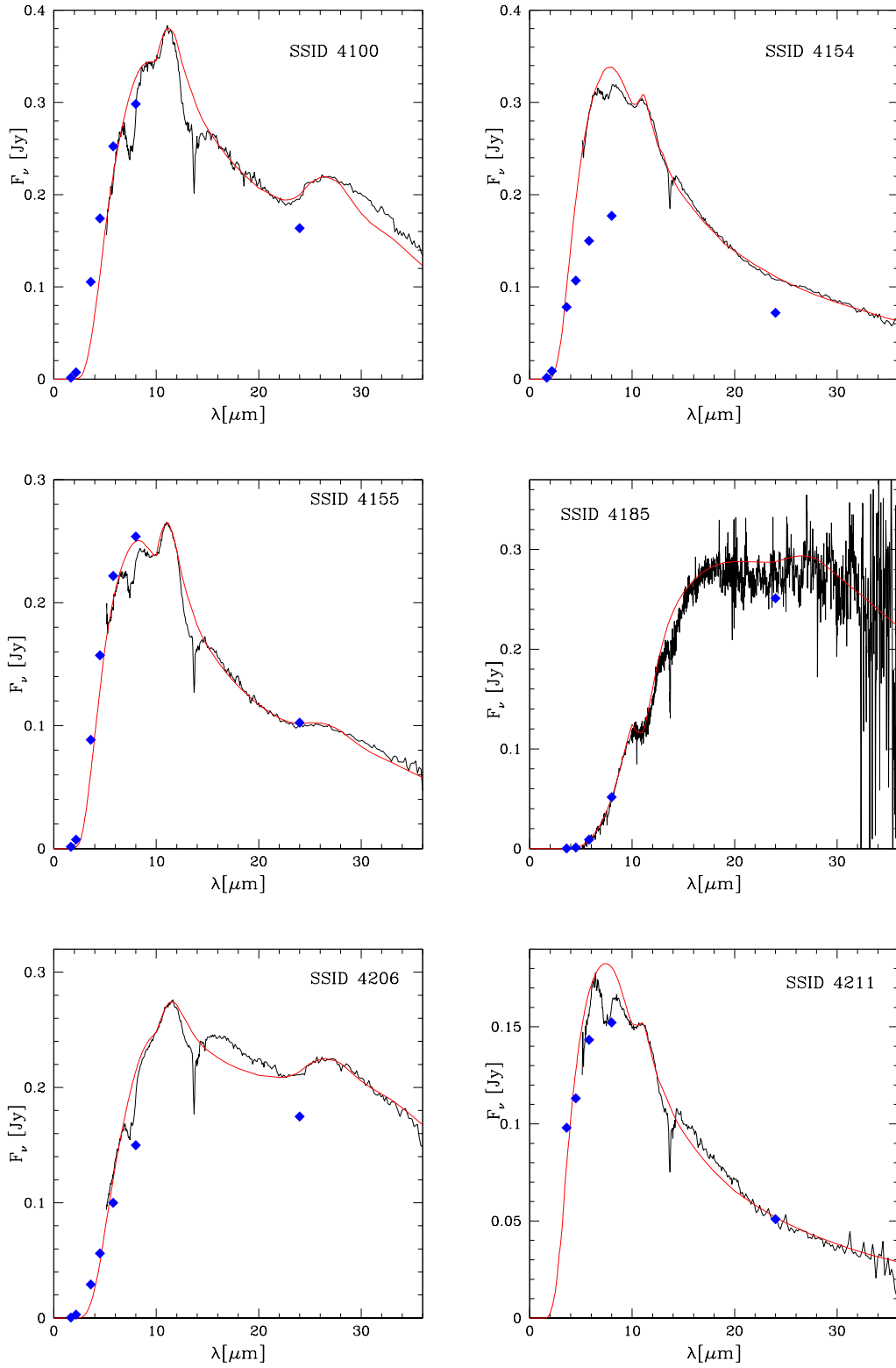


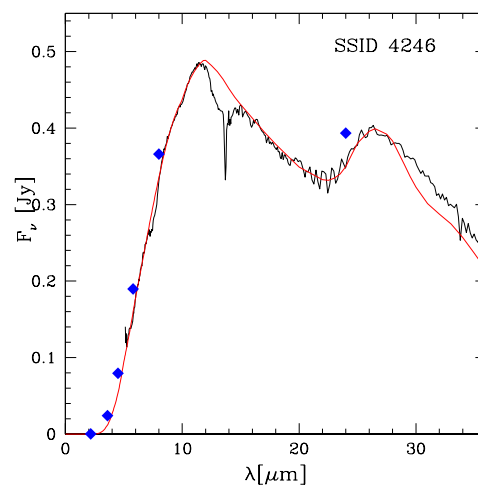
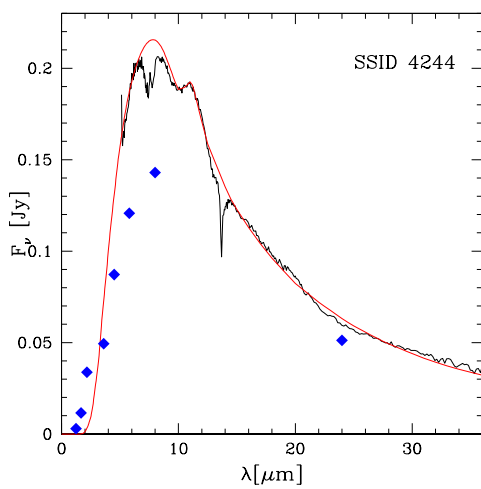
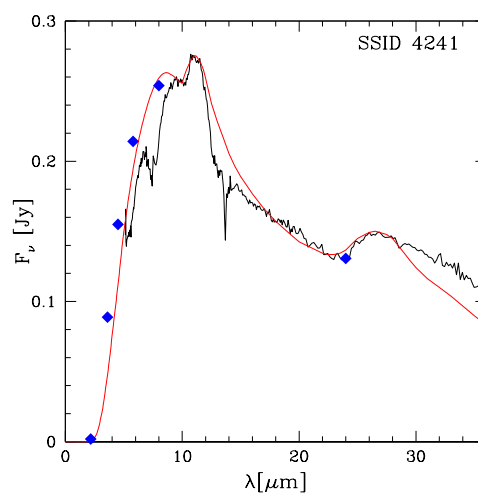
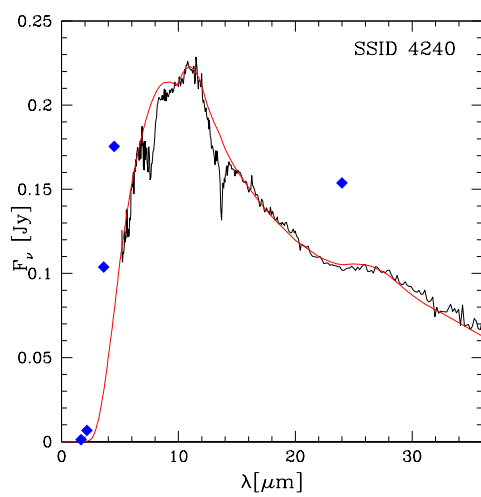
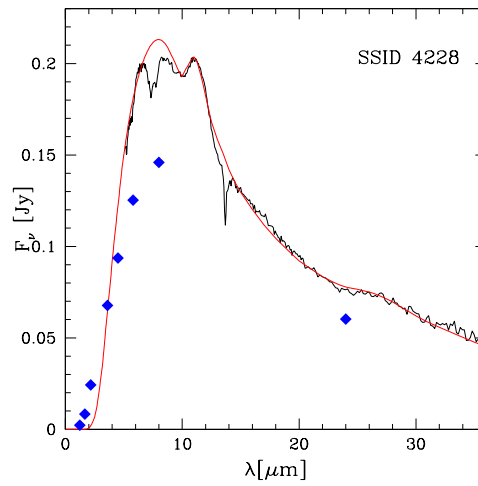
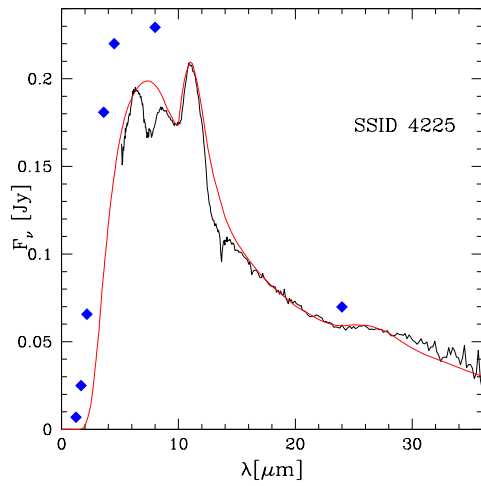


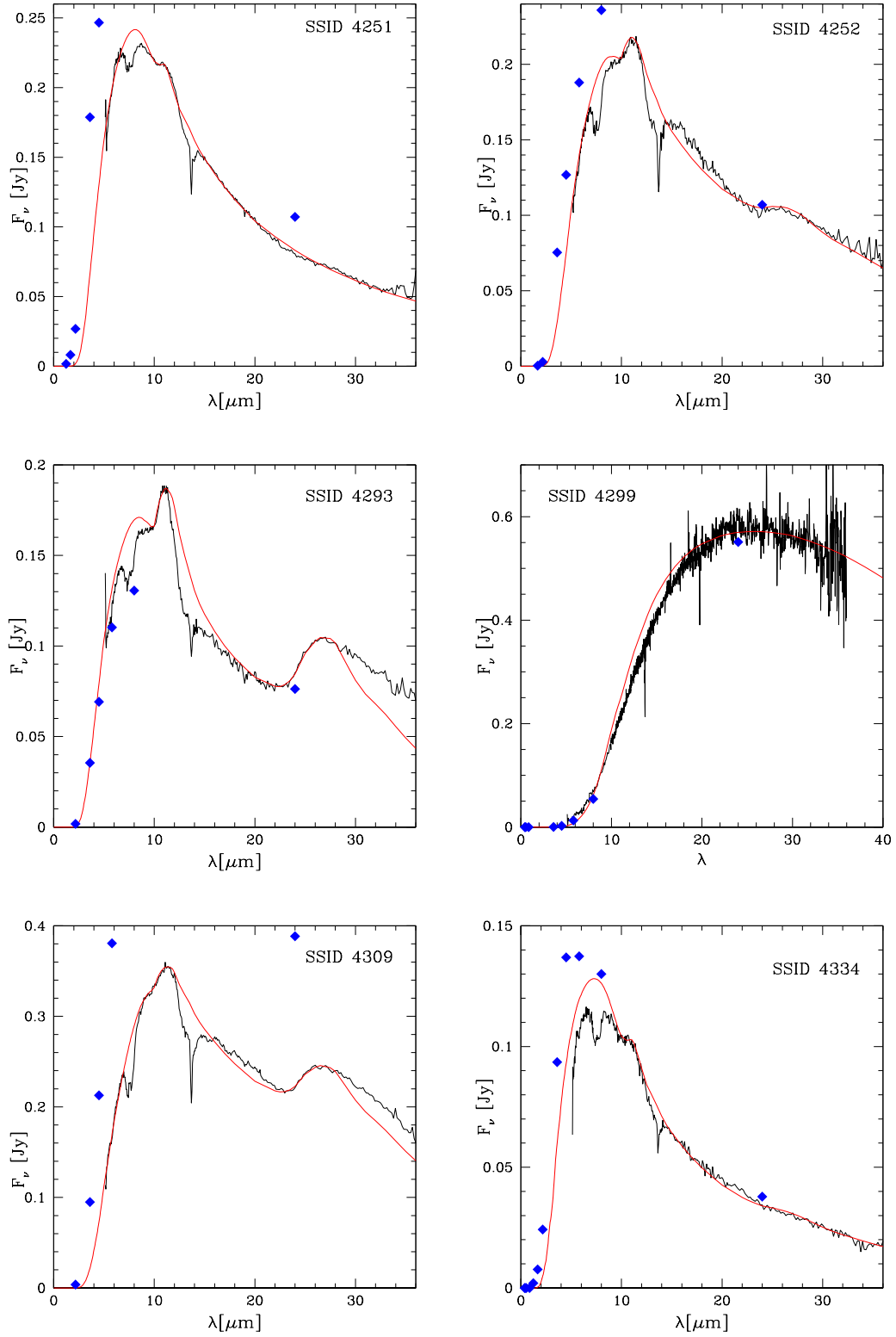


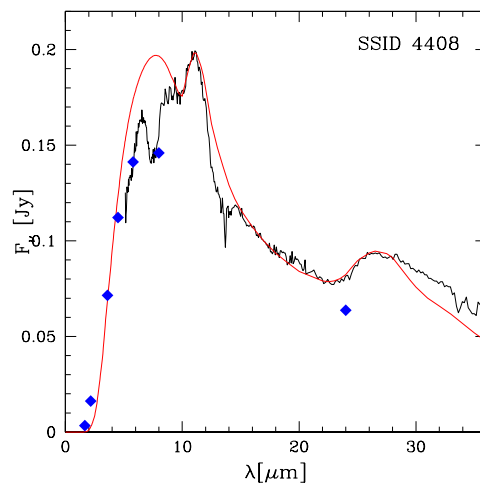
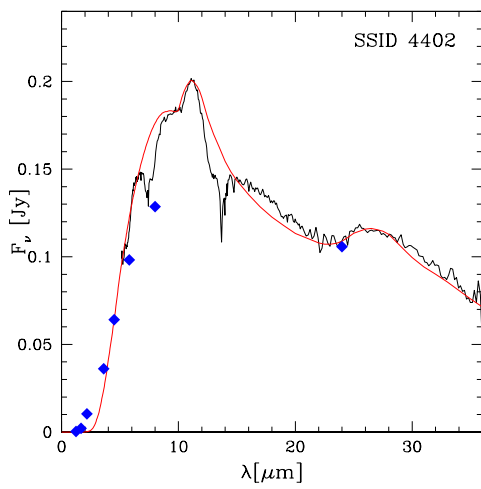
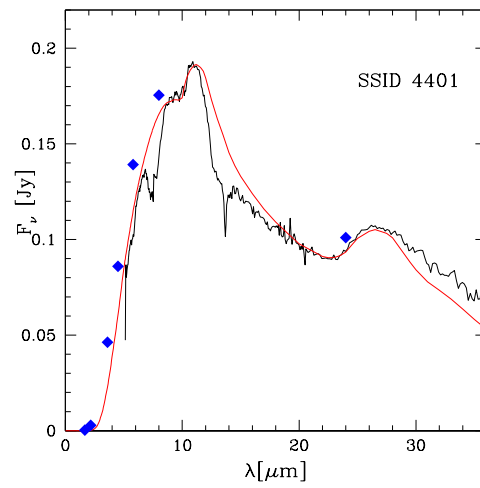
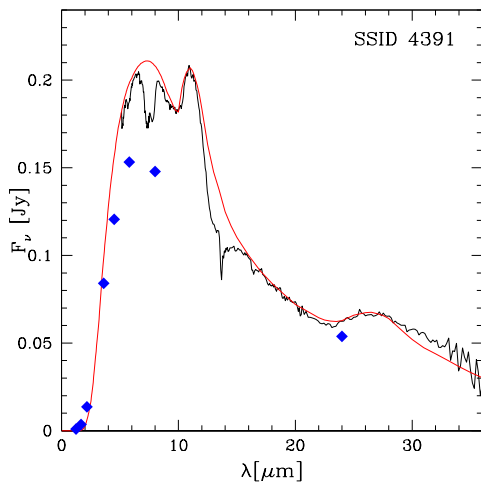
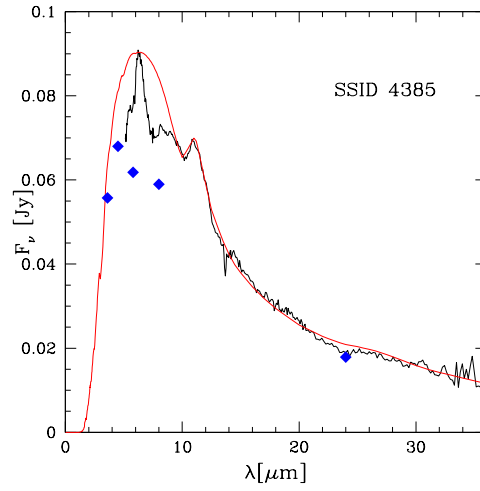
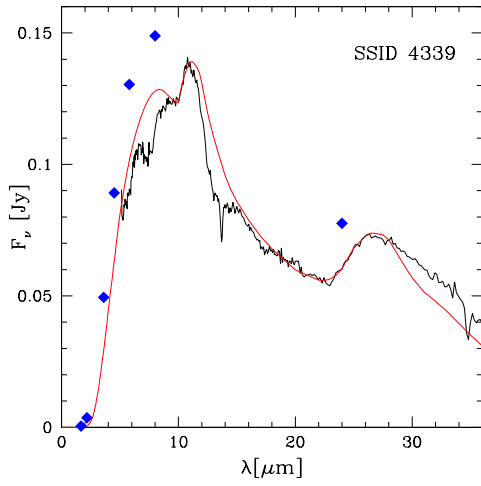


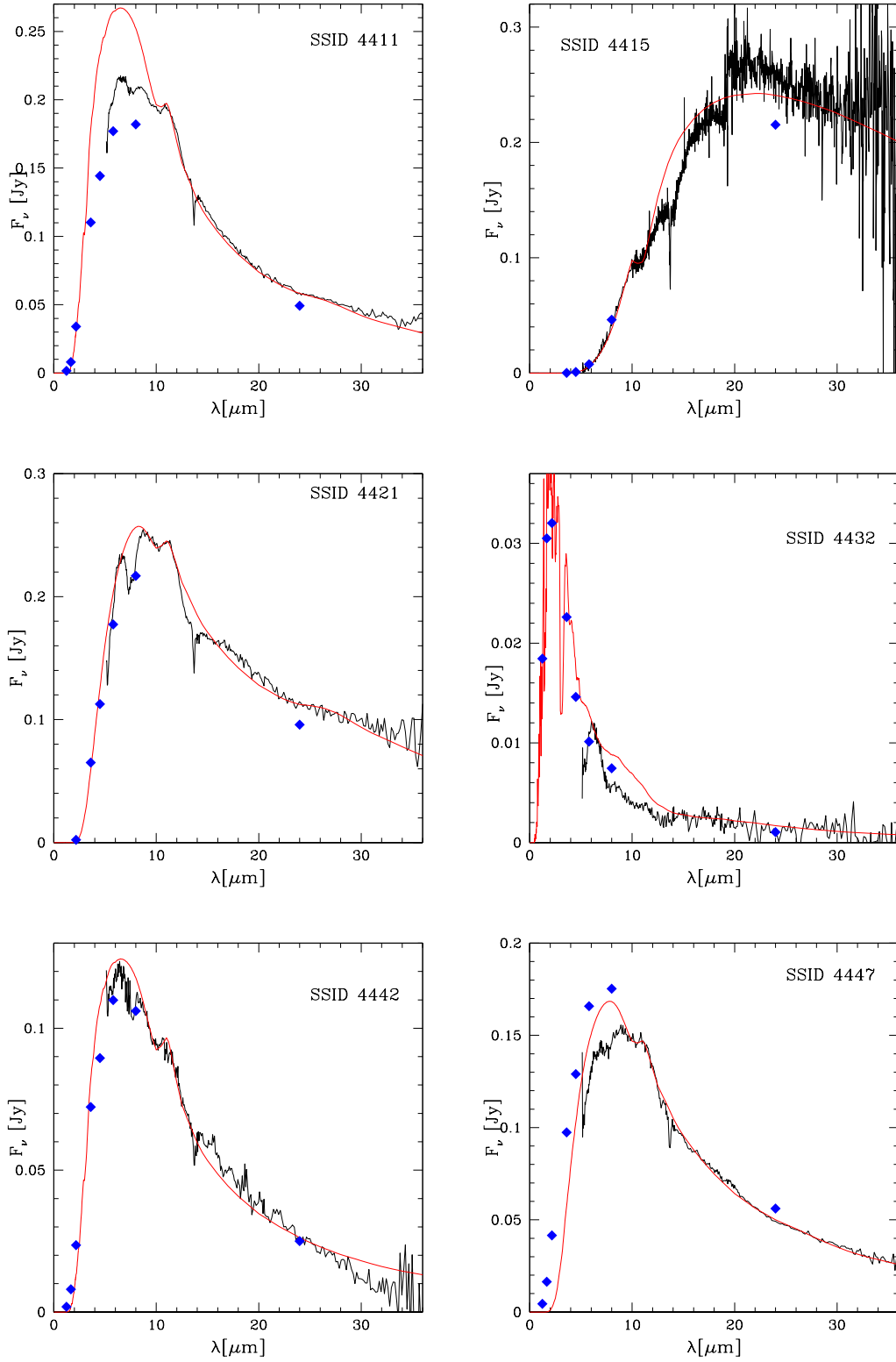


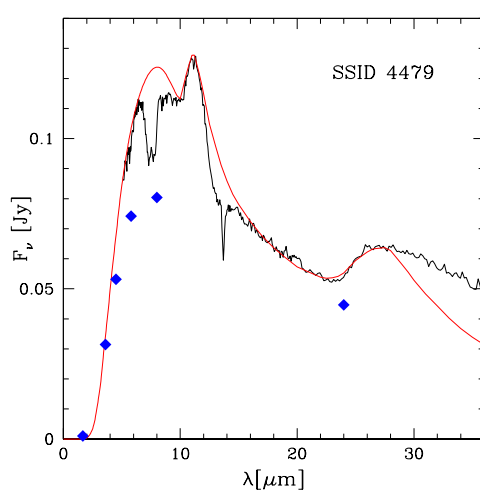
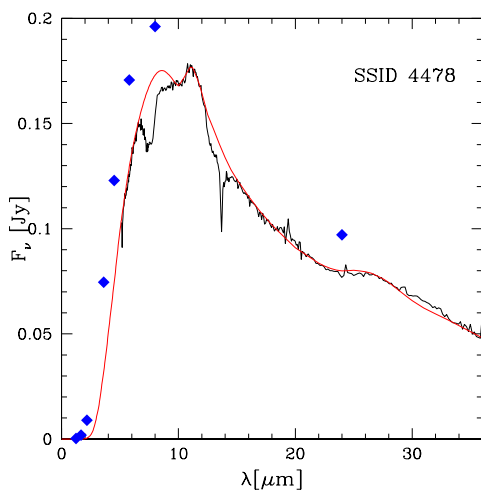
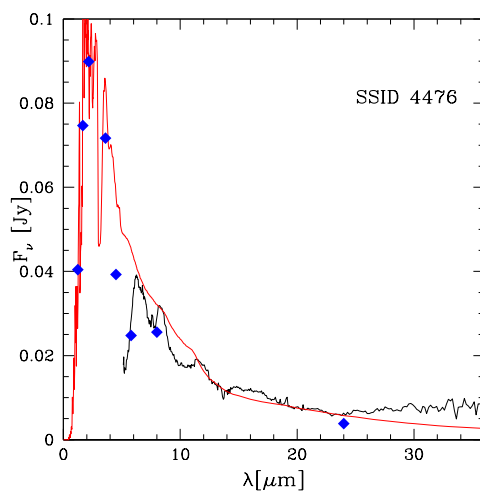
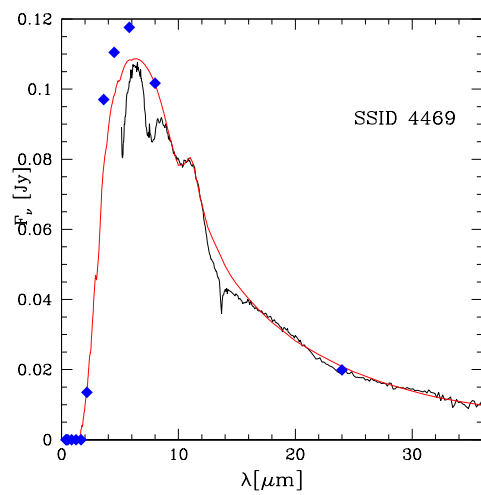
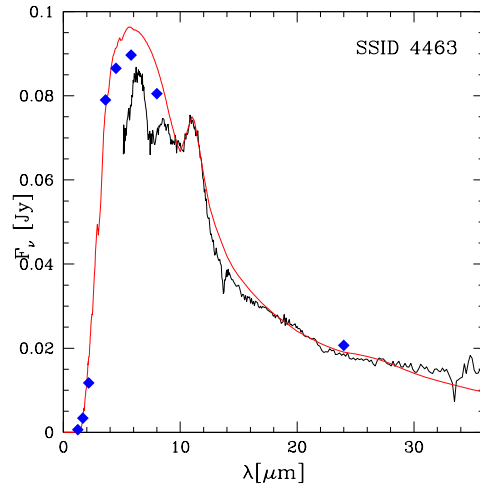
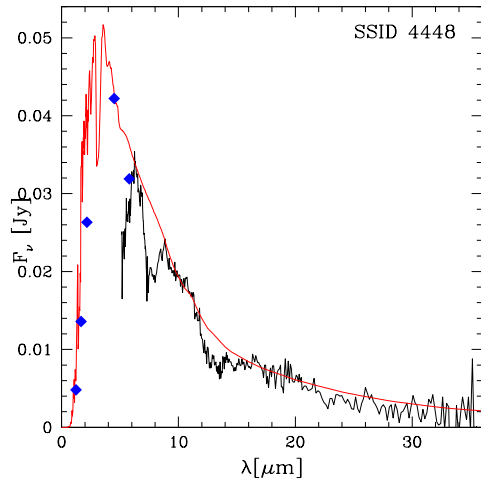


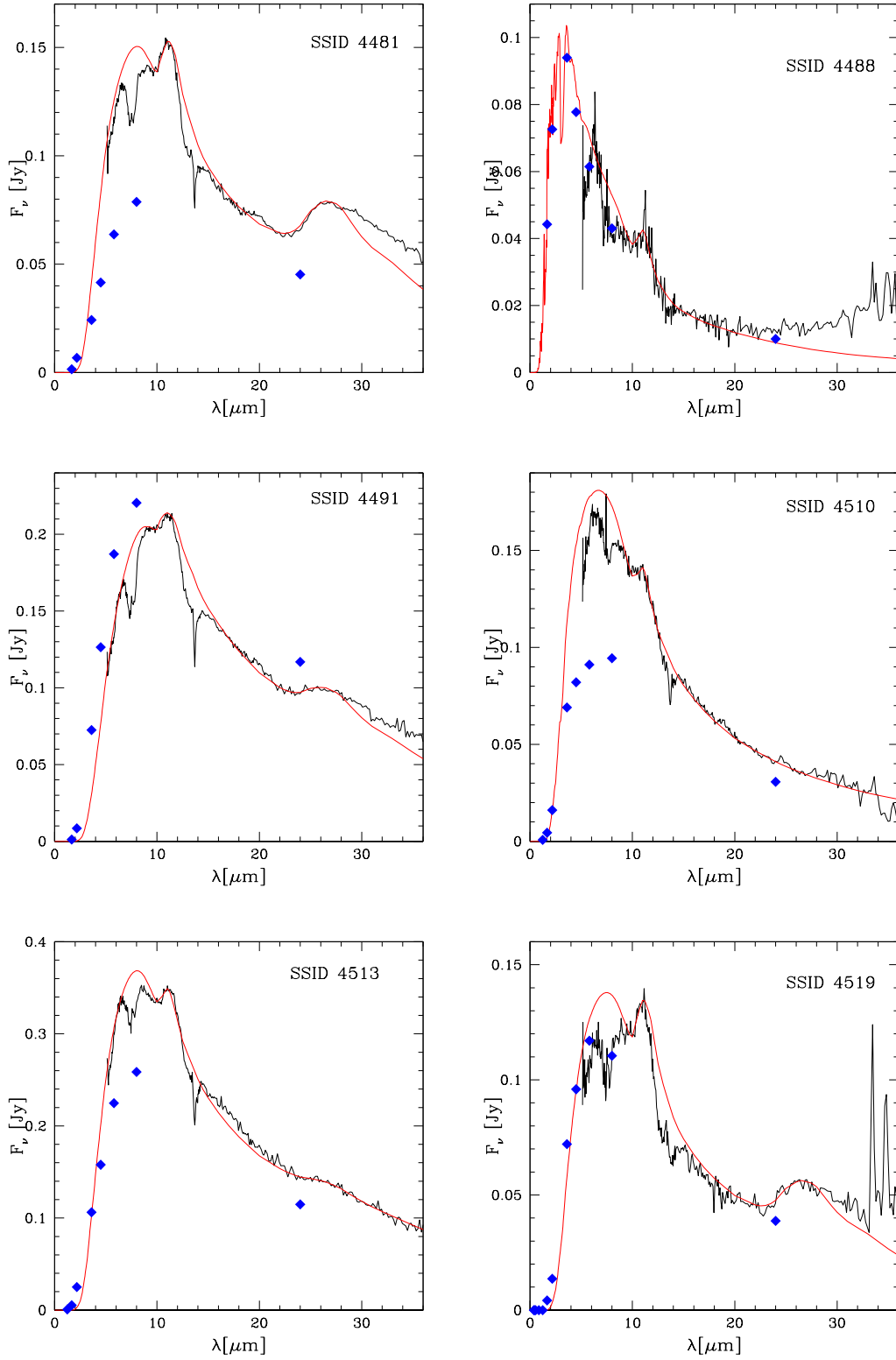


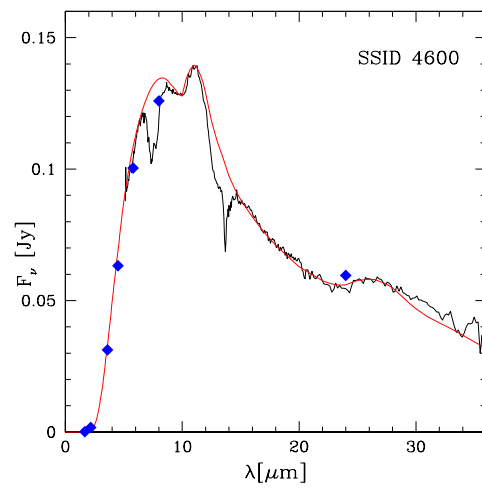
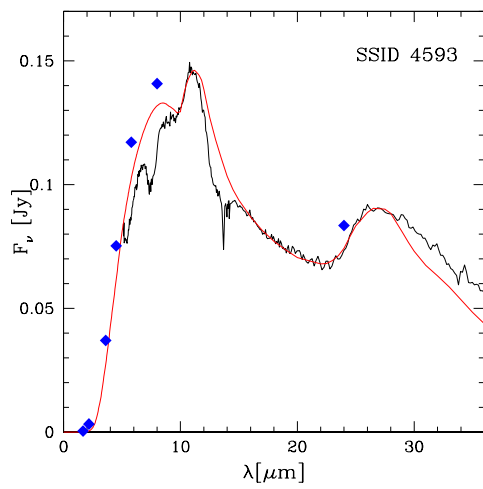
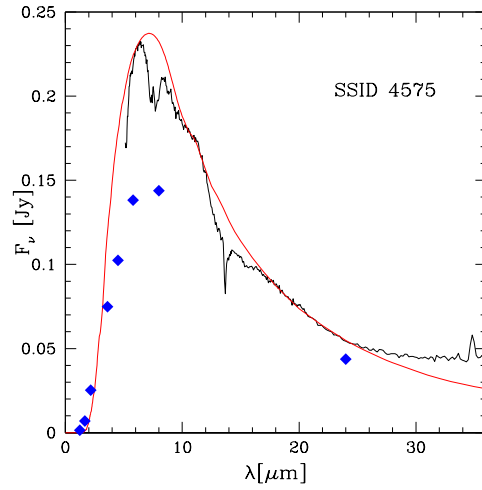
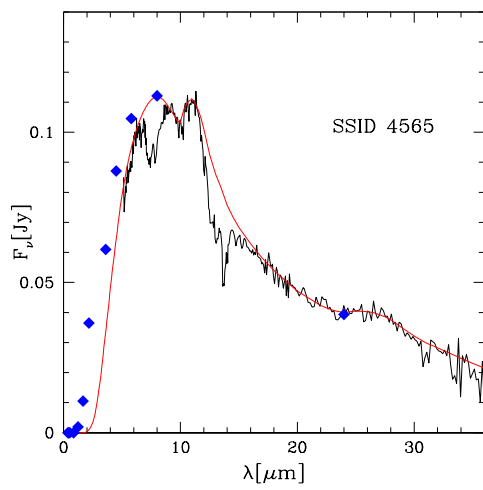
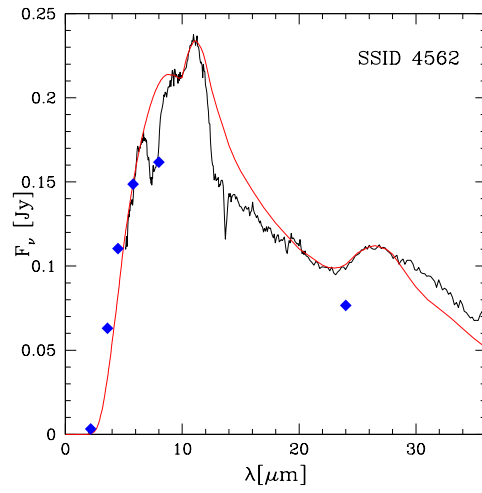
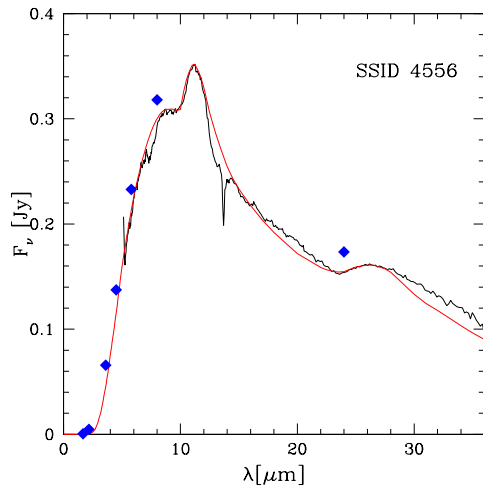


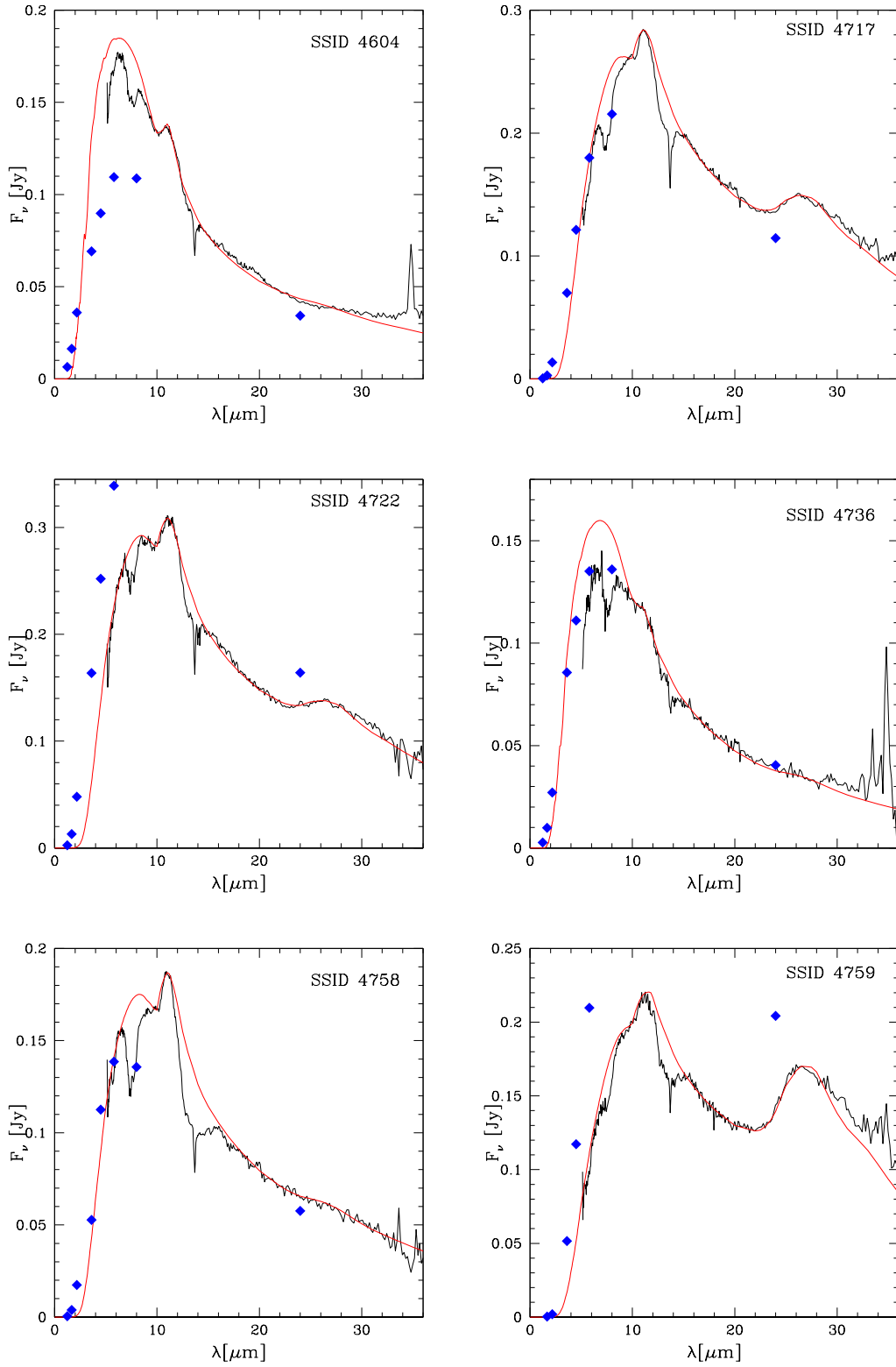


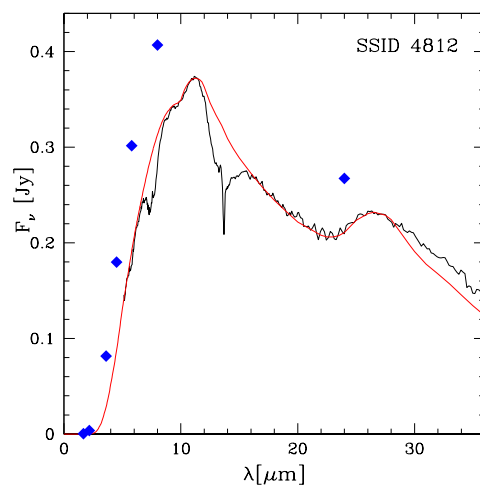
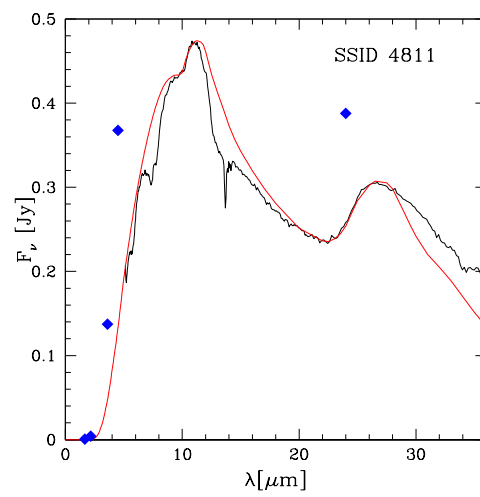
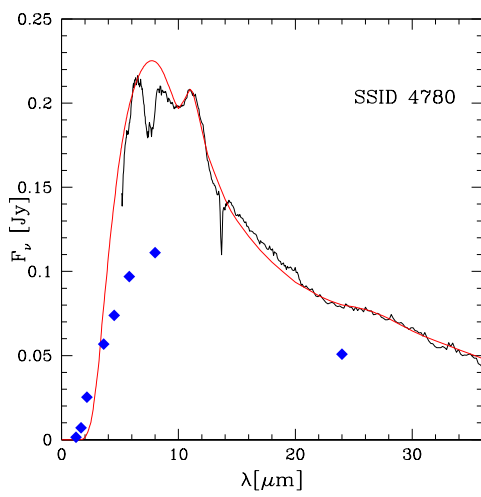
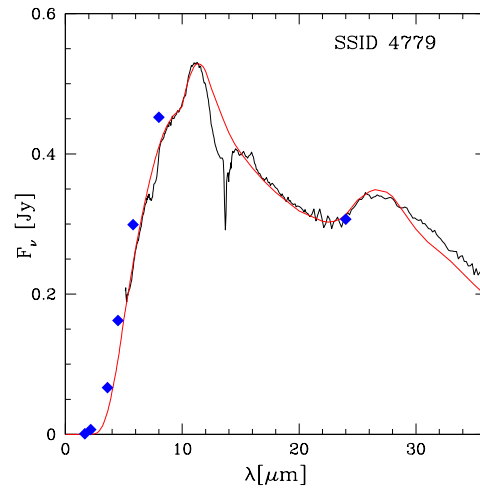
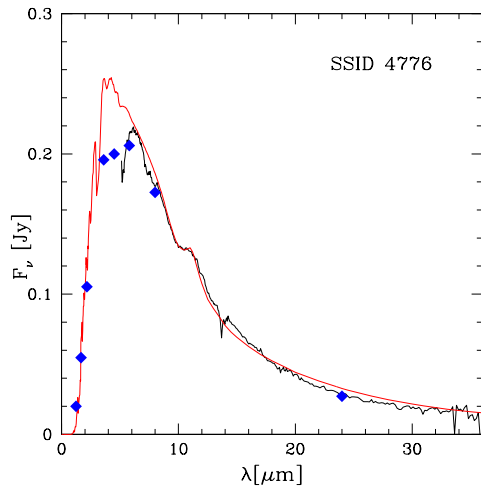












References

- Andersen, A. C., Höfner, S., & Gautschy-Loidl, R. (2003). Dust formation in winds of long-period variables. V. The influence of micro-physical dust properties in carbon stars. *A&A*, 400, 981–992.
- Angulo, C., Arnould, M., Rayet, M., Descouvemont, P., Baye, D., Leclercq-Willain, C., Coc, A., Barhoumi, S., Aguer, P., Rolfs, C., Kunz, R., Hammer, J. W., Mayer, A., Paradellis, T., Kossionides, S., Chronidou, C., Spyrou, K., degl’Innocenti, S., Fiorentini, G., Ricci, B., Zavatarelli, S., Providencia, C., Wolters, H., Soares, J., Grama, C., Rahighi, J., Shotter, A., & Laméhi Rachti, M. (1999). A compilation of charged-particle induced thermonuclear reaction rates. *NuPhA*, 656, 3–183.
- Aringer, B., Girardi, L., Nowotny, W., Marigo, P., & Lederer, M. T. (2009). Synthetic photometry for carbon rich giants. I. Hydrostatic dust-free models. *A&A*, 503, 913–928.
- Bell, K. R. & Lin, D. N. C. (1994). Using FU Orionis Outbursts to Constrain Self-regulated Protostellar Disk Models. *ApJ*, 427, 987.
- Bernard-Salas, J., Peeters, E., Sloan, G. C., Gutenkunst, S., Matsuura, M., Tielens, A. G. G. M., Zijlstra, A. A., & Houck, J. R. (2009). Unusual Dust Emission from Planetary Nebulae in the Magellanic Clouds. *ApJ*, 699, 1541–1552.
- Bertelli, G., Mateo, M., Chiosi, C., & Bressan, A. (1992). The Star Formation History of the Large Magellanic Cloud. *ApJ*, 388, 400.
- Bladh, S., Eriksson, K., Marigo, P., Liljegren, S., & Aringer, B. (2019). Carbon star wind models at solar and sub-solar metallicities: a comparative study. I. Mass loss and the properties of dust-driven winds. *A&A*, 623, A119.
- Bloecker, T. (1995). Stellar evolution of low and intermediate-mass stars. I. Mass loss on the AGB and its consequences for stellar evolution. *A&A*, 297, 727.
- Bloecker, T. & Schoenberner, D. (1991). A 7M AGB model sequence not complying with the core mass-luminosity relation. *A&A*, 244, L43–L46.
- Blum, R. D., Mould, J. R., Olsen, K. A., Frogel, J. A., Werner, M., Meixner, M., Markwick-Kemper, F., Indebetouw, R., Whitney, B., Meade, M., Babler, B., Churchwell, E. B., Gordon, K., Engelbracht, C., For, B. Q., Misselt, K., Vih, U., Leitherer, C., Volk, K., Points, S., Reach, W., Hora, J. L., Bernard, J. P., Boulanger, F., Bracker, S., Cohen, M., Fukui, Y., Gallagher, J., Gorjian, V., Harris, J., Kelly, D., Kawamura, A., Latter, W. B., Madden, S., Mizuno, A., Mizuno, N., Nota, A., Oey, M. S., Onishi, T., Paladini,

- R., Panagia, N., Perez-Gonzalez, P., Shibai, H., Sato, S., Smith, L., Staveley-Smith, L., Tielens, A. G. G. M., Ueta, T., Van Dyk, S., & Zaritsky, D. (2006). Spitzer SAGE Survey of the Large Magellanic Cloud. II. Evolved Stars and Infrared Color-Magnitude Diagrams. *AJ*, 132, 2034–2045.
- Bolatto, A. D., Leroy, A. K., Jameson, K., Ostriker, E., Gordon, K., Lawton, B., Stanimirović, S., Israel, F. P., Madden, S. C., Hony, S., Sandstrom, K. M., Bot, C., Rubio, M., Winkler, P. F., Roman-Duval, J., van Loon, J. T., Oliveira, J. M., & Indebetouw, R. (2011). The State of the Gas and the Relation between Gas and Star Formation at Low Metallicity: The Small Magellanic Cloud. *ApJ*, 741, 12.
- Boothroyd, A. I. & Sackmann, I. J. (1988). Low-Mass Stars. III. Low-Mass Stars with Steady Mass Loss: Up to the Asymptotic Giant Branch and through the Final Thermal Pulses. *ApJ*, 328, 653.
- Boothroyd, A. I., Sackmann, I. J., & Ahern, S. C. (1993). Prevention of High-Luminosity Carbon Stars by Hot Bottom Burning. *ApJ*, 416, 762.
- Bouchet, P., García-Marín, M., Lagage, P. O., Amiaux, J., Auguères, J. L., Bauwens, E., Blommaert, J. A. D. L., Chen, C. H., Detre, Ö. H., Dicken, D., Dubreuil, D., Galdemard, P., Gastaud, R., Glasse, A., Gordon, K. D., Gougnaud, F., Guillard, P., Justtanont, K., Krause, O., Leboeuf, D., Longval, Y., Martin, L., Mazy, E., Moreau, V., Olofsson, G., Ray, T. P., Rees, J. M., Renotte, E., Ressler, M. E., Ronayette, S., Salasca, S., Scheithauer, S., Sykes, J., Thelen, M. P., Wells, M., Wright, D., & Wright, G. S. (2015). The Mid-Infrared Instrument for the James Webb Space Telescope, III: MIRIM, The MIRI Imager. *PASP*, 127, 612.
- Bowen, G. H. (1988). Dynamical Modeling of Long-Period Variable Star Atmospheres. *ApJ*, 329, 299.
- Boyer, M. L., Girardi, L., Marigo, P., Williams, B. F., Aringer, B., Nowotny, W., Rosenfield, P., Dorman, C. E., Guhathakurta, P., Dalcanton, J. J., Melbourne, J. L., Olsen, K. A. G., & Weisz, D. R. (2013). Is There a Metallicity Ceiling to Form Carbon Stars?—A Novel Technique Reveals a Scarcity of C stars in the Inner M31 Disk. *ApJ*, 774, 83.
- Boyer, M. L., McQuinn, K. B. W., Barmby, P., Bonanos, A. Z., Gehrz, R. D., Gordon, K. D., Groenewegen, M. A. T., Lagadec, E., Lennon, D., Marengo, M., McDonald, I., Meixner, M., Skillman, E., Sloan, G. C., Sonneborn, G., van Loon, J. T., & Zijlstra, A. (2015a). An Infrared Census of DUST in Nearby Galaxies with Spitzer (DUSTiNGS). II. Discovery of Metal-poor Dusty AGB Stars. *ApJ*, 800, 51.
- Boyer, M. L., McQuinn, K. B. W., Barmby, P., Bonanos, A. Z., Gehrz, R. D., Gordon, K. D., Groenewegen, M. A. T., Lagadec, E., Lennon, D., Marengo, M., Meixner, M., Skillman, E., Sloan, G. C., Sonneborn, G., van Loon, J. T., & Zijlstra, A. (2015b). An Infrared Census of Dust in nearby Galaxies with Spitzer (DUSTiNGS). I. Overview. *ApJS*, 216, 10.
- Boyer, M. L., McQuinn, K. B. W., Groenewegen, M. A. T., Zijlstra, A. A., Whitelock, P. A., van Loon, J. T., Sonneborn, G., Sloan, G. C., Skillman, E. D., Meixner, M., McDonald, I., Jones, O. C., Javadi, A., Gehrz, R. D., Britavskiy, N., & Bonanos, A. Z. (2017). An Infrared Census of DUST in Nearby Galaxies with Spitzer (DUSTiNGS). IV. Discovery of High-redshift AGB Analogs. *ApJ*, 851, 152.

- Boyer, M. L., Srinivasan, S., Riebel, D., McDonald, I., van Loon, J. T., Clayton, G. C., Gordon, K. D., Meixner, M., Sargent, B. A., & Sloan, G. C. (2012). The Dust Budget of the Small Magellanic Cloud: Are Asymptotic Giant Branch Stars the Primary Dust Source at Low Metallicity? *ApJ*, 748, 40.
- Bunzel, F., García-Hernández, D. A., Engels, D., Perea-Calderón, J. V., & García-Lario, P. (2009). AKARI/IRC Observations of Heavily Obscured Oxygen-Rich AGB and Post-AGB Stars. volume 418 (pp. 431).
- Busso, M., Gallino, R., & Wasserburg, G. J. (1999). Nucleosynthesis in Asymptotic Giant Branch Stars: Relevance for Galactic Enrichment and Solar System Formation. *ARA&A*, 37, 239–309.
- Cameron, A. G. W. & Fowler, W. A. (1971). Lithium and the s-PROCESS in Red-Giant Stars. *ApJ*, 164, 111.
- Canuto, V. M. & Mazzitelli, I. (1991). Stellar Turbulent Convection: A New Model and Applications. *ApJ*, 370, 295.
- Carrera, R., Gallart, C., Aparicio, A., Costa, E., Méndez, R. A., & Noël, N. E. D. (2008a). The Chemical Enrichment History of the Small Magellanic Cloud and its Gradients. *AJ*, 136, 1039–1048.
- Carrera, R., Gallart, C., Hardy, E., Aparicio, A., & Zinn, R. (2008b). The Chemical Enrichment History of the Large Magellanic Cloud. *AJ*, 135, 836–849.
- Cerrigone, L., Hora, J. L., Umana, G., & Trigilio, C. (2009). Spitzer Detection of Polycyclic Aromatic Hydrocarbons and Silicate Features in Post-AGB Stars and Young Planetary Nebulae. *ApJ*, 703, 585–600.
- Chan, S. J. & Kwok, S. (1988). The Transition from Oxygen-rich to Carbon Stars. *ApJ*, 334, 362.
- Cherchneff, I. (2006). A chemical study of the inner winds of asymptotic giant branch stars. *A&A*, 456, 1001–1012.
- Chiosi, C. (2009). Modelling convection and semiconvection in massive stars. *Communications in Asteroseismology*, 158, 79.
- Cignoni, M., Cole, A. A., Tosi, M., Gallagher, J. S., Sabbi, E., Anderson, J., Grebel, E. K., & Nota, A. (2013). Mean Age Gradient and Asymmetry in the Star Formation History of the Small Magellanic Cloud. *ApJ*, 775, 83.
- Cioni, M. R. L. & Habing, H. J. (2003). AGB stars in the Magellanic Clouds. I. The C/M ratio. *A&A*, 402, 133–140.
- Cloutman, L. D. & Eoll, J. G. (1976). Comments on the diffusion model of turbulent mixing. *ApJ*, 206, 548–554.
- Conroy, C., Gunn, J. E., & White, M. (2009). The Propagation of Uncertainties in Stellar Population Synthesis Modeling. I. The Relevance of Uncertain Aspects of Stellar Evolution and the Initial Mass Function to the Derived Physical Properties of Galaxies. *ApJ*, 699, 486–506.

- Dell'Agli, F. (2012). Stars in the asymptotic giant branch: dust production and interpretation of infrared observations. In *PhD Thesis*.
- Dell'Agli, F., Di Criscienzo, M., Boyer, M. L., & García-Hernández, D. A. (2016). Evolved stars in the Local Group galaxies - I. AGB evolution and dust production in IC 1613. *MNRAS*, 460, 4230–4241.
- Dell'Agli, F., Di Criscienzo, M., García-Hernández, D. A., Ventura, P., Limongi, M., Marini, E., & Jones, O. C. (2019a). Evolved stars in the Local Group galaxies - III. AGB and RSG stars in Sextans A. *MNRAS*, 482, 4733–4743.
- Dell'Agli, F., Di Criscienzo, M., Ventura, P., Limongi, M., García-Hernández, D. A., Marini, E., & Rossi, C. (2018a). Evolved stars in the Local Group galaxies - II. AGB, RSG stars, and dust production in IC10. *MNRAS*, 479, 5035–5048.
- Dell'Agli, F., García-Hernández, D. A., Rossi, C., Ventura, P., Di Criscienzo, M., & Schneider, R. (2014a). On the alumina dust production in the winds of O-rich asymptotic giant branch stars. *MNRAS*, 441, 1115–1125.
- Dell'Agli, F., García-Hernández, D. A., Ventura, P., Mészáros, S., Masseron, T., Fernández-Trincado, J. G., Tang, B., Shetrone, M., Zamora, O., & Lucatello, S. (2018b). A view of the H-band light-element chemical patterns in globular clusters under the AGB self-enrichment scenario. *MNRAS*, 475, 3098–3116.
- Dell'Agli, F., García-Hernández, D. A., Ventura, P., Schneider, R., Di Criscienzo, M., & Rossi, C. (2015a). AGB stars in the SMC: evolution and dust properties based on Spitzer observations. *MNRAS*, 454, 4235–4249.
- Dell'Agli, F., Marini, E., D'Antona, F., Ventura, P., Groenewegen, M. A. T., Mattsson, L., Kamath, D., García-Hernández, D. A., & Tailo, M. (2020). Are extreme AGB stars post-common envelope binaries? *MNRASL accepted*.
- Dell'Agli, F., Valiante, R., Kamath, D., Ventura, P., & García-Hernández, D. A. (2019b). AGB dust and gas ejecta in extremely metal-poor environments. *MNRAS*, 486, 4738–4752.
- Dell'Agli, F., Ventura, P., Garcia Hernandez, D. A., Schneider, R., di Criscienzo, M., Brocato, E., D'Antona, F., & Rossi, C. (2014b). Dissecting the Spitzer colour-magnitude diagrams of extreme Large Magellanic Cloud asymptotic giant branch stars. *MNRAS*, 442, L38–L42.
- Dell'Agli, F., Ventura, P., Schneider, R., Di Criscienzo, M., García-Hernández, D. A., Rossi, C., & Brocato, E. (2015b). Asymptotic giant branch stars in the Large Magellanic Cloud: evolution of dust in circumstellar envelopes. *MNRAS*, 447, 2992–3015.
- D'Ercole, A., Vesperini, E., D'Antona, F., McMillan, S. L. W., & Recchi, S. (2008). Formation and dynamical evolution of multiple stellar generations in globular clusters. *MNRAS*, 391, 825–843.
- Doherty, C. L., Gil-Pons, P., Lau, H. H. B., Lattanzio, J. C., & Siess, L. (2014). Super and massive AGB stars - II. Nucleosynthesis and yields - $Z = 0.02, 0.008$ and 0.004 . *MNRAS*, 437, 195–214.

- Doherty, C. L., Siess, L., Lattanzio, J. C., & Gil-Pons, P. (2010). Super asymptotic giant branch stars. I - Evolution code comparison. *MNRAS*, 401, 1453–1464.
- Draine, B. T. (2003). Scattering by Interstellar Dust Grains. I. Optical and Ultraviolet. *ApJ*, 598, 1017–1025.
- Draine, B. T. & Lee, H. M. (1984). Optical Properties of Interstellar Graphite and Silicate Grains. *ApJ*, 285, 89.
- Feast, M. (1999). Cepheids as Distance Indicators. *PASP*, 111, 775–793.
- Ferrarotti, A. S. & Gail, H. P. (2001). Mineral formation in stellar winds. II. Effects of Mg/Si abundance variations on dust composition in AGB stars. *A&A*, 371.
- Ferrarotti, A. S. & Gail, H. P. (2002). Mineral formation in stellar winds. III. Dust formation in S stars. *A&A*, 382, 256–281.
- Ferrarotti, A. S. & Gail, H. P. (2006). Composition and quantities of dust produced by AGB-stars and returned to the interstellar medium. *A&A*, 447, 553–576.
- Fleischer, A. J., Gauger, A., & Sedlmayr, E. (1992). Circumstellar dust shells around long-period variables. I. Dynamical models of C-stars including dust formation, growth and evaporation. *A&A*, 266, 321–339.
- Formicola, A., Imbriani, G., Costantini, H., Angulo, C., Bemmerer, D., Bonetti, R., Broggini, C., Corvisiero, P., Cruz, J., Descouvemont, P., Fülöp, Z., Gervino, G., Guglielmetti, A., Gustavino, C., Gyürky, G., Jesus, A. P., Junker, M., Lemut, A., Menegazzo, R., Prati, P., Roca, V., Rolfs, C., Romano, M., Rossi Alvarez, C., Schümann, F., Somorjai, E., Straniero, O., Strieder, F., Terrasi, F., Trautvetter, H. P., Vomiero, A., & Zavatarelli, S. (2004). Astrophysical S-factor of $^{14}\text{N}(p,\gamma)^{15}\text{O}$. *Physics Letters B*, 591, 61–68.
- Fraser, O. J., Hawley, S. L., & Cook, K. H. (2008). The Properties of Long-Period Variables in the Large Magellanic Cloud from MACHO. *AJ*, 136, 1242–1258.
- Fujimoto, M. Y., Nomoto, K., & Sugimoto, D. (1976). Dynamical Instability of the Envelope of Red Supergiants and the Lower Mass Limit for Carbon Detonation Supernovae. *Ap&SS*, 45, 71–77.
- Gaia Collaboration, Brown, A. G. A., Vallenari, A., & Prusti, T. e. a. (2016). Gaia Data Release 1. Summary of the astrometric, photometric, and survey properties. *A&A*, 595, A2.
- Gaia Collaboration, Brown, A. G. A., Vallenari, A., & Prusti, T. e. a. (2018). Gaia Data Release 2. Summary of the contents and survey properties. *A&A*, 616, A1.
- Gail, H. P. & Sedlmayr, E. (1985). Dust formation in stellar winds. II - Carbon condensation in stationary, spherically expanding winds. *A&A*, 148(1), 183–190.
- Gail, H. P. & Sedlmayr, E. (1999). Mineral formation in stellar winds. I. Condensation sequence of silicate and iron grains in stationary oxygen rich outflows. *A&A*, 347, 594–616.
- Gail, H. P., Wetzell, S., Pucci, A., & Tamanai, A. (2013). Seed particle formation for silicate dust condensation by SiO nucleation. *A&A*, 555, A119.

- Gallerani, S., Maiolino, R., Juarez, Y., Nagao, T., Marconi, A., Bianchi, S., Schneider, R., Mannucci, F., Oliva, T., Willott, C. J., Jiang, L., & Fan, X. (2010). The extinction law at high redshift and its implications. *A&A*, 523, A85.
- García-Berro, E., Ritossa, C., & Iben, Icko, J. (1997). On the Evolution of Stars that Form Electron-Degenerate Cores Processed by Carbon Burning. III. The Inward Propagation of a Carbon-Burning Flame and Other Properties of a 9 M Model Star. *ApJ*, 485(2), 765–784.
- García-Hernández, D. A. & Górný, S. K. (2014). Chemical abundances in Galactic planetary nebulae with Spitzer spectra. *A&A*, 567, A12.
- Gardner, J. P., Mather, J. C., Clampin, M., Doyon, R., Greenhouse, M. A., Hammel, H. B., Hutchings, J. B., Jakobsen, P., Lilly, S. J., Long, K. S., Lunine, J. I., McCaughrean, M. J., Mountain, M., Nella, J., Rieke, G. H., Rieke, M. J., Rix, H.-W., Smith, E. P., Sonneborn, G., Stiavelli, M., Stockman, H. S., Windhorst, R. A., & Wright, G. S. (2006). The James Webb Space Telescope. *SSRv*, 123, 485–606.
- Gehrz, R. (1989). Sources of Stardust in the Galaxy. In L. J. Allamandola & A. G. G. M. Tielens (Eds.), *Interstellar Dust*, volume 135 (pp. 445).
- Gielen, C., Bouwman, J., van Winckel, H., Lloyd Evans, T., Woods, P. M., Kemper, F., Marengo, M., Meixner, M., Sloan, G. C., & Tielens, A. G. G. M. (2011). Silicate features in Galactic and extragalactic post-AGB discs. *A&A*, 533, A99.
- Ginolfi, M., Graziani, L., Schneider, R., Marassi, S., Valiante, R., Dell’Agli, F., Ventura, P., & Hunt, L. K. (2018). Where does galactic dust come from? *MNRAS*, 473, 4538–4543.
- Girardi, L., Williams, B. F., Gilbert, K. M., Rosenfield, P., Dalcanton, J. J., Marigo, P., Boyer, M. L., Dolphin, A., Weisz, D. R., Melbourne, J., Olsen, K. A. G., Seth, A. C., & Skillman, E. (2010). The ACS Nearby Galaxy Survey Treasury. IX. Constraining Asymptotic Giant Branch Evolution with Old Metal-poor Galaxies. *ApJ*, 724, 1030–1043.
- Gładkowski, M., Szczerba, R., Sloan, G. C., Lagadec, E., & Volk, K. (2019). 30-micron sources in galaxies with different metallicities. *A&A*, 626, A92.
- Glasse, A., Rieke, G. H., Bauwens, E., García-Marín, M., Ressler, M. E., Rost, S., Tikkanen, T. V., Vandenbussche, B., & Wright, G. S. (2015). The Mid-Infrared Instrument for the James Webb Space Telescope, IX: Predicted Sensitivity. *PASP*, 127, 686.
- Goebel, J. H. & Moseley, S. H. (1985). MgS grain component in circumstellar shells. *ApJL*, 290, L35–L39.
- Goldman, S. R., Boyer, M. L., McQuinn, K. B. W., Whitelock, P. A., McDonald, I., van Loon, J. T., Skillman, E. D., Gehrz, R. D., Javadi, A., Sloan, G. C., Jones, O. C., Groenewegen, M. A. T., & Menzies, J. W. (2019). An Infrared Census of DUST in Nearby Galaxies with Spitzer (DUSTINGS). V. The Period-Luminosity Relation for Dusty Metal-poor AGB Stars. *ApJ*, 877, 49.
- Gong, M., Ostriker, E. C., & Wolfire, M. G. (2017). A Simple and Accurate Network for Hydrogen and Carbon Chemistry in the Interstellar Medium. *ApJ*, 843, 38.

- Gordon, K. D., Meixner, M., Meade, M. R., Whitney, B., Engelbracht, C., Bot, C., Boyer, M. L., Lawton, B., Sewilo, M., Babler, B., Bernard, J. P., Bracker, S., Block, M., Blum, R., Bolatto, A., Bonanos, A., Harris, J., Hora, J. L., Indebetouw, R., Misselt, K., Reach, W., Shiao, B., Tielens, X., Carlson, L., Churchwell, E., Clayton, G. C., Chen, C. H. R., Cohen, M., Fukui, Y., Gorjian, V., Hony, S., Israel, F. P., Kawamura, A., Kemper, F., Leroy, A., Li, A., Madden, S., Marble, A. R., McDonald, I., Mizuno, A., Mizuno, N., Muller, E., Oliveira, J. M., Olsen, K., Onishi, T., Paladini, R., Paradis, D., Points, S., Robitaille, T., Rubin, D., Sandstrom, K., Sato, S., Shibai, H., Simon, J. D., Smith, L. J., Srinivasan, S., Vijh, U., Van Dyk, S., van Loon, J. T., & Zaritsky, D. (2011). Surveying the Agents of Galaxy Evolution in the Tidally Stripped, Low Metallicity Small Magellanic Cloud (SAGE-SMC). I. Overview. *AJ*, 142, 102.
- Grevesse, N. & Sauval, A. J. (1998). Standard Solar Composition. *SSRv*, 85, 161–174.
- Groenewegen, M. A. T. & de Jong, T. (1993). Synthetic AGB evolution. I. A new model. *A&A*, 267, 410–432.
- Groenewegen, M. A. T. & Sloan, G. C. (2018). Luminosities and mass-loss rates of Local Group AGB stars and red supergiants. *A&A*, 609, A114.
- Groenewegen, M. A. T., Sloan, G. C., Soszyński, I., & Petersen, E. A. (2009). Luminosities and mass-loss rates of SMC and LMC AGB stars and red supergiants. *A&A*, 506, 1277–1296.
- Groenewegen, M. A. T., Wood, P. R., Sloan, G. C., Blommaert, J. A. D. L., Cioni, M. R. L., Feast, M. W., Hony, S., Matsuura, M., Menzies, J. W., Olivier, E. A., Vanhollebeke, E., van Loon, J. T., Whitelock, P. A., Zijlstra, A. A., Habing, H. J., & Lagadec, E. (2007). Luminosities and mass-loss rates of carbon stars in the Magellanic Clouds. *MNRAS*, 376, 313–337.
- Gruendl, R. A., Chu, Y. H., Seale, J. P., Matsuura, M., Speck, A. K., Sloan, G. C., & Looney, L. W. (2008). Discovery of Extreme Carbon Stars in the Large Magellanic Cloud. *ApJL*, 688, L9.
- Gullieuszik, M., Groenewegen, M. A. T., Cioni, M. R. L., de Grijs, R., van Loon, J. T., Girardi, L., Ivanov, V. D., Oliveira, J. M., Emerson, J. P., & Guandalini, R. (2012). The VMC survey. III. Mass-loss rates and luminosities of LMC AGB stars. *A&A*, 537, A105.
- Gutenkunst, S., Bernard-Salas, J., Pottasch, S. R., Sloan, G. C., & Houck, J. R. (2008). Chemical Abundances and Dust in Planetary Nebulae in the Galactic Bulge. *ApJ*, 680, 1206–1221.
- Guzman-Ramirez, L., Zijlstra, A. A., Níchuimín, R., Gesicki, K., Lagadec, E., Millar, T. J., & Woods, P. M. (2011). Carbon chemistry in Galactic bulge planetary nebulae. *MNRAS*, 414, 1667–1678.
- Hamedani Golshan, R., Javadi, A., van Loon, J. T., Khosroshahi, H., & Saremi, E. (2017). Long-period variable stars in NGC 147 and NGC 185 - I. Their star formation histories. *MNRAS*, 466, 1764–1776.
- Harris, J. & Zaritsky, D. (2004). The Star Formation History of the Small Magellanic Cloud. *AJ*, 127, 1531–1544.

- Harris, J. & Zaritsky, D. (2009). The Star Formation History of the Large Magellanic Cloud. *AJ*, 138, 1243–1260.
- Hauschildt, P. H., Allard, F., Ferguson, J., Baron, E., & Alexander, D. R. (1999). The NEXGEN Model Atmosphere Grid. II. Spherically Symmetric Model Atmospheres for Giant Stars with Effective Temperatures between 3000 and 6800 K. *ApJ*, 525, 871–880.
- Herwig, F. (2005). Evolution of Asymptotic Giant Branch Stars. *ARA&A*, 43, 435–479.
- Herwig, F. & Austin, S. M. (2004). Nuclear Reaction Rates and Carbon Star Formation. *ApJL*, 613, L73–L76.
- Höfner, S. (2009). Dust Formation and Winds around Evolved Stars: The Good, the Bad and the Ugly Cases. volume 414 (pp.3).
- Höfner, S., Bladh, S., Aringer, B., & Ahuja, R. (2016). Dynamic atmospheres and winds of cool luminous giants. I. Al_2O_3 and silicate dust in the close vicinity of M-type AGB stars. *A&A*, 594, A108.
- Höfner, S. & Olofsson, H. (2018). Mass loss of stars on the asymptotic giant branch. Mechanisms, models and measurements. *AARv*, 26, 1.
- Hollenbach, D. & Salpeter, E. E. (1971). Surface Recombination of Hydrogen Molecules. *ApJ*, 163, 155.
- Hony, S., Waters, L. B. F. M., & Tielens, A. G. G. M. (2002). The carrier of the “30” μm emission feature in evolved stars. A simple model using magnesium sulfide. *A&A*, 390, 533–553.
- Iben, I., J. (1975). Thermal pulses: p-capture, alpha -capture, s-process nucleosynthesis; and convective mixing in a star of intermediate mass. *ApJ*, 196, 525–547.
- Iben, I., J. & Renzini, A. (1983). Asymptotic giant branch evolution and beyond. *ARA&A*, 21, 271–342.
- Iglesias, C. A. & Rogers, F. J. (1996). Updated Opal Opacities. *ApJ*, 464, 943.
- Izzard, R. G., Tout, C. A., Karakas, A. I., & Pols, O. R. (2004). A new synthetic model for asymptotic giant branch stars. *MNRAS*, 350, 407–426.
- Javadi, A., van Loon, J. T., Khosroshahi, H., & Mirtorabi, M. T. (2013). The UK Infrared Telescope M33 monitoring project - III. Feedback from dusty stellar winds in the central square kiloparsec. *MNRAS*, 432, 2824–2836.
- Javadi, A., van Loon, J. T., Khosroshahi, H. G., Tabatabaei, F., Hamedani Golshan, R., & Rashidi, M. (2017). The UK Infrared Telescope M 33 monitoring project - V. The star formation history across the galactic disc. *MNRAS*, 464, 2103–2119.
- Jones, O. C., Kemper, F., Srinivasan, S., McDonald, I., Sloan, G. C., & Zijlstra, A. A. (2014). Modelling the alumina abundance of oxygen-rich evolved stars in the Large Magellanic Cloud. *MNRAS*, 440, 631–651.

- Jones, O. C., Meixner, M., Justtanont, K., & Glasse, A. (2017). Probing the Dusty Stellar Populations of the Local Volume Galaxies with JWST/MIRI. *ApJ*, 841, 15.
- Jørgensen, U. G., Hron, J., & Loidl, R. (2000). ISO-SWS spectra of the carbon stars TX Psc, V460 Cyg, and TT Cyg. *A&A*, 356, 253–266.
- Kamath, D., Karakas, A. I., & Wood, P. R. (2012). Evolution and Nucleosynthesis of Asymptotic Giant Branch Stars in Three Magellanic Cloud Clusters. *ApJ*, 746, 20.
- Kamath, D., Wood, P. R., & Van Winckel, H. (2014). Optically visible post-AGB/RGB stars and young stellar objects in the Small Magellanic Cloud: candidate selection, spectral energy distributions and spectroscopic examination. *MNRAS*, 439, 2211–2270.
- Kamath, D., Wood, P. R., & Van Winckel, H. (2015). Optically visible post-AGB stars, post-AGB stars and young stellar objects in the Large Magellanic Cloud. *MNRAS*, 454, 1468–1502.
- Karakas, A. I. (2010). Updated stellar yields from asymptotic giant branch models. *MNRAS*, 403, 1413–1425.
- Karakas, A. I. (2011). Current Status of Stellar Evolutionary Models for AGB Stars. In F. Kerschbaum, T. Lebzelter, & R. F. Wing (Eds.), *Why Galaxies Care about AGB Stars II: Shining Examples and Common Inhabitants*, volume 445 of *Astronomical Society of the Pacific Conference Series* (pp.3).
- Karakas, A. I. & Lattanzio, J. C. (2014). The Dawes Review 2: Nucleosynthesis and Stellar Yields of Low- and Intermediate-Mass Single Stars. *PASA*, 31, e030.
- Karakas, A. I., Lattanzio, J. C., & Pols, O. R. (2002). Parameterising the Third Dredge-up in Asymptotic Giant Branch Stars. *PASA*, 19, 515–526.
- Karakas, A. I., Lugaro, M., Carlos, M., Cseh, B., Kamath, D., & García-Hernández, D. A. (2018). Heavy-element yields and abundances of asymptotic giant branch models with a Small Magellanic Cloud metallicity. *MNRAS*, 477, 421–437.
- Kemper, F., de Koter, A., Waters, L. B. F. M., Bouwman, J., & Tielens, A. G. G. M. (2002). Dust and the spectral energy distribution of the OH/IR star OH 127.8+0.0: Evidence for circumstellar metallic iron. *A&A*, 384, 585–593.
- Kemper, F., Woods, P. M., Antoniou, V., Bernard, J. P., Blum, R. D., Boyer, M. L., Chan, J., Chen, C. H. R., Cohen, M., Dijkstra, C., Engelbracht, C., Galametz, M., Galliano, F., Gielen, C., Gordon, K. D., Gorjian, V., Harris, J., Hony, S., Hora, J. L., Indebetouw, R., Jones, O., Kawamura, A., Lagadec, E., Lawton, B., Leisenring, J. M., Madden, S. C., Marengo, M., Matsuura, M., McDonald, I., McGuire, C., Meixner, M., Mulia, A. J., O’Halloran, B., Oliveira, J. M., Paladini, R., Paradis, D., Reach, W. T., Rubin, D., Sandstrom, K., Sargent, B. A., Sewilo, M., Shiao, B., Sloan, G. C., Speck, A. K., Srinivasan, S., Szczerba, R., Tielens, A. G. G. M., van Aarle, E., Van Dyk, S. D., van Loon, J. T., Van Winckel, H., Vijh, U. P., Volk, K., Whitney, B. A., Wilkins, A. N., & Zijlstra, A. A. (2010). The SAGE-Spec Spitzer Legacy Program: The Life Cycle of Dust and Gas in the Large Magellanic Cloud. *PASP*, 122, 683.

- Knapp, G. R. & Morris, M. (1985). Mass Loss from Evolved Stars. III. Mass Loss Rates for 50 Stars from CO J = 1–0 Observations. *ApJ*, 292, 640.
- Kobayashi, C., Karakas, A. I., & Umeda, H. (2011). The evolution of isotope ratios in the Milky Way Galaxy. *MNRAS*, 414, 3231–3250.
- Lagadec, E. & Zijlstra, A. A. (2008). The trigger of the asymptotic giant branch superwind: the importance of carbon. *MNRAS*, 390, L59–L63.
- Little-Marenin, I. R. (1986). Carbon Stars with Silicate Dust in Their Circumstellar Shells. *ApJL*, 307, L15.
- Lloyd Evans, T. (1990). Carbon stars with silicate dust shells - I. Carbon stars with enhanced ^{13}C (J stars). *MNRAS*, 243, 336–348.
- Lucy, L. B. (1976). Mass Loss by Cool Carbon Stars. *ApJ*, 205, 482–491.
- Maiolino, R., Schneider, R., Oliva, E., Bianchi, S., Ferrara, A., Mannucci, F., Pedani, M., & Roca Sogorb, M. (2004). A supernova origin for dust in a high-redshift quasar. *Nature*, 431, 533–535.
- Mancini, M., Schneider, R., Graziani, L., Valiante, R., Dayal, P., Maio, U., Ciardi, B., & Hunt, L. K. (2015). The dust mass in $z > 6$ normal star-forming galaxies. *MNRAS*, 451, L70–L74.
- Maraston, C., Daddi, E., Renzini, A., Cimatti, A., Dickinson, M., Papovich, C., Pasquali, A., & Pirzkal, N. (2006). Evidence for TP-AGB Stars in High-Redshift Galaxies, and Their Effect on Deriving Stellar Population Parameters. *ApJ*, 652, 85–96.
- Marigo, P. (2002). Asymptotic Giant Branch evolution at varying surface C/O ratio: effects of changes in molecular opacities. *A&A*, 387, 507–519.
- Marigo, P. & Aringer, B. (2009). Low-temperature gas opacity. *ÆSOPUS*: a versatile and quick computational tool. *A&A*, 508, 1539–1569.
- Marigo, P. & Girardi, L. (2007). Evolution of asymptotic giant branch stars. I. Updated synthetic TP-AGB models and their basic calibration. *A&A*, 469, 239–263.
- Marigo, P., Girardi, L., & Bressan, A. (1999). The third dredge-up and the carbon star luminosity functions in the Magellanic Clouds. *A&A*, 344, 123–142.
- Marigo, P., Girardi, L., Bressan, A., Groenewegen, M. A. T., Silva, L., & Granato, G. L. (2008). Evolution of asymptotic giant branch stars. II. Optical to far-infrared isochrones with improved TP-AGB models. *A&A*, 482, 883–905.
- Marini, E., Dell’Agli, F., Di Criscienzo, M., García-Hernández, D. A., Ventura, P., Groenewegen, M. A. T., Mattsson, L., Kamath, D., Puccetti, S., Tailo, M., & Villaver, E. (2020a). Characterization of M-stars in the LMC in the JWST era. *MNRAS*, 493(2), 2996–3013.
- Marini, E., Dell’Agli, F., Di Criscienzo, M., Puccetti, S., García-Hernández, D. A., Mattsson, L., & Ventura, P. (2019a). Discovery of Stars Surrounded by Iron Dust in the Large Magellanic Cloud. *ApJL*, 871, L16.

- Marini, E., Dell’Agli, F., García-Hernández, D. A., Groenewegen, M. A. T., Puccetti, S., Ventura, P., & Villaver, E. (2019b). Do evolved stars in the LMC show dual dust chemistry? *MNRAS*, 488, L85–L89.
- Marini, E., Dell’Agli, F., Groenewegen, M. A. T., García-Hernández, D. A., Mattsson, L., Kamath, D., Ventura, P., D’Antona, F., & Tailo, M. (2020b). Understanding the evolution and dust formation of carbon stars in the LMC with a look at the JWST. *A&A accepted*, (pp. arXiv:2012.12289).
- Mathis, J. S. (1990). Interstellar dust and extinction. *ARA&A*, 28, 37–70.
- Matsuura, M., Barlow, M. J., Zijlstra, A. A., Whitelock, P. A., Cioni, M. R. L., Groenewegen, M. A. T., Volk, K., Kemper, F., Kodama, T., Lagadec, E., Meixner, M., Sloan, G. C., & Srinivasan, S. (2009). The global gas and dust budget of the Large Magellanic Cloud: AGB stars and supernovae, and the impact on the ISM evolution. *MNRAS*, 396, 918–934.
- Matsuura, M., Wood, P. R., Sloan, G. C., Zijlstra, A. A., van Loon, J. T., Groenewegen, M. A. T., Blommaert, J. A. D. L., Cioni, M. R. L., Feast, M. W., Habing, H. J., Hony, S., Lagadec, E., Loup, C., Menzies, J. W., Waters, L. B. F. M., & Whitelock, P. A. (2006). Spitzer observations of acetylene bands in carbon-rich asymptotic giant branch stars in the Large Magellanic Cloud. *MNRAS*, 371, 415–420.
- Matsuura, M., Woods, P. M., & Owen, P. J. (2013). The global gas and dust budget of the Small Magellanic Cloud. *MNRAS*, 429, 2527–2536.
- McDonald, I., Sloan, G. C., Zijlstra, A. A., Matsunaga, N., Matsuura, M., Kraemer, K. E., Bernard-Salas, J., & Markwick, A. J. (2010). Rusty Old Stars: A Source of the Missing Interstellar Iron? *ApJL*, 717, L92–L97.
- McDonald, I., van Loon, J. T., Sloan, G. C., Dupree, A. K., Zijlstra, A. A., Boyer, M. L., Gehrz, R. D., Evans, A., Woodward, C. E., & Johnson, C. I. (2011). Spitzer spectra of evolved stars in ω Centauri and their low-metallicity dust production. *MNRAS*, 417, 20–31.
- McQuinn, K. B. W., Boyer, M. L., Mitchell, M. B., Skillman, E. D., Gehrz, R. D., Groenewegen, M. A. T., McDonald, I., Sloan, G. C., van Loon, J. T., Whitelock, P. A., & Zijlstra, A. A. (2017). DUSTINGS. III. Distribution of Intermediate-age and Old Stellar Populations in Disks and Outer Extremities of Dwarf Galaxies. *ApJ*, 834, 78.
- Meixner, M., Galliano, F., Hony, S., Roman-Duval, J., Robitaille, T., Panuzzo, P., Sauvage, M., Gordon, K., Engelbracht, C., Misselt, K., Okumura, K., Beck, T., Bernard, J. P., Bolatto, A., Bot, C., Boyer, M., Bracker, S., Carlson, L. R., Clayton, G. C., Chen, C. H. R., Churchwell, E., Fukui, Y., Galametz, M., Hora, J. L., Hughes, A., Indebetouw, R., Israel, F. P., Kawamura, A., Kemper, F., Kim, S., Kwon, E., Lawton, B., Li, A., Long, K. S., Marengo, M., Madden, S. C., Matsuura, M., Oliveira, J. M., Onishi, T., Otsuka, M., Paradis, D., Poglitsch, A., Riebel, D., Reach, W. T., Rubio, M., Sargent, B., Sewilo, M., Simon, J. D., Skibba, R., Smith, L. J., Srinivasan, S., Tielens, A. G. G. M., van Loon, J. T., Whitney, B., & Woods, P. M. (2010). HERschel Inventory of The Agents of Galaxy Evolution (HERITAGE): The Large Magellanic Cloud dust. *A&A*, 518, L71.

- Meixner, M., Gordon, K. D., Indebetouw, R., Hora, J. L., Whitney, B., Blum, R., Reach, W., Bernard, J.-P., Meade, M., Babler, B., Engelbracht, C. W., For, B.-Q., Misselt, K., Vijn, U., Leitherer, C., Cohen, M., Churchwell, E. B., Boulanger, F., Frogel, J. A., Fukui, Y., Gallagher, J., Gorjian, V., Harris, J., Kelly, D., Kawamura, A., Kim, S., Latter, W. B., Madden, S., Markwick-Kemper, C., Mizuno, A., Mizuno, N., Mould, J., Nota, A., Oey, M. S., Olsen, K., Onishi, T., Paladini, R., Panagia, N., Perez-Gonzalez, P., Shibai, H., Sato, S., Smith, L., Staveley-Smith, L., Tielens, A. G. G. M., Ueta, T., van Dyk, S., Volk, K., Werner, M., & Zaritsky, D. (2006). Spitzer Survey of the Large Magellanic Cloud: Surveying the Agents of a Galaxy's Evolution (SAGE). I. Overview and Initial Results. *AJ*, 132, 2268–2288.
- Meixner, M., Panuzzo, P., Roman-Duval, J., Engelbracht, C., Babler, B., Seale, J., Hony, S., Montiel, E., Sauvage, M., Gordon, K., Misselt, K., Okumura, K., Chanial, P., Beck, T., Bernard, J. P., Bolatto, A., Bot, C., Boyer, M. L., Carlson, L. R., Clayton, G. C., Chen, C. H. R., Cormier, D., Fukui, Y., Galametz, M., Galliano, F., Hora, J. L., Hughes, A., Indebetouw, R., Israel, F. P., Kawamura, A., Kemper, F., Kim, S., Kwon, E., Lebouteiller, V., Li, A., Long, K. S., Madden, S. C., Matsuura, M., Muller, E., Oliveira, J. M., Onishi, T., Otsuka, M., Paradis, D., Poglitsch, A., Reach, W. T., Robitaille, T. P., Rubio, M., Sargent, B., Sewilo, M., Skibba, R., Smith, L. J., Srinivasan, S., Tielens, A. G. G. M., van Loon, J. T., & Whitney, B. (2013). The HERSCHEL Inventory of The Agents of Galaxy Evolution in the Magellanic Clouds, a Herschel Open Time Key Program. *AJ*, 146, 62.
- Messenger, S. J., Speck, A., & Volk, K. (2013). Probing the “30 μm ” Feature: Lessons from Extreme Carbon Stars. *ApJ*, 764, 142.
- Miller Bertolami, M. M. (2016). New models for the evolution of post-asymptotic giant branch stars and central stars of planetary nebulae. *A&A*, 588, A25.
- Molster, F. J., Yamamura, I., Waters, L. B. F., Nyman, L. Å., Käufl, H. U., de Jong, T., & Loup, C. (2001). IRAS 09425-6040: A carbon star surrounded by highly crystalline silicate dust. *A&A*, 366, 923–929.
- Mowlavi, N. (1999). On the third dredge-up phenomenon in asymptotic giant branch stars. *A&A*, 344, 617–631.
- Nanni, A., Bressan, A., Marigo, P., & Girardi, L. (2013). Evolution of thermally pulsing asymptotic giant branch stars - II. Dust production at varying metallicity. *MNRAS*, 434, 2390–2417.
- Nanni, A., Bressan, A., Marigo, P., & Girardi, L. (2014). Evolution of thermally pulsing asymptotic giant branch stars - III. Dust production at supersolar metallicities. *MNRAS*, 438, 2328–2340.
- Nanni, A., Groenewegen, M. A. T., Aringer, B., Rubele, S., Bressan, A., van Loon, J. T., Goldman, S. R., & Boyer, M. L. (2019). The mass-loss, expansion velocities, and dust production rates of carbon stars in the Magellanic Clouds. *MNRAS*, 487, 502–521.
- Nanni, A., Marigo, P., Girardi, L., Rubele, S., Bressan, A., Groenewegen, M. A. T., Pastorelli, G., & Aringer, B. (2018). Estimating the dust production rate of carbon stars in the Small Magellanic Cloud. *MNRAS*, 473, 5492–5513.

- Nenkova, M., Ivezić, Z., & Elitzur, M. (1999). DUSTY: A Publicly Available Code for Continuum Radiative Transfer in Astrophysical Environments. In *Thermal Emission Spectroscopy and Analysis of Dust, Disks, and Regoliths*, volume 969 (pp.20).
- Ordal, M. A., Bell, R. J., Alexander, R. W., Newquist, L. A., & Querry, M. R. (1988). Optical properties of al, fe, ti, ta, w, and mo at submillimeter wavelengths. *Appl. Opt.*, 27, 1203–1209.
- Paczyński, B. (1970). Evolution of Single Stars. I. Stellar Evolution from Main Sequence to White Dwarf or Carbon Ignition. *AcA*, 20, 47.
- Pegourie, B. (1988). Optical properties of alpha silicon carbide. *A&A*, 194, 335–339.
- Perea-Calderón, J. V., García-Hernández, D. A., García-Lario, P., Szczerba, R., & Bobrowsky, M. (2009). The mixed chemistry phenomenon in Galactic Bulge PNe. *A&A*, 495, L5–L8.
- Piatti, A. E. (2012). The star field age-metallicity relationship of the Small Magellanic Cloud. *MNRAS*, 422, 1109–1121.
- Piatti, A. E. & Geisler, D. (2013). The Age-Metallicity Relationship of the Large Magellanic Cloud Field Star Population from Wide-field Washington Photometry. *AJ*, 145, 17.
- Renzini, A. & Voli, M. (1981). Advanced evolutionary stages of intermediate-mass stars. I. Evolution of surface compositions. *A&A*, 500, 221–239.
- Riebel, D., Meixner, M., Fraser, O., Srinivasan, S., Cook, K., & Vjih, U. (2010). Infrared Period-Luminosity Relations of Evolved Variable Stars in the Large Magellanic Cloud. *ApJ*, 723, 1195–1209.
- Riebel, D., Srinivasan, S., Sargent, B., & Meixner, M. (2012). The Mass-loss Return from Evolved Stars to the Large Magellanic Cloud. VI. Luminosities and Mass-loss Rates on Population Scales. *ApJ*, 753, 71.
- Rieke, G. H., Wright, G. S., Böker, T., Bouwman, J., Colina, L., Glasse, A., Gordon, K. D., Greene, T. P., Güdel, M., Henning, T., Justtanont, K., Lagage, P. O., Meixner, M. E., Nørgaard-Nielsen, H. U., Ray, T. P., Ressler, M. E., van Dishoeck, E. F., & Waelkens, C. (2015). The Mid-Infrared Instrument for the James Webb Space Telescope, I: Introduction. *PASP*, 127, 584.
- Ritossa, C., Garcia-Berro, E., & Iben, Icko, J. (1996). On the Evolution of Stars That Form Electron-degenerate Cores Processed by Carbon Burning. II. Isotope Abundances and Thermal Pulses in a $10 M_{sun}$ Model with an ONe Core and Applications to Long-Period Variables, Classical Novae, and Accretion-induced Collapse. *ApJ*, 460, 489.
- Romano, D., Karakas, A. I., Tosi, M., & Matteucci, F. (2010). Quantifying the uncertainties of chemical evolution studies. II. Stellar yields. *A&A*, 522, A32.
- Romano, D., Matteucci, F., Zhang, Z. Y., Papadopoulos, P. P., & Ivison, R. J. (2017). The evolution of CNO isotopes: a new window on cosmic star formation history and the stellar IMF in the age of ALMA. *MNRAS*, 470, 401–415.

- Rosenfield, P., Marigo, P., Girardi, L., Dalcanton, J. J., Bressan, A., Gullieuszik, M., Weisz, D., Williams, B. F., Dolphin, A., & Aringer, B. (2014). Evolution of Thermally Pulsing Asymptotic Giant Branch Stars. IV. Constraining Mass loss and Lifetimes of Low Mass, Low Metallicity AGB Stars. *ApJ*, 790, 22.
- Rosenfield, P., Marigo, P., Girardi, L., Dalcanton, J. J., Bressan, A., Williams, B. F., & Dolphin, A. (2016). Evolution of Thermally Pulsing Asymptotic Giant Branch Stars. V. Constraining the Mass Loss and Lifetimes of Intermediate-mass, Low-metallicity AGB Stars. *ApJ*, 822, 73.
- Sackmann, I. J. & Boothroyd, A. I. (1992). The Creation of Super-rich Lithium Giants. *ApJL*, 392, L71.
- Sackmann, I. J. & Boothroyd, A. I. (1999). Creation of ${}^7\text{Li}$ and Destruction of ${}^3\text{He}$, ${}^9\text{Be}$, ${}^{10}\text{B}$, and ${}^{11}\text{B}$ in Low-Mass Red Giants, Due to Deep Circulation. *ApJ*, 510, 217–231.
- Sandin, C. & Mattsson, L. (2020). Three-component modelling of C-rich AGB star winds - V. Effects of frequency-dependent radiative transfer including drift. *MNRAS*, 499, 1531–1560.
- Schneider, R., Hunt, L., & Valiante, R. (2016). The dust content of the most metal-poor star-forming galaxies. *MNRAS*, 457, 1842–1850.
- Schneider, R., Valiante, R., Ventura, P., dell’Agli, F., Di Criscienzo, M., Hirashita, H., & Kemper, F. (2014). Dust production rate of asymptotic giant branch stars in the Magellanic Clouds. *MNRAS*, 442, 1440–1450.
- Schwarzschild, M. & Härm, R. (1965). Thermal Instability in Non-Degenerate Stars. *ApJ*, 142.
- Schwarzschild, M. & Härm, R. (1967). Hydrogen Mixing by Helium-Shell Flashes. *ApJ*, 150, 961.
- Siess, L. (2006). Evolution of massive AGB stars. I. Carbon burning phase. *A&A*, 448, 717–729.
- Siess, L. (2007). Evolution of massive AGB stars. II. model properties at non-solar metallicity and the fate of Super-AGB stars. *A&A*, 476, 893–909.
- Skibba, R. A., Engelbracht, C. W., Aniano, G., Babler, B., Bernard, J.-P., Bot, C., Carlson, L. R., Galametz, M., Galliano, F., Gordon, K., Hony, S., Israel, F., Lebouteiller, V., Li, A., Madden, S., Meixner, M., Misselt, K., Montiel, E., Okumura, K., Panuzzo, P., Paradis, D., Roman-Duval, J., Rubio, M., Sauvage, M., Seale, J., Srinivasan, S., & van Loon, J. T. (2012). The Spatial Distribution of Dust and Stellar Emission of the Magellanic Clouds. *ApJ*, 761, 42.
- Skrutskie, M. F., Cutri, R. M., Stiening, R., Weinberg, M. D., Schneider, S., Carpenter, J. M., Beichman, C., Capps, R., Chester, T., Elias, J., Huchra, J., Liebert, J., Lonsdale, C., Monet, D. G., Price, S., Seitzer, P., Jarrett, T., Kirkpatrick, J. D., Gizis, J. E., Howard, E., Evans, T., Fowler, J., Fullmer, L., Hurt, R., Light, R., Kopan, E. L., Marsh, K. A., McCallon, H. L., Tam, R., Van Dyk, S., & Wheelock, S. (2006). The Two Micron All Sky Survey (2MASS). *AJ*, 131, 1163–1183.

- Sloan, G. C., Kraemer, K. E., McDonald, I., Groenewegen, M. A. T., Wood, P. R., Zijlstra, A. A., Lagadec, E., Boyer, M. L., Kemper, F., Matsuura, M., Sahai, R., Sargent, B. A., Srinivasan, S., van Loon, J. T., & Volk, K. (2016). The Infrared Spectral Properties of Magellanic Carbon Stars. *ApJ*, 826, 44.
- Sloan, G. C., Lagadec, E., Zijlstra, A. A., Kraemer, K. E., Weis, A. P., Matsuura, M., Volk, K., Peeters, E., Duley, W. W., Cami, J., Bernard-Salas, J., Kemper, F., & Sahai, R. (2014). Carbon-rich Dust Past the Asymptotic Giant Branch: Aliphatics, Aromatics, and Fullerenes in the Magellanic Clouds. *ApJ*, 791, 28.
- Soszyński, I., Udalski, A., Szymański, M. K., Kubiak, M., Pietrzyński, G., Wyrzykowski, Ł., Szewczyk, O., Ulaczyk, K., & Poleski, R. (2009). The Optical Gravitational Lensing Experiment. The OGLE-III Catalog of Variable Stars. IV. Long-Period Variables in the Large Magellanic Cloud. *AcA*, 59, 239–253.
- Speck, A. K., Corman, A. B., Wakeman, K., Wheeler, C. H., & Thompson, G. (2009). Silicon Carbide Absorption Features: Dust Formation in the Outflows of Extreme Carbon Stars. *ApJ*, 691, 1202–1221.
- Srinivasan, S., Meixner, M., Leitherer, C., Vijn, U., Volk, K., Blum, R. D., Babler, B. L., Block, M., Bracker, S., Cohen, M., Engelbracht, C. W., For, B.-Q., Gordon, K. D., Harris, J., Hora, J. L., Indebetouw, R., Markwick-Kemper, F., Meade, M., Misselt, K. A., Sewilo, M., & Whitney, B. (2009). The Mass Loss Return from Evolved Stars to the Large Magellanic Cloud: Empirical Relations for Excess Emission at 8 and 24 μm . *AJ*, 137, 4810–4823.
- Srinivasan, S., Sargent, B. A., Matsuura, M., Meixner, M., Kemper, F., Tielens, A. G. G. M., Volk, K., Speck, A. K., Woods, P. M., Gordon, K., Marengo, M., & Sloan, G. C. (2010). The mass-loss return from evolved stars to the Large Magellanic Cloud. III. Dust properties for carbon-rich asymptotic giant branch stars. *A&A*, 524, A49.
- Srinivasan, S., Sargent, B. A., & Meixner, M. (2011). The mass-loss return from evolved stars to the Large Magellanic Cloud. V. The GRAMS carbon-star model grid. *A&A*, 532, A54.
- Stanghellini, L., García-Lario, P., García-Hernández, D. A., Perea-Calderón, J. V., Davies, J. E., Manchado, A., Villaver, E., & Shaw, R. A. (2007). Spitzer Infrared Spectrograph Observations of Magellanic Cloud Planetary Nebulae: The Nature of Dust in Low-Metallicity Circumstellar Ejecta. *ApJ*, 671, 1669–1684.
- Tachibana, S., Nagahara, H., Ozawa, K., Ikeda, Y., Nomura, R., Tatsumi, K., & Joh, Y. (2011). Kinetic Condensation and Evaporation of Metallic Iron and Implications for Metallic Iron Dust Formation. *ApJ*, 736, 16.
- Trabucchi, M., Wood, P. R., Montalbán, J., Marigo, P., Pastorelli, G., & Girardi, L. (2018). Long-Period Variables in the Large Magellanic Cloud. In *Stellar Populations and the Distance Scale*, volume 514 of *Astronomical Society of the Pacific Conference Series* (pp. 111).
- Valiante, R., Gioannini, L., Schneider, R., Matteucci, F., Dell’Agli, F., & Di Criscienzo, M. (2017). The relative role of AGB stars and SNe as the first cosmic dust polluters. *MmSAI*, 88, 420.

- Valiante, R., Schneider, R., Bianchi, S., & Andersen, A. C. (2009). Stellar sources of dust in the high-redshift Universe. *MNRAS*, 397, 1661–1671.
- Valiante, R., Schneider, R., Salvadori, S., & Bianchi, S. (2011). The origin of the dust in high-redshift quasars: the case of SDSS J1148+5251. *MNRAS*, 416, 1916–1935.
- van Aarle, E., van Winckel, H., Lloyd Evans, T., Ueta, T., Wood, P. R., & Ginsburg, A. G. (2011). The optically bright post-AGB population of the LMC. *A&A*, 530, A90.
- van Loon, J. T. (2006). On the metallicity dependence of the winds from red supergiants and Asymptotic Giant Branch stars. In H. J. G. L. M. Lamers, N. Langer, T. Nugis, & K. Annuk (Eds.), *Stellar Evolution at Low Metallicity: Mass Loss, Explosions, Cosmology*, volume 353 of *Astronomical Society of the Pacific Conference Series* (pp. 211).
- van Loon, J. T., Cioni, M. R. L., Zijlstra, A. A., & Loup, C. (2005). An empirical formula for the mass-loss rates of dust-enshrouded red supergiants and oxygen-rich Asymptotic Giant Branch stars. *A&A*, 438(1), 273–289.
- van Loon, J. T., Groenewegen, M. A. T., de Koter, A., Trams, N. R., Waters, L. B. F. M., Zijlstra, A. A., Whitelock, P. A., & Loup, C. (1999). Mass-loss rates and luminosity functions of dust-enshrouded AGB stars and red supergiants in the LMC. *A&A*, 351, 559–572.
- van Winckel, H. (2003). Post-AGB Stars. *ARA&A*, 41, 391–427.
- Vassiliadis, E. & Wood, P. R. (1993). Evolution of Low- and Intermediate-Mass Stars to the End of the Asymptotic Giant Branch with Mass Loss. *ApJ*, 413, 641.
- Ventura, P. & D’Antona, F. (2005a). Full computation of massive AGB evolution. I. The large impact of convection on nucleosynthesis. *A&A*, 431, 279–288.
- Ventura, P. & D’Antona, F. (2005b). Full computation of massive AGB evolution. II. The role of mass loss and cross-sections. *A&A*, 439, 1075–1091.
- Ventura, P. & D’Antona, F. (2009). Massive AGB models of low metallicity: the implications for the self-enrichment scenario in metal-poor globular clusters. *A&A*, 499, 835–846.
- Ventura, P. & D’Antona, F. (2010). The role of lithium production in massive AGB and super-AGB stars for the understanding of multiple populations in globular clusters. *MNRAS*, 402, L72–L76.
- Ventura, P. & D’Antona, F. (2011). Hot bottom burning in the envelope of super asymptotic giant branch stars. *MNRAS*, 410, 2760–2766.
- Ventura, P., D’Antona, F., & Mazzitelli, I. (1999). Modeling Lithium-rich Carbon Stars in the Large Magellanic Cloud: An Independent Distance Indicator? *ApJL*, 524(2), L111–L114.
- Ventura, P., D’Antona, F., Mazzitelli, I., & Gratton, R. (2001). Predictions for Self-Pollution in Globular Cluster Stars. *ApJL*, 550, L65–L69.
- Ventura, P., Dell’Agli, F., Schneider, R., Di Criscienzo, M., Rossi, C., La Franca, F., Gallerani, S., & Valiante, R. (2014). Dust from asymptotic giant branch stars: relevant factors and modelling uncertainties. *MNRAS*, 439, 977–989.

- Ventura, P., Di Criscienzo, M., Carini, R., & D'Antona, F. (2013). Yields of AGB and SAGB models with chemistry of low- and high-metallicity globular clusters. *MNRAS*, 431, 3642–3653.
- Ventura, P., di Criscienzo, M., Schneider, R., Carini, R., Valiante, R., D'Antona, F., Gallerani, S., Maiolino, R., & Tornambé, A. (2012). The transition from carbon dust to silicate production in low-metallicity asymptotic giant branch and super-asymptotic giant branch stars. *MNRAS*, 420, 1442–1456.
- Ventura, P., García-Hernández, D. A., Dell'Agli, F., D'Antona, F., Mészáros, S., Lucatello, S., Di Criscienzo, M., Shetrone, M., Tailo, M., Tang, B., & Zamora, O. (2016a). Evidence of AGB Pollution in Galactic Globular Clusters from the Mg-Al Anticorrelations Observed by the APOGEE Survey. *ApJL*, 831, L17.
- Ventura, P., Karakas, A. I., Dell'Agli, F., García-Hernández, D. A., Boyer, M. L., & Di Criscienzo, M. (2016b). On the nature of the most obscured C-rich AGB stars in the Magellanic Clouds. *MNRAS*, 457(2), 1456–1467.
- Ventura, P. & Marigo, P. (2009). Evolution and chemical yields of AGB stars: effects of low-temperature opacities. *MNRAS*, 399, L54–L58.
- Ventura, P. & Marigo, P. (2010). Asymptotic giant branch stars at low metallicity: the challenging interplay between the mass-loss and molecular opacities. *MNRAS*, 408, 2476–2486.
- Ventura, P., Zeppieri, A., Mazzitelli, I., & D'Antona, F. (1998). Full spectrum of turbulence convective mixing: I. theoretical main sequences and turn-off for 0.6 / 15 Msun. *A&A*, 334, 953–968.
- Vincenzo, F., Belfiore, F., Maiolino, R., Matteucci, F., & Ventura, P. (2016). Nitrogen and oxygen abundances in the Local Universe. *MNRAS*, 458, 3466–3477.
- Vincenzo, F. & Kobayashi, C. (2018). Extragalactic archaeology with the C, N, and O chemical abundances. *A&A*, 610, L16.
- Volk, K., Kwok, S., Hrivnak, B. J., & Szczerba, R. (2002). Infrared Space Observatory Observations of the Unidentified 30 Micron Feature in Proto-Planetary Nebulae. *ApJ*, 567, 412–422.
- Volk, K., Sloan, G. C., & Kraemer, K. E. (2020). The 21 μm and 30 μm emission features in carbon-rich objects. *Ap&SS*, 365, 88.
- Wachter, A., Schröder, K. P., Winters, J. M., Arndt, T. U., & Sedlmayr, E. (2002). An improved mass-loss description for dust-driven superwinds and tip-AGB evolution models. *A&A*, 384, 452–459.
- Wachter, A., Winters, J. M., Schröder, K. P., & Sedlmayr, E. (2008). Dust-driven winds and mass loss of C-rich AGB stars with subsolar metallicities. *A&A*, 486, 497–504.
- Waelkens, C., Van Winckel, H., Waters, L. B. F. M., & Bakker, E. J. (1996). Variability and nature of the binary in the Red Rectangle nebula. *A&A*, 314, L17–L20.

- Weisz, D. R., Dolphin, A. E., Skillman, E. D., Holtzman, J., Dalcanton, J. J., Cole, A. A., & Neary, K. (2013). Comparing the ancient star formation histories of the Magellanic Clouds. *MNRAS*, 431, 364–371.
- Willems, F. J. & de Jong, T. (1986). Carbon Stars with Oxygen-rich Circumstellar Dust Shells: Observational Evidence for the Onset of the Carbon Star Phase. *ApJL*, 309, L39.
- Woods, P. M., Oliveira, J. M., Kemper, F., van Loon, J. T., Sargent, B. A., Matsuura, M., Szczerba, R., Volk, K., Zijlstra, A. A., Sloan, G. C., Lagadec, E., McDonald, I., Jones, O., Gorjian, V., Kraemer, K. E., Gielen, C., Meixner, M., Blum, R. D., Sewiło, M., Riebel, D., Shiao, B., Chen, C. H. R., Boyer, M. L., Indebetouw, R., Antoniou, V., Bernard, J. P., Cohen, M., Dijkstra, C., Galametz, M., Galliano, F., Gordon, K. D., Harris, J., Hony, S., Hora, J. L., Kawamura, A., Lawton, B., Leisenring, J. M., Madden, S., Marengo, M., McGuire, C., Mulia, A. J., O'Halloran, B., Olsen, K., Paladini, R., Paradis, D., Reach, W. T., Rubin, D., Sandstrom, K., Soszyński, I., Speck, A. K., Srinivasan, S., Tielens, A. G. G. M., van Aarle, E., van Dyk, S. D., van Winckel, H., Vijn, U. P., Whitney, B., & Wilkins, A. N. (2011). The SAGE-Spec Spitzer Legacy programme: the life-cycle of dust and gas in the Large Magellanic Cloud - Point source classification I. *MNRAS*, 411, 1597–1627.
- Xu, Y., Lin, Y., Zhang, J., & Hao, J. (2016). The First Discovery of Presolar Graphite Grains from the Highly Reducing Qingzhen (EH3) Meteorite. *ApJ*, 825, 111.
- Zaritsky, D., Harris, J., Thompson, I. B., & Grebel, E. K. (2004). The Magellanic Clouds Photometric Survey: The Large Magellanic Cloud Stellar Catalog and Extinction Map. *AJ*, 128, 1606–1614.
- Zhukovska, S., Gail, H. P., & Trieloff, M. (2008). Evolution of interstellar dust and stardust in the solar neighbourhood. *A&A*, 479, 453–480.
- Zijlstra, A. A., Matsuura, M., Wood, P. R., Sloan, G. C., Lagadec, E., van Loon, J. T., Groenewegen, M. A. T., Feast, M. W., Menzies, J. W., Whitelock, P. A., Blommaert, J. A. D. L., Cioni, M. R. L., Habing, H. J., Hony, S., Loup, C., & Waters, L. B. F. M. (2006). A Spitzer mid-infrared spectral survey of mass-losing carbon stars in the Large Magellanic Cloud. *MNRAS*, 370, 1961–1978.
- Zinner, E. (2008). Stardust in meteorites: A link between stars and the Solar System. In *Organic Matter in Space*, volume 251 (pp. 341–342).
- Zubko, V. G., Mennella, V., Colangeli, L., & Bussoletti, E. (1996). Optical constants of cosmic carbon analogue grains - I. Simulation of clustering by a modified continuous distribution of ellipsoids. *MNRAS*, 282, 1321–1329.